UNIVERSITY OF PATRAS
DEPARTMENT OF MECHANICAL ENGINEERING & AERONAUTICS
DIVISION OF APPLIED ENGINEERING, TECHNOLOGY OF MATERIALS & BIOMECHANICS
LABORATORY OF TECHNOLOGY & STRENGTH OF MATERIALS

DIPLOMA THESIS

STRUCTURAL ANALYSIS OF A COMMERCIAL AIRCRAFT WING WITH DISTRIBUTED PROPULSION

GIANNELOS VASILEIOS
1067248

Supervisor
PROFESSOR LABEAS GEORGE

Diploma Thesis submitted at Department of Mechanical Engineering & Aeronautics at University of Patras

PATRAS, March 7th, 2024

UNIVERSITY OF PATRAS

DEPARTMENT OF MECHANICAL ENGINEERING & AERONAUTICS

DIVISION OF APPLIED ENGINEERING, TECHNOLOGY OF MATERIALS & BIOMECHANICS

LABORATORY OF TECHNOLOGY & STRENGTH OF MATERIALS

ΔΟΜΙΚΗ ΑΝΑΛΥΣΗ ΠΤΕΡΥΓΑΣ ΕΠΙΒΑΤΙΚΟΥ ΑΕΡΟΣΚΑΦΟΥΣ ΜΕ ΚΑΤΑΝΕΜΗΜΕΝΗ ΠΡΟΩΣΗ

Η παρούσα διπλωματική εργασία παρουσιάστηκε

από τον

ΓΙΑΝΝΕΛΟ ΒΑΣΙΛΕΙΟ

1067248

την Πέμπτη 7 Μαρτίου, 2024

ΠΕΡΙΛΗΨΗ

Ο ταχέως αναπτυσσόμενος τεχνολογικός κόσμος έχει δημιουργήσει αυξανόμενες απαιτήσεις για τις αερομεταφορές όσον αφορά τις επιδόσεις, τη λειτουργία και, κυρίως, το περιβαλλοντικό αντίκτυπο. Η επιθυμία να επιτευχθεί η βιωσιμότητα των αερομεταφορών έχει οδηγήσει τη βιομηχανία να επικεντρωθεί στην εφαρμογή εναλλακτικών διαμορφώσεων, όπως τα συστήματα κατανεμημένης πρόωσης σε συνδυασμό με βιώσιμες πηγές ενέργειας. Στην παρούσα Διπλωματική Εργασία, μια διαμόρφωση κατανεμημένης ηλεκτρικής πρόωσης που τροφοδοτείται από ένα σύστημα κυψελών υγρού υδρογόνου εφαρμόζεται σε ένα μικρό, επιβατικό αεροσκάφος τύπου LSA, συγκεκριμένα το Zodiac CH 650 B που παράγεται από την Zenith Aircraft Company. Σκοπός είναι να πραγματοποιηθεί δομική ανάλυση της τροποποιημένης πτέρυγας του Zenith Zodiac CH 650 B χρησιμοποιώντας τόσο αναλυτικές μεθόδους όσο και μεθόδους πεπερασμένων στοιχείων, καθώς και να συγκριθεί με την αρχική διαμόρφωση. Η αναλυτική μέθοδος βασίζεται στην αντοχή των υλικών και την αεροδυναμική, ενώ η μέθοδος των πεπερασμένων στοιχείων απαιτεί επίσης σχεδιασμό και μοντελοποίηση της δομής της πτέρυγας σε CATIA και ANSYS αντίστοιχα. Αξιολογείται επίσης η βελτίωση των επιδόσεων του αεροσκάφους, καθώς οι δυνατότητες σύντομης απογείωσης-προσγείωσης, η μείωση του θορύβου, η αύξηση της αποδοτικότητας και οι (σχεδόν) μηδενικές εκπομπές αποτελούν απαιτούμενα χαρακτηριστικά των μελλοντικών αερομεταφορών.

Λέξεις Κλειδιά

Επιβατικό Αεροσκάφος, Δομική Ανάλυση Πτέρυγας, Κατανεμημένη Ηλεκτρική Πρόωση, Βιώσιμες Αερομεταφορές, Κυψέλες Υγρού Υδρογόνου

ABSTRACT

The rapidly developing technological world has created growing aviation demands regarding aircraft performance, operation and crucially; environmental impact. The urge to achieve aviation sustainability has led the industry to focus on implementing alternative configurations, such as Distributed Propulsion systems coupled with sustainable power sources. In this Thesis, a Distributed Electric Propulsion configuration powered by a liquid Hydrogen Fuel-Cell system is implemented on a small, commercial Light Sport Aircraft, specifically the Zodiac CH 650 B produced by Zenith Aircraft Company. The purpose is to perform a structural analysis on the Zenith Zodiac CH 650 B modified wing using both analytical and finite element methods and also compare it to the original configuration. The analytical method relies on strength of materials and aerodynamic theory while the finite element method also requires designing and modeling the wing structure in CATIA and ANSYS respectively. Aircraft performance improvements are also evaluated, as Short Take Off Landing capabilities, noise reduction, efficiency increase and (near) zero emissions are required characteristics of future aviation.

Keywords

Commercial Aircraft, Wing Structural Analysis, Distributed Electric Propulsion, Sustainable Aviation, Liquid Hydrogen Fuel-Cell

LIST OF TABLES

LIST OF FIGURES

ABBREVIATIONS

DP	Distributed Propulsion
DEP	Distributed Electric Propulsion
TeDP	Turboelectric Distributed Propulsion
ICE	Internal Combustion Engine
STOL	Short Take-Off Landing
VTOL	Vertical Take-Off Landing
MTOW	Maximum Take-Off Weight
OWE	Empty Operating Weight
PAY	Payload
HWB	Hybrid Wing Body
BWB	Blended Wing Body
NZE	Near-Zero Emissions
AEA	All-Electric Aircraft
MEA	More-Electric Aircraft
AR	Aspect Ratio
TR	Taper Ratio
v_0	Freestream Velocity
v_i	Propeller-Induced Velocity
L	Lift
D	Drag
PM	Pitching Moment
C_L	Lift Coefficient
C_D	Drag Coefficient
L/D	Lift/Drag Ratio
C_M	Pitching Moment Coefficient

AoA	Angle of Attack
Re	Reynolds Number
T	Thrust
σ	Normal Stress
q	Shear Flow
τ	Shear Stress
ε	Strain
Q	Shear Force
M	Bending Moment
M_T	Torsion Moment
c	Chord
F	Cross-Section
A	Surface Area
I_{axis}	Second Moment of Inertia
S_{axis}	First Moment of Inertia

CONTENTS - INDEX

1.0 INTRODUCTION

1.1 DISTRIBUTED PROPULSION DEFINITION

Distributed Propulsion in aircraft application is the spanwise distribution of the propulsive thrust system such that overall vehicle benefits in terms of aerodynamics, propulsive, structural and/or other efficiencies are mutually maximized to enhance the vehicle mission [2].

The concept of Distributed Propulsion is based on dividing up the thrust for the beneficiary gain of noise reduction, shorter take-off and landing, enhanced specific fuel consumption and flight range [1].

1.2 THESIS PURPOSE

The current Thesis' purpose is to investigate the effects of installing a Distributed Propulsion system on the wing structure of a commercial aircraft. The implementation of the Distributed Propulsion system will define whether the wing structure should either be further reinforced or could be made more lightweight.

Potential advantages such as the increased generation of Lift, the elimination of wing tip vortices and potential disadvantages such as the creation of Pitching Moments or a weight penalty of such a configuration will be reviewed.

The influence of a Distributed Propulsion system with electric motor-driven propellers on aircraft operation and performance will also be investigated, as critical flight attributes such as Noise, Emissions, Short Take-Off Landing (STOL) are involved.

Conclusions reached in this Thesis can be further evaluated and utilized in larger aircraft if the Distributed Propulsion configurations reviewed are deemed beneficiary and can contribute to the satisfaction of the growing aviation demands.

1.3 THESIS STRUCTURE

The first Chapter is an introduction to the topic of the Diploma Thesis, presenting the definition of distributed propulsion and important notions used extensively in the Thesis.

The second Chapter consists of the literature review regarding distributed propulsion and its types, along with potential advantages and disadvantages. A historical overview of conceptual and actual Distributed Propulsion aircraft as well as some words about electric aviation and sustainability are also included.

The third Chapter presents lightweight structure philosophy, the material used in this Thesis, aircraft specifications of the Zenith Zodiac CH 650 B, its wing structure and the concept of DEP conversion implemented on this exact aircraft.

The fourth Chapter presents the analytical structural analysis of the DEP converted wing, while also comparing it with a reference configuration, albeit first having included the theoretical structural and aerodynamic background.

The fifth Chapter presents the ANSYS modeling and the resulting computational structural analysis of the DEP converted wing, while also comparing it with a reference configuration, albeit first having included the finite element theory.

The sixth Chapter explains the differences between the theoretical and computational methods of analysis, presents the Thesis results and review, while also proposing subjects of future research based on this Thesis findings.

2.0 LITERATURE REVIEW

2.1 TYPES OF DISTRIBUTED PROPULSION

A number of fixed wing aircraft using Distributed Propulsion have been proposed and flown before. These configurations can also be categorized based on the overall concept, type of propulsion system and/or the energy source. For example, we have:

- **Multiple Discrete Engines:** Various types of aircraft using multiple propulsors have been proposed and flown. For these aircraft, propulsors such as propellers, turbojets, or turbofans are mounted in front of the wing, at the back of wing, or within the thick section of wing.
- **Distributed Multi-Fans driven by few Engine Cores:** Distributed propulsion employing multiple propulsors driven by a few fuel-efficient engine cores has been studied and is being pursued under NASA's SFW N+3 project (presented in Chapter 2.4, Sustainability in Aviation). Under this category, three types of propulsion system are identified and described below.
    1. *Gas-driven Multi-Fans:*
       Multi-Fans operation actuated via hot exhaust gases from a number of Gas Generators.
    2. *Gear-driven Multi-Fans:*
       Multi-Fans powered by an engine core and transferred via Gear mechanism.
    3. *Electrically-driven Multi-Fans:*
       The electricity is provided to the Multi-Fans via power lines, utilizing Battery, Fuel-Cell, hybrid Turboelectric (TeDP) systems etc.
- **Jet Flaps:** A concept where a high-velocity thin jet sheet emanates from a tangential slot at or near the wing trailing edge and provides spanwise thrust for cruise and supercirculation for high lift around the whole wing section during take-off and landing.

- **Cross-Flow Fan:** The cross-flow fan (CFF), or transverse fan, is a two-dimensional spanwise propulsor that is integrated within a wing structure to distribute the thrust along the wingspan. The fan ingests the wing upper and lower surface boundary layer air and ejects the air at the wing trailing edge. In this configuration, two gas generators mounted at the wing root and the wing tip transmit the power to the CFF rotors that are placed near the wing trailing edge and connected by flex-couplings or universal joints. However, because of low performance of the fan and difficulty of installation within an aircraft wing structure, this transport concept was never put into practice.

In the broad aspect of engine configurations, one can also divide distributed vectored propulsion into three main categories [1] (while also seeing the similarities with the categorization above):

- **Distributed Engines (DEN):** Distribution of Thrust via Distribution of Engines
  (Multiple Discrete Engines)
- **Distributed Exhausts (DEX):** Distribution of Thrust via Distribution of Exhaust Gases
  (Jet Flaps, Cross-Flow Fan)
- **Common-core Multi-Fans/Propulsors (CMF/CMP):** Multiple Fans/Propellers powered by a common energy source
  (Distributed Multi-Fans driven by few Engine Cores)

An All-Electric Aircraft (AEA) concept in combination with Distributed Propulsion technology is considered, as the electric aircraft trend displays one of the environmentally friendly propulsion options for future commercial aircraft [1].

2.2 ADVANTAGES OF DISTRIBUTED PROPULSION

A Distributed Propulsion configuration can present plenty of advantages in aircraft applications, through improvement in operation, performance and environmental impact, according to various studies. Some of them are mentioned below.

- DP can result in **Fuel Consumption reduction** by ingesting the thick boundary layer flow and filling in the wake generated by the airframe with the distributed engine thrust stream.
- DP can provide **High Lift spanwise** via high-aspect-ratio trailing edge nozzles for **Thrust Vectoring** (TV) providing **powered lift**, **boundary layer control** and/or **supercirculation** around the wing, all of which enable **Short Take-Off Landing** (STOL) capabilities.
- DP can lead to better integration of the propulsion system with the airframe for **reduction in Noise** to the surrounding community through **airframe shielding**.
- DP can offer **reduction of aircraft propulsion Installation Weight** through inlet/nozzle/wing **structure integration**.
- DP can **eliminate aircraft Control Surfaces** through differential and vectoring thrust for pitch, roll and yaw moments.
- DP can offer **high production rates and easy replacement** of engines or propulsors that are small and light.
- For the Multi-Fan/Single Engine Core concept such as TeDP, the configuration provides a very **high bypass ratio**, enabling **low fuel burn**, **emissions and noise** to surrounding communities [2].

- Distributing the propulsion system using a number of small engines instead of a few large ones could **reduce the total propulsion system noise**.
- Another advantage is the **improvement in safety due to engine redundancy**. With numerous engines, an engine-out condition is not as critical to the aircraft's operation in terms of loss of available thrust and controllability.

- The **minimization of heavy concentrated weight** burden on the wing structure and **load re-distribution** provided by the engines/propulsors has the potential to alleviate passive load alleviation problems, thus resulting in a **lower Wing Weight**.
- Possible improvement in **affordability** due to the use of smaller, easily-**interchangeable engines** [3].

- DP systems can be **more efficient** than traditional centralized propulsion systems. They allow for better control of power distribution, which can lead to reduced energy losses and **increased overall system efficiency**.
- DP allows for **greater design flexibility** in terms of **aircraft layout** and configuration. It can lead to more innovative and unconventional aircraft designs.
- DEP configurations offer **local Zero-Emissions** and if combined with electricity or hydrogen produced by renewable sources, **carbon neutral** operation can be achieved. Carbon neutrality would prove that **sustainable aviation** is achievable.
- DEP Propeller systems that are powered by **Electric Motors** can significantly **reduce the noise** due to the absence of fuel-burning Turbojets/Turbofans or aircraft Internal Combustion Engines.
- DEP configurations also provide **additional power for take-off**, **reduction of runway length** and **propeller drag force** and finally **skid avoidance during the landing phase**.
- For a given wing surface area and conditions (density, freestream velocity and angle of attack), a DEP configuration provides a **significant increase in Lift production**. Therefore, either the surface area can be reduced, resulting in **friction drag reduction**, or the increased lift can be utilized for **STOL capabilities**.

The increase of Lift during Take-Off and Landing and the resulting STOL capabilities and Runway Length reduction is a crucial advantage in aircraft performance and will be investigated more thoroughly in Chapter 4.1.2, where the propeller-air interaction and the Slipstream effect are studied.

2.3 DISADVANTAGES OF DISTRIBUTED PROPULSION

Distributed Propulsion can present important advantages albeit without ignoring potential disadvantages. Some of them are mentioned below.

- Usually, DP configurations result in **weight penalties**, due to the need for additional components, such as multiple engines, motors, batteries, hydrogen tanks etc. Such weight penalties might reduce the passenger capacity or the payload.
- Big Turbojets/Turbofans Engines achieve high **thermal efficiency** (partly due to higher bypass ratios), whereas smaller such engines significantly lack this kind of efficiency.
- The added **complexity** and components of DP systems can lead to **higher manufacturing and maintenance costs**. DEP systems, in particular, may have higher initial costs due to the expense of Electric Motors, Inverters, Batteries and Fuel-Cells.
- Another challenge of DP configurations is the **thermal management**. Managing heat generated by multiple propulsion units in a distributed system can be challenging. Efficient thermal management is crucial to prevent overheating and ensure safe operation.
- **Technology** that could prove vital to DP application is **not adequately advanced**, such as the superconductors/superconducting materials that are required in TeDP configurations to improve drastically the system efficiency.
- DP configurations may present **challenges in integrating** multiple propulsion units into the aircraft's design, requiring careful consideration of aerodynamics, structural integrity, and thermal management.

2.4 SUSTAINABILITY IN AVIATION

Concerns about the environment and the energy usage, along with the constant increase of air passengers, have resulted in increased aviation demands and led the aerospace and the engineering sector to explore alternative solutions in materials, propulsion systems etc. in order to achieve technological innovation and sustainability in aviation.

The needs for aviation sustainability currently motivate the identification of propulsion systems solutions that address some of the published goals for future aviation. These visions primarily target reduction of fuel consumption, aircraft emissions, aircraft noise and may also stress the minimization of the industrial impact on the global on the global environment [1].

In response to the growing aviation demands and concerns about the environment and energy usage, **NASA's Subsonic Fixed Wing program** (SFW) focuses on 4 'corners' of the technical trade spaces for future aircraft design: fuel burn, emissions, noise, field length. Created in 2010, NASA set three timeframes of accomplishments, named N+1 (2015), N+2 (2020), N+3 (2025) respectively. Although it may not be feasible to meet all the goals for each time frame, the multi-objective studies attempt to identify possible vehicle concepts that have the best potential to meet the combined goals. In order to meet NASA's N+3 goals, drastic changes in propulsion and airframe systems are required and proposed. One such proposed concept is based on a distributed propulsion system using advanced electric power generation and transfer of power to remotely located distributed electric fans [2].

European Union's **FlightPath2050** goals have already been set and agreed by the aviation partners. Among them, one set goal is protecting the environment and the energy supply (75% reduction in CO2 emission per passenger kilometer, 90% reduction in NOx emissions, 65% reduction in noise emission and emission-free aircraft movement when taxiing) [4].

CORNERS OF THE TRADE SPACE	N+1 (2015)*** Technology Benefits Relative to a Single Aisle Reference Configuration	N+2 (2020)*** Technology Benefits Relative to a Large Twin Aisle Reference Configuration	N+3 (2025)*** Technology Benefits
Noise (cum below Stage 4)	- 32 dB	- 42 dB	- 71 dB
LTO NOx Emissions (below CAEP 6)	-60%	-75%	better than -75%
Performance: Aircraft Fuel Burn	-33%**	-50%**	better than -70%
Performance: Field Length	-33%	-50%	exploit metroplex* concepts

*** Technology Readiness Level for key technologies = 4-6
** Additional gains may be possible through operational improvements
* Concepts that enable optimal use of runways at multiple airports within the metropolitan areas

Εικόνα 1: NASA's Future Aviation Goals

2.5 THE ELECTRIC AIRCRAFT

Tracing the evolution of the electric aircraft is interesting from both a historical point of view and for future considerations of civil aviation, especially taking into account the rising aviation demands in terms of sustainability.

One of the distinct characteristics of the electric aircraft is that it employs electric motors instead of internal combustion engines. For this purpose, the electricity can be supplied to the electric motors using different methods. In the past, fuel cells, batteries, solar cells, ultra capacitors and other means have been considered for this purpose.

The electric aircraft can broadly be divided into two main categories: the All-Electric Aircraft (AEA) and the More-Electric Aircraft (MEA). A deeper understanding of the Primary Power Systems (PPS) referring to the main propulsion power, and Secondary Power Systems (SPS) referring to the distributed power around the airframe and the engine systems can cast light on the AEA and MEA concepts.

Many complexities with electric aircraft propulsion have played a noteworthy role in the evolution of the AEA. Restrictions in a given technology have further motivated the exploration of alternative systems to be used in the electric aircraft. An important example for this is the introduction of Fuel-Cells in aeronautics. Early Fuel-Cells were associated with other technical objectives rather than used as electrochemical devices to produce electricity. Fuel-Cells provided an alternative technology for the electric aircraft. As knowledge, research and technology have significantly advanced, Fuel-Cells are now a serious proposal in AEA applications and could be the answer to sustainability demands as explained further in this Thesis.

Electric aircraft propulsion system topologies are presented below. While all or most topologies will be covered in this Thesis, focus will be mainly given to the All-Electric topologies due to the sustainable aviation demands in the industry. The electric aircraft propulsion topology chosen to implement in the Zenith Zodiac CH 650 B is the Fuel Cell based one, with only Fuel Cell powered electric propulsors.

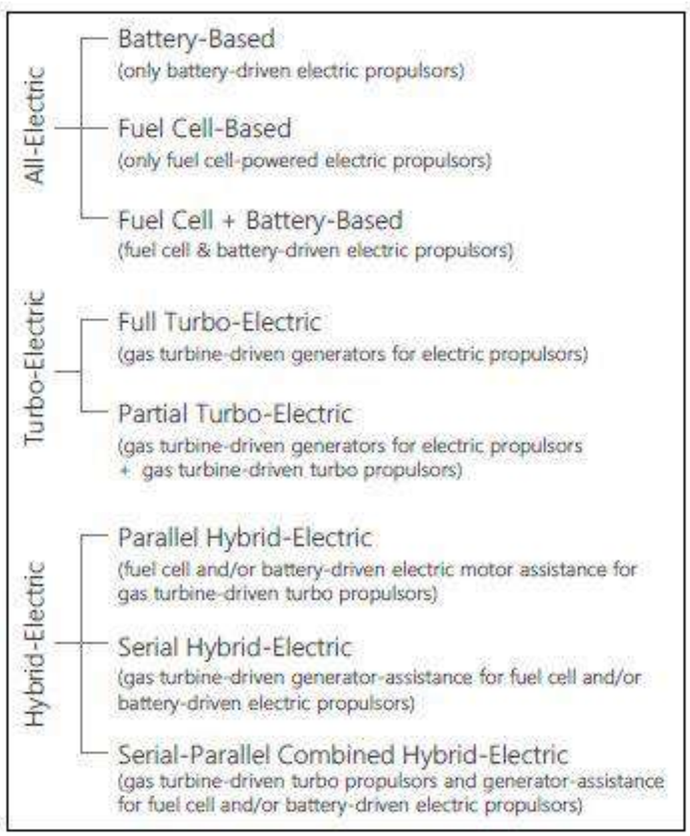

Εικόνα 2: Electric Aircraft Propulsion Architectures

2.6 HISTORICAL REVIEW

The idea of Distributed Propulsion and All-Electric Aircraft concepts in aviation is not a matter of the last few decades. A brief Historical Review of the respective milestones is presented below.

2.6.1 Conceptual Milestones of Aircraft Distributed Propulsion

In 1924, Manzel proposed multiple propeller units arranged in rows or series as the propelling mechanism for airships, aircrafts etc. The motivation behind this concept was the feasibility of ascent without a special landing field.

In 1932, Altieri's invention was based on using auxiliary propellers fore and aft of the aircraft wings. Recognizing the small effect of supplemental propulsion assistance, using additional propellers, this concept was primarily aimed for proper and safe landings.

In 1954, Griffith replaced the earlier propositions of propellers with gas turbines and presented the concept of an aircraft with a master combustion engine unit in combination with a number of gas turbine 'slave' units that were spaced in the spanwise direction of the aircraft wing structure, providing the means for Thrust Vectoring (TV), Short Take-Off and Landing (STOL) and low fuel consumption. This invention combined many new technical features of significant potential [1].

In the late 1960's, a Vertical/Short Take-off and Landing (V/STOL) air-deflection and modulation (ADAM III) fighter concept was studied for various missions, utilizing a Distributed Propulsion system with Gas-driven Multi-Fans. The design never went into production possibly because of the problem of ducting hot gas through the wing structure. In this concept, the gas generators and their inlets were installed near the fuselage to provide hot gas to the wing mounted turbines that drove high-bypass-ratio turbofans. The turbofans and turbines were co-located in the wing section away from the gas generators. The hot gases from the gas generators were routed through long ducts across the wingspan to the location where the turbines and fans were installed. The inlets and nozzles for the turbofans and turbines were also all within the wing structure away from the gas generators and provided distributed thrust to the vehicle.

Then in the 1970's, a Gas-driven Multi-Fan transport aircraft was conceived, and a model was tested for STOL operation. It was based on a conventional 'tube and wing' airframe configuration with 16 tip-driven fans spread along the top surface near the wing trailing edge. The tip-driven fans with fan pressure ratio of 1.25 were powered by high-pressure discharge air from the low-pressure compressor stages and mounted on a hinged flap to achieve high lift via supercirculation. In addition, the massive suction effect in front of inlets created additional lift on the airframe and delayed flow separation on the wing upper surface [2].

In 1974, pursuing another research front, Malvestuto Jr. took interest in an aircraft capable of carrying substantial payloads. Using a wing structure, divided into several wing portions equipped with rotors together with rotors in arrangement with lighter-than-air buoyancy units, this rotor-wing combination distributed the power over a much larger effective area to achieve considerably higher power loadings, in comparison to a conventional power loading of a helicopter. As a result, distributed propulsion was also considered and introduced for Vertical Take-Off and Landing (VTOL) aircraft. One could argue that this concept brought Manzel's 1924 concept to a new level, using a wealth of knowledge that was gained over almost 60 years.

In 1983, a concept for a solar powered aircraft with a cruciform wing structure was proposed. Equipped with solar cells and multiple propellers positioned on the wingtips, details were provided on how to maintain surfaces normal to the sun's rays to utilize the direct solar energy. This concept, amongst others, served as a crucial step towards the development of solar airplanes, such as the first generation High-Altitude Long Endurance (HALE) vehicle, Pathfinder.

In 1988, NASA proposed a number of derailed concepts for airframe and propulsion interactions and integrations. A commonality between these concepts is the employment of different propulsion systems.

SnAPII featured twin fuselages separated by a circulation-control wing that contributed to high lift coefficients during takeoff and landing. Using two tail-mounted engines at the end of each fuselage with Thrust Vectoring (TV) and reversing, fuselage Boundary Layer Ingestion (BLI) and smart inlet and nozzle technology, SnAPII also used a device to power flow control on the outer portions of the wing. Wing tip turbines could further reduce the wake hazard at takeoff and landing. This concept merged two individual fuselages with their propulsive units into one main body.

A hypothetical scenario of total engine failure for either one of the combined fuselages was simplified in the subsequent proposal for a Distributed Engines (DEN) regional STOL aircraft.

This airplane made use of an array of wing-integrated mini-engines to provide lift augmentation and distribution with increased redundancy. Employing another array of mini-engines at the tail, integrated with inlet and nozzle, deflectors enabled the Coanda effect for TV.

Using a similar circulation-control wing similar to SnAPII, a blended forward swept wing body concept was envisioned. This aircraft used three aft-mounted high-bypass ratio turbofans with BLI, TV and reversing, smart inlet, nozzle technology and flow control systems.

The Trans-Oceanic Air-Train was characterized by two vehicles, the Lead and the Mule. These vehicles rendezvous to complete the cruise configuration of a long-range transport of cargo. Although the design was aimed at freight flight in the low transonic regime, in favor of high aspect ratio wings and span loading for minimal fuel consumption, parts of this concept could potentially also be applied to commercial aviation. Equipped with TV-technology for optimal takeoff performance, the Lead vehicle was designated as the primary fuel carrier and responsible for flight control activities of all Mule vehicles [1].

A Gear-driven Distributed Propulsion concept employing a dual fan driven by one engine core on a HWB airframe was recently studied by NASA . The study was to determine the effects of a dual-fan engine configuration on the vehicle-level performance (i.e., range) of a representative subsonic transport and to develop a preliminary understanding of the challenges associated with the implementation of distributed propulsion schemes. The mentioned study shows one such concept where an engine core drives two large-diameter fans via gears and shafts, providing a very high bypass ratio. In this configuration, the core engine is outside the airframe boundary layer flow with almost 100% inlet total pressure recovery, and the dual fan ingests full boundary layer flow approaching the inlet cowl lip.

For the Silent Aircraft Initiative, the Cambridge-MIT Institute developed the SAX-40 conceptual HWB aircraft using a similar Gear-driven Multi-Fan propulsion concept. The purpose of this study was to design an aircraft with noise being the primary design variable addressed, such that the noise would be contained within the perimeter of an urban airport. This aircraft employs three engine nacelles where each nacelle houses three fans that are connected to a single engine core through gears and shafts. Similar to NASA’s study, this propulsion concept also has a very high bypass ratio and low engine noise. Also, it features inlets with a high amount of airframe upper surface boundary layer ingestion.

Recently, a cruise-efficient STOL (CESTOL) aircraft was proposed based on a high subsonic HWB or BWB transport configuration because of its high cruise efficiency, low noise characteristics, and a large internal volume for integrating embedded distributed propulsion system. The propulsion system employed 12 small conventional engines partially embedded within the wing structure and mounted along the wing upper surface near the trailing edge to enable STOL operation using low-pressure-fan diverted-bypass air. The vehicle concept uses distributed propulsion for quiet powered lift using an internally blown flap, with substantial engine noise shielding effect by the airframe, rapid climb out, and steep descent approach to provide a very low noise footprint on the ground. These characteristics of the aircraft may enable 24-hour use of the underutilized regional and city-center airports to increase the capacity of the overall airspace while still maintaining efficient high subsonic cruise flight capability.

To improve performance and to reduce environmental impacts even further, a drastic change in the power transmission of distributed propulsion system for large transport aircraft was proposed and studied on HWB as well as tube and wing airframes. Thus, the N3-X Vehicle was conceived by NASA. Using a new concept called “Turboelectric Distributed Propulsion (TeDP)”, one of the vehicles adopts the mentioned above 12-engine CESTOL-HWB airframe but employs two (2) remotely located gas turbine-driven superconducting generators to drive 14 distributed fans instead of using many small conventional engines. This arrangement allows the use of many small partially embedded fans while retaining the superior efficiency of large core engines, which are physically separated but connected to the fans through electric power lines. The airframe is derived from Boeing’s N2A HWB configuration with similar mission characteristics of a 6,000-nmi | 11,112-km range, a 103,000-lb | 46,720-kg payload capacity, and the ability to fly at the aerodynamic design point (ADP) of Mach 0.8 at 31,000 ft | 9445 m altitude. The propulsion system utilizes superconducting electrically driven, distributed low-pressure-ratio (1.35) fans with power provided by two remote superconducting electric generators based on a conventional turbofan core engine design. The use of electrical power transmission allows a high degree of flexibility in positioning the turbogenerators and propulsor modules to best advantage. In the aircraft configuration examined the turbogenerators were located at the wing tips where the turbogenerator would experience undisturbed free-stream conditions, while the fan modules were positioned in a continuous fan nacelle across the rear fuselage where they ingest the thick boundary-layer flow, fill the wake of aircraft with fan discharge air, and thereby reduce the thrust required by the vehicle. This concept is one of the several concepts pursued by NASA to meet N+3 goals.

As a part of NASA's Small Business Innovative Research (SBIR) phase 1 contract study, Empirical Systems Aerospace, LLC, conducted a system study of integrating an advanced cryogenic electric propulsion system onto a 150-passenger STOL regional airliner, the ECO-150, and a larger 250-passenger large transport, the ECO-250. A key feature of these two concepts, is the integration of the superconducting-electric motor-driven fans with the wing such that the inboard wing is separated into top and bottom sections, and all electric-driven propulsors are completely embedded within the airfoil or wing structure. This feature provides a benefit of wing weight reduction through wing bending moment relief because the distributed electric fans and the use of the common nacelle as wing rib structure provide stress relief to the wing structure. In addition, a favorable aerodynamic advantage exists such that at low speed, thrust vectoring of a two-dimensional low temperature nozzle may provide supercirculation of airflow around the airfoil for a large improvement in lift coefficient. Another key feature of the concepts is the use of liquid hydrogen both as a cooling fluid for the superconducting system and as fuel for the turboelectric generator engine. Although the study was very preliminary in nature, these propulsion system features along with the vehicle configuration itself did certainly point toward large reduction in fuel burn for both ECO-150 and ECO-250 configurations.

Another TeDP vehicle concept named "H3.1" was recently proposed and studied by MIT as a part of NASA's SFW N+3 cooperative work. The vehicle is based on the HWB configuration with a range of 7,600 nmi (14,075 km), 354 passengers, and cruise Mach 0.8 at 35,000 ft (10,668 m) altitude. Similar to NASA's N3-X vehicle, this vehicle also ingests upper airframe surface boundary-layer flow to improve propulsive and hence the fuel efficiency while minimizing noise impact to the surrounding community by shielding the propulsion-related noise with the airframe. Another key feature of this configuration is the use of cryogenic methane as fuel because of its higher specific energy, which improve the fuel efficiency of the aircraft. In addition, the cryogenic fuel allows the use of superconducting materials to distribute the electric power from three turboelectric generators to 23 electric fans that are semi-embedded in the upper surface of the airframe [2].

Depiction	Aircraft	Year
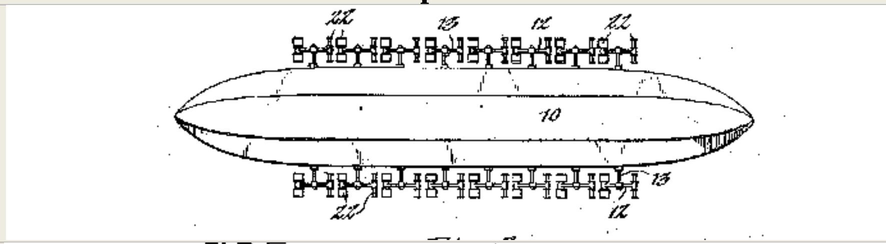	Manzel's Propeller-Array Airship Concept	1924
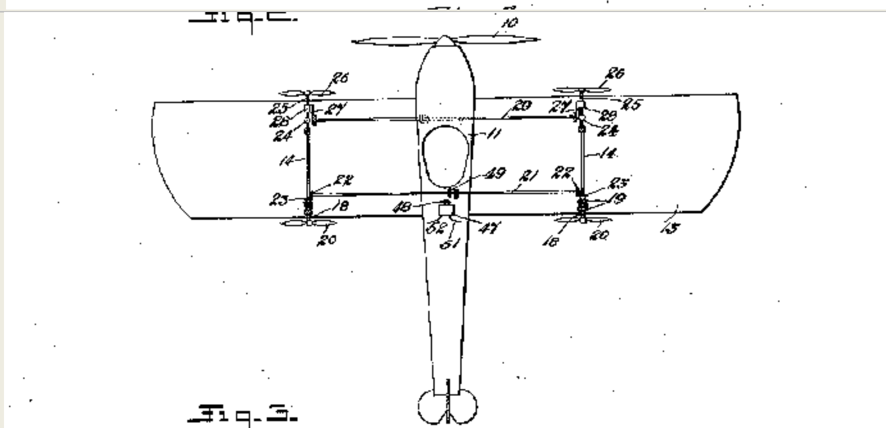	Altieri's 5-Propeller Concept	1932
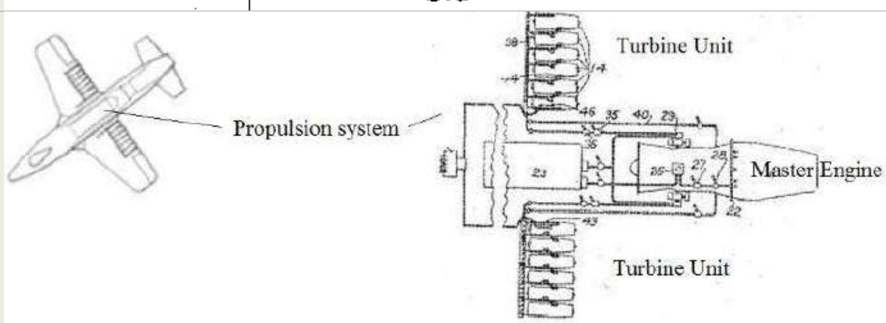	Griffith's Concept	1954
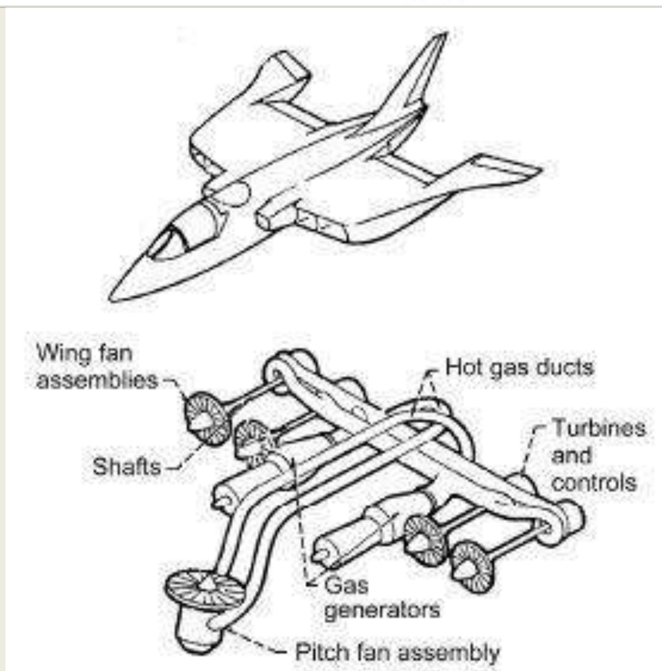	ADAM III Gas-Driven Multi-Fans Fighter Plane Concept	1960s

	Gas-Driven Multi-Fans STOL Transport Concept	1970s
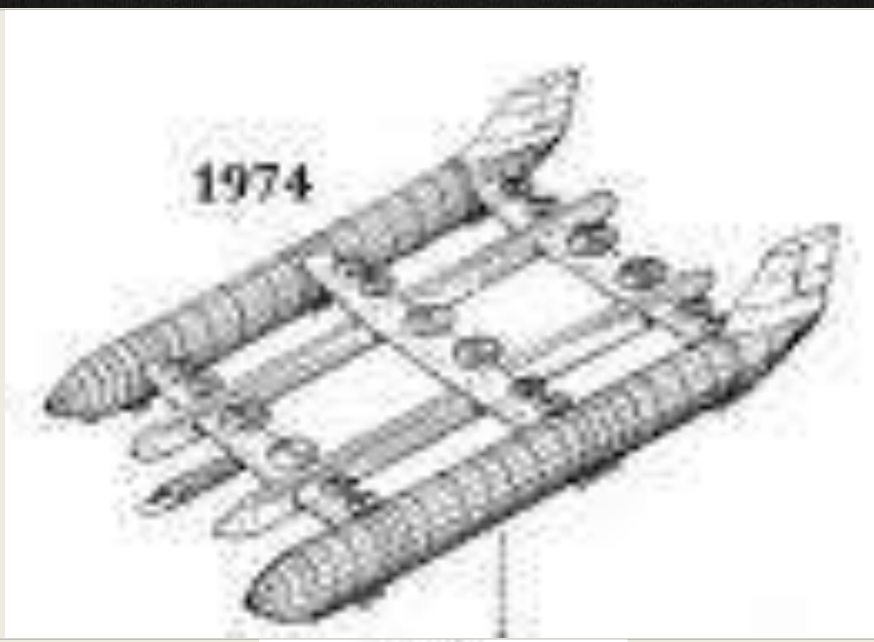	Malvestuto Jr.'s VTOL Aircraft Concept	1974
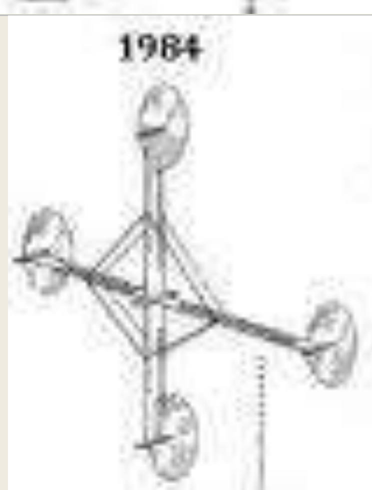	Cruciform Solar-powered Aircraft Concept	1983

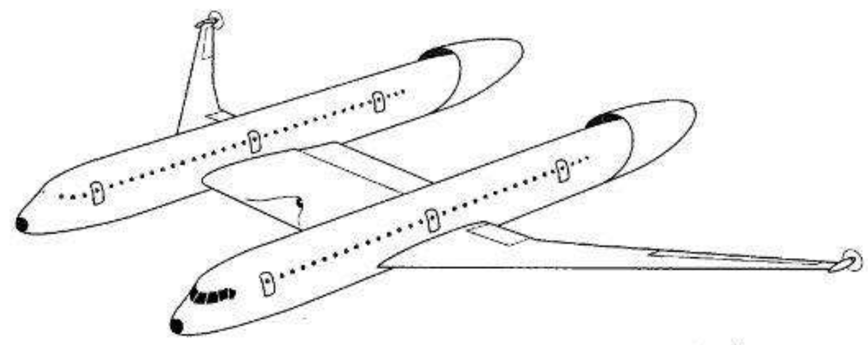	NASA's SnAPII Twin-Fuselage Wingtip Turbines Concept	1988
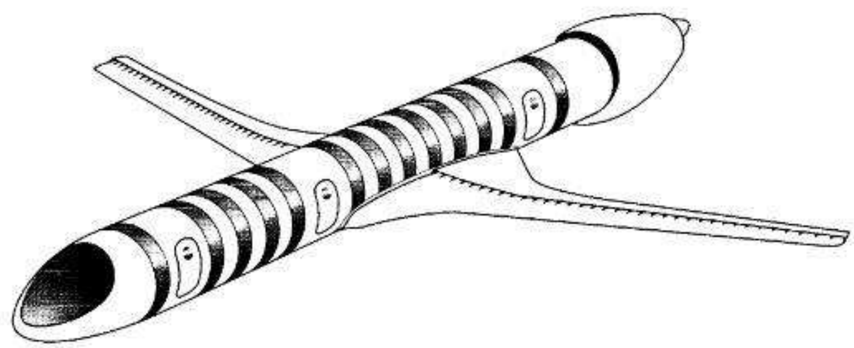	NASA's Distributed Engine Regional STOL Concept	1988
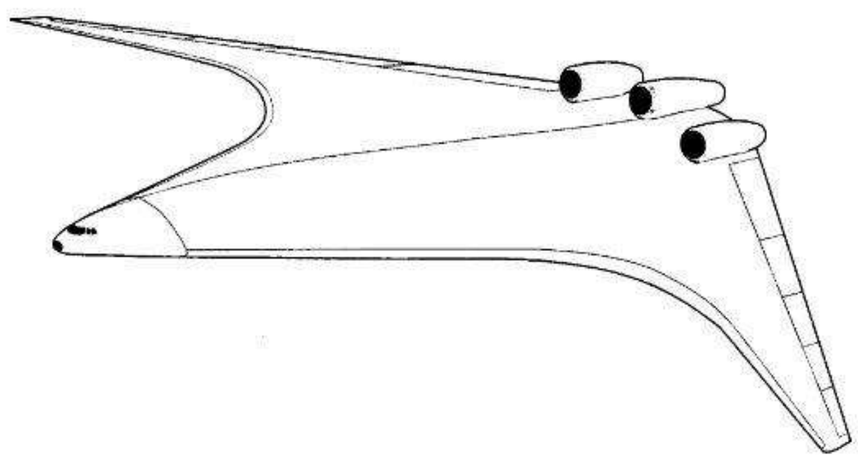	NASA's Forward Swept BWB Concept	1988
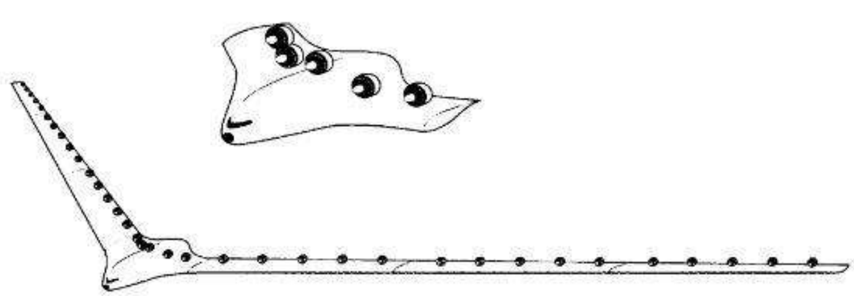	Trans-Oceanic Air-Train Concept	1988

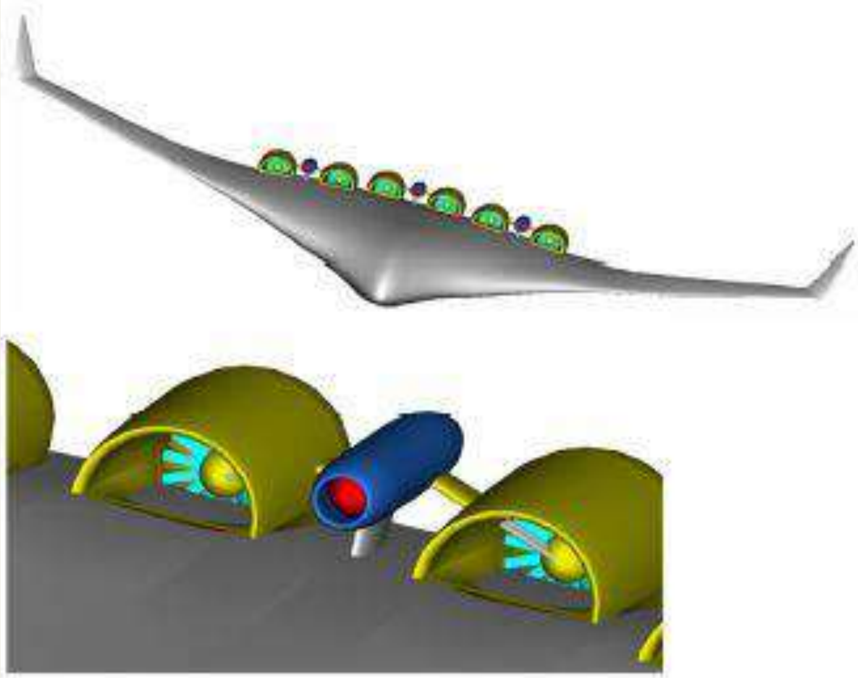		Gear-Driven Dual Fan, Single Core HWB Concept	Present Day
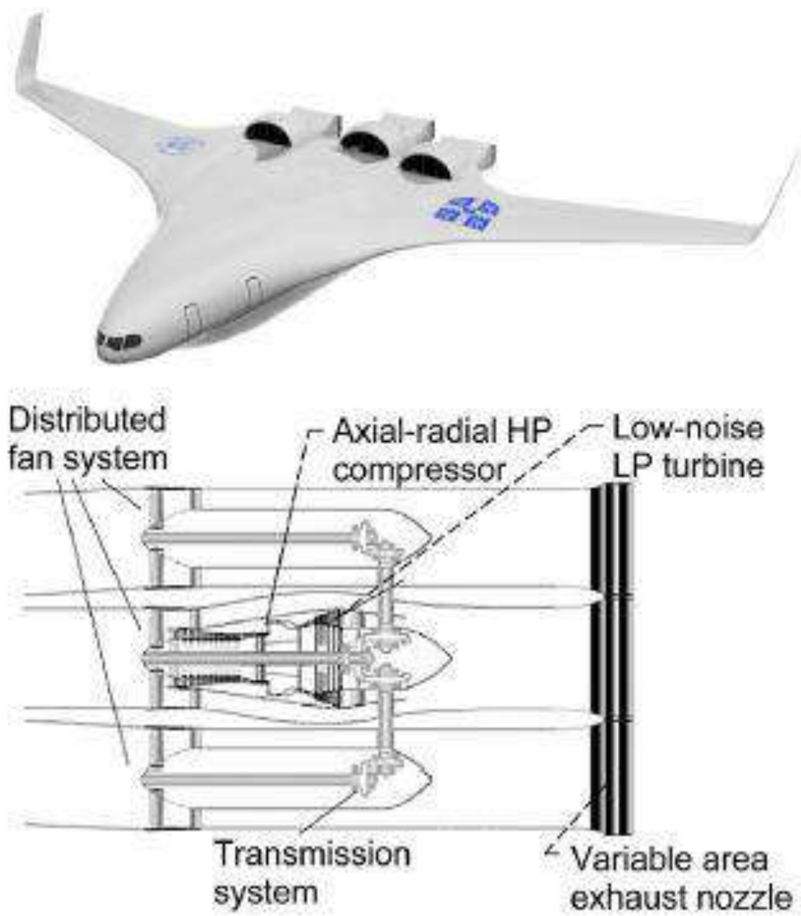		Cambridge & NASA's Gear-Driven Multi-Fans SAX-40 Concept	Present Day

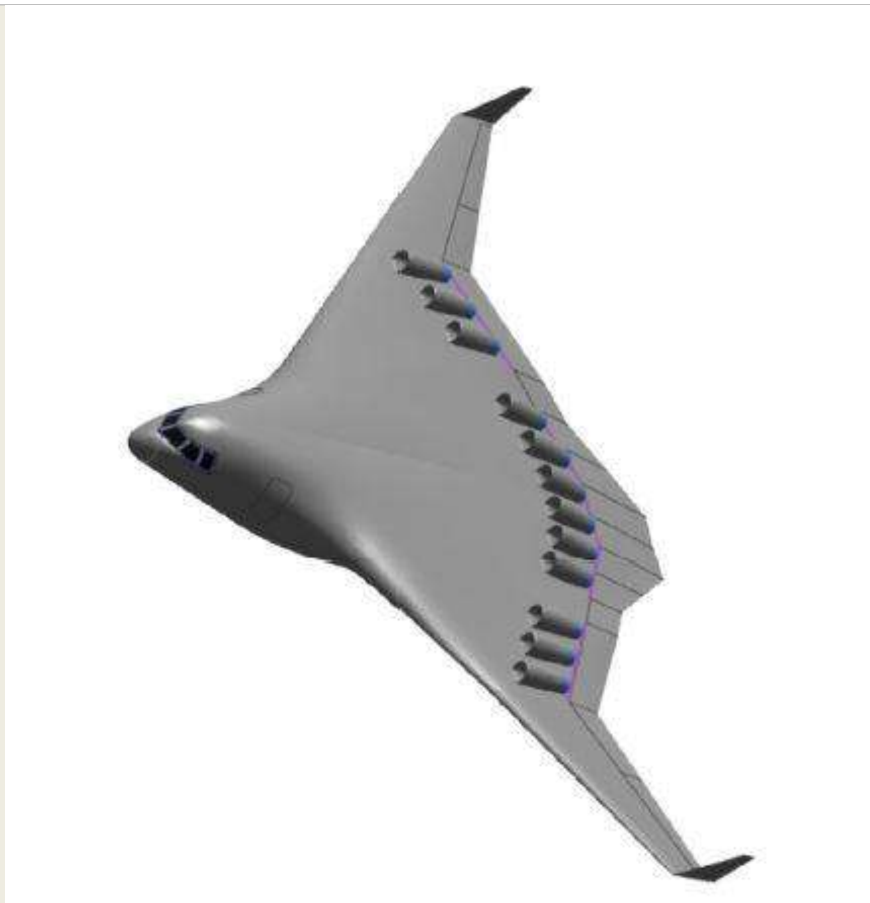	NASA's CESTOL Concept	Present Day
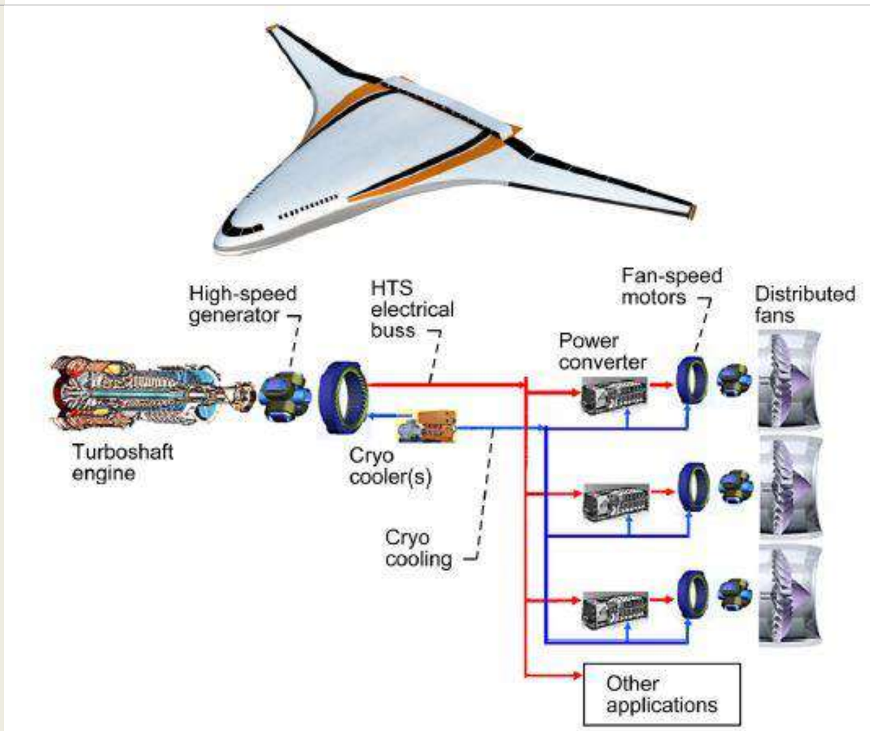	NASA's TeDP N3-X Concept	Present Day

 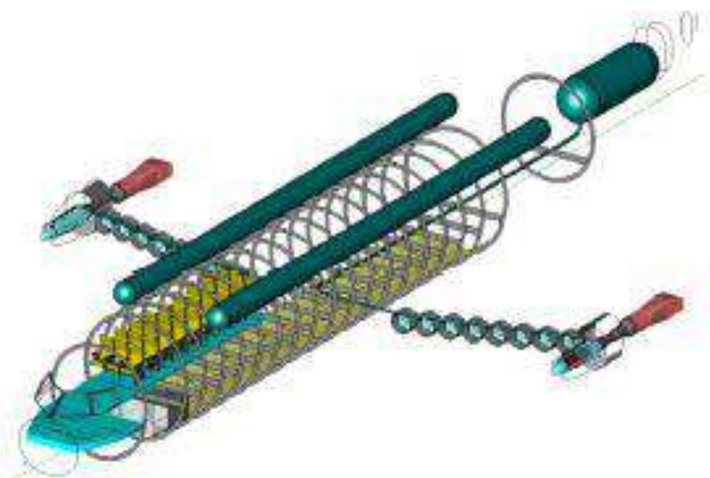	Empirical Systems Aerospace TeDP ECO-150 Concept	Present Day
	NASA & MIT's TeDP H3.1 Concept	Present Day

Πίνακας 1: Conceptual Milestones of Aircraft Distributed Propulsion

2.6.2 Actual Milestones of Aircraft Distributed Propulsion

For the purpose of elucidating ideas that became reality, a short visit is made along the historical axis of time, to point out some aircraft that implemented three or more units of propulsion and were chosen for commercial, experimental, cargo, research and military applications. Unlike the early days of conceptual aviation where distributed propulsion was introduced in the airship industry, many promising proposals that would have progressed into production were never funded. One possible cause for this, at least in the latter part of the 20th century, emerged from the misconception that hydrogen was the primary cause of the Hindenburg catastrophe. Doubtlessly, the term “Hindenburg syndrome” had a negative influence on the general public and the airship industry, but regardless of this significant impact, the aviation industry embraced many different designs featuring distributed propulsion [1]. Here are some actual milestones of Aircraft Distributed Propulsion:

In 1929, Dornier Do X, the world’s largest aircraft at the time, flew for the first time. Intended for transatlantic flights, this aircraft left Friedrichshafen, Germany, on 2 November 1930 with 17 passengers and crew for the USA. It was equipped with faired-in engine supports for its 12 engines. Early long-range flight attempts with Distributed Propulsion revealed many unforeseen parameters that could not be efficiently addressed or investigated during the conceptual design phase. Engine cooling was one of these problems. Using multiple engines without any cooling measures caused a thrust reduction for the rear engines.

The same year the Dornier Do X aircraft left Friedrichshafen, Handley Page H.P.42 made its first flight. Intended for the purpose of linking various parts of the British Empire, this aircraft used two engines on each of the large unequal-span biplanes, leaving a brilliant record of safety with no fatal accidents after a decade of service. An innovative part of H.P.42’s design was to position the propulsion units on different wings.

Seemingly a successful trend for long-range missions, multiple engine solutions were chosen more often, and this involved also two historical flying boats. The first aircraft, Blohm und Voss BV222 Wiking, the largest operational flying-boat during World War II, was specifically designed for long-range passenger transport in the late 1930s and was equipped with six vertically opposed engines distributed over the wing.

Following this success, a historical flight was made by Howard Hughes' famous H-4 Hercules in 1947. H-4 Hercules was the largest flying boat ever built and consisted of a single hull and eight radial engines. Taking into consideration the significant size of the aircraft, a substitution of wood for metal served as a new gateway for non-conventional approaches to aircraft design The design practices of this aircraft revealed, however, many technical difficulties ranging from the integration of power systems to large control surfaces. These problems added a new dimension to the earlier observed difficulties with engine cooling procedures in aircraft DP [1].

The DP configuration of Multiple Discrete Engines was implemented on the 1940's flying wing Northprop YB-49. It had four linearly arranged conventional turbojet engines in each side of wing with subsonic rectangular inlets at the leading edge and conventional circular nozzles at the trailing edge of the wing.

An aircraft utilizing the DP concept of Jet Flaps (DEX) was the Hunting H.126 aircraft, that was built and flown in the 1960's at lift coefficient C_L = 7.5 and maximum operationally usable C_L = 5.5. To enable such high lift, the engine diverted almost 60% of its thrust across its wing trailing edge to achieve very high lift capability. Its first flight was completed in 1963 [2].

The Bell D-2127 aircraft (X-22) took the concept of distributed propulsion one step further with its tilting arrangement of ducted fans. 1966 was the first time this aircraft took to the skies and almost two decades later it had contributed significantly to the VTOL/STOL research through programs at NASA and Federal Aviation Administration (FAA).

1969 was the year when the Boeing 747 aircraft, perhaps one of the most commonly known historical airplanes in commercial aviation, had its first flight. The Boeing 747 used four turbofan engines in pods pylon-mounted on wing leadings edges. Equipped with air-cooled generators mounted on each wing for electrical supply, two additional generators could provide primary electrical power when the engine-mounted generators were not operational. Technological advancement and the Boeing 747's efficient propulsion system integration were evident in a blunt comparison to the Dornier Do X's engine mishaps. The engine arrangement on the Boeing 747 has become a standard configuration for many commercial aircraft.

The Antonov An-225 MRIYA was an aircraft which was not designed to transport air travelers, but rather to transport the Soviet space shuttle. In 1989, Antonov An-225 completed this task with its six engines fitted with thrust reversers and glass fiber engine cowlings.

Nine years later, two DP systems were combined in a propulsion scheme with virtually no harmful emissions. Centurion, an unmanned solar-powered aircraft, first flown in 1997, with 61.8 meters wingspan and 14 brushless direct-electric motors, could reach altitudes of 30km. Envisioned as the ‘Eternal Airplane’ with the objective to fly for months, solar arrays were used to power electrical motors. The environmental impact of this aircraft has contributed to considerations for more environmentally friendly propulsion systems [1].

Depiction	Aircraft	Year
	Dornier Do X	1929
	Handley Page H.P.42	1929
	Blohm und Voss BV222 Wiking	1930s

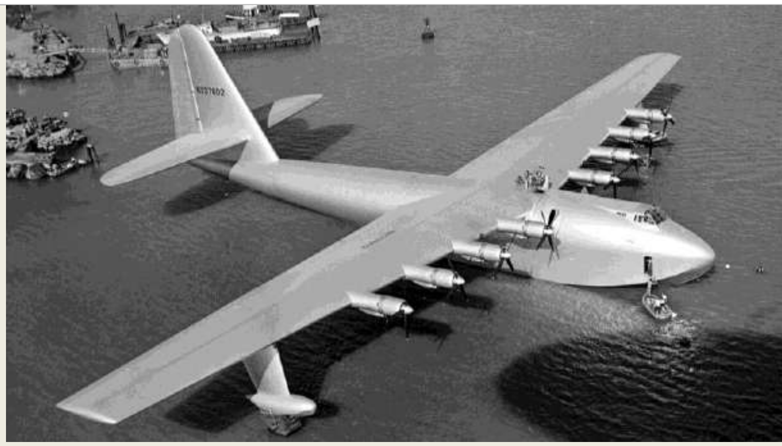	Howard Hughes H-4 Hercules	1947
	Northprop YB-49	1949
	Hunting H.126	1962

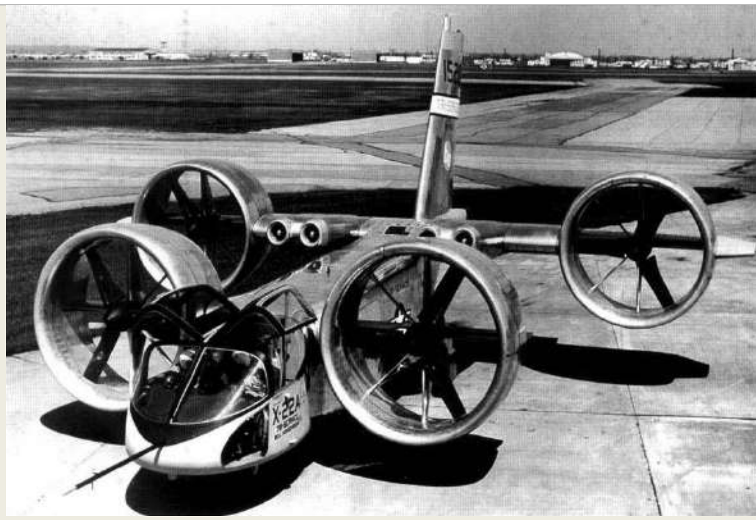	Bell D-2127	1966
	Boeing 747	1969
	Antonov Ant-225 MRIYA	1989
	NASA’s Centurion	1997

Πίνακας 2: Actual Milestones of Aircraft Distributed Propulsion

2.6.3 Milestones of the All-Electric Aircraft

Since we are investigating alternative aircraft solutions that will satisfy the growing aviation and sustainability demands and one of those solutions is the electric propulsion, here are some actual milestones of the All-Electric Aircraft:

Early days of the electric aircraft included a minimal electric part, which primarily consisted of the electrical power dependency for ignition purposes for the very first powered flights in 1903. Growing dependency on electrical power was soon evident with more electrical subsystems, for example radio communication.

In 1943, Kilgore proposed the electrical airplane propulsion system shown below to drive multiple rotating propellers. Equipped with one or a small number of poly-phase synchronous generators in the speed range of 10,000 RPM to 20,000 RPM, a pole-number range of 4 and 8, and a number of propeller-driving poly-phase motors energized from the generators, this power plant arrangement revealed a number of advantages. Additional power for take-off, reduction of runway length and propeller drag force, skid avoidance during the landing phase, wheel brakes, reduction of detachable conductors, elimination of sparks using induction-motors to drive the motors, and minimization of heavy concentrated weight burden on the wing structure, were some of the significant benefits of this concept.

In 1974, an electro-motorically driven aircraft was suggested by Meier. This configuration employed fuel cells or batteries for driving the propellers. The perennial drawback of the weight-to-power ratio, along with the excessive weights of fuel cells and batteries, constantly motivated researchers to restrict the usage of electric aircraft to unmanned, low speed aircraft with high aspect ratios wings. Many of these concepts employed a distributed propulsion arrangement. Even though substantial efforts were made to increase the power-to-weight ratios, many of the goals in favor of the electric aircraft could not be achieved. Suggestions made by the team of Meier, and other scientists around the world, considered a variety of possibilities for the electric aircraft. A true display of the electric aircraft technology came to reality through the solar-powered research programs initiated by NASA and AeroVironment, Inc., in the beginning of the 1970s. Similar research endeavors were also pursued around the globe by other scientists and research teams. The highlighted research programs at NASA represent a small portion of the technologies involved with the electric aircraft, and thus a few milestones of this specific era will be revisited.

The concept of the Sunrise I airplane was born in the early 1970s and this aircraft made its first flight on November 4, 1974, as the world's first solar-powered airplane. Although the usage of solar power limited the aircraft today flight and cloud avoidance, it served as a proof-of-concept to develop electric-powered fixed-wing aircraft. Even though Sunrise did not attain extended solar flights, it was able to provide the tools for an improved version of solar- powered aircraft, called the Sunrise II.

Sunrise II displayed even more potential to reach high altitudes and could benefit from improved aerodynamics. In 1980, Gossamer Penguin used the removed solar panels from Sunrise II for its initial flights. The aircraft had a 71-foot wingspan and used 3920 solar cells to produce 541 Watts of power. After flight tests with solar cells, batteries and an electric motor, it was proven that electric aircraft could also be manned.

The first official manned flight of direct solar power was completed on 7 April 1980, and this concept was evolved into Solar Challenger that had a 46.5-foot wingspan and accommodated 16128 solar cells. Solar Challenger was designed to with stand normal turbulence levels and was equipped with batteries, solar cells, an electric motor and a propeller. In late 1980, the initial flights were moved from California to Marana Airpark, northwest of Tucson, Arizona. By that time the aircraft had already moved from flights using batteries to solar-powered flights. Solar Challenger was able to complete a manned flight from Paris to London on 7 July 1981 in an attempt to show the feasibility of the aircraft's efficiency.

The same year Solar Challenger took to the skies, the classified program High Altitude SOLar Energy (HALSOL) was launched by the U.S. Government to explore the feasibility of solar-electric flight above 65,000 feet. About a decade later some of the findings from the HALSOL program contributed to Pathfinder, an unmanned aircraft that was able to reach a record altitude of 50500 feet for solar-powered aircraft. In 1997, Pathfinder was eventually transferred to Hawaii, due to the high levels of sunlight available in that location. Pathfinder was able to reach a world altitude record of 71530 feet for solar-powered and propeller-driven aircraft.

Moreover, Pathfinder was upgraded to Pathfinder Plus during 1988. This aircraft was able to reach even higher altitudes than the original Pathfinder by reaching an altitude of 80210 feet and breaking the record altitude of propeller-driven aircraft. Some notable changes made to the

Pathfinder Plus enabled it to reach higher altitudes than ever before and served as a framework for an even more improved solar aircraft called the Centurion. Increased wingspan, additional motors, and more efficient silicon solar cells provided Pathfinder Plus with an additional 5000 Watts power in comparison to the 7500 Watts power used for the Pathfinder.

An interesting observation regarding the engine power output is that the number of engines has steadily increased from the Solar Challenger to the Centurion aircraft. Centurion evolved the ideas of a solar-powered aircraft to higher levels and proved that it was possible for an aircraft to use telecommunications relay platforms and stay airborne for weeks and collect scientific sampling data and imaging data. Centurion’s flexible wing made of kevlar, carbon fiber and graphite epoxy composites was divided up into five sections and had no taper or sweep. Solar cells were used to power the electric motors, communications, electronic systems and avionics. Centurion was further equipped with a backup lithium battery system that could allow additional two to five hours limited flight after dark. Extensive research progress made for the HALE aircraft category placed solar-powered aircraft concepts into practice. Many of these aircraft employed electric motors, driven by batteries and solar cells. NASA’s solar-powered and electrical aircraft initiatives were only a fraction of the extensive research work, done in the direction of the electric aircraft. In many ways, the HALE aircraft are the true representatives of AEA. Further, an increasing number of electric aircraft have entered the manufacturing phase over the years.

IFB Hydrogenius stands out amongst the different electric aircraft, as this particular aircraft also uses liquid hydrogen, batteries and a fuel cell onboard. IFB Hydrogenius delivers the largest engine power through its combination of different power systems, which seems to be the most suitable option for larger MTOWs. This rather simplistic survey exhibits one of the distinguished traits of the electric aircraft which is the limited power densities for given airframe weights. Thus, a combination of different power systems is more likely to present a solution for larger engine powers and should therefore be considered in the future. NASA explored this direction through an analytical performance assessment of a fuel cell powered small electric airplane. Similarly, researchers of the ENFICA-FC project have also looked into the feasibility of powering an all-electric propulsion aircraft with fuel cells. For the sake of AEA discussions, it should be emphasized that fuel cells do not represent the only proposed complementary technology for AEA but are still considered important components in electric aircraft schemes and as possible Auxiliary Power Units (APUs) [1].

Depiction	Aircraft	Year
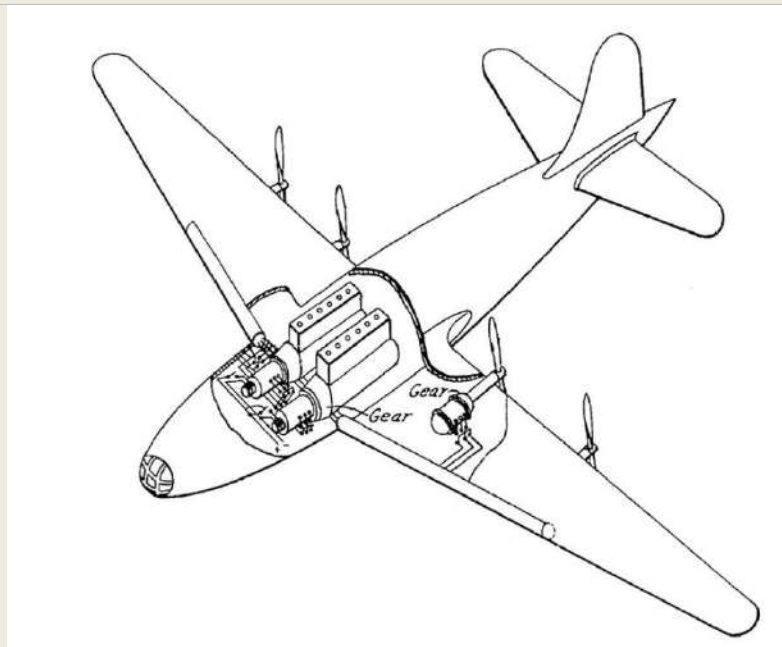	Kilgore's AEA Proposal	1943
	World's First Solar-powered Aircraft, Sunrise I	1974
	Solar-powered Aircraft, Sunrise II	1977

	Solar-powered Aircraft, Solar Challenger	1980
	NASA's Solar-powered Aircraft, Pathfinder	1987
	NASA's Solar-powered Aircraft, Pathfinder Plus	1988
	NASA's Solar-powered Aircraft, Centurion	1997
	Liquid Hydrogen Fuel-Cell AEA, IFB Hydrogenius	2011

Πίνακας 3: All-Electric Aircraft Milestones

2.6.4 Distributed Propulsion and All-Electric Aircraft ongoing Programs

After a brief Historical Review of aircraft Distributed Propulsion and Electric Aviation, it is important to mention several aerospace programs that have been initiated to design and develop airplanes that satisfy the characteristics of sustainability while employing DP and/or AEA configurations.

A state-of-the-art application of a sustainable AEA is the **HY4** aircraft by H2FLY. H2FLY was founded by five engineers from the University of Ulm. H2FLY GmbH is working to deliver a hydrogen-electric aircraft powertrain. Clean hydrogen is converted into electricity in the fuel cell system to power the HY4, proving that zero-emission aviation is within reach. The company develops hydrogen-electric aircraft propulsion systems and is a global leader in the development and testing of such systems. In just a few years, hydrogen-electric aircraft are expected to be able to transport 40 passengers over distances of up to 2,000 km. The HY4 first took off in 2016. On September 7, 2023, H2FLY announced that the HY4 has successfully completed the world's first piloted flight of an electric aircraft powered by *liquid* hydrogen. The twin-prop took off from Maribor, Slovenia before completing four flights. The company says that using cryogenically stored liquid hydrogen instead of a gaseous alternative can double the range of the HY4, taking it from 750 km to 1,500 km, as liquified hydrogen enables significantly lower tank weights and volume, meaning more onboard carrying to increase range and improve payload is possible [8].

Another prime example is the **UNIFIER19** program initiated by Slovenian light aircraft manufacturer Pipistrel. It is a new, environmentally friendly and cost-efficient air mobility solution regarding the development and certification of a hybrid electric commuter, designed as a community friendly miniliner. The potential of the proposed design goes beyond a mere cleaner replacement of existing commuters: UNIFIER19 aims at providing an innovative near-zero emission (NZE) air mobility solution. The UNIFIER19 is a 19-passenger commuter with multiple cargo and passenger-seating cabin layouts powered by a modular hybrid-electric powertrain. It is an AEA with CMF type of Distributed Propulsion and deploys a Hydrogen Fuel-Cell system, powering the distributed electric motors that rotate the wing propellers [7].

Project HEAVEN, a European-government-supported consortium assembled to demonstrate the feasibility of using liquid, cryogenic hydrogen in aircraft. The consortium is led by H2FLY and includes the partners Air Liquide, Pipistrel Vertical Solutions, the German Aerospace Center (DLR), EKPO Fuel Cell Technologies, and Fundación Ayesa. Project HEAVEN is funded by the Fuel Cells and Hydrogen 2 Joint Undertaking (FCH 2 JU) under grant agreement no. 826247. The public-private partnership FCH 2 JU supports research, technology development and demonstration activities in fuel cell and hydrogen energy technologies in Europe. HEAVEN is part of the "Horizon 2020" research and innovation program funded by the European Union as well as Spain, France, Germany and Slovenia. In addition to H2FLY, the HEAVEN consortium is made up of the following partners: Air Liquide (designer-supplier of cryogenic tanks), Pipistrel Vertical Solutions d.o.o., a Textron Inc. (NYSE: TXT) company (tank integration and testing), the DLR German Aerospace Center (fuel cell and system architecture operation and testing), EKPO (fuel cell stack) and Fundación Ayesa (cost analysis) [8].

Last but not least, NASA's concept **X-57 Maxwell** is the agency's first all-electric experimental aircraft, or X-plane, and is NASA's first crewed X-plane in two decades. The primary goal of the X-57 project is to share the aircraft's electric-propulsion-focused design and airworthiness process with regulators, which will advance certification approaches for distributed electric propulsion in emerging electric aircraft markets. The X-57 will undergo as many as three configurations as an electric aircraft, with the final configuration to feature 14 electric motors and propellers (12 high-lift motors along the leading edge of the wing and two large wingtip cruise motors) powered through a lithium-ion Battery system. This design driver includes a 500 percent increase in high-speed cruise efficiency, zero in-flight carbon emissions, and flight that is much quieter for the community on the ground. X-57 will also seek to reach the goal of zero carbon emissions in flight, which would surpass the 2035 N+3 efficiency goals. Electric propulsion provides not only a five-to-ten times reduction in greenhouse gas emissions, but it also provides a technology path for aircraft to eliminate 100 Low Lead AvGas, which is the leading contributor to current lead environmental emissions. Additionally, since the X-57 will be battery-powered, it can run off renewable based electricity, making clear the environmental and economic advantages [9].

Εικόνα 3: H2FLY HY4 (1/2)

Εικόνα 4: H2FLY HY4 (2/2)

Εικόνα 5: Pipistrel UNIFIER-19 (1/2)

Εικόνα 6: Pipistrel UNIFIER-19 (2/2)

Εικόνα 7: NASA's X-57 Maxwell (1/2)

Εικόνα 8: NASA's X-57 Maxwell (2/2)

2.7 THESIS SYSTEM TYPE

As proved in the Historical Review, the concept of aircraft Distributed Propulsion is not new. Applications of such systems have been considered and developed in the aviation and military industry since the 1930s. These applications albeit were mostly employing only a larger number of regular turbine engines (4-6 instead of 2), thus a DEN system.

This Thesis revolves around the implementation of a state-of-the-art CMF/Distributed Electric Multi-Fans system, according to the categorization in Chapter 2.1.

This Distributed Electric Propulsion system utilizes -among plenty of advantages- the aerodynamic benefits of augmented Lift during Take-Off and Landing and Wing Tip Vortex elimination, the structural benefits of heavy concentrated Load minimization and Wing Weight reduction and the topological benefits of Power Production-Propulsion separation.

Since the studied aircraft will be converted to an AEA, the concept provides the opportunity to utilize a liquid Hydrogen Fuel-Cell system, thus satisfying Zero-Emission flight targets, as well as the growing technological and environmental demands regarding Sustainability and Performance improvements.

The All-Electric Aircraft with Distributed Electric Propulsion conversion will be implemented on a general aviation vehicle which involves low cost and ease of experimentation. Thus, a small, fixed-wing, two-seater Light Sport Aircraft is selected for simplicity and CAD geometry access reasons, as far as this Thesis is concerned.

3.0 AIRCRAFT SPECIFICATIONS

3.1 LIGHTWEIGHT STRUCTURES

The Design Philosophy of Lightweight Structures refers to the design of a structure with the lowest possible weight, while at the same time maintaining or enhancing the required strength. The goal of lightweight structures is to achieve optimal stiffness, stability and functionality while using less material, which can lead to various benefits, such as energy savings, reduced environmental impact and improved transportability.

Applications of Lightweight Structures can be found in aerospace and motorsport, where one of the most critical performance factors is weight. Lightweight Structure applications can also be found in the automotive and marine industry, civil engineering projects and sports equipment. Essentially, when designing a lightweight structure, the strength-to-weight ratio must be maximized, either by minimizing the weight/material used while maintaining the desirable strength, or by using materials with higher stiffness-to-weight ratio.

This can be achieved through advanced Structural Mechanics, Finite Element Analysis, computational tools such as Topology Optimization or utilization of high strength-to-weight ratio Materials such as composites, aluminum, titanium, and high strength steels.

Depicted below are; a honeycomb sandwich panel that presents a notably increased bending stiffness with a minimal weight penalty; an airframe that is the definition of an aircraft lightweight structure, and finally a metal component with levels of topology optimization, that could be a motorsport application such as a suspension mount part.

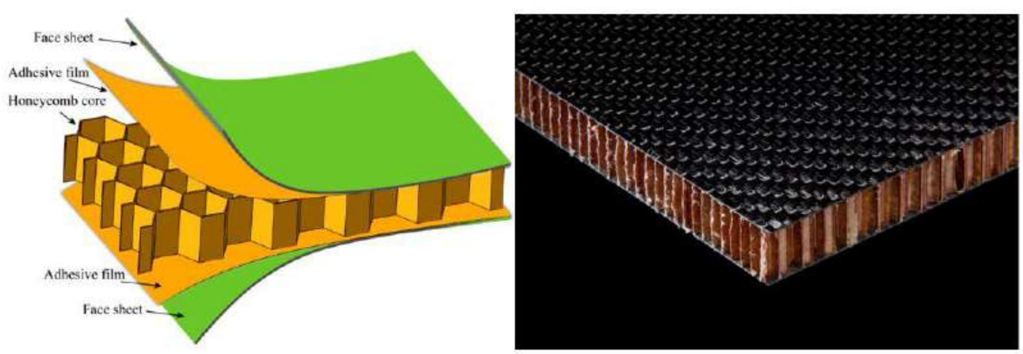

Εικόνα 9: Honeycomb Sandwich Panel

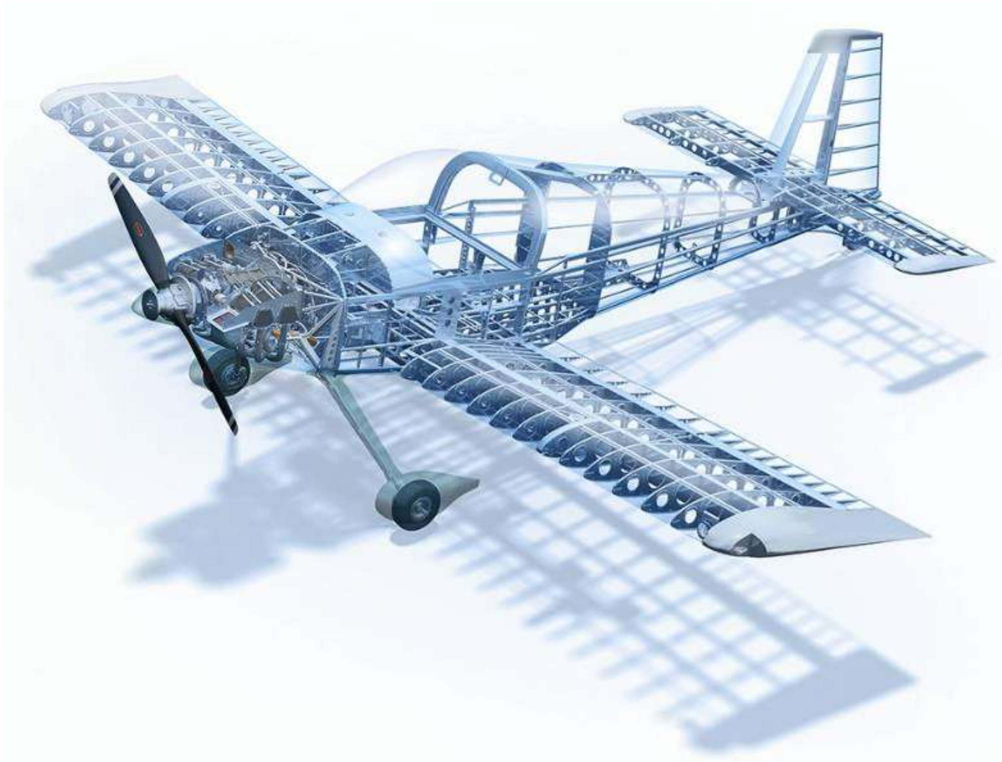

Εικόνα 10: Lightweight Structure Airframe

Εικόνα 11: Stages of Topology Optimization on a Metal Part

3.2 MATERIAL USED

The material used in the components of the Zenith Zodiac CH 650 B wing structure is the Aluminum Alloy series Al 6061-T6. Besides the recent surge in composite materials utilization, Aluminum Alloys are the most common material used in the aerospace industry. That is due to the low weight it presents compared to other metals, the excellent mechanical properties, strength-to-weight ratio and machinability, the decent corrosion resistance, the satisfying recyclability and the relatively low cost.

The material properties of Al 6061-T6 are presented below, along with the tensile experiment figures [10].

6061-T6 Aluminum

Material Notes

Component	Wt. %	Component	Wt. %	Component	Wt. %
Al	95.8 - 98.6	Mg	0.8 - 1.2	Si	0.4 - 0.8
Cr	0.04 - 0.35	Mn	Max 0.15	Ti	Max 0.15
Cu	0.15 - 0.4	Other, each	Max 0.05	Zn	Max 0.25
Fe	Max 0.7	Other, total	Max 0.15		

Physical Properties	Metric	English	Comments
Density	2.7 g/cc	0.0975 lb/in³	AA; Typical
Mechanical Properties			
Hardness, Rockwell B	60	60	Converted from Brinell Hardness Value
Hardness, Vickers	107	107	Converted from Brinell Hardness Value
Ultimate Tensile Strength	310 MPa	45000 psi	AA; Typical
Tensile Yield Strength	276 MPa	40000 psi	AA; Typical
Elongation at Break	12 %	12 %	AA; Typical; 1/16 in. (1.6 mm) Thickness
Modulus of Elasticity	68.9 GPa	10000 ksi	AA; Typical; Average of tension and compression. Compression modulus is about 2% greater than tensile modulus.
Poisson's Ratio	0.33	0.33	Estimated from trends in similar Al alloys.
Fatigue Strength	96.5 MPa	14000 psi	AA; 500,000,000 cycles completely reversed stress; RR Moore machine/specimen
Fracture Toughness	29 MPa-m½	26.4 ksi-in½	KIC; TL orientation.
Shear Strength	207 MPa	30000 psi	AA; Typical

Πίνακας 4: Al6061-T6 Properties

<u>AL6061-T6 Strength properties:</u>

Yield Tensile/Compression Strength: 276 MPa

Ultimate Tensile/Compression Strength: 310 MPa

Shear Strength: 207 MPa

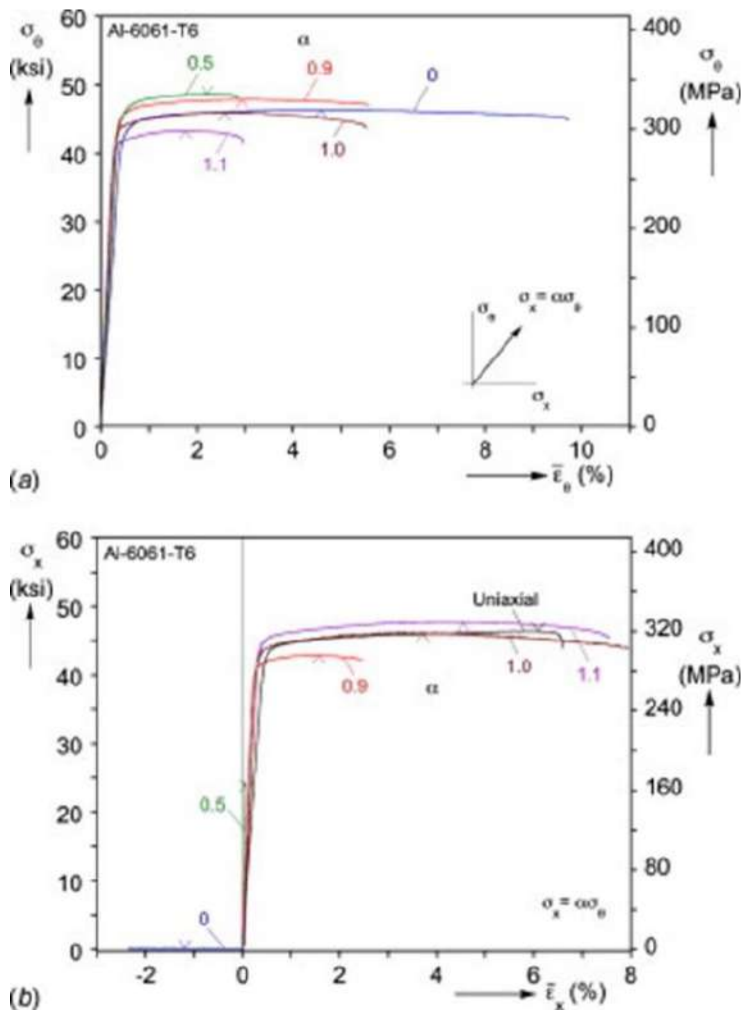

Εικόνα 12: Al6061-T6 Compression Tensile Diagrams

Every component of the Zenith Zodiac CH 650 B wing structure is made from Al6061-T6. However, the fasteners used in the Wing-Fuselage joint (AN-5 Bolts) and the Spar-Root Doubler joint (AN-4 Bolts) are made from Alloy Steel, usually 8740 or 4037.

According to [25], AN Bolts have a minimum tensile strength of 125000 psi and a shear strength of 76000 psi.

STEEL AN BOLTS Strength properties:

Tensile/Compression Strength: 862 MPa

Shear Strength: 524 MPa

3.3 AIRCRAFT DESCRIPTION

The aircraft studied in this Diploma Thesis is the Zodiac CH 650 B, produced by Zenith Aircraft Company, that belongs to the Light Sport Aircraft (LSA) category. It is a 2-seat, single engine, non-pressurized cabin aircraft, that due to its design flexibility can be equipped with a plethora of engines, usually with an engine power of 100-130 HP [12].

The Zenith Zodiac CH 650 B has all the typical characteristics of a small single engine aircraft. Its design principles revolve around simplicity, ease of assembly with basic tools, while the chosen method of structural assembling is riveting. Finally, reliability and safe flight has been a great focus with the Zodiac CH 650 B, due to its predecessor's (CH 601) failure history. With the CH 650 B's wing design, no structural failure has been recorded [12].

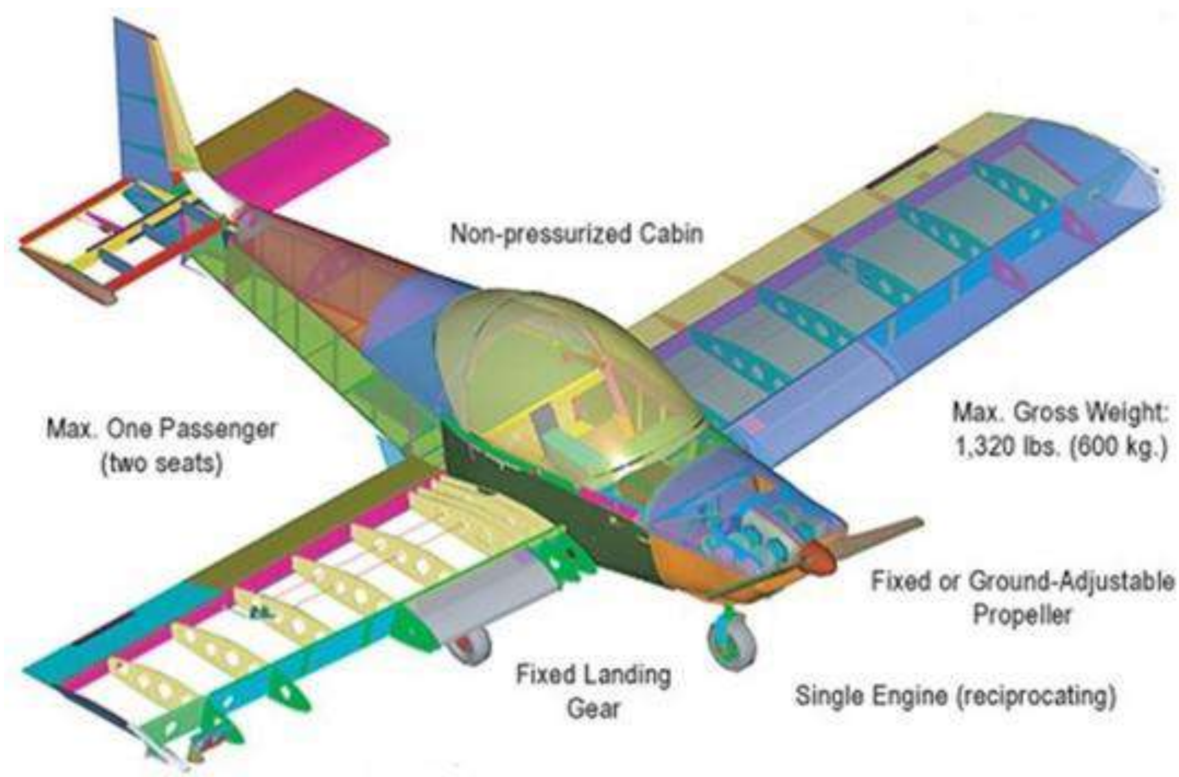

Εικόνα 13: Zenith Zodiac CH 650 B

SPECIFICATIONS	Jabiru 3300		Continental O-200	
LENGTH	20 Ft. 0 In.	6.1 m.	20 Ft. 0 In.	6.1 m.
HEIGHT (rudder tip)	6 Ft. 6 In.	1.98 m.	6 Ft. 6 In.	1.98 m.
WING SPAN	27 Ft. 0 In.	8.23 m.	27 Ft. 0 In.	8.23 m.
WING AREA	132 Sq. Ft.	12.3 m.sq.	132 Sq. Ft.	12.3 m.sq.
WING CHORD (root / tip)	5' 3" / 4' 7"	1.6 m. / 1.4 m.	5' 3" / 4' 7"	1.6 m. / 1.4 m.
HORIZONTAL TAIL SPAN	7 Ft. 7 In.	2.3 m.	7 Ft. 7 In.	2.3 m.
HORIZONTAL TAIL AREA	20 Sq.Ft.	2.24 m.sq.	20 Sq.Ft.	2.24 m.sq.
EMPTY WEIGHT	695 Lbs.	318 kg.	750 Lbs.	340 kg.
DESIGN GROSS WEIGHT	1,320 Lbs.	600 kg.	1,320 Lbs.	600 kg.
USEFUL LOAD	625 Lbs.	282 kg.	570 Lbs.	260 kg.
FUEL CAPACITY (Standard) – FUEL WEIGHT	24 US Gal. = 144 Lbs.	92 *l.* = 65 kg.	24 US Gal. = 144 Lbs.	92 *l.* = 65 kg.
FUEL CAPACITY (Extended Option) – FUEL WEIGHT	30 US Gal. = 180 Lbs.	112 *l.* = 82 kg.	30 US Gal. = 180 Lbs.	112 *l.* = 82 kg.
WING LOADING	9.8 Lbs./Sq.Ft.	48 kg./m.sq.	9.8 Lbs./Sq.Ft.	48 kg./m.sq.
POWER LOADING	13.2 Lbs./BHP	6 kg./HP	13.2 Lbs./BHP	6 kg./HP
DESIGN LOAD FACTOR (Ultimate)	+6 / –3 G	+6 / –3 G	+6 / –3 G	+6 / –3 G
CABIN WIDTH (Shoulders)	44 In.	112 cm.	44 In.	112 cm.
NEVER EXCEED SPEED (V_{NE})	160 MPH	260 km/h	160 MPH	260 km/h

Πίνακας 5: Zenith Zodiac CH 650 B Specifications

PERFORMANCE

Peformance at Gross Weight	Jabiru 3300		Continental O-200: 100 hp	
TOP SPEED	148 MPH	238 km/h	140 MPH	225 km/h
CRUISE SPEED (75%)	138 MPH	222 km/h	135 MPH	218 km/h
STALL SPEED (Flaps Down)	44 MPH	70 km/h	44 MPH	70 km/h
RATE OF CLIMB	930 fpm	4.8 m/s	1,000 fpm	5 m/s
TAKE OFF ROLL	500 Ft.	152 Ft.	500 Ft.	152 Ft.
LANDING ROLL	500 Ft.	152 Ft.	500 Ft.	152 Ft.
SERVICE CEILING	16000+ Ft.	4875+ m.	16000+ Ft.	4875+ m.
RANGE (Standard)	575 statute miles	925 km.	560 miles	900 km.
ENDURANCE (Standard)	4.2 Hours	4.2 Hours	4.0 Hours	4.0 Hours

Πίνακας 6: Zenith Zodiac CH 650 B Performance

Note: *The Stall Speed with Flaps Up increases from 70km/h to 80km/h.*

The Wing of the Zenith Zodiac CH 650 B has a straight leading edge and a tapered trailing edge, as seen in the aircraft Dimensions below. That means that the chord length is variable spanwise, with the wing root chord being slightly larger than the wing tip chord. The Taper Ratio (TR) is equal to:

$$TR = \frac{tip\ chord}{root\ chord} = \frac{1.4\ m}{1.6\ m} = 0.875$$

The Aspect Ratio (AR) is equal to:

$$AR = \frac{wingspan^2}{wing\ area} = \frac{8.23^2\ m^2}{12.3\ m^2} = 5.5$$

Also, the Wing presents a dihedral design, meaning that the Wings are tilted upwards and thus are not parallel to the ground plane. The primary reason of applying the wing dihedral is to improve the lateral stability of the aircraft. The lateral stability is mainly a tendency of an aircraft to return to original trim level wing flight condition if disturbed by a gust and rolls around the x axis. The dihedral angle of the Zenith Zodiac CH 650 B is equal to $\Gamma = 5.65°$ (10%).

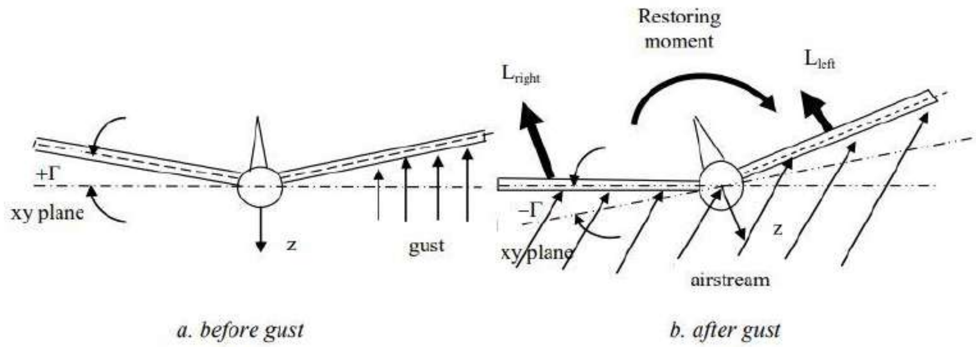

Εικόνα 14: Dihedral Angle

The airfoil used in the Zenith Zodiac CH 650 B is a RIBLETT GA 35-A-415 [16] and is the airfoil used also in the predecessor model, the Zenith Zodiac CH 601.

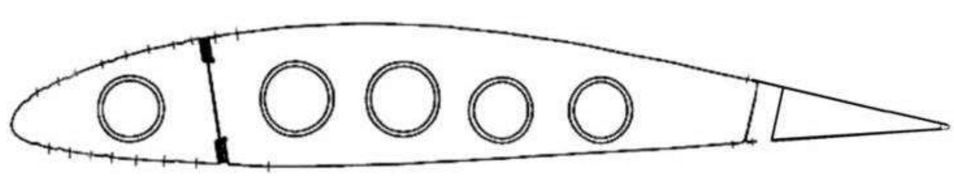

Εικόνα 15: Riblett GA 35-A-415 Wing Sideview

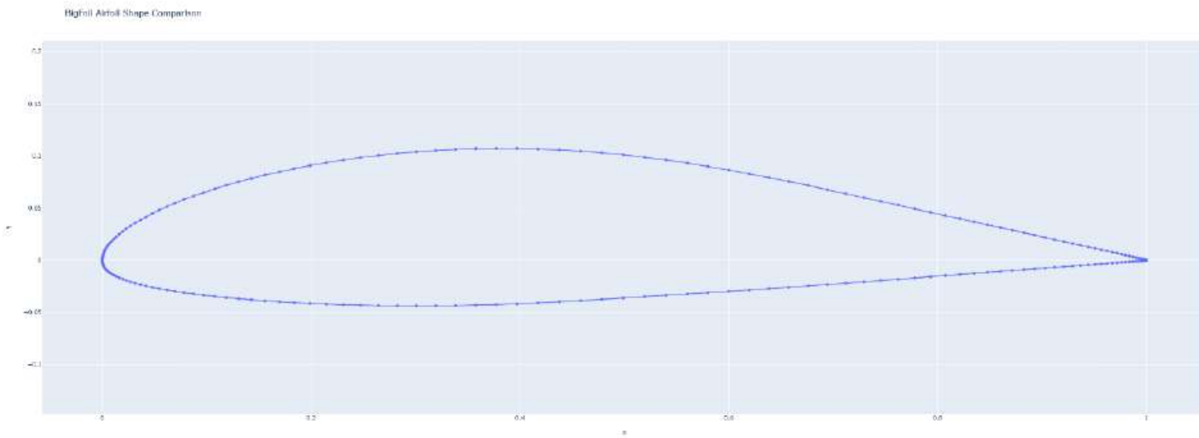

Εικόνα 16: Riblett GA 35-A-415 Airfoil Shape

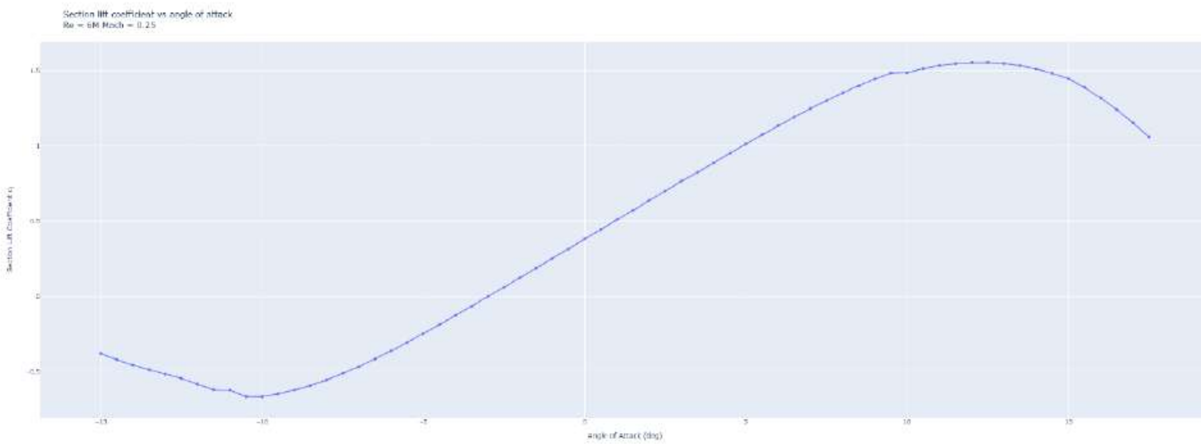

Εικόνα 17: Riblett GA 35-A-415 Lift Coefficient vs Angle of Attack

Εικόνα 18: Riblett GA 35-A-415 Drag Coefficient vs Angle of Attack

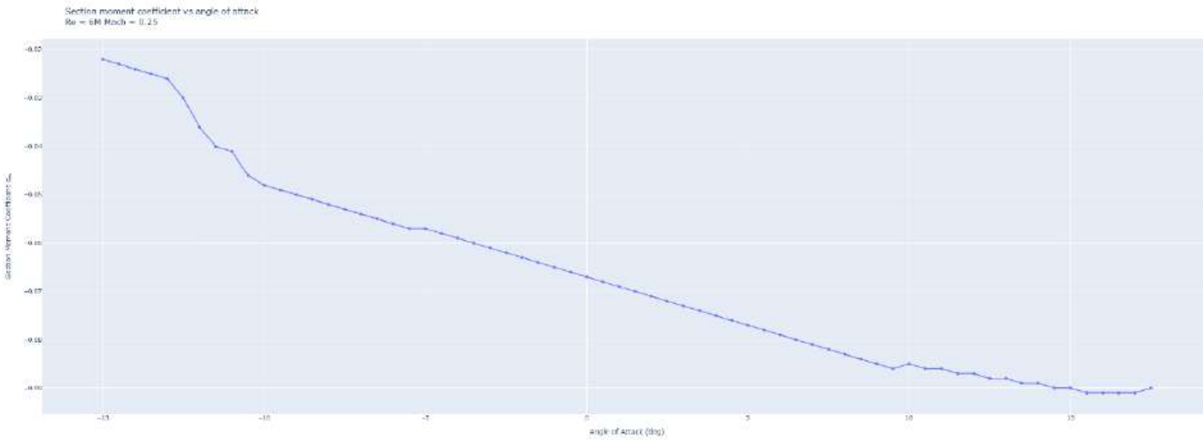

Εικόνα 19: Riblett GA 35-A-415 Pitching Moment Coefficient vs Angle of Attack

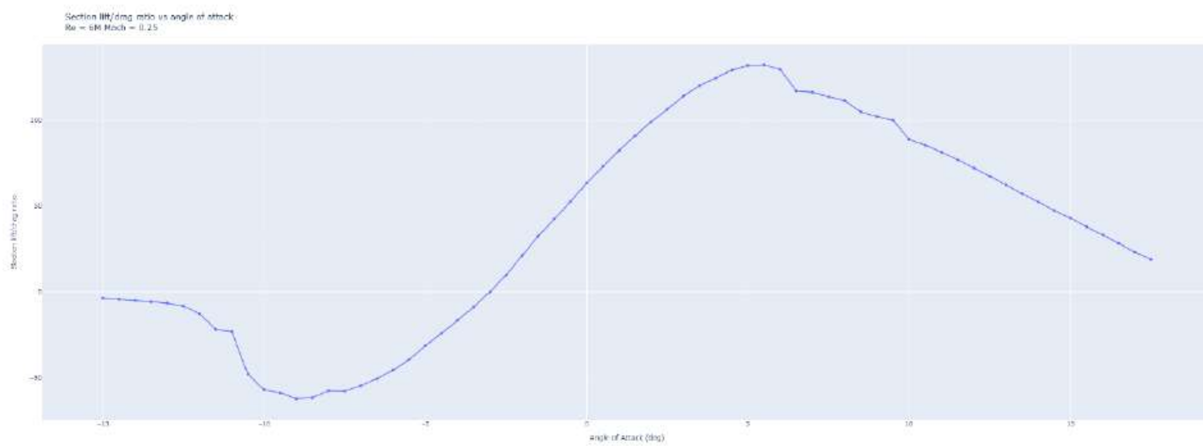

Εικόνα 20: Riblett GA 35-A-415 Lift/Drag Ratio vs Angle of Attack

Εικόνα 21: Riblett GA 35-A-415 Lift/Drag Ratio vs Lift Coefficient

The GA 35-A-415 Airfoil Figures and Data are obtained from [16]. For a Mach number equal to $Mach = 0.25$, a Reynolds number equal to $Re = 6 \cdot 10^6$ and Angles of Attack equal to $AoA = 5\ deg$ & $12.5\ deg$, the following coefficients are obtained:

Airfoil Coefficients for Mach $= \mathbf{0.25}$, Re $= \mathbf{6 \cdot 10^6}$			
Angle of Attack (deg)	$\boldsymbol{AoA}$	5	12.5
Lift Coefficient	$\boldsymbol{C_L}$	1.014	1.555
Drag Coefficient	$\boldsymbol{C_D}$	0.00769	0.02306
Pitching Moment Coefficient	$\boldsymbol{C_M}$	-0.077	-0.088
Lift/Drag Ratio	$\boldsymbol{L/D}$	131.795	67.427

Πίνακας 7: Riblett GA 35-A-415 Airfoil Coefficients

The Internal Combustion Engines originally used in the Zodiac CH 650 B are the Jabiru 3300 and the Continental O-200 [11]. Here are some technical specifications of these ICEs that will be useful during the AEA modification later in this Thesis.

	Jabiru 3300	**Continental O-200**
Type | Cylinders	Boxer | 6	Boxer | 4
Power @ 2750 RPM (kW | HP)	89 | 120	75 | 100
Weight (kg | lbs)	81 | 180	91 | 200

Πίνακας 8: Zenith Zodiac CH 650 B Original ICE Specifications

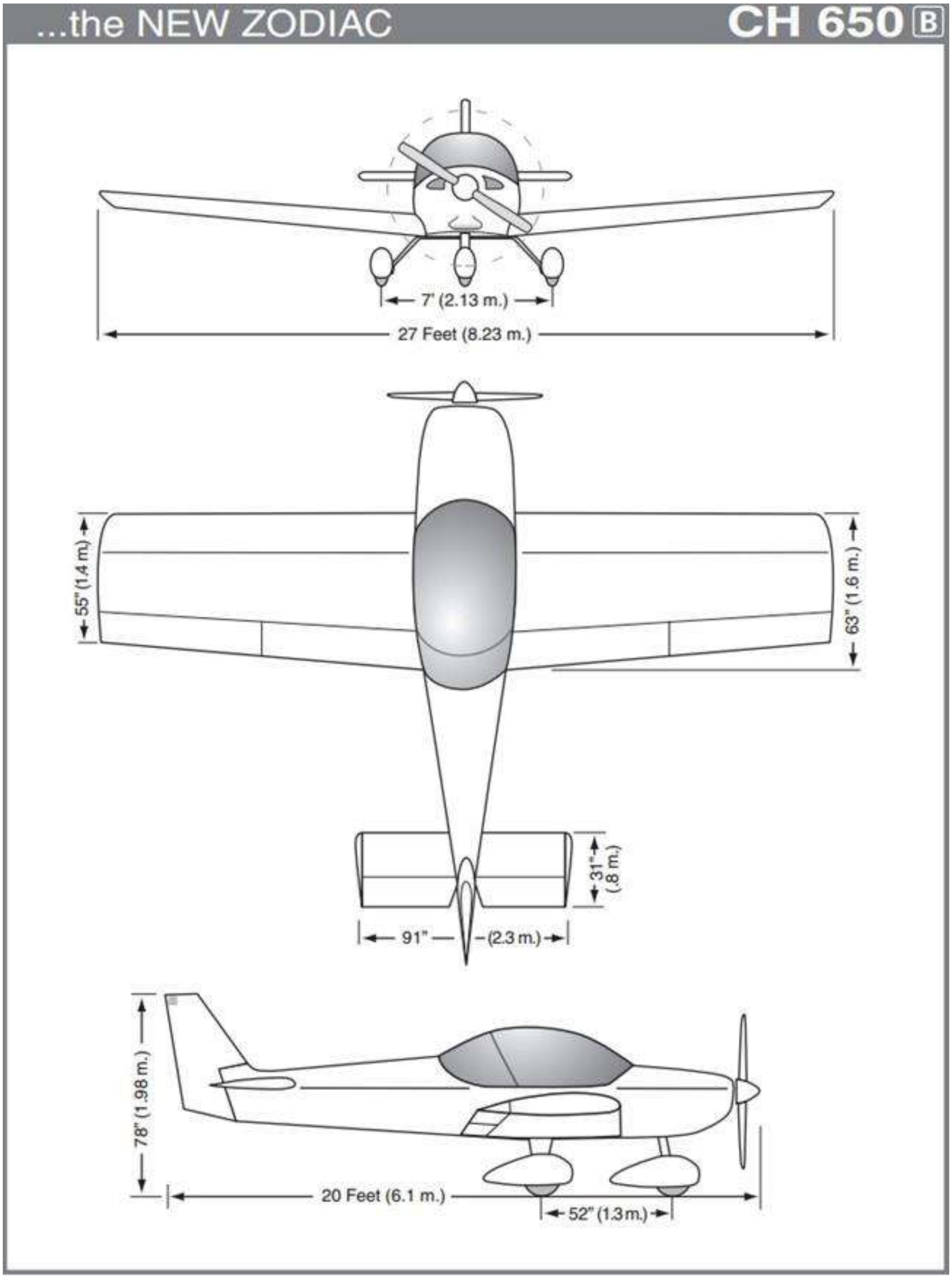

Εικόνα 22: Zenith Zodiac CH 650 B Dimensions

3.4 WING STRUCTURE

A typical wing structure is designed to carry and transmit the loads towards the fuselage safely while also preventing displacements that impact the aerodynamic behavior of the aircraft.

The wing structure consists of the external wing structure (Skin) and the primary and secondary internal wing structure.

The wing structure is responsible for transmitting the mentioned loads, thus longitudinal beams from the wing root to the wing tip (Spars) are used. The number of Spars varies, depending on the wing geometry and the magnitude of the loads. For example, an airfoil with a large chord requires at least two spars due to increased torsional loads. The most common number of Spars used is two, but the number of spars is ultimately a design choice.

The number of Spars used to shape the Wing Box in an aircraft wing could be a subject of further academic research.

The primary wing structure is the Wing Box or Torsion Box and consists of the combination of multiple spars. It is the structural center of the wing and most of the wing components (engines, landing mechanisms) and moving surfaces (slats, flaps, ailerons) are bolted on it. The Torsion Box is also utilized as fuel storage and is designed accordingly to meet the range requirements, as well as the demands of the structural engineer and the aerodynamicist.

The secondary wing structure consists of sheets perpendicular to the Spars (Ribs) and beams parallel to the Spars (Stringers) that support the sheets forming the external surface of the wing (Skin) against Buckling and fuel moving during maneuvers.

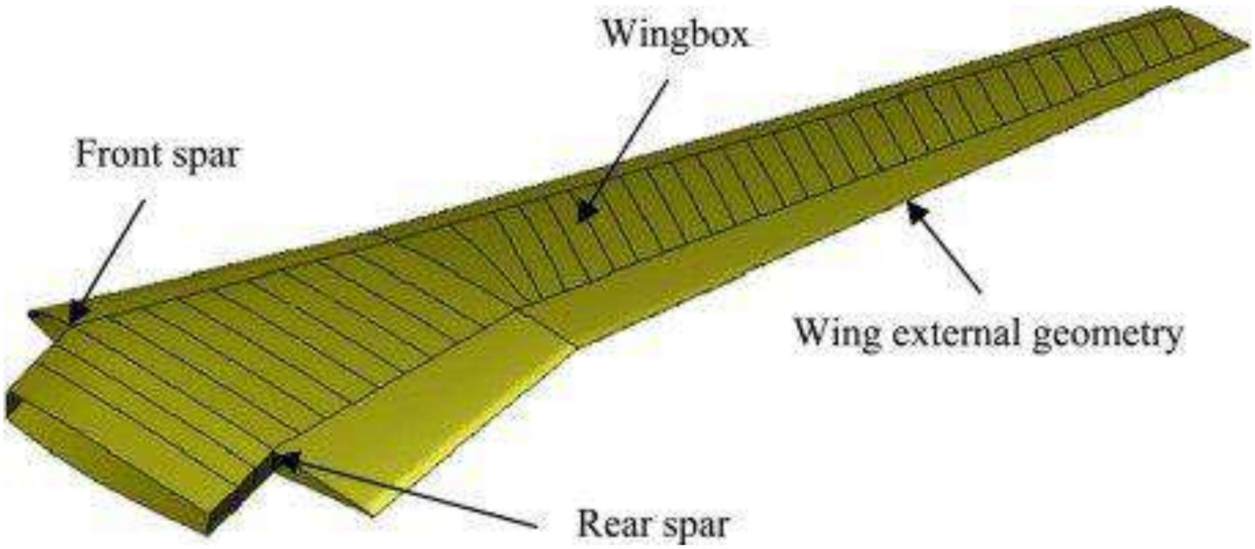

Εικόνα 23: Torsion Box of Aircraft Wing

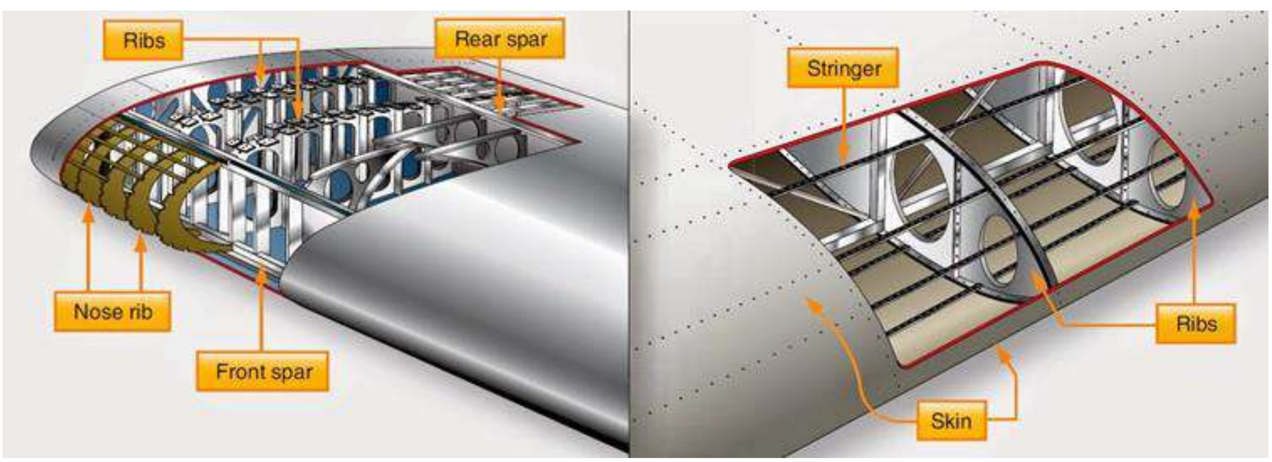

Εικόνα 24: Wing Structure Stiffeners

As we can see below, the components of the Zenith Zodiac CH 650 B wing structure are:

- **Wing Spar**: The Wing Spar is defined as the main lateral member of the aircraft's wing structure. In a fixed wing aircraft, the Wing Spar is usually the main structural wing component, running across the wingspan, while other wing components such as the Ribs are bolted on it. The Wing Spar handles most of the wing Load, such as its own weight, static, aerodynamic and other forces.
- **Stringers**: Stringers are essentially stiffeners, usually of L cross section, that provide more wing structural stability.
- **Ribs**: Ribs are longitudinal components that provide the wing's aerodynamic shape and contribute to the increase of its strength. Ribs are bolted on the Wing Spar and constitute the wing's lightweight structure. The wing's Skin follows the geometry created by said lightweight structure.
- **Rear Spar Channel**: The Rear Spar Channel provides extra wing stability, while the Ribs' other edges, the Flaps and the Ailerons are bolted on it.
- **Skin**: The wing's Skin is a thin-walled sheet metal that covers the wing structure.
- **Flaps**: The Flap is a fixed or rotating component of an aircraft's wing that is used to manipulate the Lift and the Drag for a shorter takeoff and a landing with a lower speed. When the Flaps are deployed, the curvature of the airfoil is changed, and the rate of descent is increased while landing. Also, the Lift is increased, allowing the aircraft to produce the same Lift in lower speeds, albeit with Drag being increased too. Flaps can be partially deployed during takeoff for STOL.
- **Ailerons**: The Ailerons provide Roll control. They are usually coupled so that when one is moving upwards, the other is moving downwards. The Lift is increased in the side of the upwards moving Aileron, while decreased in the side of the downwards moving Aileron, thus instigating the aircraft's Roll movement.
- **Wing Tip**: The Wing Tip is the wing's free edge. It can have different geometries and shapes, impacting the generated Drag and the Wing Tip vortices.

Longitudinal is the fuselage axis, also known as the Roll axis. Lateral is the spanwise axis perpendicular to the longitudinal axis, also known as the Pitch axis, as also shown below.

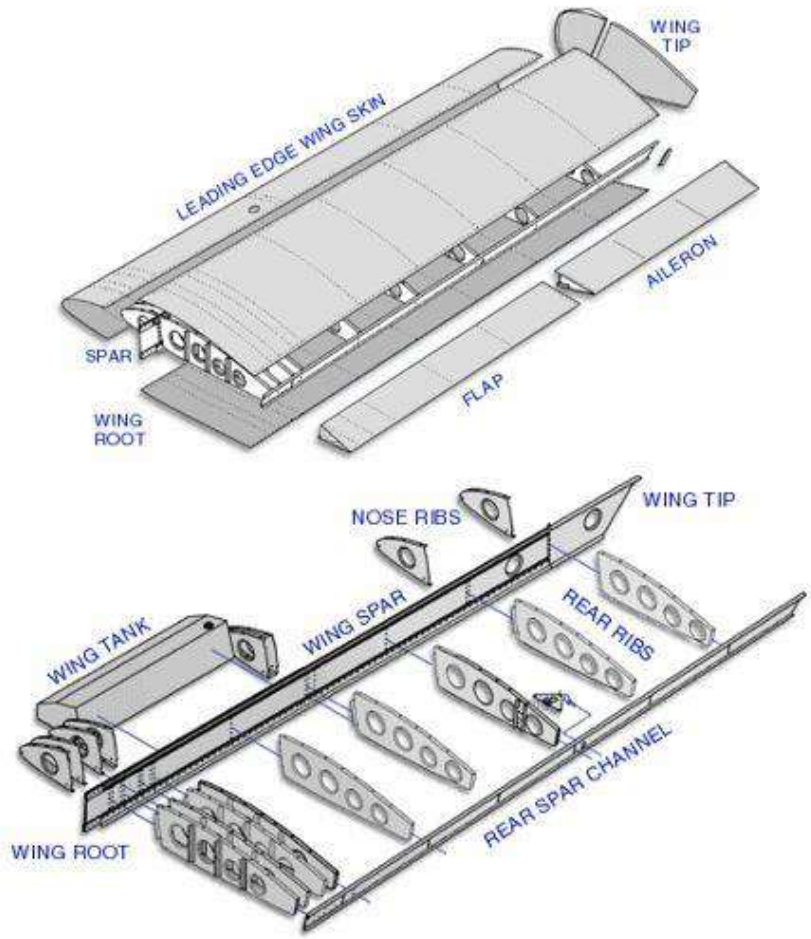

Εικόνα 25: Zenith Zodiac CH 650 B Wing Structure

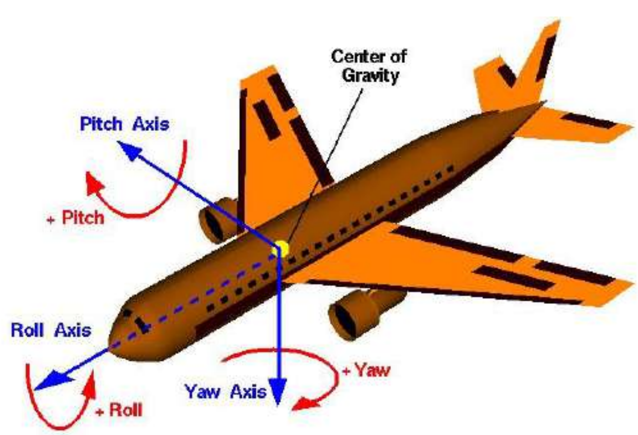

Εικόνα 26: Aircraft Coordinate System

3.5 DISTRIBUTED ELECTRIC PROPULSION CONVERSION

3.5.1 Inspiration

The previously mentioned X-57 Maxwell concept aircraft by NASA serves as a great inspiration for this Thesis, as it is built by modifying a baseline Italian Tecnam P2006T to be powered by a Distributed Electric Propulsion system. The advantage of using an existing general aviation aircraft design is that data from the baseline model, powered by traditional combustion engines, can be compared to data produced by the same model powered by electric propulsion.

As presented below, the Tecnam P2006T is a twin-prop aircraft with two Rotax 912S3 horizontally opposed four-cylinder geared piston engines, 75 kW | 100 HP each, offering a total horsepower of 200 HP and powering two 2-bladed MT Propellers MTV-21, 1.78 m | 5 ft. 10 in. diameter constant-speed, fully feathering. Each Rotax Engine along with its MT Propeller weighs 56.7 kg | 125 lbs [9].

Εικόνα 27: Tecnam P2006T

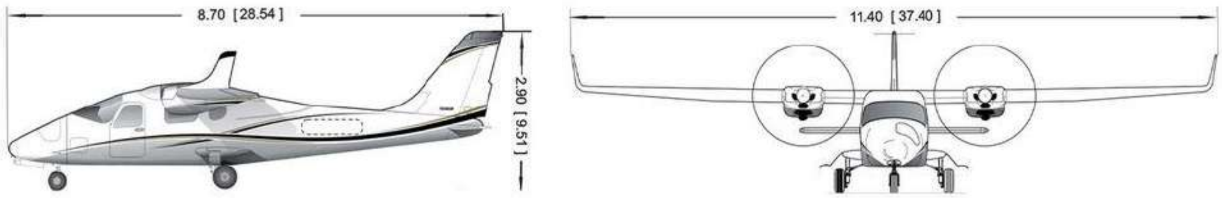

EXTERIOR

Length	28.5 ft (8,7 m)
Height	8.46 ft (2,58 m)
Wingspan	37.4 ft (11,4 m)
Area	159 ft2 (14,8 m2)

INTERIOR

Main Door Width	25 in (634 mm)
Main Door Height	38 in (970 mm)
Max Seating capacity	4

PERFORMANCE

Max cruise speed	145 kts 269 km/h
Stall Speed (Flaps Down Power Off)	55 kts (102 km/h)
Max Operating Altitude	14000 ft (4267 m)
Take off run	988 ft (301 m)
Take off distance	1293 ft (394 m)
Rate of climb	1036 ft/min (5.3 m/sec)
Landing Run	758 ft (231 m)
Landing Distance	1145 ft (349 m)
Range	650 nm (1204 km)

WEIGHT & LOADING

Maximum Take Off Weight	2712 lb (1230 kg)
Empty Weight, Standard	1.896 lb (860 kg)
Useful Load	816 lb (370 kg)
Baggage allowance	176 lb (80 kg)
Fuel tank capacity	200 lt (52.8 US Gal)

POWERPLANT

Engine Manufacturer	ROTAX 912 S3
Engine Power	200 hp
Propeller	Two-Bladed Constant Speed Full Feathering MT Propeller
Fuel Consumption	9 USG/h (34 lt/h)
Fuel Type	Mogas and Avgas

Εικόνα 28: Tecnam P2006T Dimensions, Specifications and Performance

NASA performed the installation of the DEP system in four steps or Modifications. The first Modification was to define the requirements of the research, along with systems analysis, design, and a number of tests, both in the air and on the ground. One of the earliest evaluations during the Mod I phase included ground validation of the distributed electric propulsion high-lift system, in 2015. An experimental electric wing, named the Hybrid Electric Integrated Systems

Testbed, or HEIST, was hoisted atop a heavily modified big rig, which drove at speeds close to 80 mph to simulate the effects of a wind tunnel. The wing was outfitted with 18 electric motors and propellers, which ran simultaneously during the lakebed runs. The tests showed that the motors produced a total of 300 HP. It validated that the airflow from the distributed 18 motors generated more than double the lift of the unblown wing.

The second Modification was to replace the two ICEs with two inboard electric motors, essentially turning the aircraft's propulsion system into electric. A Battery Redesign and Validation also took place, many Simulator flights were performed, and Tests and Validation were performed regarding the electric system.

The third Modification was to replace the original wing with an experimental, high aspect ratio wing that has a reduced wing area, thus increasing the wing load from 17 lbs/ft^2 to 45 lbs/ft^2. The large Cruise Motors were also relocated to the Wing Tips. The replacement of the 100 HP Rotax 912S engines with 60 kW | ~80 HP motors, developed by Joby Aviation, reduces the weight of each motor and propeller from approximately 56.7 kg | 125 lbs to about 25.8 kg | 57 lbs. The much lighter-weight electric motors allow for their relocation outboard. By moving the cruise motors from their Mod II inboard position to the wingtips for Mod III, the cruise motors recover energy that would otherwise be lost in the Wingtip vortices. Nacelles, which are outer casings that can generally act as housing for an aircraft's engine, are also installed along the leading edge of the wing where 12 high-lift motors will eventually be positioned.

The fourth Modification presents the X-57 in its final form. It features 12 high-lift motors along the leading edge of the distributed electric propulsion wing. Similar to the 18 small motors used during LEAPTech ground tests, the high-lift motors are electrically powered to generate enough lift for X-57 to be able to take off at standard Tecnam P2006T speeds, even with the high aspect ratio experimental wing. The high-lift motors and propellers are designed to activate, along with the Wingtip Cruise Motors, to get the X-plane airborne. When the plane levels out for cruise mode, the High-Lift Motors will then deactivate, and the five propeller blades for each motor will then stop rotating, and will fold into the nacelles, so that they don't create unwanted drag during cruise. The two Wingtip Cruise Motors will maintain flight during this phase of the flight. When the time comes to land, the High-Lift Motors will then reactivate, and centrifugal force will cause the propeller blades to unfold and create the appropriate lift for approach and landing.

To summarize, the X-57 Maxwell is an all-electric airplane that implements a Distributed Electric Propulsion system to demonstrate that high-efficiency electric propulsion can be integrated with aerodynamics to increase the performance of an airplane. To this end, distributed electric fans were installed on the wing to provide increased flow over the wing at the low takeoff and landing speeds of the X-57. The low-speed lift augmentation allows for a reduction in wing area for cruise optimization. The X-57 wing area was reduced to 42 percent of the wing area of the baseline aircraft, a Tecnam P2006T. With this reduced wing area and the electric propulsion system, it is estimated that the X-57 will cruise on less than one-third the total energy compared to the baseline aircraft. To meet the cruise performance goal at a Mach number of 0.233 at an altitude of 8000 feet, the X-57 has a cruise lift coefficient of 0.7516 and needs to have a cruise drag coefficient of 0.05423 or less. Based on specific criteria addressed in this paper, the X-57 Maxwell is estimated to meet its powered landing goal of a maximum lift coefficient of 4.0 [9].

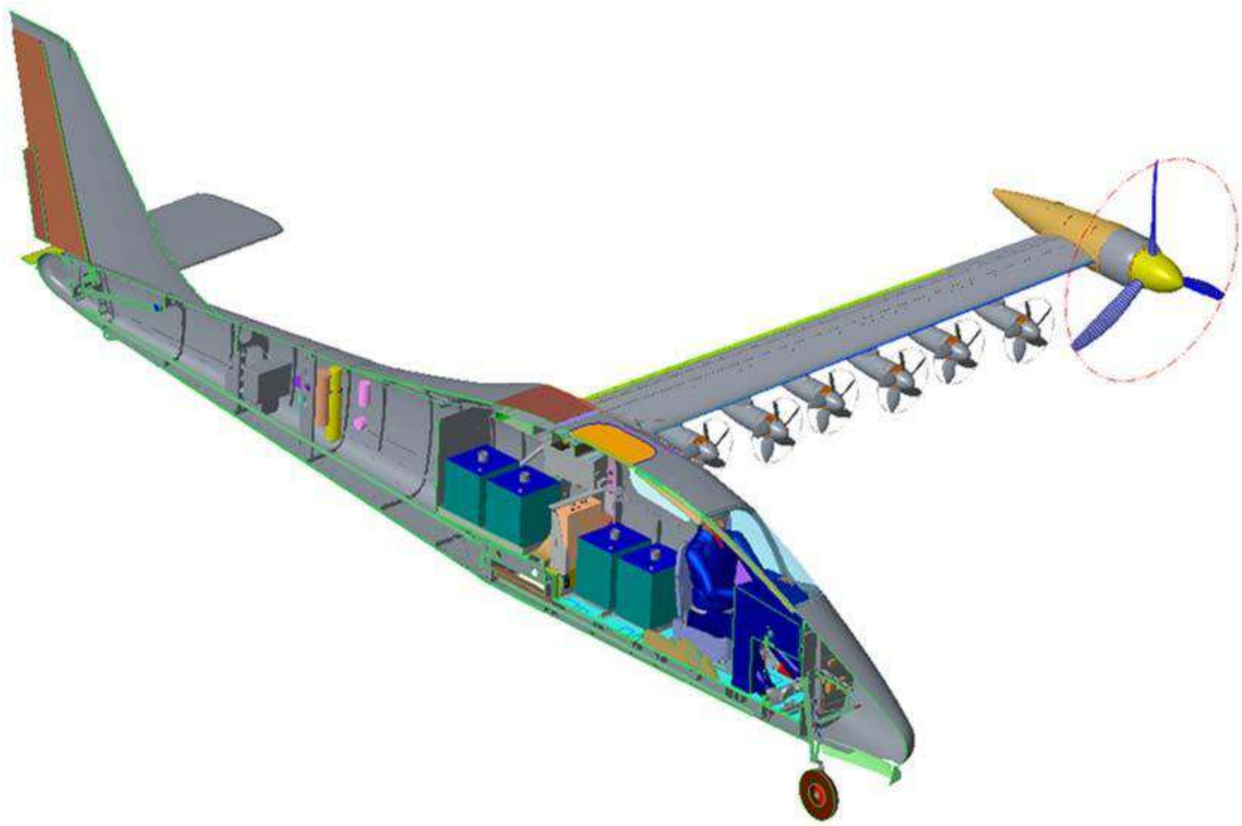

Εικόνα 29: X-57 Maxwell AEA Configuration

X-57 Maxwell SPECIFICATIONS

(Based on Mod IV configuration)

Goal: Help develop certification standards for emerging electric aircraft markets.

Design Driver: 500% increase in high-speed cruise efficiency, zero in-flight carbon emissions, and flight that is much quieter for the community on the ground.

Objectives are to:

Mod II: 3.3-times lower energy use at high speed compared to original P2006T.

Mod III: 1.5-times lower energy use at high speed compared to Mod II.

Aircraft Weight: Approximately 3,000 lbs | 1360 kg.

Maximum Operational Altitude: 14,000 ft.

Cruise Speed: 172 mph | 277 kmph (at 8,000 feet)

Critical Takeoff Speed: 58 knots (67 mph | 108 kmph).

Batteries:

- Lithium Ion.
- 860 lbs | 390 kg.
- 69.1 kWh (47 kWh usable)

Cruise Motors and Propellers (2):

- 60 kW | ~80 HP.
- Air-cooled.
- 5-ft | 1.524 m diameter propeller, 2250 RPM
- Out-runner, 14-inch | 0.3556 m diameter.
- 57 lbs | 25.8 kg each, combined weight.

High-Lift Motors and Propellers (12):

- 5-blade, folding propeller.
- 10.5 kW / 14 HP.
- Air-cooled.
- 1.9 ft | 0.58 m diameter propeller, 4548 RPM
- 15 lbs | 6.8 kg each, combined weight.

3.5.2 Concept

The Zenith Zodiac CH 650 B propulsion system configuration will be modified in this Thesis in order to investigate the effects of Distributed Electric Propulsion on the wing structure of the aircraft.

The Zodiac's nose-located ICE and propeller are replaced with a Distributed Electric Propulsion system with the electric motors and the fans/propellers mounted spanwise across the wings. The placement of the fuel-cell system powering the electric motors and the distributed propellers, as well as the placement of the tank storing the liquid Hydrogen, are not a matter of particular concern in this Thesis, as it is assumed that they are placed in the fuselage.

NASA's X-57 Maxwell configuration will be significantly followed, so that two Cruise Motors and their Propellers are mounted on the Wingtips and a number of small High-Lift Motors with their Propellers are mounted across the Wingspan of the Zodiac CH 650 B. The Wings now must be able to handle extra loads, due to the weight of the Electric Motors and the Propellers, albeit with fuel no longer needed to be stored in the wing box.

The small spanwise-mounted propellers will be used during take-off and landing in order to increase Lift and provide STOL capabilities, while folding during flight in order to reduce Drag and increase Cruising Efficiency.

Both the high-lift and cruise propellers have a "Inboard Up, Outboard Down" rotation direction. The "Inboard Up, Outboard Down" in the high-lift propellers is preferred due to the lift distribution augmentation towards the fuselage rather than the wing tip, caused by the slipstream effect, explained further in Chapter 4.1.5. A lift distribution stronger towards the fuselage is desirable for structural reasons. The "Inboard Up, Outboard Down" in the cruise propellers presents the advantage of cruise propellers essentially rotating counter to the wing tip vortex direction in order to eliminate induced drag.

3.5.3 Proposed Architecture

The DEP system architecture implemented on the Zenith Zodiac CH 650 B is presented below. The aircraft presents an ICE as the original propulsion system and the AEA conversion proposal in this Thesis is a liquid Hydrogen Fuel-Cell system.

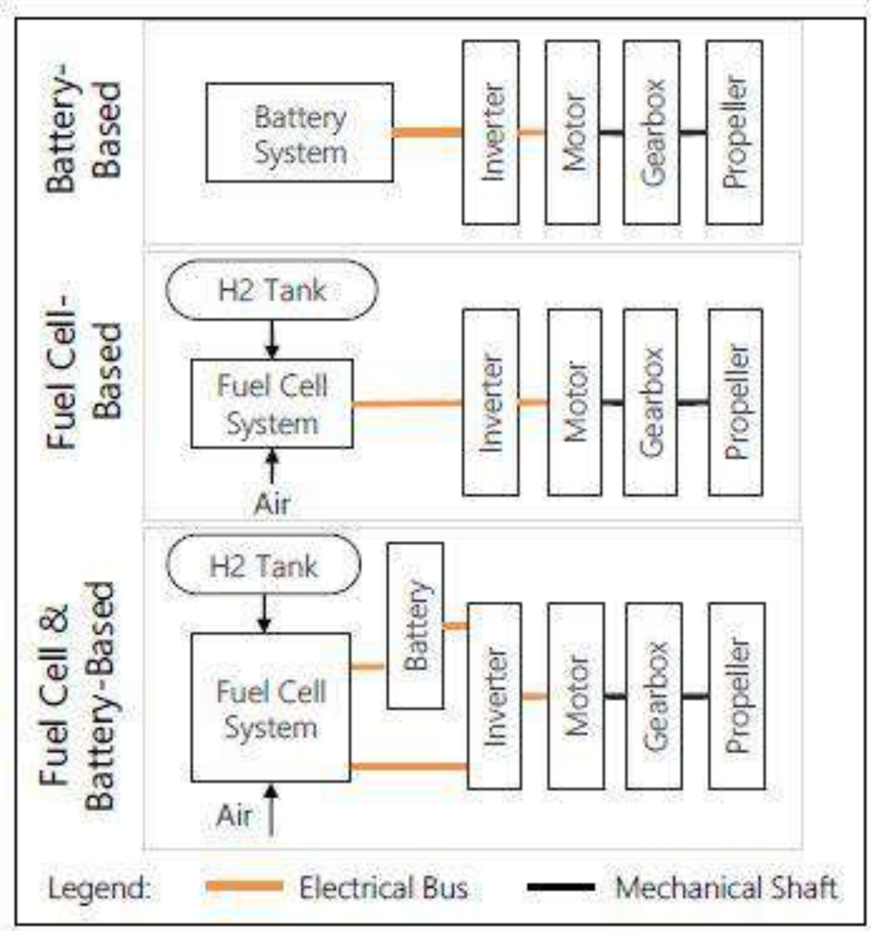

Εικόνα 30: Block Diagrams for AEA Propulsion Topologies

The electricity is produced by a Fuel-Cell system, utilizing Air and Hydrogen, with the latter being stored in a Hydrogen Tank in liquid state (-253 °C). The produced electricity is then transferred via Power Lines to the Inverters. Then, electricity is transferred to the Electric Motors (Cruise and High-Lift) that in turn power the Propellers.

	E-Motors (Cruise)	**E-Motors (High-Lift)**	**Propellers (Cruise)**	**Propellers (High-Lift)**	**Inverter**
Model	Siemens SP90G	MGM Compro REG60	E-Props 3-T-27-C4 3-blade Adjustable	Custom E-Props 5-P-72-115 5-blade Folding	RedPrime Fuel-Cell DC-DC converter 210kW, 850V
Continuous Power (HP | kW)	80 | 60	14 | 10.5	-	-	282 | 210
Max Power (HP | kW)	87 | 65	20 | 15	94 | 70	27 | 20	282 | 210
RPM	1000-4000	3000-12000	2500	4500	-
Thrust	-	-	1961	618	-
Weight (kg)	13	3.75	12	3.25	20
Cooling	Air	Air	-	-	Air
Diameter (m)	0.224	0.114	1.6	0.58	-

Πίνακας 9: Proposed DEP System Specifications

The configuration includes two (2) Cruise Electric Motors and their Propellers as the primary power source, mounted on the Wing Tips and eight (8) High-Lift Electric Motors and their Propellers as the secondary power source, mounted across the aircraft's Wingspan.

The AEA DEP configuration increases the maximum aircraft power to 272 HP, compared to 120 HP of the original configuration. 112 HP of the total output belongs to the High-Lift Motor-Propeller Units, used mostly in Take-Off and Landing, meaning 160 HP is left for Cruising, an ideal output taking into account the increased aircraft weight.

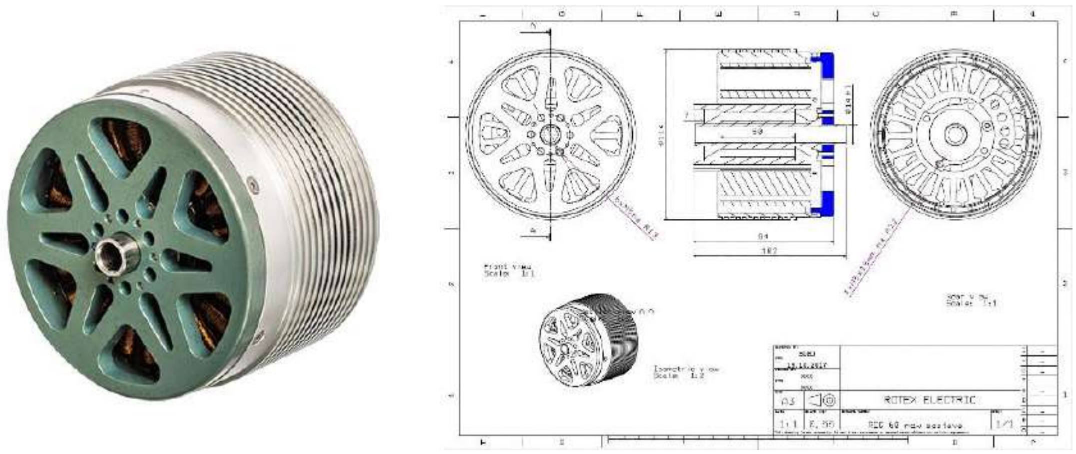

Εικόνα 31: MGM Compro REG 60 Electric Motor (High-Lift Units)

Εικόνα 32: Siemens SP90G Electric Motor (Cruise Unit)

The Cruise Propeller model is the 3-T-27-C4 3-blade Adjustable from E-Props, made from carbon-fiber, with a diameter of 1.6 m, a total weight of 12 kg including the spinner, ability to handle a maximum power of 97 HP and spinning at 2500 RPM. At 2500 RPM, the Cruise Propeller produces 300 Nm of Torque and 1961 N of Thrust [17].

The High-Lift Propeller model is the 5-P-72-115 5-blade Custom Folding from E-Props, made from carbon-fiber, with a diameter of 0.58 m, a total weight of 3.25 kg including the spinner, ability to handle a maximum power of 27 HP and spinning at 4500 RPM. At 4500 RPM, the High-Lift Propeller produces 65 Nm of Torque and 618 N of Thrust [17].

The original configuration includes several weights that are relieved during the aircraft's DEP implementation. The original propulsion system includes the ICE (Jabiru 3300) and the nose propeller (MTV-33, including the spinner), weighing 91 kg and 35 kg respectively. The fuel weight relieved is equal to 65 kg.

Naturally, weight is also added as a result of the new configuration, mainly associated with the electrical system. Each High-Lift Motor-Propeller unit weighs 7 kg, with eight (8) such units deployed. Each Cruise Motor-Propeller unit weighs 25 kg, with two (2) such units deployed on each wing tip. The Inverter weighs 20 kg and the Hydrogen Fuel-Cell system combined with the Hydrogen Tank are assumed to weigh approximately 265 kg. The equivalent of 92 L or 65 kg of AvGas is 160 L or 11.2 kg of liquid Hydrogen, due to Hydrogen being approximately three times more energy dense than AvGas [21] and also due to Fuel-Cell systems (>60% thermal efficiency) being approximately two times more efficient than turboprop ICEs (25-35% thermal efficiency) [23]. An LSA has a gravimetric index of $GI = 0.37$, with the gravimetric index being equal to: $GI = \frac{fuel\,weight}{fuel+tank\,weight}$. It is evident that the Hydrogen tank weighs 19 kg and the Fuel-Cell unit capitalizes most of the 265 kg system mass.

The original MTOW of the Zenith Zodiac CH 650 B is equal to 600 kg, prior to the DEP conversion. After installing the electricity production and propulsion systems, the new MTOW of the aircraft rises to 800 kg. The structural weight of each wing remains equal to approximately 50kg. Each wing is now relieved from 32.5 kg of fuel storage, but new inertial loads include electric motor and propeller units and nacelles mounting.

The axis of High-Lift Motor-Propeller unit 1, moving from the wing root towards the wing tip, has a horizontal distance of $y_{HL,1} = 350\ mm$ from the fuselage. The High-Lift unit axes have a horizontal distance of $y_{HL,2} = y_{HL,3} = y_{HL,4} = 600\ mm$ from each other and the Cruise unit axis has a horizontal distance of $y_{CR} = 1105\ mm$ from the axis of High-Lift unit 4.

All High-Lift and Cruise Propeller planes are positioned in a horizontal distance of $s_{horizontal} = 0.3\ m$ from the wing leading edge.

The High-Lift Motor-Propeller units are mounted under the wing, with the Motor-Propeller axis positioned in a vertical distance (or Relative Height) of $s_{vertical} = 0.115\ m$ from the leading edge. The High-Lift Motor-Propeller spinner is the CCU120, with a diameter of 120mm and a length of 180mm. Each motor is housed in an aerodynamically-efficient shaped nacelle with a length of 750mm.

The Cruise Motor-Propeller units are integrated into the wing, with the Motor-Propeller axis coinciding with the leading edge. The High-Lift Motor-Propeller spinner is the CCU240, with a diameter of 240mm and a length of 350mm. Each motor is housed in an aerodynamically-efficient shaped nacelle with a length of 2000 mm.

The tilt angle defined as the angle between the propeller axis and the symmetry plane of the wing (XY plane) is zero. The toe angle, defined as the angle between the propeller axis and the XZ plane is set to zero.

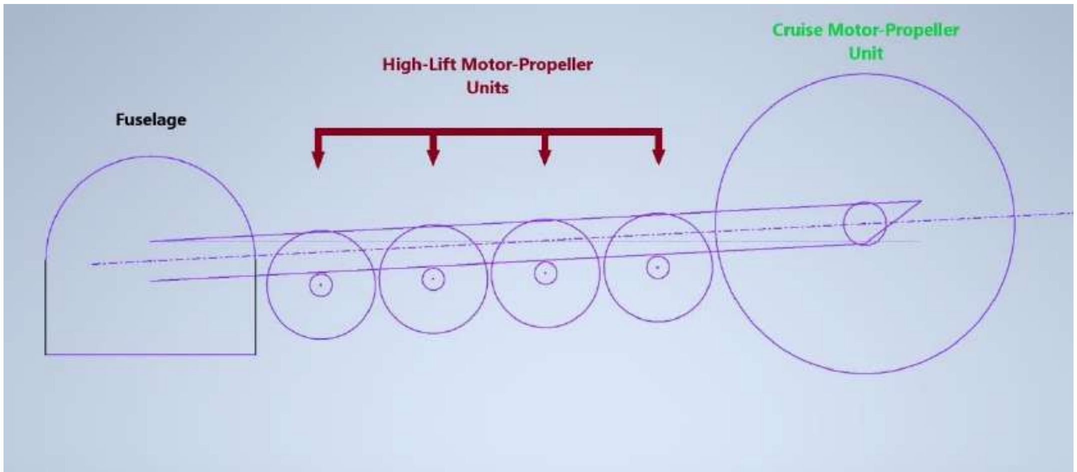

Εικόνα 33: Simplified DEP Topology Sketch (Front View)

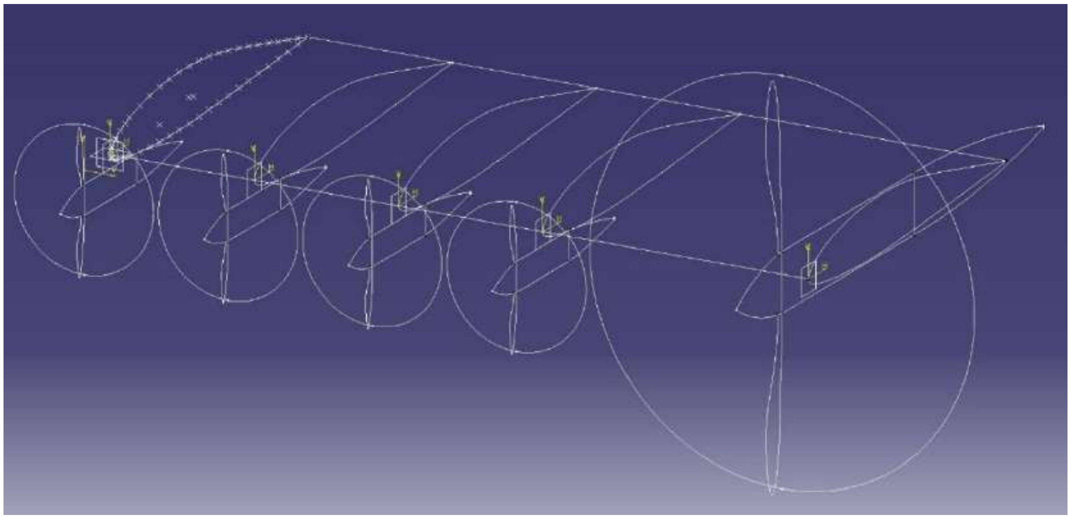

Εικόνα 34: DEP Topology Wireframe

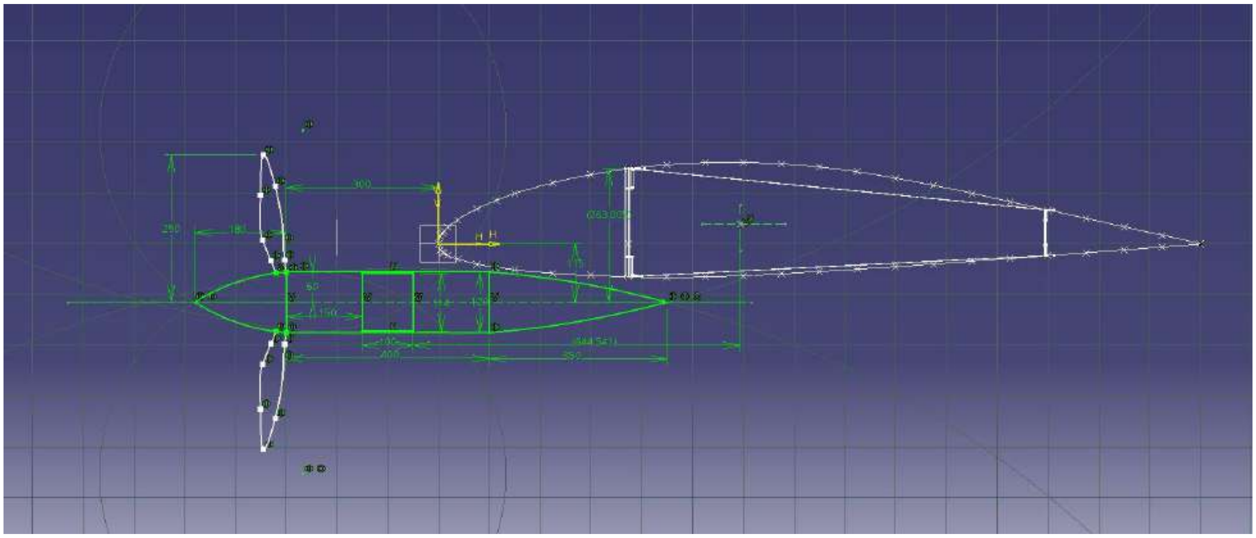

Εικόνα 35: DEP High-Lift Unit Sketch (Side View)

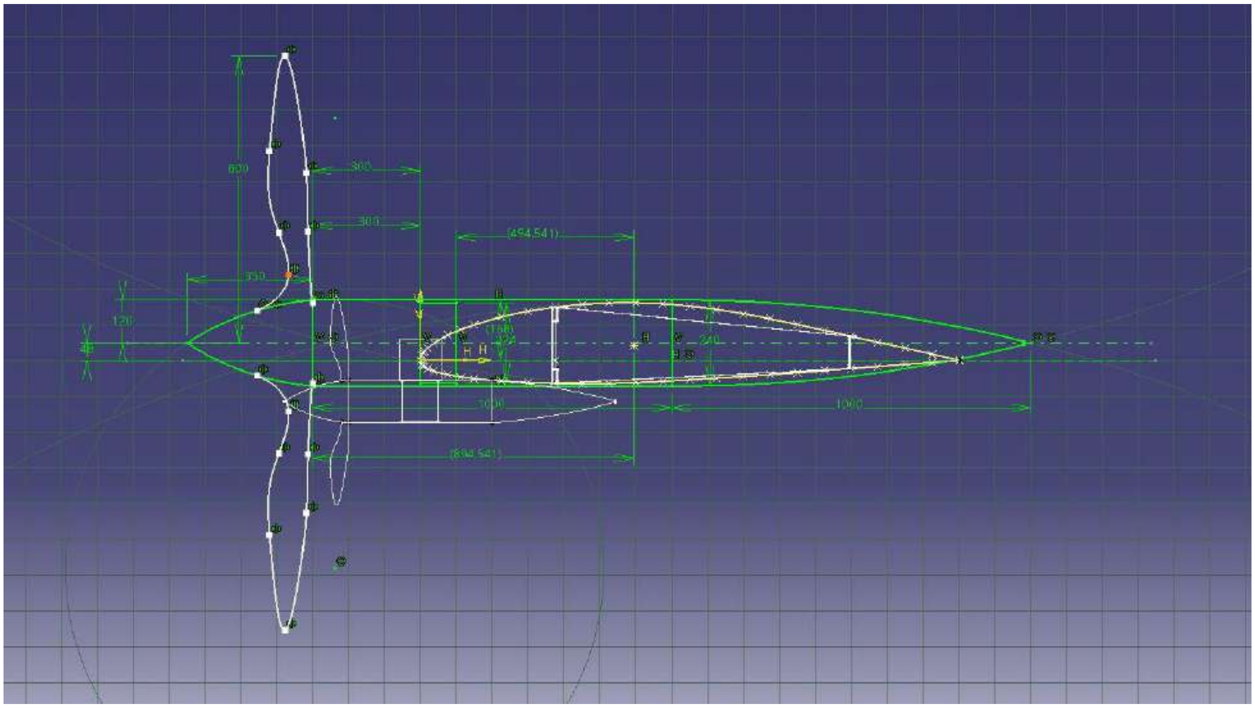

Εικόνα 36: DEP Cruise Unit Sketch (Side View)

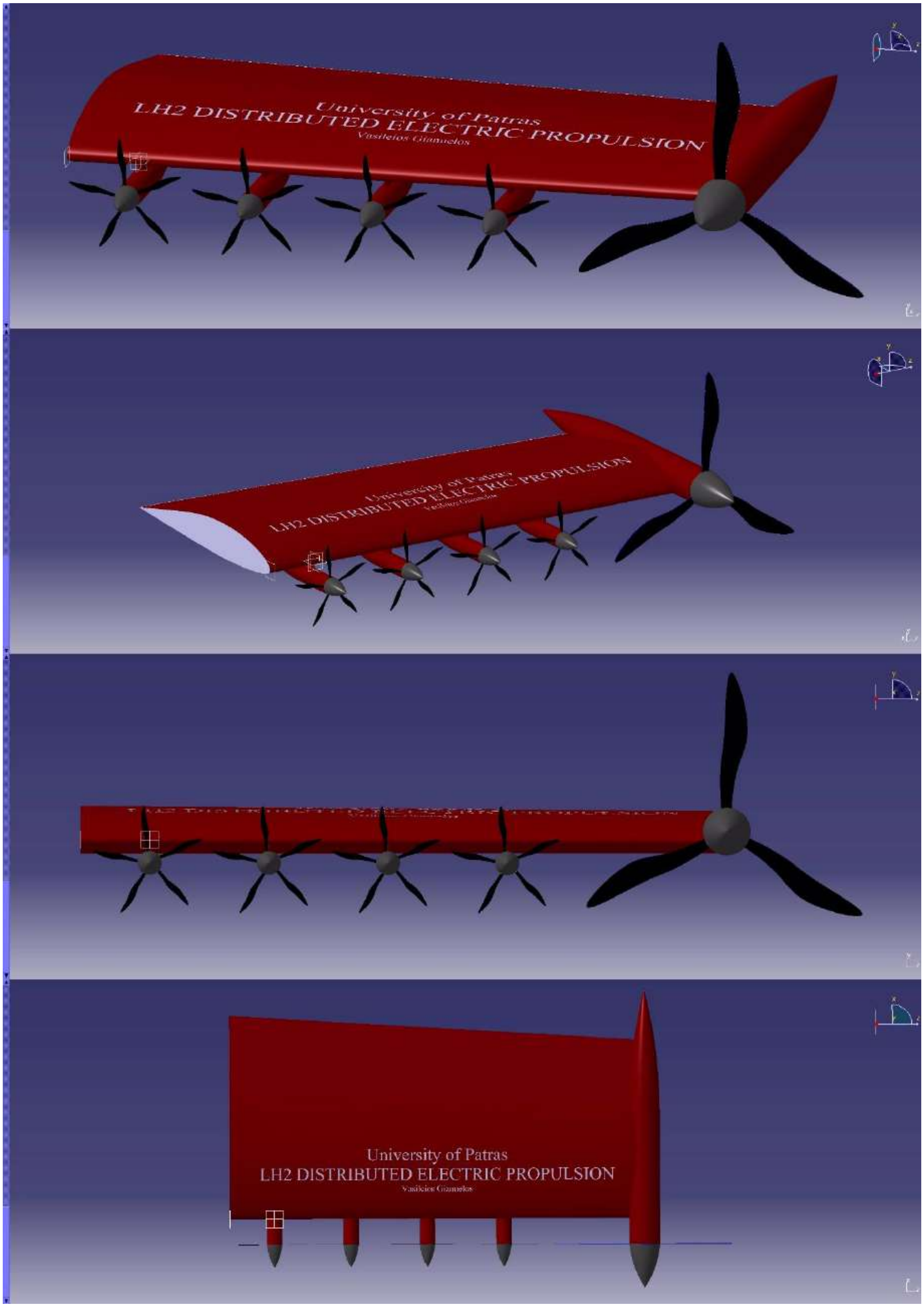

Εικόνα 37: DEP Configuration Render

4.0 WING STRUCTURAL ANALYSIS WITH ANALYTICAL METHOD

4.1 THEORETICAL BACKGROUND

4.1.1 Bending Theory

Assuming a beam similar to the one pictured below, with the coordinate system X,Y,Z as seen. The Bending Theory is used in applied mechanics to explain the way a beam behaves when exposed to external force. When a beam is subjected to a loading system or by a force couple acting on a plane passing through the axis, then the beam deforms. This axial deformation is called bending of a beam. Due to the shear force and bending moment, the beam undergoes deformation. These normal stresses due to bending are called bending normal stresses. The bending moment, M, along the length of the beam can be determined from the moment diagram M.

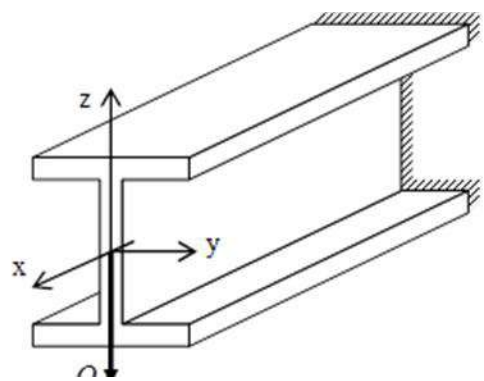

Εικόνα 38: Simple Beam

The Bending Law states:

$$\sigma = \frac{M_y}{I_y} z - \frac{M_z}{I_z} y \quad [MPa]$$

where σ is the bending normal stress, M is the bending moment and I is the second moment of inertia of the cross-section about the axes y, z.

The neutral zone is the locus of points with zero bending normal stress. If the Bending Law is solved for $\sigma = 0$, the neutral zone expression can be obtained:

$$z = \frac{M_z I_y}{M_y I_z} y \quad [m]$$

In the case of simple bending about the y-axis, the Bending Law is simplified as the $-\frac{M_z}{I_z} y$ factor is equal to zero. Hence:

$$\sigma = \frac{M_y}{I_y} z \quad [MPa]$$

The bending stress is zero at the beam's neutral zone and it increases linearly away from the neutral zone until the maximum values at the top and bottom of the beam cross-section. It is the line that passes through the centroid of the cross-section and is perpendicular to the plane of bending.

The maximum bending stress occurs at the extreme fiber of the beam and is calculated as:

$$\sigma_{max} = \frac{M_y}{I_y} z_{max} \quad [MPa]$$

where σ is the bending stress, M is the bending moment and I is the second moment of inertia of the cross-section.

The shear stress is zero at the free surfaces (the top and bottom of the beam), and it is maximum at the center of the cross-section. The equation for shear stress at any point located a distance from the center of the cross-section is given by:

$$\tau = Q_z \frac{S_y(z)}{I_y \cdot t} \quad [MPa]$$

where τ is the shear stress, Q is the shear force, S is the first moment of inertia of the cross-section about the neutral zone, I is the moment of inertia of the cross-section, and t is the width of the cross-section.

4.1.2 Shear Flow Theory

As previously mentioned, the philosophy behind Lightweight Structures is the minimization of weight without compromising the stiffness and the strength of the structure. Thus, thin sheet metal beams are designed, reinforced with strong Flanges and Ribs, due to their sensitivity to low load buckling. This philosophy produces thin-walled beams capable of safely handling the applied loads. Loads are transmitted to the structure mostly through sheet metal shear flows and as a result the beams are also called shear beams [5].

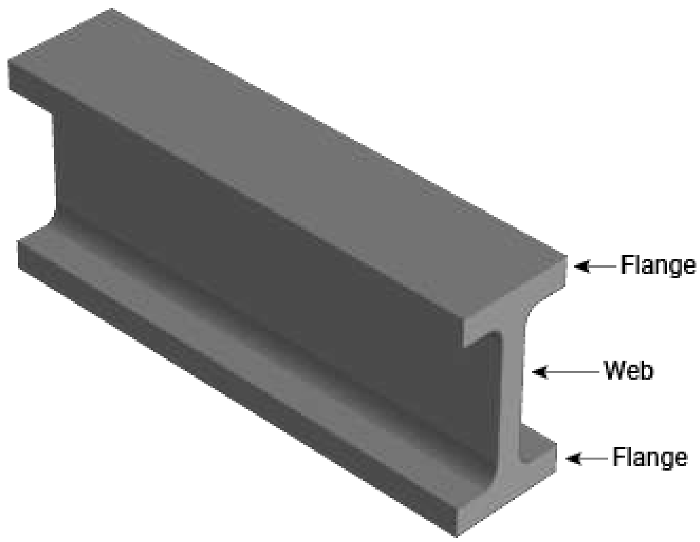

Εικόνα 39: I-Beam Anatomy

Shear Flow Theory's aim is to express simple equations so that an engineer can easily calculate the shear load flow of complicated structures and perform simple analyses with satisfying result precision, as often a quick and satisfying analysis is more important than a detailed one. The theory assumptions are mostly related to the simplification of the structure and its behavior to certain loads. The analysis is performed in the simplified structure model and the accuracy of results depends on the quality of simplification.

In the example of the H-Beam below, the impact of simple assumptions on the analysis and on the results accuracy is examined. From simple Bending Theory, it is known that normal bending stresses (flexural stresses) develop in the beam, which increase linearly with the distance from the neutral zone and become maximum in the outer zones of the beam.

$$\sigma_x(z) = \frac{M_y}{I_y} \cdot z, \qquad \sigma_{max} = \frac{M_y}{I_y}\frac{h}{2} \tag{4.1}$$

Shear stresses are also developed in the beam, and mostly in the Web. The shear stress distribution is parabolic and is function of the distance from the cross-section's center of gravity. The maximum value of the shear stress is located at the cross-section's center of gravity.

$$q(z) = \tau_{xz}(z) \cdot t = Q_z \frac{S_y(z)}{I_y}, \qquad q_{max} = Q_z \frac{S_y^{max}}{I_y} \tag{4.2}$$

In the Equations (4.1), (4.2), Q_y is the applied bending Force, I_y is the Second Moment of Inertia about the bending axis y and S_y is the First (or Static) Moment of Inertia of part of the cross-section, between z and h/2, about the bending axis y.

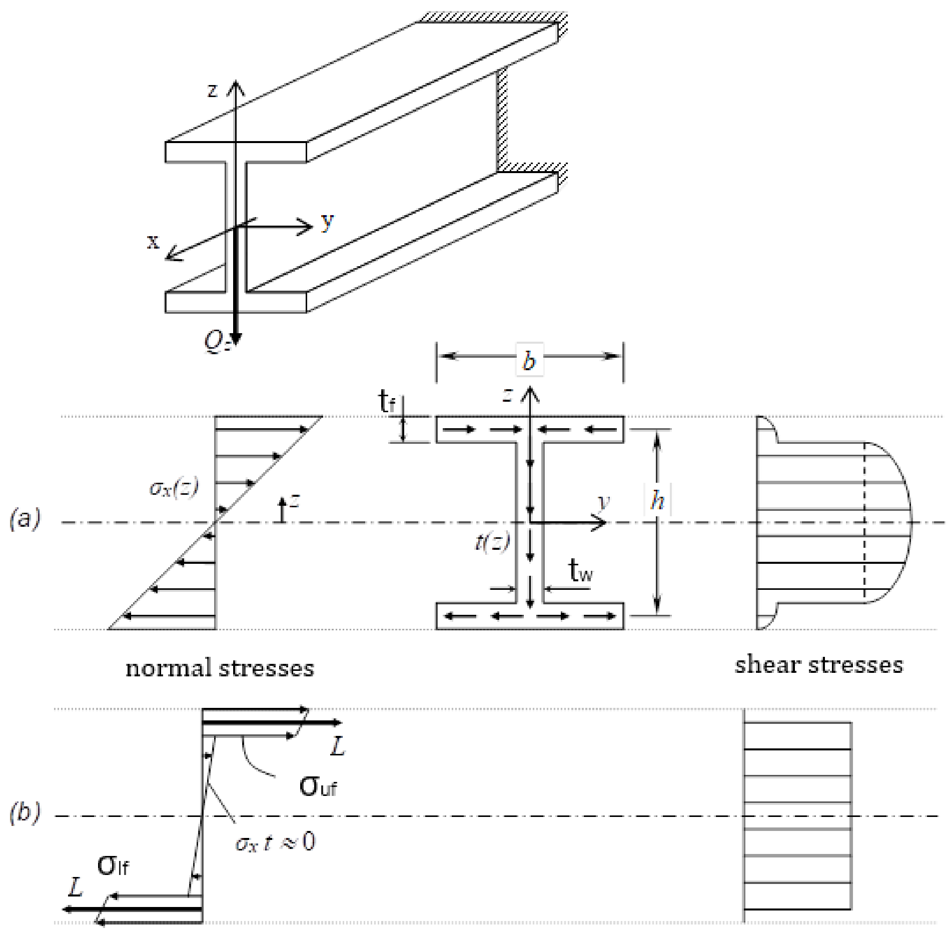

Εικόνα 40: I-Beam Cross Section (Normal and Shear) Stress Distribution

In the Figure above, the distribution of normal and shear stresses in the cross section in a position x of the beam is depicted. The majority of the load is applied to the Flanges, while the Web handles a very small part of the load.

If the assumption that the load handled by the Web is negligible compared to the respective load handled by the Flanges is made, the equations (4.1), (4.2) are significantly simplified. Then, it can be assumed that the normal stresses are received exclusively by the Flanges. Thus, each Flange handles a normal force $L = \sigma F$ where F is the Flange cross-section and σ is the Flange mean normal stress, so that the static equivalence $M_y(x) = Lh$ between the moment $M_y(x)$ and the pair of forces L applies:

$$\sigma = \sigma_{uf} = -\sigma_{lf} = \frac{L}{F_f} = \frac{M_y(x)}{h \cdot F_f} \tag{4.3}$$

In Equation 4.3, σ_{uf} is the normal stress of the upper flange, while σ_{lf} is the normal stress of the lower flange.

Assuming that the Web does not handle any normal stresses, the Web shear flow $q = \tau t$ is constant across the Web's height. This conclusion can be reached by studying the equivalence of a differential section dx of the beam's Flange in the direction x, as shown in the Figure below:

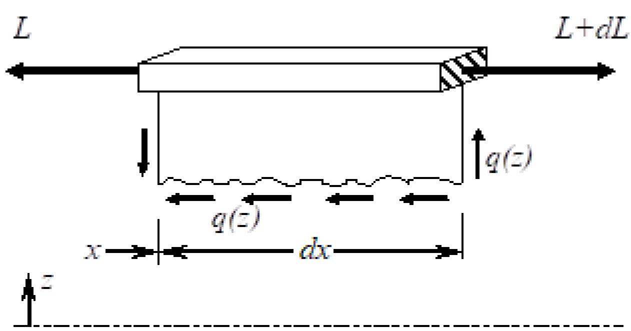

Εικόνα 41: Shear Flow (constant) across Web's height

$$dL = q(z)dx$$

$$q(z) = \frac{dL}{dx} = \frac{d(^M/_h)}{dx} = \frac{1}{h}\frac{dM}{dx} = \frac{Q}{h} \tag{4.4}$$

It is now mathematically proven that the Web shear flow is constant and not parabolic, and is only a function of the shear force Q and the Web height h.

An easy mistake would be to compare the theoretical maximum normal and shear stresses given by Eq. (4.1) and (4.2) with the respective approximate values given by Eq. (4.3) and (4.4). To compare the normal stresses, the second moment of inertia I_y of the I-beam's cross-section must be calculated first. To calculate the I-beam's second moment of inertia, the cross section is divided into three rectangular sections, the Web and the two Flanges. Apart from the three rectangular sections' moments of inertia, the Flanges' Steiner Factor must be taken into account since the Flanges' center of gravity does not coincide with the I-beam's respective CoG. Thus:

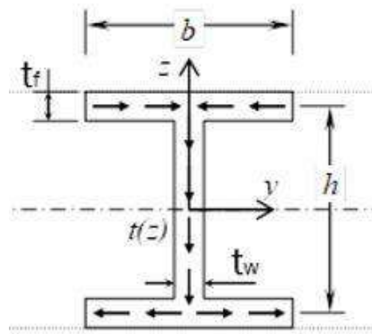

Εικόνα 42: I-Beam Parameters

$$I_y = I_y^{web} + 2 \cdot I_y^{flange} + 2 \cdot SteinerFactor = \frac{t_w \cdot h^3}{12} + 2\frac{b \cdot t_f^3}{12} + 2\left(\frac{h}{2}\right)^2 F_{flange} \Rightarrow$$

$$I_y = \frac{t_w \cdot h^3}{12} + 2\frac{b \cdot t_f^3}{12} + 2\left(\frac{h}{2}\right)^2 F_f = 2F_f\left(\frac{h}{2}\right)^2 \left(1 + \frac{1}{6}\frac{t_w h}{t_f b} + \frac{1}{3}\frac{t_f^2}{h^2}\right) \tag{4.5}$$

If we assume that the factor $\frac{t_f^2}{h^2} \ll 1$, then the Eq. (4.5) gives the second moment of inertia approximate value:

$$I_y \simeq 2\left(\frac{h}{2}\right)^2 F_f\left(1 + \frac{1}{6}\frac{F_w}{F_f}\right) \tag{4.6}$$

Normal Stress: Using Eq.(4.6) in Eq. (4.1), the maximum normal stress in an I-beam is:

$$\sigma_{max} \simeq \frac{M_y}{2\left(\frac{h}{2}\right)^2 F_f\left(1 + \frac{1}{6}\frac{F_w}{F_f}\right)} \tag{4.7}$$

The difference between the approximate and the theoretical maximum normal stress is only the factor $\frac{1}{6}\frac{F_w}{F_f}$, thus the error is equal to:

$$e = \frac{\sigma_{max} - \sigma_{uf}}{\sigma_{max}} = \frac{1}{6}\frac{F_w}{F_f} \tag{4.8}$$

If we assume that $\frac{1}{6}\frac{F_w}{F_f} \ll 1$, then the error regarding the approximate and the theoretical maximum normal stress is negligible.

Shear Stress: To compare the shear stresses, the maximum first (static) moment of inertia S_y of the I-beam's cross-section must be calculated first.

$$S_y^{max} = \sum z_i F_i = z_f F_f + z_w F'_w = \left(\frac{h}{2}\right) F_f + \frac{\frac{(h - t_f)}{2}}{2} F'_w = \left(\frac{h}{2}\right) F_f + \frac{(h - t_f)}{8} F_w \Rightarrow$$

$$S_y^{max} = \left(\frac{h}{2}\right) F_f + \frac{(h - t_f)}{8} F_w \simeq \frac{h}{2}\ F_f (1 + \frac{1}{4}\frac{F_w}{F_f}) \tag{4.9}$$

If we assume that $\frac{1}{4}\frac{F_w}{F_f} \ll 1$, then the Eq. (4.2) is simplified:

$$q_{max} \simeq Q_z \frac{F_f\left(\frac{h}{2}\right)}{2F_f\left(\frac{h}{2}\right)^2} \simeq \frac{Q_z}{h} \tag{4.10}$$

Thus, the maximum shear flow is equal to the approximate value of Eq. (4.4).

Conclusion: If the Web's width t_w is negligible compared to height h so that $\frac{t_w^2}{h^2} \ll 1$ and the Flanges' cross-section area to the Web's cross-section area ratio is equal to $\frac{F_w}{F_f} \ll 4$, then the Flanges' normal stresses and the Web's shear stress can be calculated with satisfying accuracy using the simplified expressions:

$$\boldsymbol{\sigma_f} = \pm \frac{\boldsymbol{M}}{\boldsymbol{hF_f}} = \pm \frac{\boldsymbol{L}}{\boldsymbol{F_f}}, \text{ where } L = \frac{M}{h} \text{ and } \boldsymbol{\tau} = \frac{\boldsymbol{q}}{\boldsymbol{t}}, \text{ with } \boldsymbol{q} = \frac{\boldsymbol{Q}}{\boldsymbol{h}} \tag{4.11}$$

The Equations (4.11) describe the stress problem of a beam that is composed of two Flanges (the upper and the lower) and a thin sheet metal (Web), with the assumption that the Web does not handle the bending moment M, but does handle only the shear force Q. Such a beam is called a shear beam. The shear beam's cross section is simplified into two concentrated areas (Flanges) and a thin Web.

As previously mentioned, the simplified beam's first and second moments of inertia are equal to:

$$\boldsymbol{I_y = 2\left(\frac{h}{2}\right)^2 F_f} \tag{4.12}$$

$$\boldsymbol{S(y) = F_f \frac{h}{2}} \tag{4.13}$$

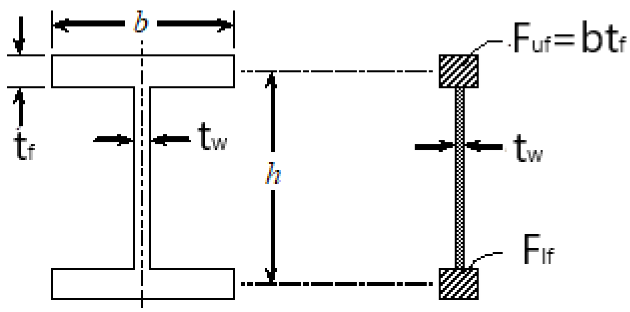

Εικόνα 43: Simplified I-Beam Cross-Section

The accuracy of Equation (4.11) depends mostly on the ratio $\frac{F_W}{F_f}$, where F_W is the Web cross-section area and F_f the Flange cross-section area. Thus, the importance of shear beams in Lightweight Structure Design -where the structure's weight minimization is critical- can be recognized. As a result, a beam's weight is minimized by placing Flanges where high bending stresses are developed and connecting them with thin Webs.

The smooth transmission of concentrated forces to the structure must also be taken into account, leading to the use of appropriate stiffeners. The Flanges usually consist of thin-walled industrial or pressed profiles or combinations of such profiles. Thin sheet metal presents minimal buckling resistance and can easily break when concentrated forces are applied. It is vital for the engineer to use appropriate stiffeners such as rods and ribs in order to ensure a smooth transmission of the concentrated forces to the structure.

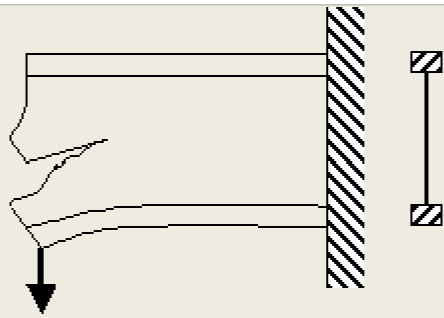	Danger of breaking if the concentrated force is not transmitted smoothly.
	Danger of buckling if the concentrated force is not transmitted smoothly.
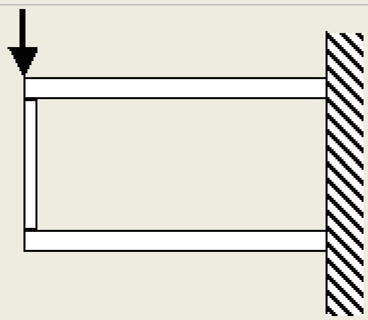	Rod placement to ensure the concentrated force is transmitted smoothly.
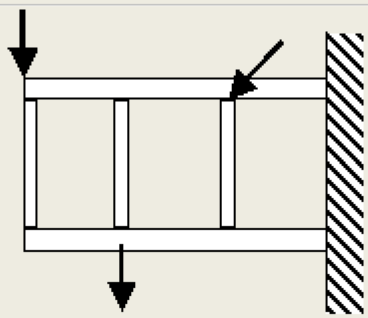	Appropriate stiffener placement where concentrated forces are applied, to ensure smooth transmission.

Πίνακας 10: Examples of Concentrated Force Transfer

4.1.3 Flight Design Envelope

It is understood that during the flight, from take-off to landing, the nature and the magnitude of external loads constantly change. Thus, the Flight Envelope of the aircraft is used. The Flight Envelope describes every possible aircraft load case, for example straight horizontal flight, maneuver, aerodynamic turbulence, landing etc. The Flight Envelope of each aircraft is unique, as different types of aircraft need to satisfy different demands.

As mentioned earlier, the Zenith Zodiac CH 650 B is classified as a Light Sport Aircraft (LSA). The Flight Envelope of the LSA category is presented below. In this Thesis' analysis the load case used will be the one with the maximum loads, thus a load factor equal to +3.8.

LSA aircrafts are designed to a design limit factor of +3.8/-2 G. Exceeding the design envelope may result in permanent deformation of the structure or catastrophic structural failure [19].

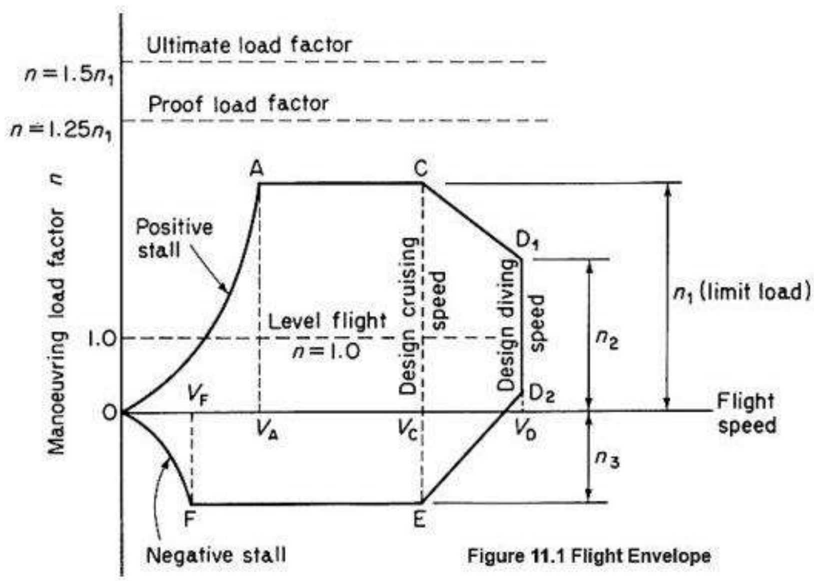

Εικόνα 44: Flight Design Envelope

The structural analysis in this Thesis is performed in a load case scenario where the aircraft is operating at Line AC, where the maximum positive load factor is applied.

Also, the aircraft is operating a correctly banked turn with full thrust. In this maneuver, the aircraft flies in a horizontal turn with no sideslip at constant speed [15]. If the radius of turn is R and the angle of bank is Φ, then the forces acting on the aircraft are those shown below:

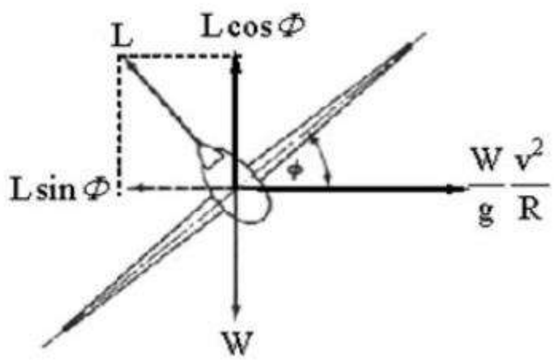

Εικόνα 45: Correctly Banked Turn

$$L \cdot sin\Phi = \frac{W}{g} \cdot \frac{V^2}{R}$$
$$L \cdot cos\Phi = W$$

$$n = \frac{L}{W} = \frac{L}{L \cdot cos\Phi} = \frac{1}{cos\Phi}$$

$$tan\Phi = \frac{V^2}{gR} \Rightarrow R = \frac{V^2}{g \cdot tan\Phi} \quad [m]$$

For horizontal flight turn, the tighter the turn, i.e. R is reduced, the greater the angle of bank Φ should be. If Φ is increased, load factor n is increased also. Aerodynamic theory shows that, for a limiting value of n, the minimum time taken to turn through a given angle occurs when the lift coefficient C_L is maximum, that is with the aircraft on the point of stalling [15].

When studying a load case, for example in this Thesis, with the maximum load factor applied at a correctly banked turn with the minimum time taken to turn, with the load factor known, the aircraft speed can be obtained from the Wing Lift Equation:

$$L_{wing} = \frac{1}{2}\rho V_{stall}^2 S_{wing} C_{L,max} \Rightarrow nW = \frac{1}{2}\rho V_{stall}^2 S C_{L,max} \Rightarrow V_{stall} = \sqrt{\frac{2nW}{\rho S_{wing} C_{L,max}}} \quad \left[\frac{m}{s}\right]$$

4.1.4 Aerodynamic Fundamentals

The main loads acting on the wing are:

- Aerodynamic Loads: Lift, Drag, Pitching Moment
- Engine Loads: Thrust, Engine Weight
- Landing Mechanism Loads: Vertical Loads, Braking
- Fuel Load
- Inertial Loads: Acceleration (translative and rotational), Oscillations (Aeroelasticity)

Weight: The wing structure must be strong enough to withstand not only aerodynamic loads acting on it but also its own structural weight along with the weight of the propulsion system mounted usually on the wing of the aircraft.

Thrust: Thrust is defined as the force produced by an aircraft's engines or propulsion system that propels the aircraft forward. It is a crucial aerodynamic force that opposes drag and is necessary for an aircraft to move through the air and maintain flight.

Airfoil: An airfoil is a streamlined shape that is designed to produce lift when it moves through a fluid. An airfoil typically has a curved shape, with the upper curved more than the lower surface. This curved shape is called an airfoil profile. Some important airfoil parameters such as the chord, the mean camber line and the leading and trailing edges are presented below.

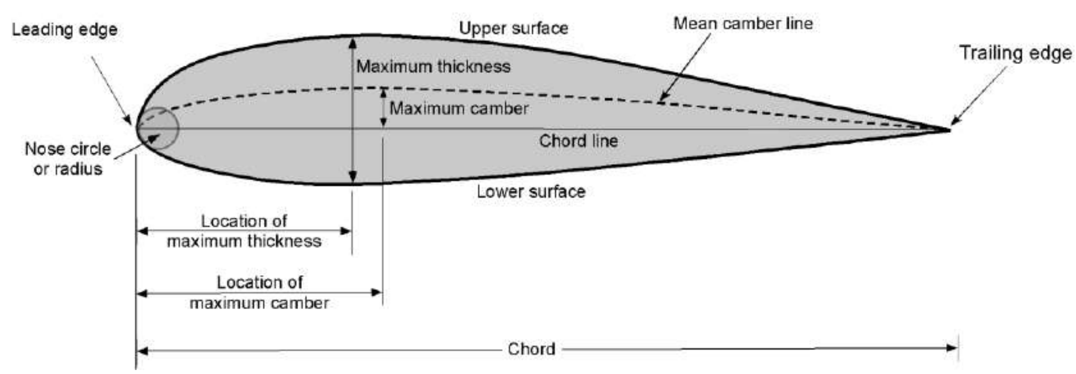

Εικόνα 46: Airfoil Parameters

Airfoil Pressure Distribution: Air pressure varies across the surfaces of the airfoil. Typically, the pressure on the upper surface of the airfoil is lower than the pressure on the lower surface. This pressure difference creates a net force called Lift, which is responsible for the aircraft's ability to generate upward force and stay aloft. The pressure distribution on an airfoil is explained by Bernoulli's principle, which states that as the airspeed increases, the air pressure decreases. On the upper surface of the airfoil, the airflow is faster, resulting in lower pressure, while on the lower surface, the airflow is slower, resulting in higher pressure. This pressure difference contributes to the Lift force.

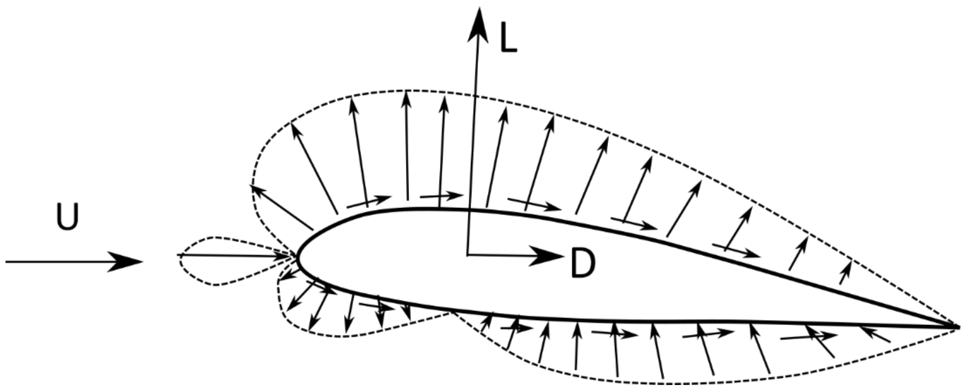

Εικόνα 47: Pressure Distribution around an Airfoil

Lift: Lift refers to the aerodynamic force that acts perpendicular to the relative motion of an object moving through a fluid. Lift is the force that opposes the force of gravity, allowing an aircraft to become airborne, stay aloft, and control its altitude and flight path.

Drag: It is the resistance or force that opposes the motion of an object as it moves through a fluid, such as air or water. Drag acts in the direction opposite to the object's motion and is caused by the interaction between the object and the fluid. Drag is divided in Parasitic and Induced Drag. Induced Drag is specific to lifting surfaces, such as the wings of an aircraft. It occurs as a byproduct of generating lift and is related to the production of wingtip vortices. Parasitic Drag includes all forms of Drag except for Induced Drag. It encompasses Pressure Drag (which is associated with the pressure differences between the front and rear surfaces of an object moving through a fluid) and Skin Friction Drag (which is caused by the resistance of the fluid to slide along the surface of the object).

The Lift and Drag forces can be expressed either as a function of the air velocity direction or as a function of the chord line. These two expressions are L,D and N,A respectively. The constituted force is R. The Angle of Attack (AoA) is the angle between the aircraft's chord line and the air's velocity direction. It is an important parameter regarding the generated Lift and Drag. It is depicted below as the angle α [6].

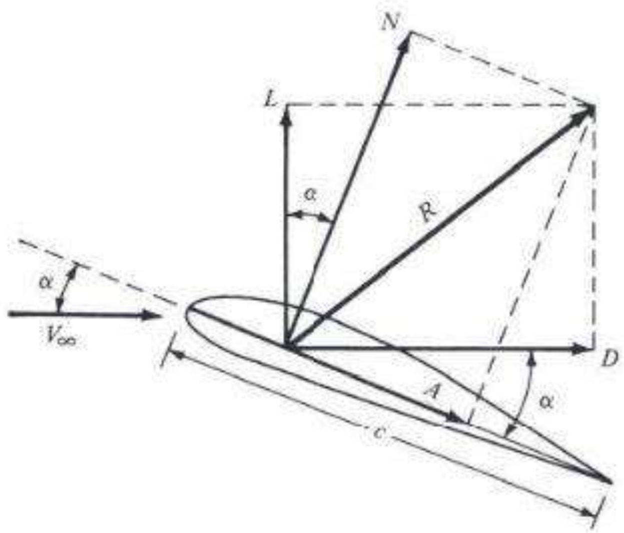

Εικόνα 48: Aerodynamic Lift (L,N) and Drag (D,A) Forces on an Airfoil

When the oncoming air interacts with an airfoil, the resultant constituted force is R, and there also a resultant moment or torque M, which is the Pitching Moment [6].

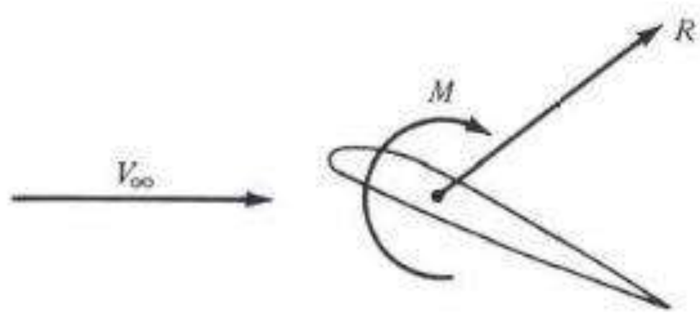

Εικόνα 49: Aerodynamic Constituted Force (R) and Moment (M)

Pitching Moment: It is the moment or torque that tends to cause an aircraft to rotate or pitch about its lateral axis. It is a measure of the tendency of the aircraft to rotate nose-up or nose-down and also one of the important parameters used to describe the stability and control characteristics of an aircraft. Pitching moments can be caused by various factors, including changes in the angle of attack, changes in airspeed, control surface deflections (elevator or stabilator movements), and shifts in the center of gravity (CoG) location.

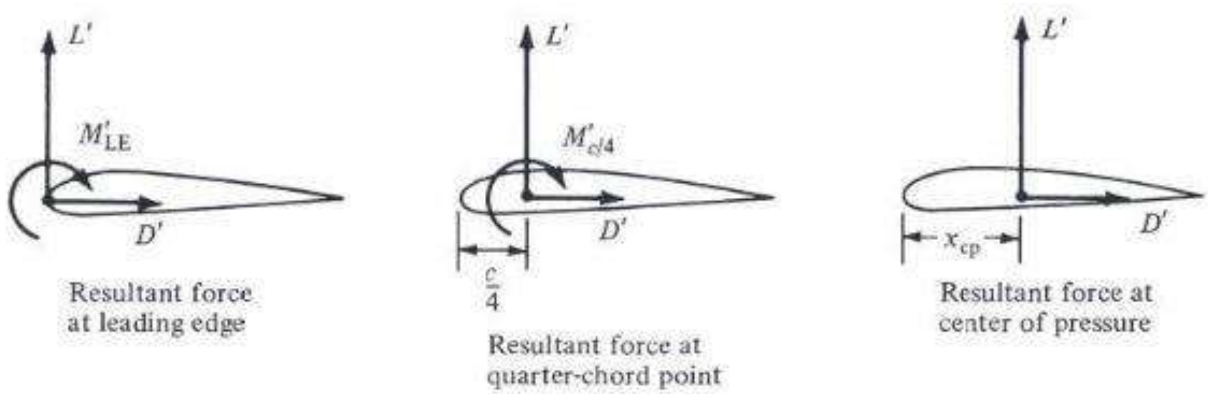

Εικόνα 50: Equivalent Aerodynamic Forces and Moments

Pressure Center: It is the location where the resultant of a distributed load effectively acts on the body. If moments were taken about the center of pressure, the integrated effect of the distributed loads would be zero. Hence, an alternate definition of the center of pressure is that point on the body about which the aerodynamic moment is zero [6].

Aerodynamic Center: The Pressure Center is not always a convenient concept in aerodynamics. However, this is no problem. To define the force-and-moment system due to a distributed load on a body, the resultant force can be placed at any point on the body, as long as the value of the moment about that point is also given. The Aerodynamic Center is usually assumed to be located at 25% of the chord line, towards the leading edge.

Lift Distribution: The spanwise distribution of Lift and Drag can be obtained from Aerodynamics [6]. As seen below, according to Prandl, the ideal distribution of Lift across the aircraft's wingspan follows an elliptical distribution in an elliptical wing. In rectangular and trapezoid wings, the ideal Lift distribution is not achieved and hence, the Schrenk distribution is applied. The Schrenk distribution essentially is the mean distribution of the ideal elliptical and the wing planform distributions [15].

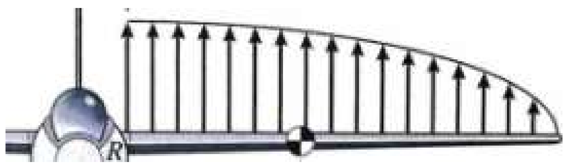

Εικόνα 51: Spanwise Elliptical Lift Distribution

Schrenk Distribution: The Schrenk distribution is an approximation method for the spanwise lift distribution which has been proposed by Dr. Ing Oster Schrenk and has been accepted by the Civil Aeronautics Administration (CAA) as a satisfactory method for civil aircraft [15]. The Schrenk method relies on the fact that the lift distribution does not differ much from elliptical planform shape if the wing is not swept and has no aerodynamic twist, i.e., zero lift lines for all wing sections lie in the same plane (constant airfoil section). The Schrenk method proposed that the lift distribution per unit span length is the mean value of actual wing chord distribution and an elliptical wing chord distribution that has the *same area* and the *same span*.

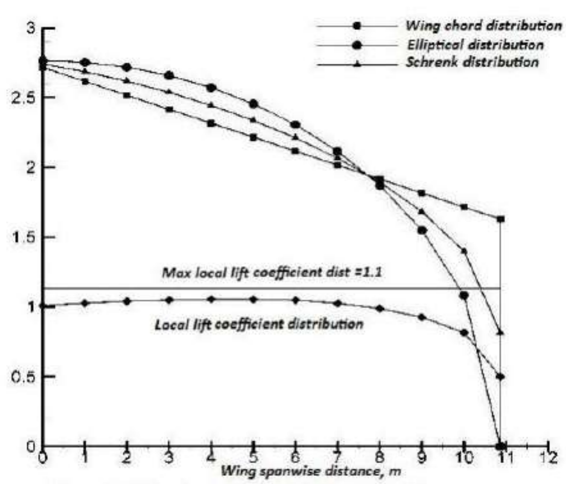

Εικόνα 52: Spanwise Schrenk Lift Distribution

Drag Distribution: The spanwise distribution of Lift and Drag can be obtained from Aerodynamics [6]. As seen below, according to Prandl, the ideal distribution of Drag across the aircraft's wingspan follows an elliptical distribution in an elliptical wing. The induced Drag is not taken into account due to its calculation escaping the purposes of this Diploma Thesis. Therefore, the Schrenk distribution is applied in rectangular and trapezoid wings. The Schrenk distribution essentially is the mean distribution of the ideal elliptical and the wing planform distributions [15].

4.1.5 Slipstream Effect

The slipstream effect is an aerodynamic effect related to propeller use and as a result impacts the production of Lift and Drag in an aircraft wing. In general, the stream tube behind a propeller in which the velocity of the axial flow is higher than the undisturbed flow and a rotational velocity is present, is called the propeller slipstream [13].

Aircraft components which are located behind the propeller experience the slipstream as a variation in the oncoming airflow, which have no parallel streamlines and different pressure distribution (consequently lift, drag and pitching moment). In general, all effects coming from the slipstream interaction with aircraft components are defined as indirect effects [13].

In this case, the beneficial effect of the propeller-fluid interaction allows for obtaining a higher lift capability for the wing. Indeed, the use of DEP and the effects of slipstream, among many benefits, involve a large reduction of the wing area, decreasing the friction drag, a higher cruise lift coefficient (close to the maximum efficiency point), less gust/turbulence sensitivity and comparable take-off and landing speed [13].

As previously mentioned, the use of Propellers in a DEP system in this Thesis, presents the tremendous advantage of increasing the Lift during Take-Off, resulting in significant reduction of the needed Runway Length (STOL capabilities). The Slipstream effect will be studied as the Propeller use alters the **spanwise Lift Distribution** that a fixed wing would otherwise have, and thus the Load applied on the Wing Structure.

The Lift Distribution is altered when propellers are used, compared to a bare wing. The slipstream effect can be divided into the impact of slipstream velocity and the impact of slipstream rotation. The impact of slipstream velocity in Lift Distribution is due to the increase of air dynamic pressure, caused by the axially-induced propeller velocity, whereas the impact of slipstream rotation is due to the change of local angle of attack, caused by the tangentially-induced propeller velocity.

Lift is a function of the air dynamic pressure. The dynamic pressure in the wingspan region where the propeller is operating is increased, due to the propeller axially-induced velocity increased the total air velocity interacting with the wing.

Lift is also a function of the lift coefficient C_L which is dependent on the angle of attack. The local angle of attack is increased in the propeller rotating-up region and decreased in the propeller rotating-down region due to the propeller tangentially-induced velocity.

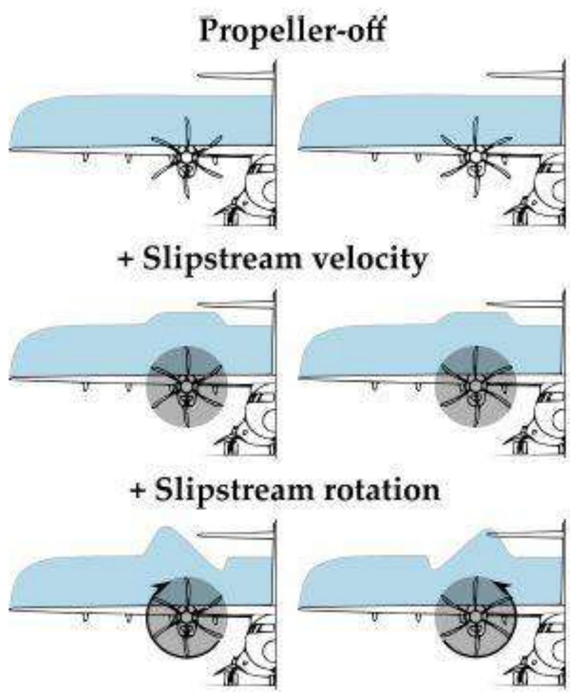

Εικόνα 53: Effects of Inboard-Up and Outboard-Up Propeller Slipstream on Lift Distribution

The calculation of the propeller slipstream velocity is completed below, using the Momentum Theory and the Disk Actuator Theory, where the propeller is considered a one-dimensional disk with an infinite number of blades [18].

Slipstream Velocity

The overall scheme of the velocity evolution in the propeller stream [14] and the definition of the distance between the propeller and the wing is shown below:

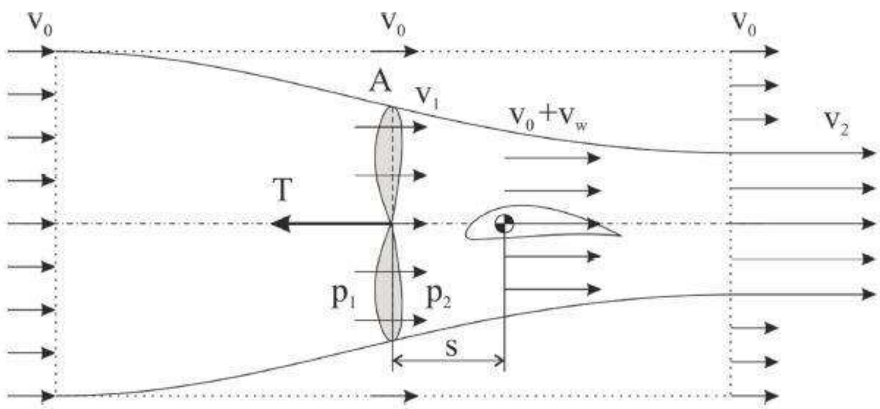

Εικόνα 54: Propeller-Air Interaction Flow Field

The additional axial velocity interacting with the wing is a function of propeller axially-induced velocity v_i and multiplied by the development factor k_d:

$$v_w = v_i k_d \quad [\frac{m}{s}] \tag{4.14}$$

The increase in velocity from the propeller is described by the development factor k_d, which depends on the distance of the propeller from the wing s and the propeller radius r:

$$k_d = 1 + \frac{s}{\sqrt{r^2+s^2}} \tag{4.15}$$

In order to calculate the propeller-induced velocity, the relationship between the propeller thrust and the propeller-induced velocity must be utilized. Using the Momentum Theory to model the flow field behind the propeller and the Actuator Disk Theory, the propeller thrust is equal to:

$$T = \dot{m}(v_2 - v_0) \tag{4.16}$$

Where T is the propeller thrust, v_0 is the freestream velocity and v_2 is the velocity behind the propeller [14]. The mass flow $\dot{m}$ corresponds to:

$$\dot{m} = A\rho v_1 \tag{4.17}$$

Where A is the area of the propeller disk and v_1 is the velocity at the propeller location. The propellers studied are designed to increase the dynamic pressure in landing and take-off conditions, i.e., at low flight speeds, so we could consider the flow without the effect of compressibility [14]. Thus, the speed v_1 can be thought of as the average of the input and output velocity and as the sum of freestream and induced velocity:

$$v_1 = \frac{v_2+v_0}{2} = v_0 + v_i \ \left[\frac{m}{s}\right] \tag{4.18}$$

After inserting the Equations (4.17) and (4.18) into Equation (4.16), Thrust is a function of the speed of flight and the value of the induced velocity:

$$T = A\rho(v_0 + v_i)2v_i \tag{4.19}$$

With the propeller Thrust known, the axially induced velocity is calculated from Eq. (4.19):

$$v_i^2 + v_0 v_i - \frac{T}{2A\rho} = 0 \tag{4.20}$$

The air velocity that interacts with the wing is:

$$\boldsymbol{v_{wing}} = \boldsymbol{v_0} + \boldsymbol{v_w} = \boldsymbol{v_0} + \boldsymbol{v_i k_d} \ \left[\frac{m}{s}\right] \tag{4.21}$$

The Equation (4.21) proves mathematically the Lift augmentation in a propeller-blown wing, as the velocity of the air interacting with the wing and producing Lift, is higher than the freestream air velocity.

Also, the Lift Equation equilibrium regarding a normal wing versus a DEP one, proves mathematically that for similar conditions (density, freestream velocity and angle of attack), the DEP wing produces the same amount of Lift that a normal wing with much larger surface area does.

$$L = L_{DEP} \Rightarrow$$

$$\frac{1}{2}\rho v_0^2 c_L S = \frac{1}{2}\rho(v_0 + v_w)^2 c_L S_{DEP} \Rightarrow$$

$$\frac{S}{S_{DEP}} = \frac{(v_0 + v_w)^2}{v_0^2}$$

Slipstream Rotation

The tangentially-induced velocity impacts the distribution of the already augmented lift, rather than the magnitude of it [18].

Essentially, in an "Inboard-Up, Outboard-Down" propeller, the local angle of attack is increased inboard and decreased outboard, following a sinusoidal form. Therefore, the point where the distributed Lift acts as a concentrated force is moved further inboard, improving the aircraft stability.

On the contrary, in an "Inboard-Down, Outboard-Up" propeller, the local angle of attack is decreased inboard and increased outboard, following a sinusoidal form. Therefore, the point where the distributed Lift acts as a concentrated force is moved further outboard, hampering the aircraft stability.

As seen below, the wingspan is divided in sections I, II, III and IV, moving from the wing root towards the wing tip. Since it is an "Inboard-Up, Outboard-Down" propeller, the local AoA is increased in sections I and II, and decreased in sections III and IV. The dynamic pressure is increased in sections II and III due to the propeller axially-induced velocity.

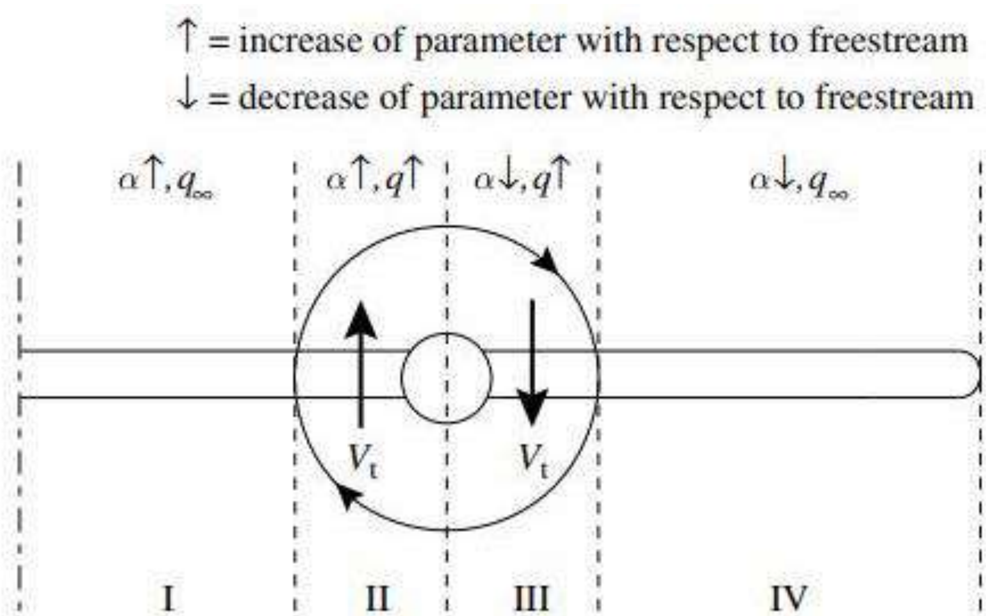

Εικόνα 55: AoA and Dynamic Pressure Change due to Inboard-Up Propeller Rotation

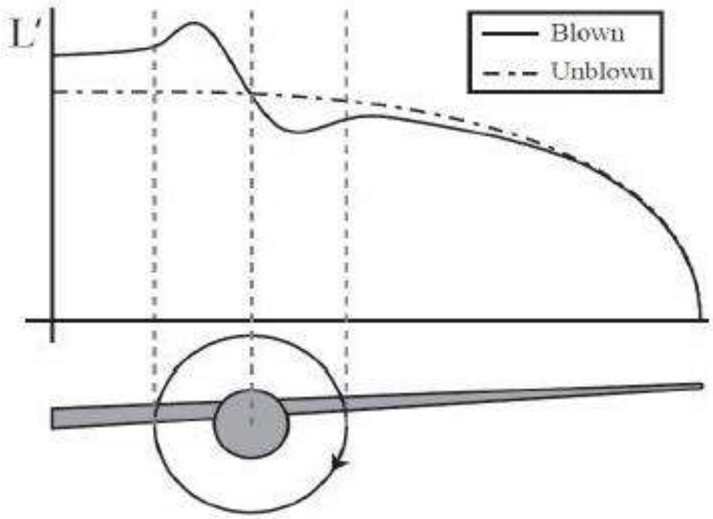

Εικόνα 56: Sinusoidal Variation in Lift Distribution due to Propeller Rotation

Due to this Thesis centered around a conceptual structural study and with the Momentum Theory and Disk Actuator Theory being followed as a low-fidelity, quick estimation method, the Slipstream rotation factor will not be taken into consideration regarding the tangentially-induced velocity. As a result, only the axially-induced velocity will influence the air interacting with the wing, and thus the Lift and Drag distribution.

The limitations of the methods referenced above are the lack of the tangential component in the propeller induced velocities, the oversight of the presence of the propeller hub and the inability to account for the drag component and the thrust deterioration at blade tips [18].

For the purposes of this Thesis, it is also assumed that the axially-induced velocity is constant along the propeller radius [18].

4.1.6 Wing Loads

Normal Stress

The first step in the Structural Analysis is the calculation of normal stresses. The normal stress will be calculated at the critical cross-section of the Spar. In order to locate the critical cross-section, the Shear Force Q and the Bending Moment M must be known. The Shear Force Q diagram is obtained by integrating the spanwise Load Distribution area and the Bending Moment M diagram is obtained by integrating the Shear Force Q area.

The Load Distribution is obtained by superposition of the wing distributed loads, such as Lift Distribution, Wing Structural Weight, Engine/Motor and Propeller Weights.

The Lift Distribution is obtained using the Schrenk Approximation Method [15], as the studied aircraft wing has a trapezoid planform (straight leading edge and tapered trailing edge).

$$L_y = \frac{1}{2} \cdot \rho \cdot V_y^2 \cdot c_y^{schrenk} \cdot C_{L,wing} \;\; [\frac{N}{m}] \tag{4.22}$$

where ρ the air density, V_y the air velocity in each section, c_y the wing chord in each section and C_L the wing lift coefficient. Thus, the Chord Distribution must be calculated. The studied span of one wing is $l = 3.255\ m$ will be discretized to a number of sections ranging in the y-axis, starting from $y = 0m$ to $y = 3.255m$ with a step of $h = 0.005m$.

Zenith Zodiac CH 650 B Wing Parameters			
Root Chord	$\boldsymbol{c_r}$	1.6	m
Tip Chord	$\boldsymbol{c_t}$	1.4	m
Area (One Wing)	$\boldsymbol{S_w}$	4.8825	m^2
Span (One Wing)	$\boldsymbol{l}$	3.255	m

Πίνακας 11: Wing Parameters

The aircraft's wing root chord is equal to $c_r = 1.6\ m$ and the wing tip chord is equal to $c_t = 1.4\ m$. Since the wing planform is trapezoid, the area of one wing is equal to:

$$S_w = S_{rectangular} + S_{triangle} = c_t l + \frac{1}{2}(c_r - c_t)l = 3.255\left(\frac{3}{2}1.6 - \frac{1}{2}1.4\right) = 4.8825\ m^2$$

The trapezoidal chord distribution is equal to:

$$c_y^{trap} = c_r\left(1 - 0.125\frac{y}{l}\right) = 1.6\left(1 - 0.125\frac{y}{3.255}\right)\ [m] \tag{4.23}$$

The Schrenk method proposes that the lift distribution per section is the mean value of actual wing chord distribution and an elliptical wing chord distribution that has the *same area* and the *same span*. In order to satisfy those two demands, we have an ellipse with radiuses r_1, r_2 with $r_2 > r_1$, $r_2 = l = 3.255m$ and $S_e = S_w = 4.8825m^2$. The ellipse quarter area is equal to $S_e = \frac{\pi}{4}r_1 r_2$, hence the radius $r_1 = \frac{4S_e}{\pi r_2} = 1.909m$.

The elliptical chord distribution is equal to:

$$c_y^{ellip} = r_1\sqrt{(1 - \left(\frac{y}{l}\right)^2} = 1.909\sqrt{(1 - \left(\frac{y}{3.255}\right)^2}\ \ [m] \tag{4.24}$$

The Schrenk chord distribution is equal to:

$$c_y^{schrenk} = \frac{1}{2}\left(c_y^{trap} + c_y^{ellip}\right)\ \ [m] \tag{4.25}$$

The local lift coefficient can be calculated by dividing the Schrenk chord distribution by the actual wing chord distribution, which in this case is trapezoidal. Essentially, the local lift coefficient in each section is equal to:

$$C_{L,local}(y) = \frac{c^{schrenk}(y)}{c^{trapezoidal}(y)}$$

The wing lift coefficient can be calculated by the expression [20]:

$$C_{L,wing} = \frac{C_{L_{airfoil}}}{0.95} \tag{4.26}$$

The wing Lift equation with the appropriate load factor provides the air velocity that the wing interacts with during Lift production.

With the propeller Thrust values known, the velocities v_0, v_i, v_{wing} of Eq. (4.14), (4.20), (4.21) from Slipstream Effect (Chapter 4.1.5) can be calculated for a DEP system.

Then, the Lift Distribution of each section can be obtained from Eq. (4.22). The overall Load Distribution can be calculated by subtracting the inertial loads (wing structural, fuel, motor or propeller distributed loads) from Lift Distribution:

$$p(y) = L_y - w_{total}(y) \quad [\frac{N}{m}] \tag{4.27}$$

Since the span is discretized, the Shear Force Q and the Bending Moment diagrams are obtained by numerical integration. The Trapezoid Rule is used:

$$Q_z(y) = -\int_0^{y_{tip}} p(y)dy = -\sum E(p) \text{ where } E(p) = \frac{p_i(y)+p_{i+1}(y)}{2} h \;\; [N] \tag{4.28}$$

$$M_x(y) = -\int_0^{y_{tip}} Q_z(y)dy = -\sum E(Q) \text{ where } E(Q) = \frac{Q_i(y)+Q_{i+1}(y)}{2} h \;\; [Nm] \tag{4.29}$$

The normal stress can be calculated using the Shear Flow Theory - explained in Chapter 4.1.2 - and specifically from Eq. (4.11). It is equal to:

$$\sigma_y(y) = \frac{M_x(y)}{h \cdot F_f(y)} \quad [MPa]$$

The Drag Distribution is obtained using the Schrenk Approximation Method [15], as the studied aircraft wing has a trapezoid planform (straight leading edge and tapered trailing edge).

$$D_y = \frac{1}{2} \cdot \rho \cdot V_y^2 \cdot c_y^{schrenk} \cdot C_{D,wing} \;\; [\frac{N}{m}] \tag{4.30}$$

where ρ the air density, V_y the air velocity in each section, c_y the wing chord in each section and C_L the wing lift coefficient.

The wing drag coefficient can be calculated by the expression [20]:

$$C_{D,wing} = \frac{C_{D_{airfoil}}}{0.95}$$

Drag is acting on the direction of the chord, while Lift is acting on a direction perpendicular to the chord. A simplified explanatory figure is presented below:

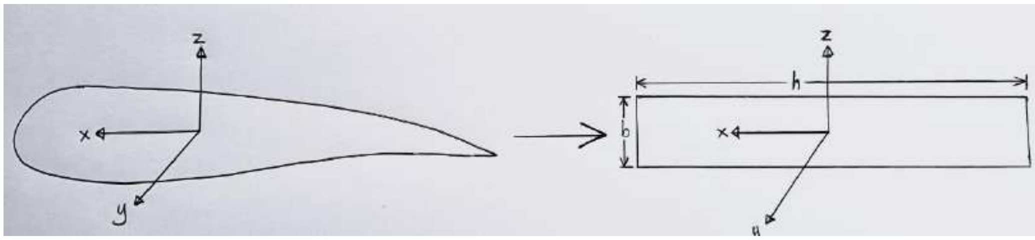

Εικόνα 57: Airfoil Cross-Section Simplification

Assuming that Lift acts on the figure’s z-axis and Drag acts on the figure's x-axis, the second moment of inertia of the airfoil about axis x and z respectively is significantly different. If the airfoil is simplified as a rectangular beam, the second moments of inertia are equal to:

$$I_x = \frac{1}{12} hb^3$$

$$I_z = \frac{1}{12} h^3 b$$

Taking also into account the high Lift-to-Drag ratio of airfoils $(L \gg D)$, the bending moment created by Lift is significantly higher than the respective bending moment created by Drag. Furthermore, a higher second moment of inertia equals a lower normal bending stress. Therefore, the normal bending stress created by Drag is minimal compared to the normal bending stress created by Lift. As a result, the contribution of Drag in normal stress calculation is often ignored, due to Drag corresponding to a low-magnitude, high-inertia load case, contrary to Lift which corresponds to a high-magnitude, low-inertia load case.

<u>CoG of Distributed Load</u>

The distributed load center of gravity corresponding to the equivalent concentrated force (for example the CoG of Lift Distribution) in a discretized area can be obtained by the equation:

$$y_{CG} = \frac{\sum y_{c,i} F_i}{\sum F_i} \ \ [m]$$

where $y_{c,i}$ the centroid of each rectangular section area and F_i the area of each rectangular section.

Shear Stress

The Pitching Moment is equal to:

$$M_P = \frac{1}{2}\rho V^2 S\bar{c}C_M \quad [\text{Nm}] \tag{4.31}$$

where $\bar{c}$ is the mean chord and C_M is the pitching moment coefficient.

Additional Moments are created by loads when they are not applied to the airfoil CoG which is also the Shear Center due to the airfoil being a closed section. As a result, the Torsion Moment is equal to:

$$M_T = M_P \pm \sum M = M_P \pm \sum(F \cdot d) \quad [Nm] \tag{4.32}$$

where F is a force and d is the lever arm of force F to the CoG/Shear Center.

The Shear Flow due to ***torsion***, according to Bredt's law, is equal to:

$$q_T = \frac{M_T}{2\Omega} \quad [\frac{N}{mm}] \tag{4.33}$$

where Ω the airfoil section surface area.

The Shear Flow due to ***shear*** is obtained by the superposition method [5], by addition of a closed section shear flow and an assumed-open section shear flow.

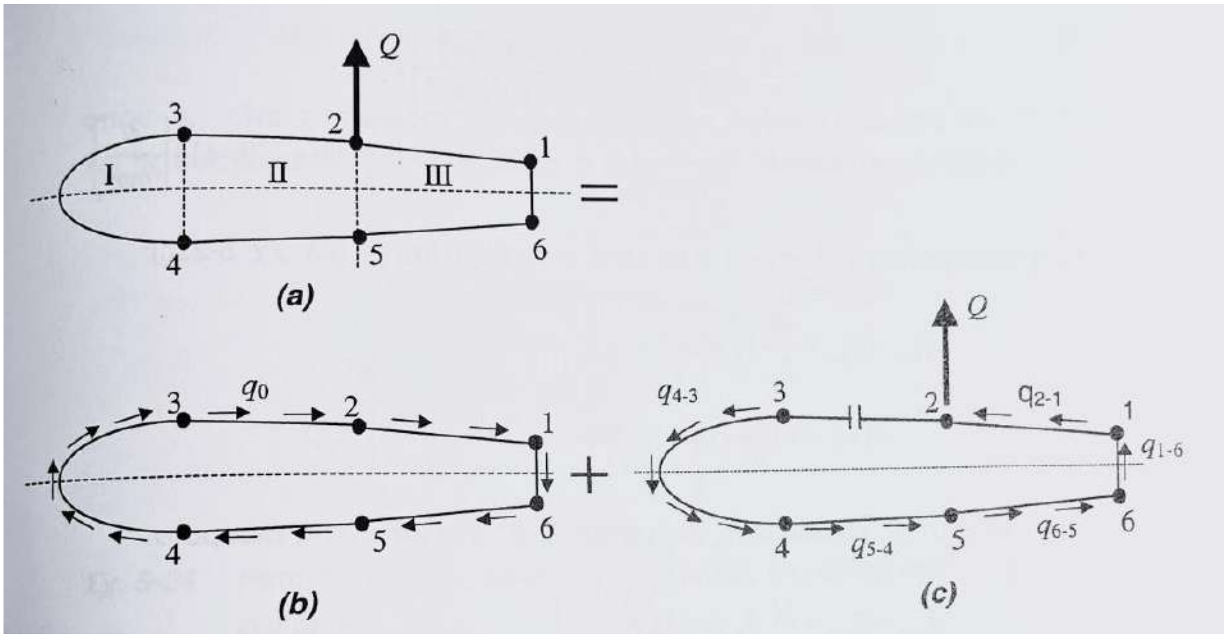

Εικόνα 58: Shear Flow Superposition [5], Closed (b) & Open (c) Sections

The assumed-open section Shear Flow is equal to:

$$\tilde{q}_n = \tilde{q}_{n-1} + \frac{Q_z}{I_x}\int z\,dF \simeq \tilde{q}_{n-1} + \frac{Q_z}{I_x}F_n z_n \quad \left[\frac{N}{mm}\right] \tag{4.34}$$

The closed section Shear Flow q_0 can be calculated from the aerodynamic center Moment equilibrium $\sum M_{i-j} = 0$, where $M_{i-j} = 2A_{i-j}\tilde{q}_{i-j}$.

$$q_0 = -\frac{\sum A_{i-j}\tilde{q}_{i-j}}{\sum A_{i-j}} \quad [\frac{N}{mm}] \tag{4.35}$$

The total Shear Flow due to shear can be obtained by superposition of Eq. (4.34), (4.35) and combined with the Shear Flow due to torsion, the Shear Stress is equal to:

$$q = q_0 + \tilde{q} \quad [\frac{N}{mm}] \tag{4.36}$$

$$\tau = \frac{q+q_T}{t} \quad [MPa] \tag{4.37}$$

<u>Equivalent Stress</u>

The equivalent stress according to Von Mises is equal to:

$$\sigma_{eq} = \sqrt{\sigma^2 + 3\tau_{max}^2} \quad [MPa] \tag{4.38}$$

Riveting

When forces are applied to a riveting, the bearing pressure applied to the rivet is equal to:

$$p_b = \frac{T}{d \cdot t_1} \quad [MPa]$$

The pressure applied to the rest of the joint is equal to:

$$p_b = \frac{T}{d \cdot (t_2 + t_3)} \quad [MPa]$$

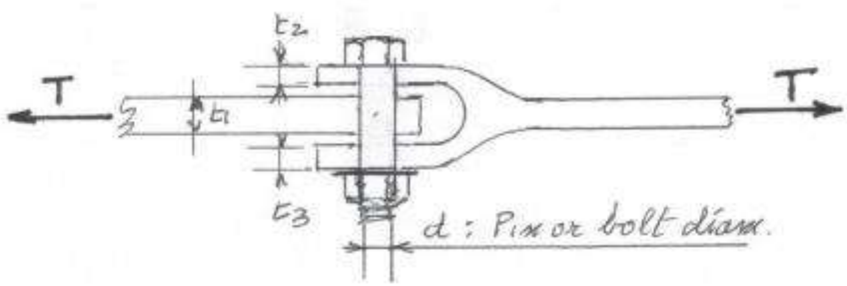

Εικόνα 59: Forces Acting on a Riveting

Holes created in order to house riveting result in increased stress values, as seen below. This phenomenon is called stress concentration and is associated with the geometry.

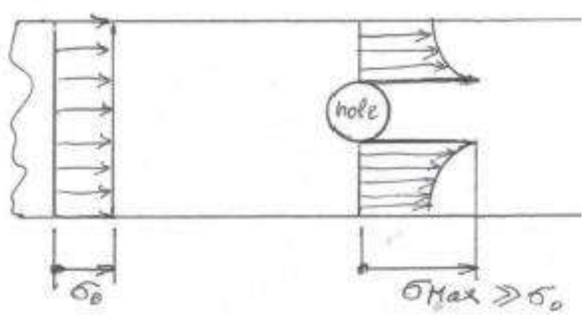

Εικόνα 60: Riveting Stress Concentration

A usual measure to combat stress concentration is to align the holes and to alternate their diameters.

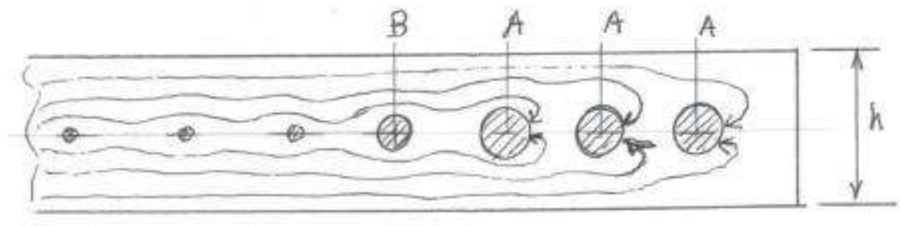

Εικόνα 61: Methods of Alleviating Stress Concentration

When 2 rivets are used, each rivet handles ½ of the load. When 3 rivets are used, each rivet handles 1/3 of the load etc. For safety reasons (increased factor of safety), the ratio below can be used:

2 ηλώσεις				
	0.5	0.5		για N=1
	0.6	0.4		για N=1.2
	0.4	0.6		για N=1.2
	0.75	0.75		για N=1.5
3 ηλώσεις				
	0.33	0.33	0.33	για N=1
	0.4	0.2	0.4	για N=1.2
	0.5	0	0.5	για N=1.5

Εικόνα 62: Riveting Ratios for different Factors of Safety and Number of Rivets

The riveting bearing pressure must be checked at the rivets handling the largest loads.

Deflection

The Curvature Surfaces Method is used to calculate the wing's deflection. The beam's bending moment M diagram is divided by the Young's elastic modulus E and the cross-section's second moment of inertia I. The new M/EI diagram expresses the beam's curvature as a function of its length. The surface area of the M/EI diagram is called the curvature surface of the beam.

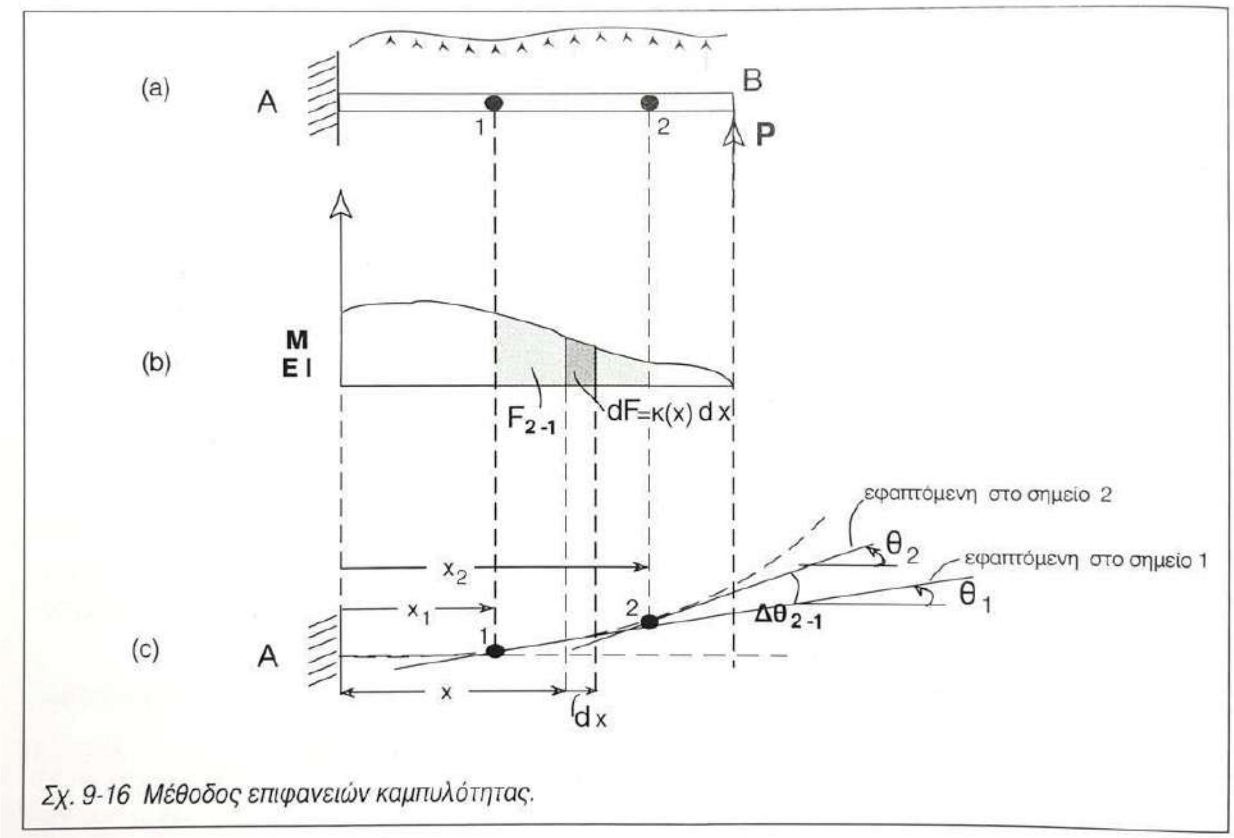

Εικόνα 63: Curvature Surfaces Method (1/3)

Assuming two beam axis points 1 and 2, as pictured above. In the deformed state, an angle $\Delta\theta_{2-1}$ between the tangent lines θ_1 and θ_2 is created. This angle must be equal to the curvature surface between points 1 and 2. Therefore:

$$\Delta\theta_{2-1} = \theta_2 - \theta_1 = \int_{x_1}^{x_2} \frac{M(x)}{E \cdot I(x)} dx \qquad (4.39)$$

Symbolizing the curvature surface area as F_{2-1}, the equation above can be expressed in a simpler manner as $\Delta\theta_{2-1} = F_{2-1}$.

In order to calculate the deflection of the beam at point 2 relative to point 1, the impact of curvature on an infinitesimal element dx must be investigated. Therefore, it is assumed that the beam besides the element dx is undeformed. The elastic element dx with the bending moment M(x) acting on it, is deformed as a cycle arc, as seen below, and the tangent lines at points 1 and 2 form an angle dθ equal to the curvature surface corresponding to the infinitesimal element. Those tangent lines intersect the vertical line at point 2 of the beam at two points separated by a distance of $dv = d\theta(x_2 - x)$.

Substituting the distance, $dv = \frac{M(x)}{EI(x)}(x_2 - x) = dF(x_2 - x)$. The factor $dF(x_2 - x)$ is the static or first moment of inertia of surface dF about the vertical axis intersecting point 2.

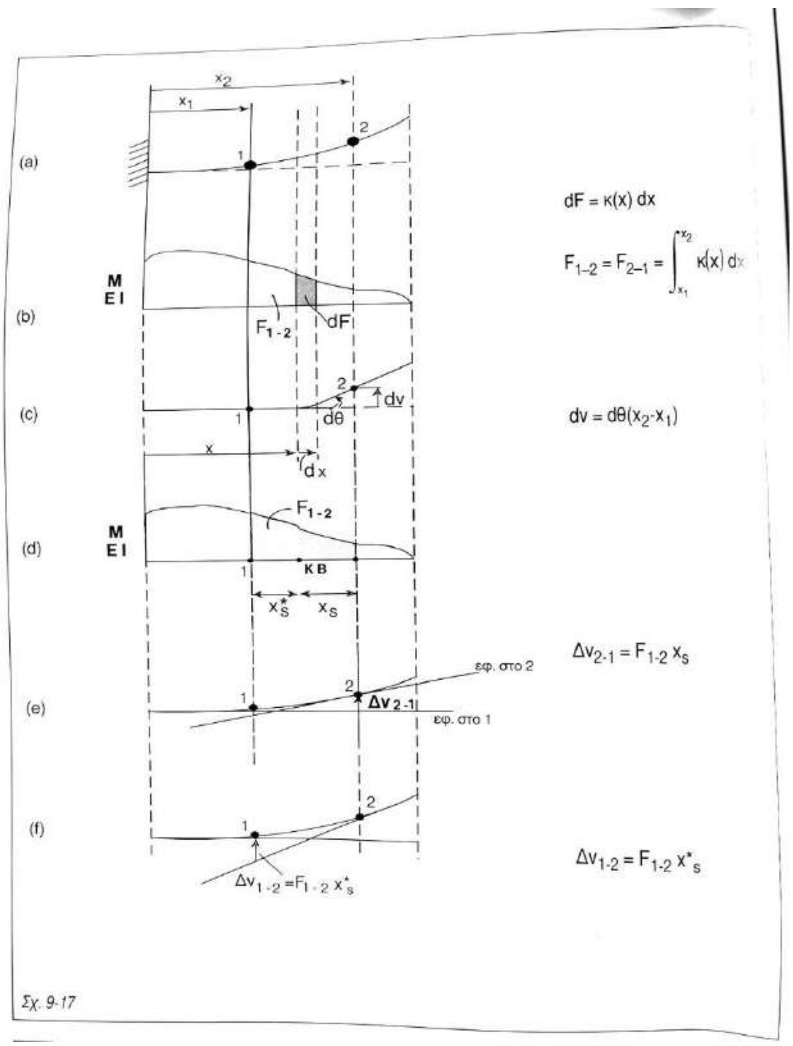

Εικόνα 64: Curvature Surfaces Method (2/3)

Assuming the whole section between points 1 and 2 is elastic, the impact of every element's curvature on the deflection will occur by integration between x1 and x2. Therefore, the deflection Δv_{2-1} of point 2, caused by the deformation of the beam section between points 1 and 2 is equal to:

$$\Delta v_{2-1} = \int_{v_1}^{v_2} dv = \int_{x_1}^{x_2} d\theta (x_2 - x) = \int_{x_1}^{x_2} \frac{M(x)}{EI(x)} (x_2 - x)\, dx$$

Knowing that the static or first moment of inertia of a surface about an axis is equal to the surface area times the center of gravity distance from the axis, the formula above can be expressed as $\Delta v_{2-1} = F_{2-1} x_s$, where F_{2-1} is the curvature surface area between points 1 and 2, and x_s is the distance separating the center of gravity of the surface F_{2-1} from the vertical line at point 2.

As seen below, the total displacement of point 2 is equal to the deflection of point 1, plus the slope of point 1 θ_1 times the distance $x_2 - x_1$, plus the quantity Δv_{2-1}.

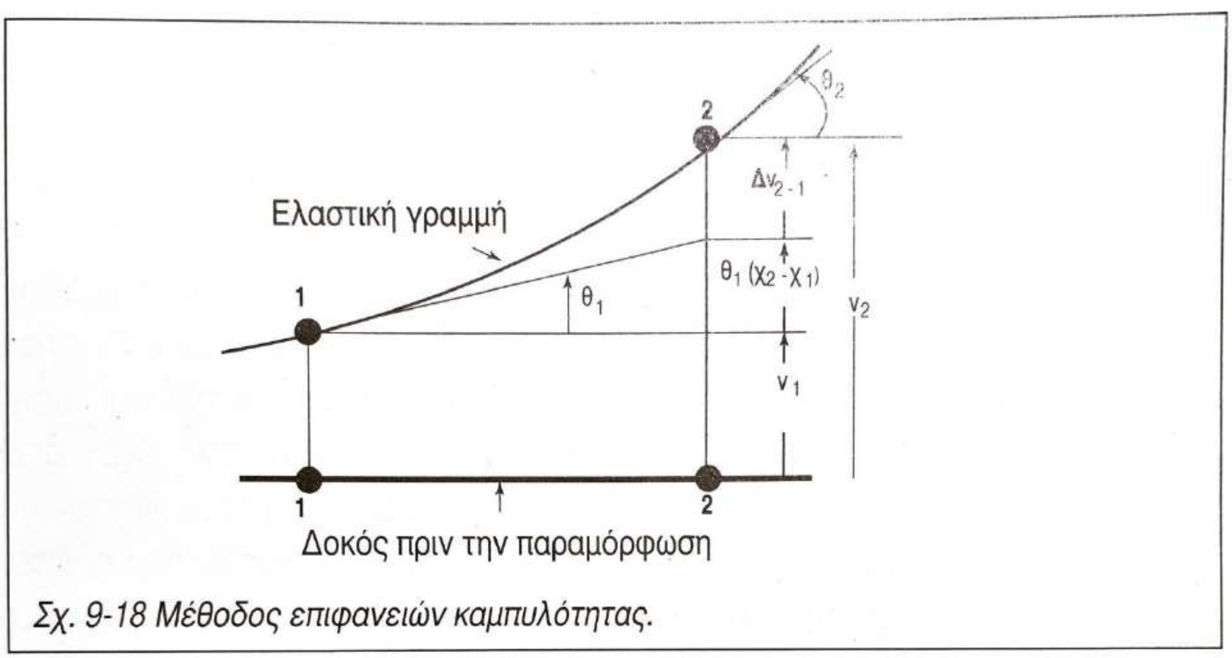

Εικόνα 65: Curvature Surfaces Method (3/3)

$$v_2 = v_1 + \theta_1 (x_2 - x_1) + \int_{x_1}^{x_2} \frac{M(x)}{E \cdot I(x)} (x_2 - x_1) dx \quad [m] \tag{4.40}$$

4.1.7 Runway Length

The Takeoff distance can be calculated from Raymer's book [24]. Takeoff distance is calculated from the graph below, using the Take Off Parameter (TOP). The (TOP) can be calculated from the equation below:

$$(TOP) = \frac{(W/S)}{\sigma C_{L,max}(HP/W)}$$

where W/S is the wing loading in $\frac{lb}{ft^2}$, i.e. the aircraft MTOW divided by the wing surface, $\sigma = \frac{\rho}{\rho_{@sea\ level}}$ is the density ratio and obviously equal to $\sigma = 1$ at sea level, $C_{L,max}$ is the maximum lift coefficient and (HP/W) is the aircraft power-to-weight ratio in $\frac{HP}{lb}$.

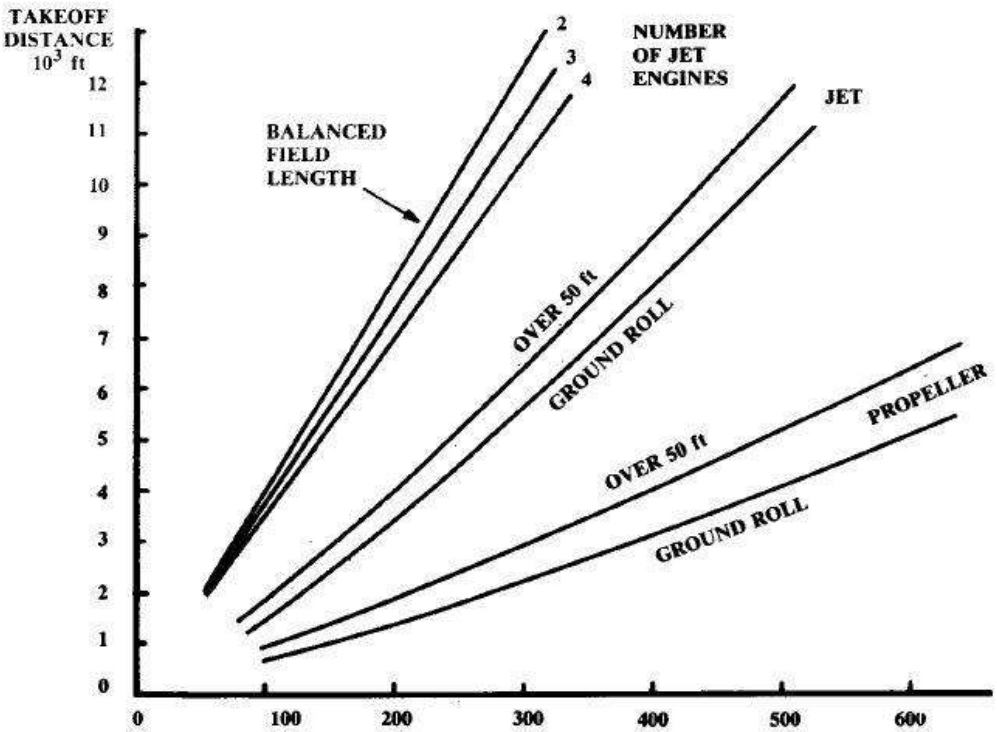

Εικόνα 66: Takeoff Distance Estimation Graph

After calculating the (TOP), Takeoff Distance can be estimated using the graph above and specifically the Ground Roll curve.

4.2 WING ANALYSIS

4.2.1 Reference Configuration

The Zenith Zodiac CH 650 B in its original configuration is powered by a nose-mounted Internal Combustion Engine and the respective propeller. No motors or propellers are mounted on the straight leading edge - tapered trailing edge wings, with structural weight and fuel being the only inertial loads applied.

The maximum take-off weight is $MTOW = 600\,kg$ and the load factor used in this analysis is $n = 3.8$. The procedure described in Chapter 4.1.6 will be followed.

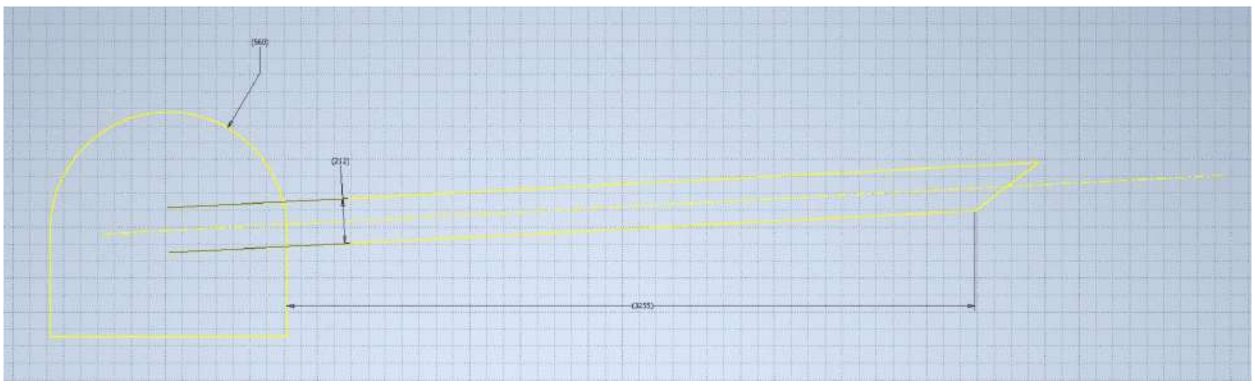

Εικόνα 67: Analysis 1 Wing Configuration Front View

As mentioned in Chapter 4.1.3, the analysis is performed in a load case scenario where the maximum positive load factor is applied ($n = 3.8$), while also performing a correctly banked turn.

For a limiting value of n, the minimum time taken to turn through a given angle occurs when the lift coefficient C_L is maximum, that is with the aircraft on the point of stalling [15]. The airfoil max lift coefficient is obtained from [16], while the wing lift coefficient is obtained from Eq. (4.26) and is equal to:

$$C_{L,airfoil_{max}} = 1.555$$

$$C_{L,wing_{max}} = \frac{C_{L,airfoil_{max}}}{0.95} = 1.64$$

Useful Parameters		
Area (One Wing)	$\boldsymbol{S}$	$4.8825\ m^2$
Half Aircraft Weight (One Wing)	$\boldsymbol{MTOW/2}$	$2943\ N$
Air Density (at 8000 feet)	$\boldsymbol{\rho}$	$0.9627\ kg/m^3$

Πίνακας 12: Analysis 1 Useful Parameters

With the load factor equal to $n = 3.8$, $MTOW = 600\ kg = 5886\ N$, the wing air velocity and also true aircraft speed will be calculated using the wing Lift Equation:

$$V_{stall} = \sqrt{\frac{2nW}{\rho S_{wing} C_{L,wing_{max}}}} = \sqrt{\frac{2 \cdot 3.8 \cdot 2943}{0.9627 \cdot 4.8825 \cdot 1.64}} \Rightarrow \boldsymbol{V = 54\frac{m}{s}}$$

The angle of bank Φ and the turn radius R are equal to:

$$L \cdot sin\Phi = \frac{W}{g} \cdot \frac{V^2}{R}$$
$$L \cdot cos\Phi = W$$

$$n = \frac{L}{W} = \frac{L}{L \cdot cos\Phi} = \frac{1}{cos\Phi} \Rightarrow cos\Phi = \frac{1}{n} \Rightarrow \Phi = arccos\left(\frac{1}{n}\right) \Rightarrow \boldsymbol{\Phi = 74.74°}$$

$$tan\Phi = \frac{V^2}{gR} \Rightarrow R = \frac{V^2}{g \cdot tan\Phi} = \frac{\left(54\frac{m}{s}\right)^2}{9.81\frac{m}{s^2} \cdot tan\,(74.74°)} \Rightarrow \boldsymbol{R = 81\ m}$$

The wing chord distribution for each section of the span $l = 3.255\ m$, regarding one of the two wings is obtained from Equations (4.23), (4.24), (4.25) and the calculations are made on Excel sheet:

$$c_y^{trap} = 1.6\left(1 - 0.125\frac{y}{3.255}\right)\ [m]$$

$$c_y^{ellip} = 1.909\sqrt{(1 - \left(\frac{y}{3.255}\right)^2}\ [m]$$

$$c_y^{schrenk} = \frac{1}{2}\left(c_y^{trap} + c_y^{ellip}\right)\ [m]$$

Εικόνα 68: Analysis 1 Wing Chord Distribution c

The lift distribution for each section of the span $l = 3.255\ m$, regarding one of the two wings is obtained from Eq. (4.22):

$$L_y = \frac{1}{2} \cdot \rho \cdot V_y^2 \cdot c_y \cdot C_L = \frac{1}{2} \cdot 0.9627 \cdot 54^2 \cdot c_y^{schrenk} \cdot 1.64 = 2302 \cdot c_y^{schrenk} \qquad [\frac{N}{m}]$$

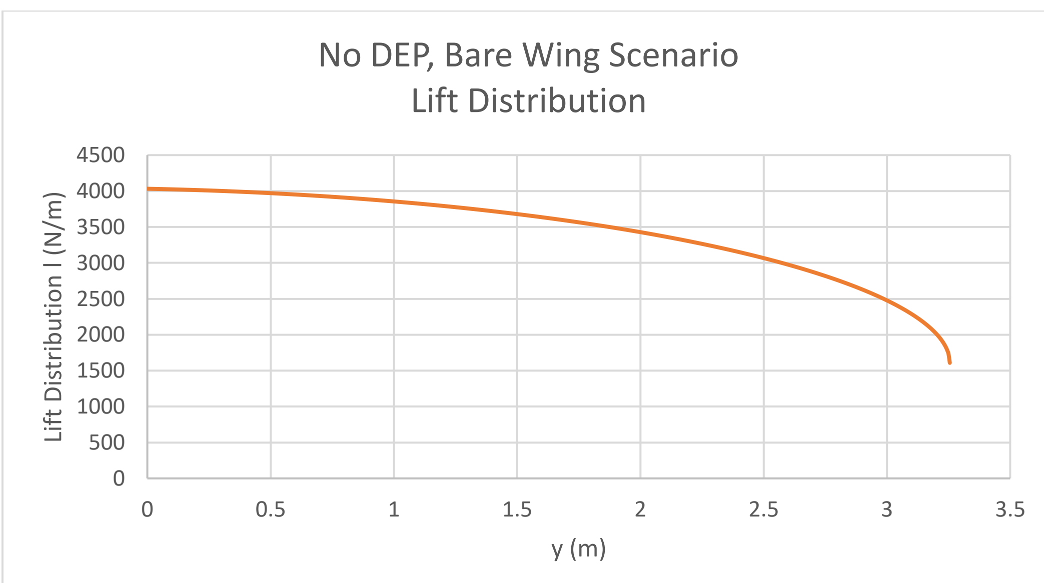

Εικόνα 69: Analysis 1 Lift Distribution l

The structural weight of the wing is distributed equally across the span $l = 3.255\ m$. The structural weight and the respective distributed load regarding one of the two wings are:

$$W_{wing} = 50\ kg = 50g\ N = 50 \cdot 9.81 = 490.5\ N$$

$$w_{wing} = \frac{W_{wing}}{l}\frac{N}{m} = \frac{490.5}{3.255}\frac{N}{m} = 150\frac{N}{m}$$

The fuel tank is located from $y_{t1} = 0.470\ m$ to $y_{t2} = 1.51\ m$ spanwise. The fuel weight and the respective distributed load regarding one of the two wings are:

$$W_{fuel} = \frac{1}{2}65\ kg = 32.5\ kg = 32.5g\ N = 32.5 \cdot 9.81 = 318.8\ N$$

$$w_{fuel} = \frac{W_{fuel}}{y_{tank}}\frac{N}{m} = \frac{318.8}{1.51 - 0.47}\frac{N}{m} = 306.5\frac{N}{m}$$

Due to the analysis describing the most severe load case applied to the aircraft, the inertial distributed loads are multiplied [15] by the load factor $n = 3.8$ in order to calculate the wing load distribution in the expression below.

The load distribution is obtained from Eq.(4.27), by superposition of the Lift, Fuel and Wing Distributions regarding the span $l = 3.255\ m$ with a y-step of $h = 0.005\ m$:

$$p(y) = L(y) - n \cdot w_{fuel}(y) - n \cdot w_{wing}(y)\ \ [\frac{N}{m}]$$

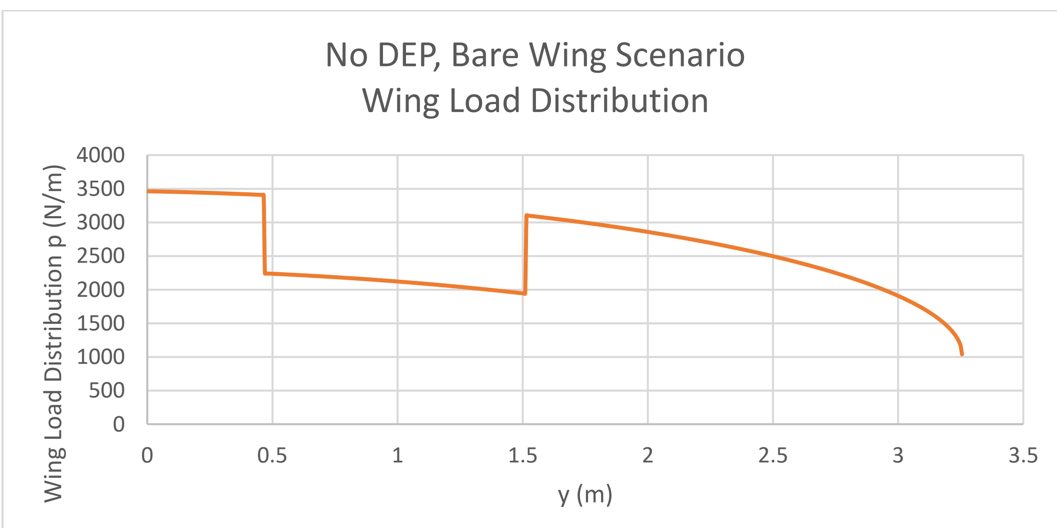

Εικόνα 70: Analysis 1 Load Distribution p

Using the Trapezoid Rule:

$$Q_z(y) = -\int_0^{y_{tip}} p(y)dy = -\sum E(p) \text{ where } E(p) = \frac{p_i(y)+p_{i+1}(y)}{2}h \ [N]$$

$$M_x(y) = -\int_0^{y_{tip}} Q_z(y)dy = -\sum E(Q) \text{ where } E(Q) = \frac{Q_i(y)+Q_{i+1}(y)}{2}h \ [Nm]$$

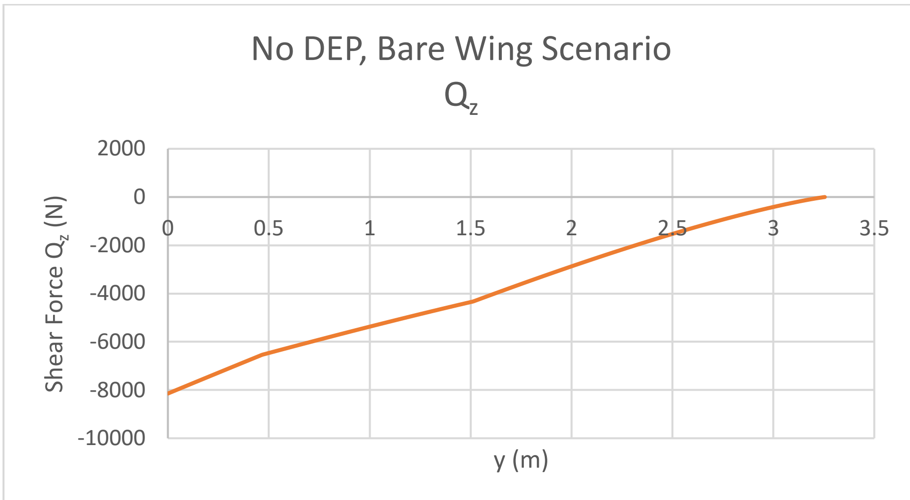

Εικόνα 71: Analysis 1 Shear Force Qz (caused by Lift)

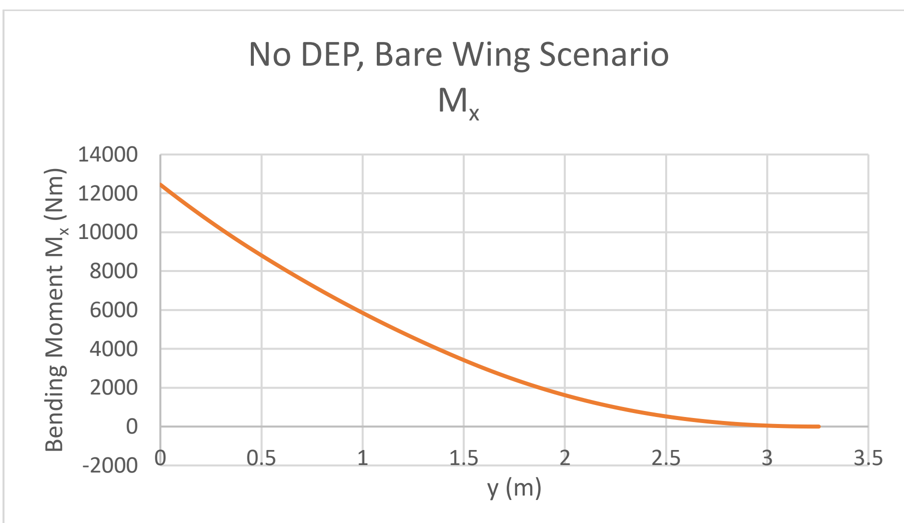

Εικόνα 72: Analysis 1 Bending Moment Mx (caused by Lift)

The Lift Force at the wing root must be equal to the aircraft's half weight, as a validation. The Lift Force is equal to $L = 11217\ N$. Dividing it by the load factor and the gravity acceleration gives $\frac{L}{ng} = \frac{11217\ N}{3.8 \cdot 9.81 \frac{m}{s^2}} = 300.9\ kg$, with the aircraft's half MTOW being equal to 300kg.

The airfoil max drag coefficient is obtained from [16], while the wing drag coefficient is equal to:

$$C_{D,airfoil_{max}} = 0.02306$$

$$C_{D,wing_{max}} = \frac{C_{D,airfoil_{max}}}{0.95} = 0.02427$$

The drag distribution for each section of the span $l = 3.255\ m$, regarding one of the two wings is obtained from Eq. (4.30):

$$D_y = \frac{1}{2} \cdot \rho \cdot V_y^2 \cdot c_y \cdot C_D = \frac{1}{2} \cdot 0.9627 \cdot 54^2 \cdot c_y^{schrenk} \cdot 0.02427 = 34 \cdot c_y^{schrenk} \quad [\frac{N}{m}]$$

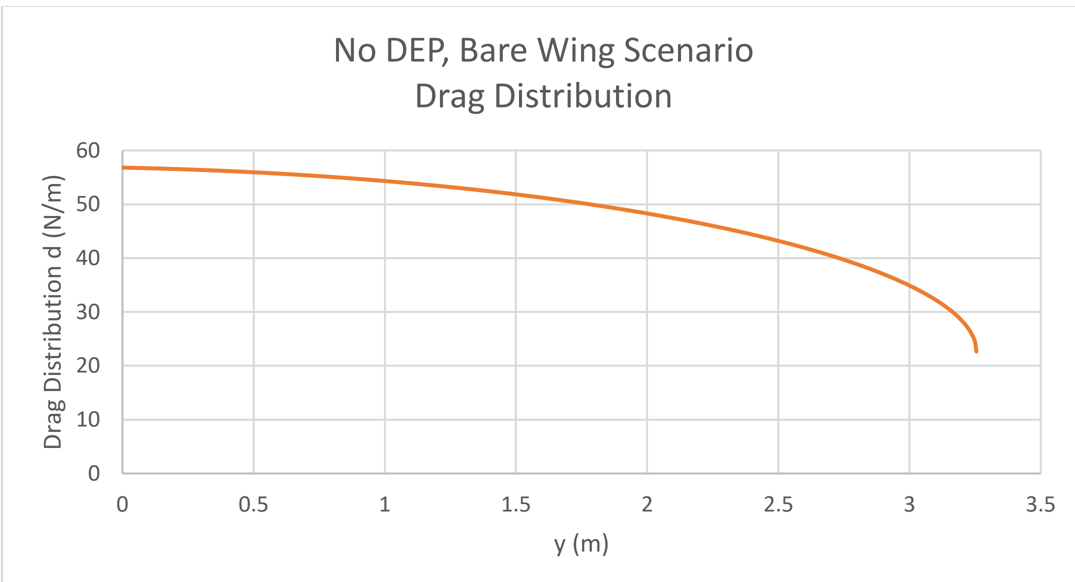

Εικόνα 73: Analysis 1 Drag Distribution d

Using the Trapezoid Rule:

$$Q_x(y) = -\int_0^{y_{tip}} D_y dy = -\sum E(D_y) \text{ where } E(D_y) = \frac{D_y^i + D_y^{i+1}}{2} h \ \ [N]$$

and:

$$M_z(y) = -\int_0^{y_{tip}} Q_x(y) dy = -\sum E(Q) \text{ where } E(Q) = \frac{Q_i(y) + Q_{i+1}(y)}{2} h \ \ [Nm]$$

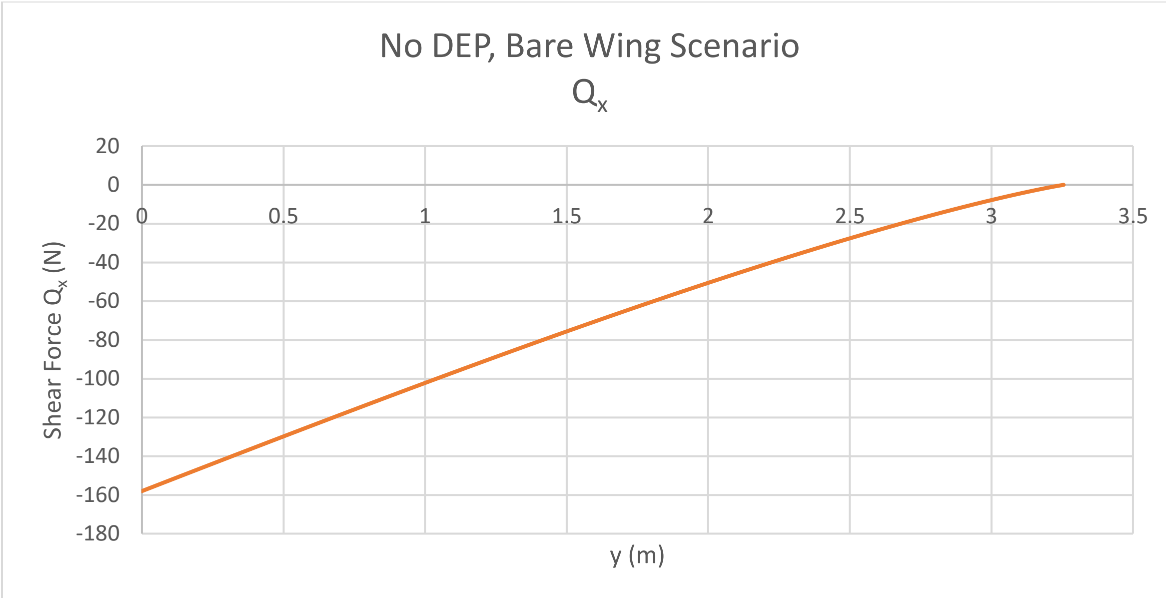

Εικόνα 74: Analysis 1 Shear Force Qx (caused by Drag)

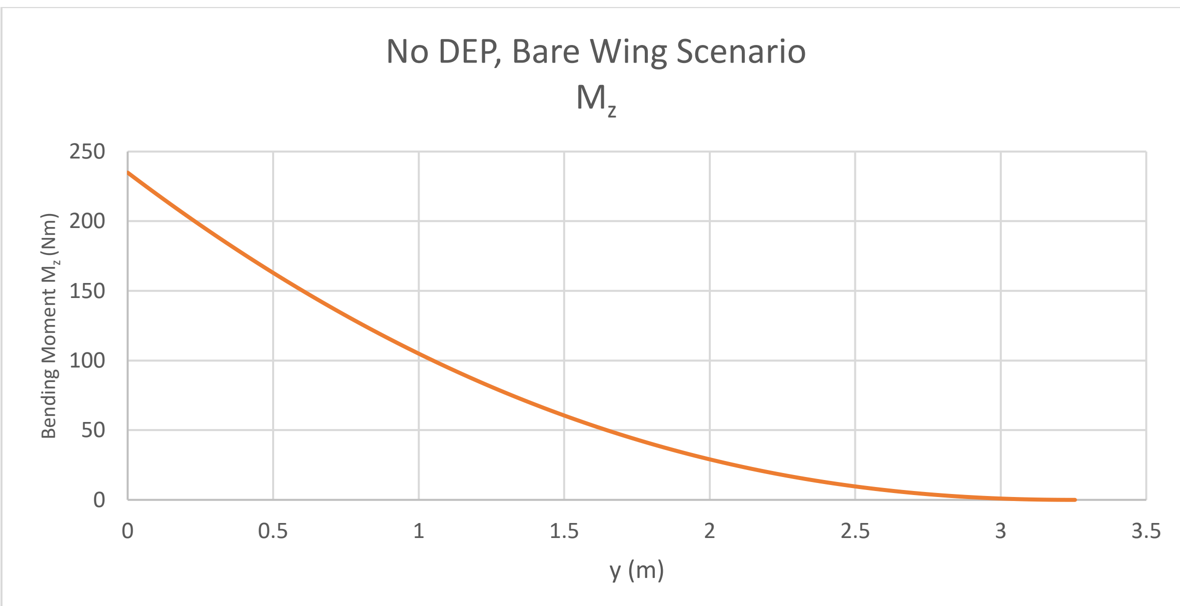

Εικόνα 75: Analysis 1 Bending Moment Mz (caused by Drag)

Comparing the Q,M figures created by Lift and Drag respectively, it is evident that the load caused by drag is significantly lower than the load caused by lift. Combined with the magnitude difference in second moments of inertia ($I_x \ll I_z$), Q_x and M_z are ignored in normal stress calculation.

4.2.1.1 Normal Stresses

<u>Critical Cross-Section I</u>

The maximum Shear Force and Bending Moment can be located at the wing root, where the wing is connected to the fuselage, meaning that is critical cross-section I. Hence, obtaining the data from the Excel sheet for $y = 0$:

$$\boldsymbol{Q_{z,root} = -8145\ N}$$

$$\boldsymbol{M_{x,root} = 12449\ Nm}$$

The critical cross-section I consists of the following components and depicted below:

Wing Root Spar Components			
No.	***Component***	***Thickness***	***mm***
1	Wing Root Doubler	t	3.175
2	Front Upper Spar Doubler	t	5
3	Rear Upper Spar Cap	t	5
4	Upper Extrusion Angle	t	2.5
5	Wing Spar Web	t	1
6	Bottom Spar Cap Angle	t	1.6
7	Rear Lower Spar Cap	t	5
8	Front Lower Spar Doubler	t	5

Πίνακας 13: Analysis 1 Wing Root Spar Components (Critical Cross-Section I)

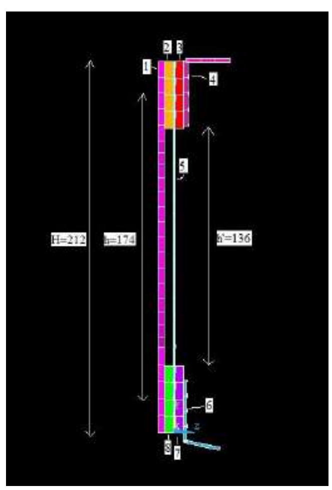

Εικόνα 76: Analysis 1 Wing Root Spar Cross-Section (Critical I)

Wing Spar Component Blueprints		
No.	***Component***	***Blueprint***
1	Wing Root Doubler	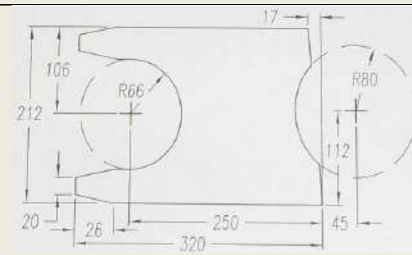
2	Front Upper Spar Doubler	 38mm x 5mm
3	Rear Upper Spar Cap	 38mm x 5mm
4	Upper Extrusion Angle	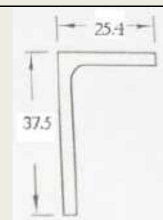
5	Wing Spar Web	212mm x 1mm
6	Bottom Spar Cap Angle	
7	Rear Lower Spar Cap	 38mm x 5mm
8	Front Lower Spar Doubler	 38mm x 5mm

Πίνακας 14: Analysis 1 Wing Spar Component Blueprints

The cross-section area under tensile load (upper spar cap) and under compression load (lower spar cap) are equal to:

$$F_{uf,I} = 38 \cdot (3.175 + 5 + 1 + 5) + 37.5 \cdot 2.5 + (25.4 - 2.5) \cdot 2.5 = 689.25\ mm^2$$

$$F_{lf,I} = 38 \cdot (3.175 + 5 + 1 + 5) + 35 \cdot 1.6 + (19.6 - 1.6) \cdot 1.6 = 623.45\ mm^2$$

The tensile and compression normal stresses at the critical cross-section can be obtained from Eq. (4.3):

$$\sigma_{upper,I} = \sigma_{uf} = \frac{M_{x,root}}{h \cdot F_{uf,I}} = \frac{12449\ Nm}{0.174\ m \cdot 689.25\ mm^2} = 103.8\ \frac{N}{mm^2} = 103.8\ MPa$$

$$\sigma_{lower,I} = \sigma_{lf} = \frac{M_{x,root}}{h \cdot F_{lf,I}} = \frac{12449\ Nm}{0.174\ m \cdot 623.45\ mm^2} = 114.8\ \frac{N}{mm^2} = 114.8\ MPa$$

The wing spar Web shear flow and shear stress can be obtained from Eq. (4.2) and (4.11) and are equal to:

$$q_I = \frac{Q_{z,root}}{h} = \frac{8145\ N}{174\ mm} = 46.8 \frac{N}{mm}$$

$$\tau_I = \frac{q}{t} = \frac{Q_{z,root}}{h \cdot t} = \frac{8145\ N}{174\ mm \cdot 1\ mm} = 46.8\ \frac{N}{mm^2} = 46.8\ MPa$$

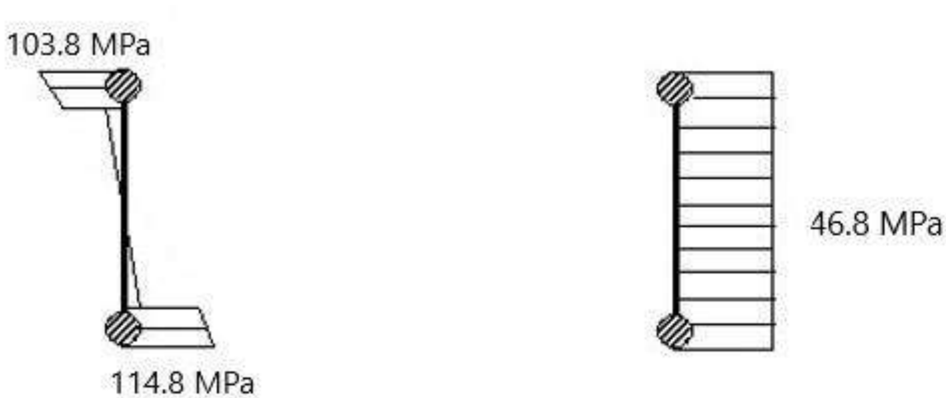

Εικόνα 77: Analysis 1 Stresses (Critical Cross-Section I)

Critical Cross-Section II

Another critical cross-section examined is where the root doubler ends. The critical cross-section II is the same compared to critical cross-section I minus the Root Doubler. It consists of the following components:

Component	***Thickness***	***mm***
Front Upper Spar Doubler	t	5
Rear Upper Spar Cap	t	5
Upper Extrusion Angle	t	2.5
Wing Spar Web	t	1
Bottom Spar Cap Angle	t	1.6
Rear Lower Spar Cap	t	5
Front Lower Spar Doubler	t	5

Πίνακας 15: Analysis 1 Wing Spar Components (Critical Cross-Section II)

The cross-section area under tensile load (upper spar cap) and under compression load (lower spar cap) are equal to:

$$F_{uf,II} = 38 \cdot (1 + 5 + 5) + 37.5 \cdot 2.5 + (25.4 - 2.5) \cdot 2.5 = 569\; mm^2$$

$$F_{lf,II} = 38 \cdot (1 + 5 + 5) + 35 \cdot 1.6 + (19.6 - 1.6) \cdot 1.6 = 502.8\; mm^2$$

The Shear Force and Bending Moment at critical cross-section II can be obtained from the Excel sheet for $y = 0.32\; m$:

$$\boldsymbol{Q_{z,II} = -7042\; N}$$

$$\boldsymbol{M_{x,II} = 10019\; Nm}$$

The tensile and compression normal stresses at the critical cross-section can be obtained from Eq. (4.3):

$$\sigma_{upper,II} = \sigma_{uf} = \frac{M_{x,II}}{h \cdot F_{uf,II}} = \frac{10019\; Nm}{0.174\; m \cdot 569\; mm^2} = 101.2\; \frac{N}{mm^2} = 101.2\; MPa$$

$$\sigma_{lower,II} = \sigma_{lf} = \frac{M_{x,II}}{h \cdot F_{lf,II}} = \frac{10019\; Nm}{0.174\; m \cdot 502.8\; mm^2} = 114.5\; \frac{N}{mm^2} = 114.5\; MPa$$

The wing spar Web shear flow and shear stress can be obtained from Eq. (4.2) and (4.11) and are equal to:

$$q_{II} = \frac{Q_{z,II}}{h} = \frac{7042\ N}{174\ mm} = 40.5\frac{N}{mm}$$

$$\tau_{II} = \frac{q}{t} = \frac{Q_{z,II}}{h \cdot t} = \frac{7042\ N}{174\ mm \cdot 1\ mm} = 40.5\ \frac{N}{mm^2} = 40.5\ MPa$$

Εικόνα 78: Analysis 1 Stresses (Critical Cross-Section II)

Critical Cross-Section III

Another critical cross-section examined is where the spar doublers end. The critical cross-section III is the same compared to critical cross-section I minus the Root Doubler and the Front Upper and Front Lower Spar Caps. It consists of the following components:

Component	***Thickness***	***mm***
Rear Upper Spar Cap	t	5
Upper Extrusion Angle	t	2.5
Wing Spar Web	t	1
Bottom Spar Cap Angle	t	1.6
Rear Lower Spar Cap	t	5

Πίνακας 16: Analysis 1 Wing Spar Components (Critical Cross-Section III)

The wing root spar cross-section (critical III) is depicted below:

Εικόνα 79: Analysis 1 Wing Spar Cross-Section (Critical III)

The cross-section area under tensile load (upper spar cap) and under compression load (lower spar cap) are equal to:

$$F_{uf,III} = 38 \cdot (1+5) + 37.5 \cdot 2.5 + (25.4 - 2.5) \cdot 2.5 = 379\ mm^2$$

$$F_{lf,III} = 38 \cdot (1+5) + 35 \cdot 1.6 + (19.6 - 1.6) \cdot 1.6 = 312.8\ mm^2$$

The Shear Force and Bending Moment at critical cross-section III can be obtained from the Excel sheet for $y = 1.48\ m$:

$$\boldsymbol{Q_{z,III} = -4393\ N}$$

$$\boldsymbol{M_{x,III} = 3508\ Nm}$$

The tensile and compression normal stresses at the critical cross-section can be obtained from Eq. (4.3):

$$\sigma_{upper,III} = \sigma_{uf} = \frac{M_{x,III}}{h \cdot F_{uf,III}} = \frac{3508\ Nm}{0.174\ m \cdot 379\ mm^2} = 53.2\ \frac{N}{mm^2} = 53.2\ MPa$$

$$\sigma_{lower,III} = \sigma_{lf} = \frac{M_{x,III}}{h \cdot F_{lf,III}} = \frac{3508\ Nm}{0.174\ m \cdot 312.8\ mm^2} = 64.5\ \frac{N}{mm^2} = 64.5\ MPa$$

The wing spar Web shear flow and shear stress can be obtained from Eq. (4.2) and (4.11) and are equal to:

$$q_{III} = \frac{Q_{z,III}}{h} = \frac{4393\ N}{174\ mm} = 25.3\frac{N}{mm}$$

$$\tau_{III} = \frac{q}{t} = \frac{Q_{z,III}}{h \cdot t} = \frac{4393\ N}{174\ mm \cdot 1\ mm} = 25.3\ \frac{N}{mm^2} = 25.3\ MPa$$

Εικόνα 80: Analysis 1 Stresses (Critical Cross-Section III)

Finally, the equivalent force of the Lift Distribution of each wing has a magnitude of $\boldsymbol{L = 11217}$ **N** at a lever arm to the fuselage axis of $\boldsymbol{y_{Lift,CG} = 1.53 + \frac{1.12}{2} = 2.1\ m}$

4.2.1.2 Shear Stresses

The airfoil coordinates were inserted into CATIA where the program can easily calculate the desired area and distances (measuring from the airfoil leading edge).

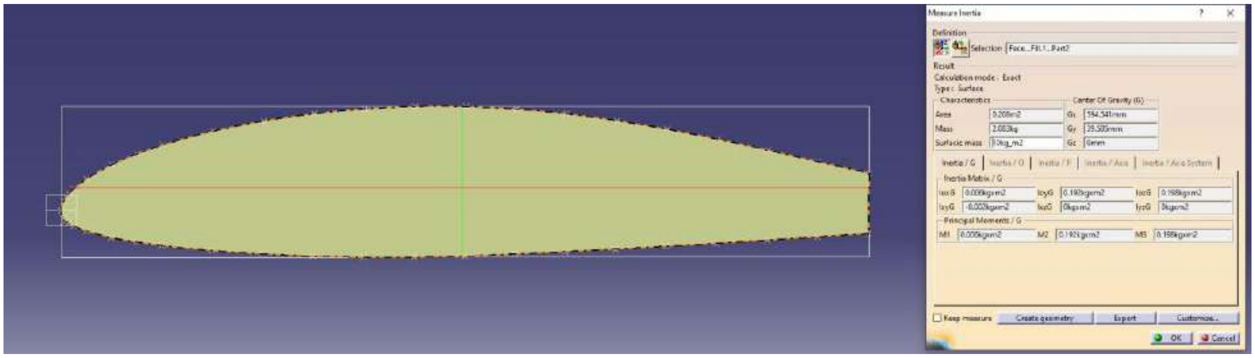

Εικόνα 81: Analysis 1 Airfoil Section CoG and Surface Area

Therefore, the wing's airfoil centroid, aerodynamic center lever arms and profile surface area are equal to:

$$x_c = 594.541\,mm = 0.594541\,m$$
$$z_c = 39.585\,mm = 0.039585\,m$$

$$d_x = x_c - \frac{c}{4} = 594.541 - 375 = 219.5\,mm = 0.2195\,m$$
$$d_z = z_c - z_{chord} = 39.585 - 0 = 39.585\,mm = 0.039585\,m$$

$$\Omega = \Omega_1 + \Omega_2 = 208\,m \cdot mm$$

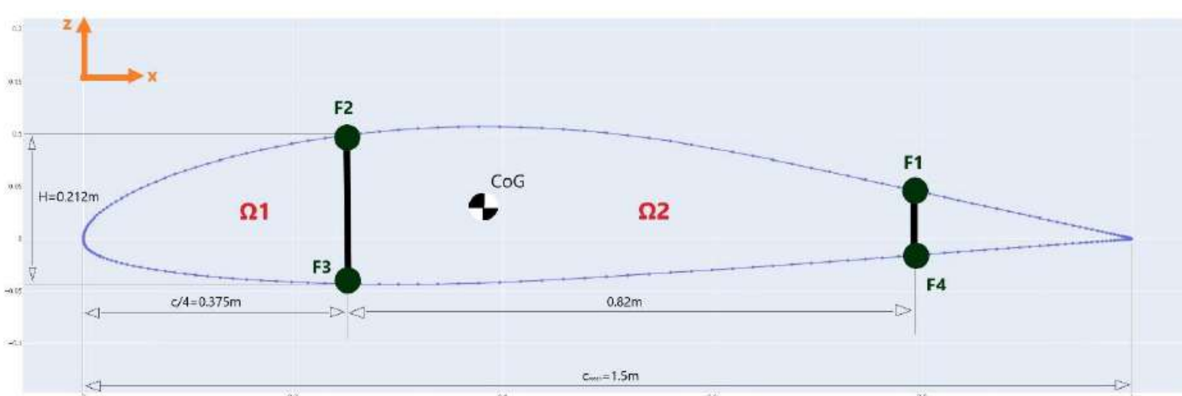

Εικόνα 82: Analysis 1 Airfoil Section for Shear Flow Calculation

Examination Point I (Wing Root, $y = 0$)

The Pitching Moment is obtained from Eq. (4.31) and is equal to:

$$M_P = \frac{1}{2}\rho V^2 S\bar{c}C_{M,wing} = \frac{1}{2} \cdot 0.9627 \frac{kg}{m^3} \cdot 54^2 \left(\frac{m}{s}\right)^2 \cdot 4.8825\, m^2 \cdot 1.5\, m \cdot \left(-\frac{0.088}{0.95}\right) = -952\, Nm$$

A negative value of Pitching Moment corresponds to a "nose-down" moment or a counter-clockwise direction. Additional Moments are created by loads when they are not applied to the airfoil CoG which is also the Shear Center due to the airfoil being a closed section.

The total Torsion Moment is obtained by addition of the Pitching Moment and the Moment produced by the Shear Force Q_z about the Shear Center (which is the same with the airfoil CoG since it is a closed section).

The total Torsion Moment is therefore equal to:

$$M_T = M_P + M' = M_P + Q_z \cdot d_x = -952\, Nm - 8145\, N \cdot 0.2195\, m = -2740\, Nm$$

$$\boldsymbol{M_T = -2740\, Nm}$$

The shear flow due to torsion can be obtained from Eq. (4.33) and is equal to:

$$q_T = \frac{M_T}{2 \cdot \Omega} = \frac{-2740\, Nm}{2 \cdot 208\, m \cdot mm} = -6.58 \frac{N}{mm}$$

The assumed-open section shear flows can be obtained from Eq. (4.34). The surfaces of the wing root cross section are equal to $F_{1,I} = 113\, mm^2$, $F_{2,I} = 689.25\, mm^2$, $F_{3,I} = 623.45\, mm^2$, $F_{4,I} = 113\, mm^2$. The shear flow between surfaces F_1 and F_4 is assumed equal to zero [5], $\tilde{q}_{4-1} = 0$ and it is also calculated in the end for validation.

The shear force at the wing root is equal to $Q_z = -8145\, N$ and the wing root airfoil cross-section's second moment of inertia can be obtained from the Shear Flow Theory [5] and is equal to:

$$I_x = F_1(z_1 - z_c)^2 + F_2(z_2 - z_c)^2 + F_3(z_3 - z_c)^2 + F_4(z_4 - z_c)^2 = 40.5 \cdot 10^6\, mm^4$$

$$\tilde{q}_{4-1} = 0$$

$$\tilde{q}_{4-3} = \tilde{q}_{4-1} + \frac{Q_z}{I_x} F_3(z_3 - z_c) = 1.42 \frac{N}{mm}$$

$$\tilde{q}_{3-2} = \tilde{q}_{4-3} + \frac{Q_z}{I_x} F_2(z_2 - z_c) = 14.49 \frac{N}{mm}$$

$$\tilde{q}_{2-1} = \tilde{q}_{3-2} + \frac{Q_z}{I_x} F_1(z_1 - z_c) = -15.92 \frac{N}{mm}$$

$$\tilde{q}_{1-4} = \tilde{q}_{2-1} + \frac{Q_z}{I_x} F_4(z_4 - z_c) = -1.65 \frac{N}{mm} \simeq 0$$

The surface areas A_{i-j} are consisted of the area formed by the examined element and the reference point which in this case is the aerodynamic center. The areas A_{i-j} are calculated in CATIA and are equal to $A_{1-2} = 0.082\, m^2$, $A_{2-3} = 0.057\, m^2$, $A_{3-4} = 0.032\, m^2$, $A_{4-1} = 0.037\, m^2$.

$$q_0 = -\frac{A_{1-2}\tilde{q}_{1-2} + A_{2-3}\tilde{q}_{2-3} + A_{3-4}\tilde{q}_{3-4} + A_{4-1}\tilde{q}_{4-1}}{A_{1-2} + A_{2-3} + A_{3-4} + A_{4-1}} = 2.09 \frac{N}{mm}$$

The total shear flows due to shear can be obtained by superposition from Eq. (4.36):

$$q_{4-1} = q_0 = 2.09 \frac{N}{mm}$$

$$q_{4-3} = q_0 + \tilde{q}_{4-3} = 3.51 \frac{N}{mm}$$

$$q_{3-2} = q_0 + \tilde{q}_{3-2} = 16.58 \frac{N}{mm}$$

$$q_{2-1} = q_0 + \tilde{q}_{2-1} = -13.83 \frac{N}{mm}$$

The positive value of the Shear Flows refers to a clockwise direction and the negative value refers to a counter-clockwise direction (“nose down”).

The skin Shear Stress for each section can be obtained from Eq. (4.37). The skin width is equal to $t_{skin} = 0.635\, m$, hence:

$$\tau_{4-1} = \frac{q_{4-1} + q_T}{t_{skin}} = \frac{2.09 - 6.58 \frac{N}{mm}}{0.635\, mm} = -7.1 \text{ MPa}$$

$$\tau_{4-3} = \frac{q_{4-3} + q_T}{t_{skin}} = \frac{3.51 - 6.58 \frac{N}{mm}}{0.635\, mm} = -4.8 \text{ MPa}$$

$$\tau_{3-2} = \frac{q_{3-2} + q_T}{t_{skin}} = \frac{16.58 - 6.58 \frac{N}{mm}}{0.635\, mm} = 15.7 \text{ MPa}$$

$$\tau_{2-1} = \frac{q_{2-1} + q_T}{t_{skin}} = \frac{-13.83 - 6.58 \frac{N}{mm}}{0.635\, mm} = -32.1 \text{ MPa}$$

4.2.1.3 Equivalent Stresses

The equivalent normal stress in the most critical cross-section, therefore the upper flange of cross-section I, using the Von Mises criterion, is equal to:

$$\sigma_{eq} = \sqrt{\sigma_{max}^2 + 3\tau_{max}^2} \quad [MPa]$$

For $\sigma_{uf,I} = 103.8\ MPa$ and $t_{us,I} = -32\ MPa$ the equivalent Von Mises stress is equal to:

$$\sigma_{eq,I} = \sqrt{103.8^2 + 3 \cdot 32.1^2} = 118\ \ MPa$$

The Al6061-T6 Tensile Yield Strength and Shear Strength are equal to $S_{yield} = 276\ MPa$, $S_{shear} = 207\ MPa$.

$$n_I = \frac{S_y}{\sigma_{eq,I}} = \frac{276}{118} = 2.3$$

4.2.1.4 Riveting

The riveting strength study requires knowledge of the rivet type, rivet diameter and the riveting pitch. The rivet types and riveting pitch used are presented below and their diameter can be obtained from the Table below:

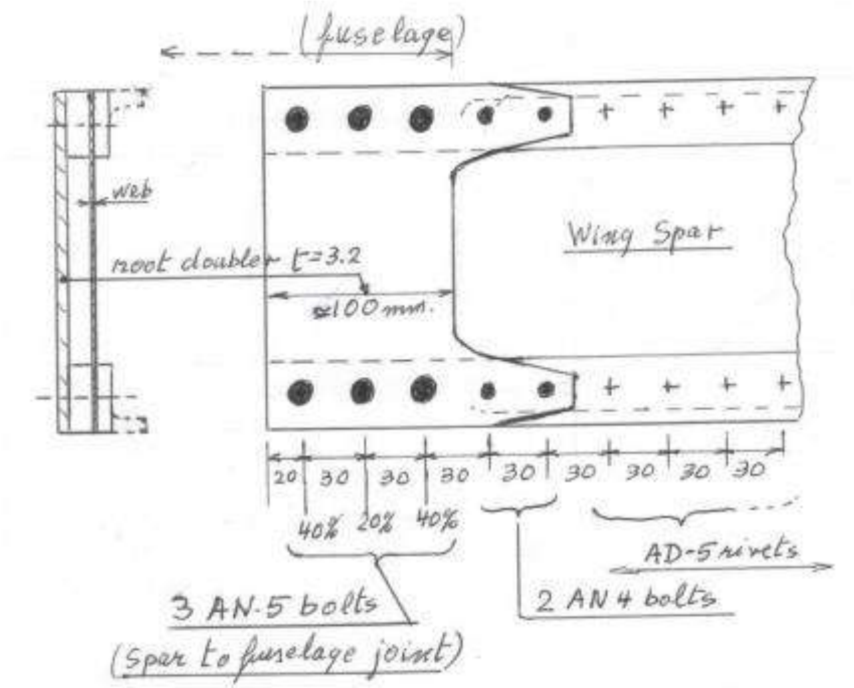

Εικόνα 83: Analysis 1 Spar Rivets at the Wing Root

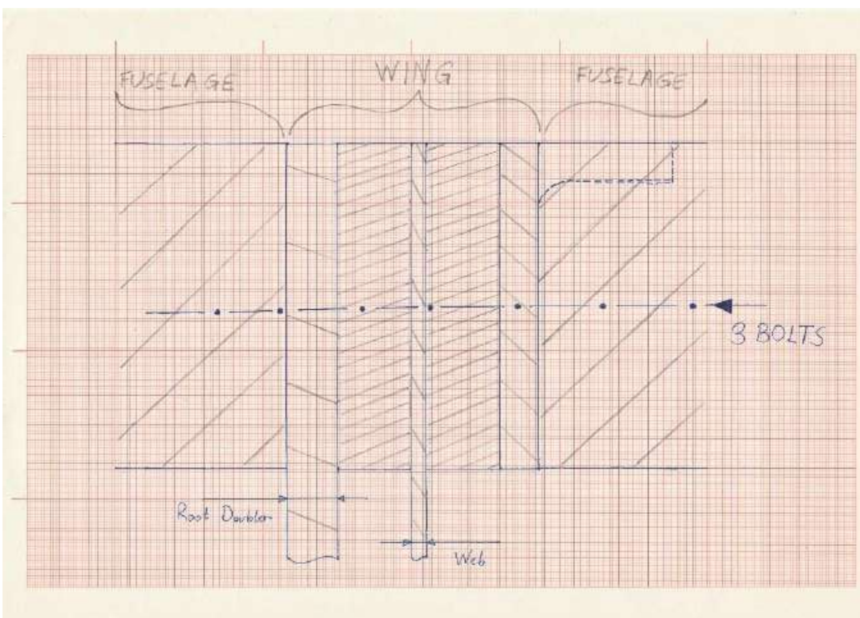

Εικόνα 84: Analysis 1 Wing-Fuselage Joint with AN-5 Bolts

Wing Root-Fuselage Joint

A Root Doubler is added to the Spar structure in the Wing-Fuselage joint. AN-5 Bolts with a diameter of $D = 8\ mm$ are used. The area S, without the Bolt holes is equal to:

$$S = (38 - 8) \cdot (3.175 + 5 + 1 + 5) = 425.25\ mm^2$$

The normal stress is obtained from Eq. (4.11) of Shear Flow Theory. The bending moment at the wing root is $M_o = 12449\ Nm$ and the normal stress is equal to:

$$\sigma = \frac{M_o}{h \cdot S} = \frac{12449\ Nm}{0.174\ m \cdot 425.25\ mm^2} = 168.2\ MPa$$

The applied Bolt pressure (with a safety factor of $N = 1.2$ for three bolts) is equal to:

$$p_B = \frac{q_{Bolt}}{d_{Bolt} \cdot t} = \frac{\frac{12449}{0.174} \frac{Nm}{m} \cdot 0.4}{8\ mm \cdot (3.175 + 5 + 1 + 5)\ mm} = 252.3\ MPa$$

Root Doubler-Spar Joint

The load applied to the Root Doubler is equal to:

$$q_{RootDoubler} = \frac{12449\ Nm}{0.174\ m} \cdot \frac{3.175\ mm}{(3.175 + 5 + 1 + 5 + 2.5)\ mm} = 13622.7\ N$$

This load is transferred from the front Spar Doubler to the Root Doubler through two (2) AN-4 Bolts with a diameter of $D = 6.35\ mm$. The load is applied to each Bolt is equal to:

$$q_{Bolt} = \frac{q_{RootDoubler}}{N_{AN-4}} = \frac{13622.7\ N}{2} = 6811.35\ N$$

The pressure applied in each Bolt is equal to:

$$p_B = \frac{q_{Bolt}}{d_{Bolt} \cdot t} = \frac{6811.35\ N}{6.35\ mm \cdot (3.175 + 5 + 1 + 5 + 2.5)\ mm} = 64.3\ MPa$$

Bolt diameter	3/16	1/4	5/16	3/8	7/8	1/2	inches
Designation	AN-3	-4	-5	-6	-7	-8	in inch/16
Diameter	4.8	6.3	8	9.5	11.1	12.7	mm
Ult. shear	940	1670	2600	3700	5100	6600	kg
Ult. tension	1000	1850	2900	4500	6100	8400	kg

Πίνακας 17: Analysis 1 Common Types of AN Bolts

4.2.1.5 Deflection

The wing tip deflection can be obtained from Eq. (4.40). Since the integration point 1 is $y = 0$, therefore it refers to the wing root, which is clamped to the aircraft fuselage, it is $v_1 = 0$ and $\theta_1 = 0$. The Young's elastic modulus is constant and equal to $E = 68.9\ GPa = 68.9 \cdot 10^9 \frac{N}{m^2}$, since the material (Al6061-T6) is isotropic. The cross-section's second moment of inertia is not constant along the wingspan as the flange surfaces vary. From Eq. (4.12), the second moment of inertia is equal to $I = 2\left(\frac{h}{2}\right)^2 F_f = \left(\frac{h}{2}\right)^2 (F_{uf} + F_{lf})$. The upper flange surface is slightly larger than the respective lower flange one, thus the mean value will be used. The second moment of inertia has three different values, concerning the sections $[0, 0.32\ m], [0.32\ m, 1.48\ m]$ and $[1.48\ m, 3.255\ m]$. Hence:

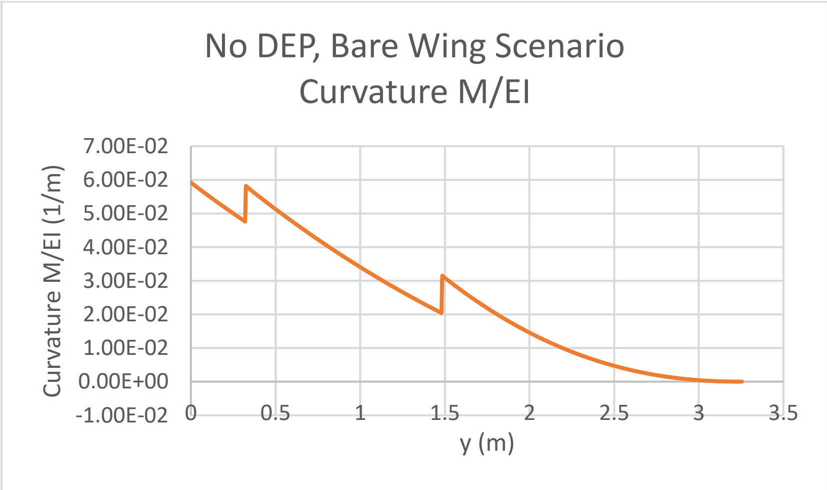

Εικόνα 85: Analysis 1 Curvature M/EI

$$v_2 = v_1 + \theta_1 (y_2 - y_1) + \int_{y_1}^{y_2} \frac{M_x(y)}{E \cdot I_x(y)} (y_2 - y_1) dy$$

$$v_2 = 0 + 0 \cdot (3.255 - 0) + \int_0^{3.255} \frac{M_x(y)\ Nm}{68.9 \cdot 10^9 \frac{N}{m^2} \cdot I_x(y)\ m^4} (3.255 - 0) m\ dy = 0.0784\ m$$

with the integration completed numerically in the Excel sheet. The wing tip deflection is therefore equal to:

$$v_{wing\ tip} = v_2 = 0.0784\ m = 78.4\ mm$$

4.2.1.6 Runway Length

The air density at sea level is equal to $\rho = 1.225\,\frac{kg}{m^3}$ and the wing surface is equal to $S = 9.765\,m^2$. The aircraft MTOW is 600kg or 1320lbs, and the flaps-down stall speed of the Reference configuration is 70km/h or 19.4 m/s.

Therefore, the flaps-down maximum lift coefficient is equal to:

$$L = \frac{1}{2}\rho V_{stall}^2 C_{L,max} \xRightarrow{L=W=5886N} C_{L,max} = 2.61$$

The wing loading is equal to:

$$\left(\frac{W}{S}\right)_{TO} = \frac{600kg}{9.765m^2} = 12.58\,\frac{lb}{ft^2}$$

The power-to-weight ratio is equal to:

$$\frac{HP}{W} = \frac{120HP}{600kg} = \frac{120HP}{1320lb} = 0.091\,\frac{HP}{lb}$$

The Take Off Parameter (TOP) is equal to:

$$(TOP)_{Ref} = \frac{(W/S)}{\sigma C_{L,max}(HP/W)} = \frac{600kg/9.765m^2}{1 \cdot 2.61 \cdot 120HP/600kg} = \frac{12.58\ lb/ft^2}{1 \cdot 4.2 \cdot 120HP/1320\ lb} = 53$$

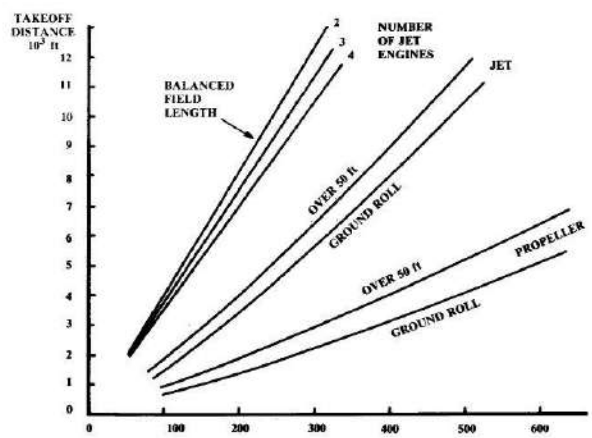

The takeoff distance in the Reference configuration is given by Zenith as $TOD_{Ref} = 500ft\ or\ 152m$ and can be verified from the graph above.

4.2.2 Distributed Electric Propulsion Configuration

The Zenith Zodiac CH 650 B in AEA DEP conversion is powered by a hydrogen fuel-cell system. One cruise and four high-lift motor-propeller units are mounted on each straight leading edge - tapered trailing edge wing, with structural, electric motor and propeller assembly weights being the inertial loads applied.

The maximum take-off weight is $MTOW = 800\ kg$ and the load factor used in this analysis is $n = 3.8$. The procedure described in Chapter 4.1.6 will be followed.

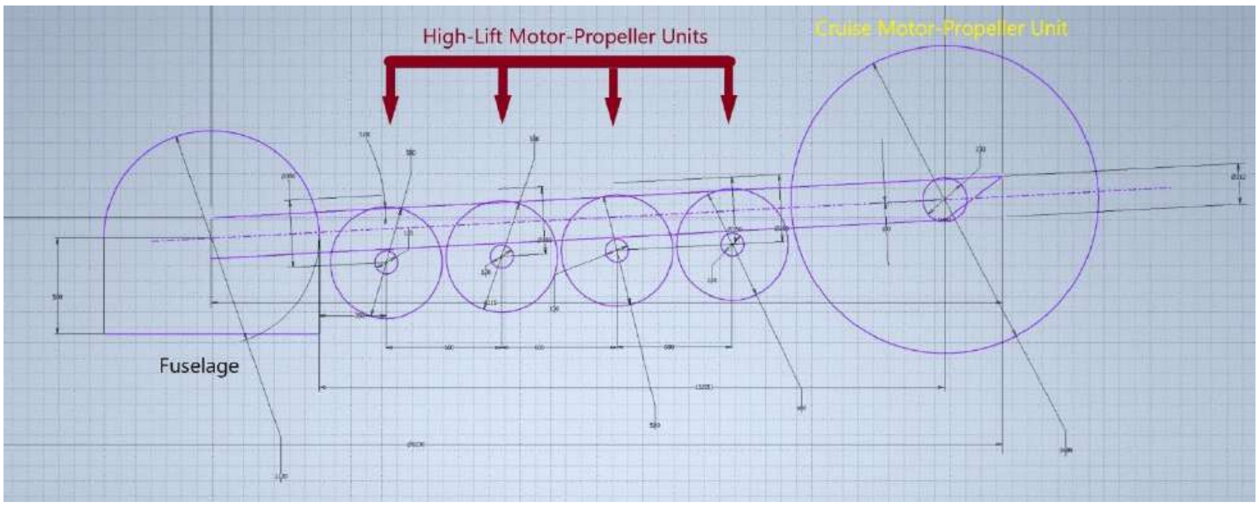

Εικόνα 86: Analysis 2 Wing Configuration Front View

As mentioned in Chapter 4.1.3, the analysis is performed in a load case scenario where the maximum positive load factor is applied ($n = 3.8$), while also performing a correctly banked turn.

For a limiting value of n, the minimum time taken to turn through a given angle occurs when the lift coefficient C_L is maximum, that is with the aircraft on the point of stalling [15]. The airfoil max lift coefficient is obtained from [16], while the wing lift coefficient is obtained from Eq. (4.26) and is equal to:

$$C_{L,airfoil_{max}} = 1.555$$

$$C_{L,wing_{max}} = \frac{C_{L,airfoil_{max}}}{0.95} = 1.64$$

Useful Parameters		
Area (One Wing)	$\boldsymbol{S}$	$4.8825\ m^2$
Half Aircraft Weight (One Wing)	$\boldsymbol{MTOW/2}$	$3924\ N$
Air Density (@8000 ft)	$\boldsymbol{\rho}$	$0.9627\ kg/m^3$

Πίνακας 18: Analysis 2 Useful Parameters

With the load factor equal to $n = 3.8$, $MTOW = 800\ kg = 7848\ N$, the wing air velocity and also true aircraft speed will be calculated using the wing Lift Equation:

$$V_{stall} = \sqrt{\frac{2nW}{\rho S_{wing} C_{L,wing_{max}}}} = \sqrt{\frac{2 \cdot 3.8 \cdot 3924}{0.9627 \cdot 4.8825 \cdot 1.64}} \Rightarrow V = 62 \frac{m}{s}$$

As explained also in the Analysis Assumptions (Chapter 4.3) the calculated velocity is assumed to be the air velocity interacting with the wing behind the High-Lift propellers as those 4 High-Lift propellers cover most of the studied wingspan (72%).

Since the High-Lift region does not cover 100% of the studied wingspan, a correction in velocity has to be made, in order to produce sufficient Lift to satisfy the load factor $n = 3.8$ condition. The correction is made in Excel through trial and error and the corrected velocity in order for the wing to produce the necessary Lift is equal to:

$$\boldsymbol{V = 67 \frac{m}{s}}$$

Therefore, with the propeller Thrust values known, the true aircraft speed (TAS) and the air velocity interacting with the wing in the Cruise propeller region are calculated using the velocities v_0, v_i, v_{wing} of Eq. (4.14), (4.20), (4.21) from Slipstream Effect (Chapter 4.1.5).

For $r_{HL} = \frac{0.58}{2} = 0.29\ m$, $r_C = \frac{1.6}{2} = 0.8\ m$ and $s = 0.3\ m$, the development factor k_d for both High-Lift and Cruise regions is calculated from Eq. (4.15) and is equal to:

$$k_{d,HL} = 1 + \frac{s}{\sqrt{r^2 + s^2}} = 1.56$$

$$k_{d,C} = 1 + \frac{s}{\sqrt{r^2 + s^2}} = 1.24$$

For $v_{wing} = 67\frac{m}{s}$, $T_{HL} = 618\ N$, $A_{HL} = 0.264\ m^2$, $\rho = 0.9627\frac{kg}{m^3}$, the system consisting of Eq. (4.14), (4.20) and (4.21) and regarding the High-Lift region is solved in Excel:

$$v_w = v_i k_d$$

$$v_i^2 + v_0 v_i - \frac{T}{2A\rho} = 0$$

$$v_{wing} = v_0 + v_w$$

The axially-induced velocity v_i, the additional velocity v_w and the freestream air velocity v_0 are equal to:

$$v_{i,HL} = 22.3\frac{m}{s}$$

$$v_{w,HL} = v_{i,HL} \cdot k_d = 22.3\frac{m}{s} \cdot 1.56 = 35\frac{m}{s}$$

$$v_0 = 32\frac{m}{s}$$

Therefore, the true aircraft speed is equal to the freestream air velocity and thus:

$$\boldsymbol{v_{TAS} = 32\frac{m}{s}}$$

For $v_0 = 32\frac{m}{s}$, , $T_c = 1961\ N$, $A_C = 2\ m^2$, $\rho = 0.9627\frac{kg}{m^3}$, the system consisting of Eq. (4.14), (4.20) and (4.21) and regarding the Cruise region is solved in Excel. The axially-induced velocity v_i, the additional velocity v_w and the velocity interacting with the wing v_{wing} are equal to:

$$v_{i,C} = 11.6\frac{m}{s}$$

$$v_{w,C} = v_{i,C} \cdot k_{d,C} = 11.6\frac{m}{s} \cdot 1.24 \simeq 14\frac{m}{s}$$

$$v_{wing,C} = 46\frac{m}{s}$$

The angle of bank Φ and the turn radius R of the maneuver performed by the aircraft in this Thesis are equal to:

$$L \cdot sin\Phi = \frac{W}{g} \cdot \frac{V^2}{R}$$
$$L \cdot cos\Phi = W$$

$$n = \frac{L}{W} = \frac{L}{L \cdot cos\Phi} = \frac{1}{cos\Phi} \Rightarrow cos\Phi = \frac{1}{n} \Rightarrow \Phi = arccos\left(\frac{1}{n}\right) \Rightarrow \boldsymbol{\Phi = 74.74°}$$

$$tan\Phi = \frac{V_{TAS}^2}{gR} \Rightarrow R = \frac{V_{TAS}^2}{g \cdot tan\Phi} = \frac{\left(32\,\frac{m}{s}\right)^2}{9.81\,\frac{m}{s^2} \cdot tan\,(74.74°)} \Rightarrow \boldsymbol{R = 28.5\ m}$$

The wing chord distribution for each section of the span $l = 3.255\ m$, regarding one of the two wings is obtained from Equations (4.23), (4.24), (4.25) and the calculations are made on Excel sheet:

$$c_y^{trap} = 1.6\left(1 - 0.125\,\frac{y}{3.255}\right)\ \ [m]$$

$$c_y^{ellip} = 1.909\sqrt{(1 - \left(\frac{y}{3.255}\right)^2}\ \ [m]$$

$$c_y^{schrenk} = \frac{1}{2}\left(c_y^{trap} + c_y^{ellip}\right)\ \ [m]$$

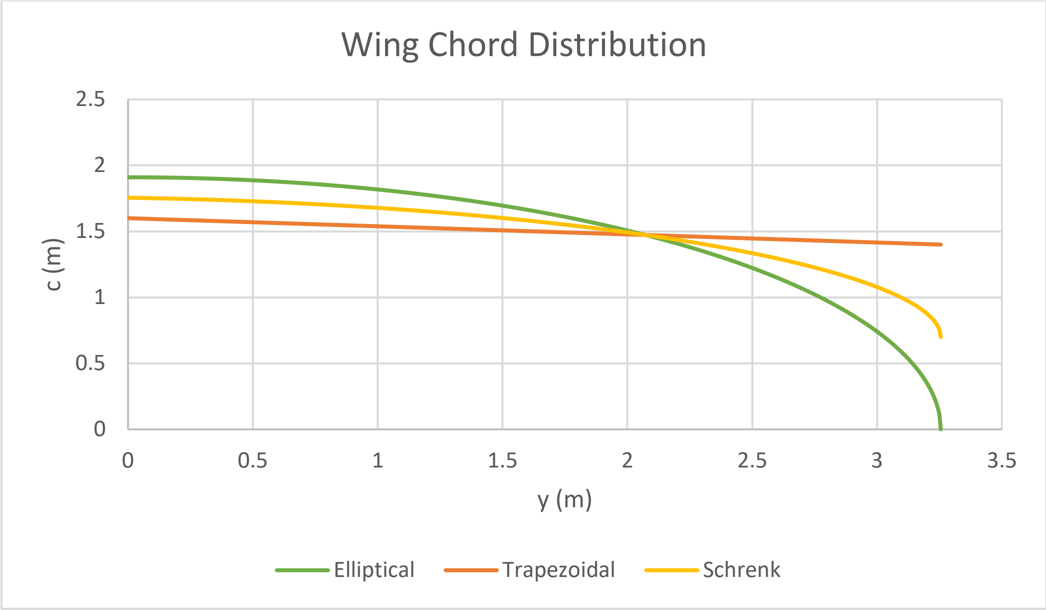

Εικόνα 87: Analysis 2 Wing Chord Distribution c

The lift distribution of the span $l = 3.255\ m$, regarding one of the two wings is obtained for each region (unblown, high-lift and cruise respectively) from Eq. (4.22):

The lift distribution of the **Unblown** region [0, 0.06m], [0.64m, 0.66m], [1.24m, 1.26m], [1.84m, 1.86m], [2.44m, 2.455m] is equal to:

$$L_y = \frac{1}{2} \cdot \rho \cdot V_y^2 \cdot c_y \cdot C_L = \frac{1}{2} \cdot 0.9627 \cdot 22^2 \cdot c_y^{schrenk} \cdot 1.64 = 382 \cdot c_y^{schrenk} \quad [\frac{N}{m}]$$

The lift distribution of the **High-Lift** region [0.06m, 0.64m], [0.66m, 1.24m], [1.26m, 1.84m], [1.86m, 2.44m] is equal to:

$$L_y = \frac{1}{2} \cdot \rho \cdot V_y^2 \cdot c_y \cdot C_L = \frac{1}{2} \cdot 0.9627 \cdot 62^2 \cdot c_y^{schrenk} \cdot 1.64 = 3034.5 \cdot c_y^{schrenk} \quad [\frac{N}{m}]$$

The lift distribution of the **Cruise** region [2.455m, 3.255m] is equal to:

$$L_y = \frac{1}{2} \cdot \rho \cdot V_y^2 \cdot c_y \cdot C_L = \frac{1}{2} \cdot 0.9627 \cdot 40^2 \cdot c_y^{schrenk} \cdot 1.64 = 1263 \cdot c_y^{schrenk} \quad [\frac{N}{m}]$$

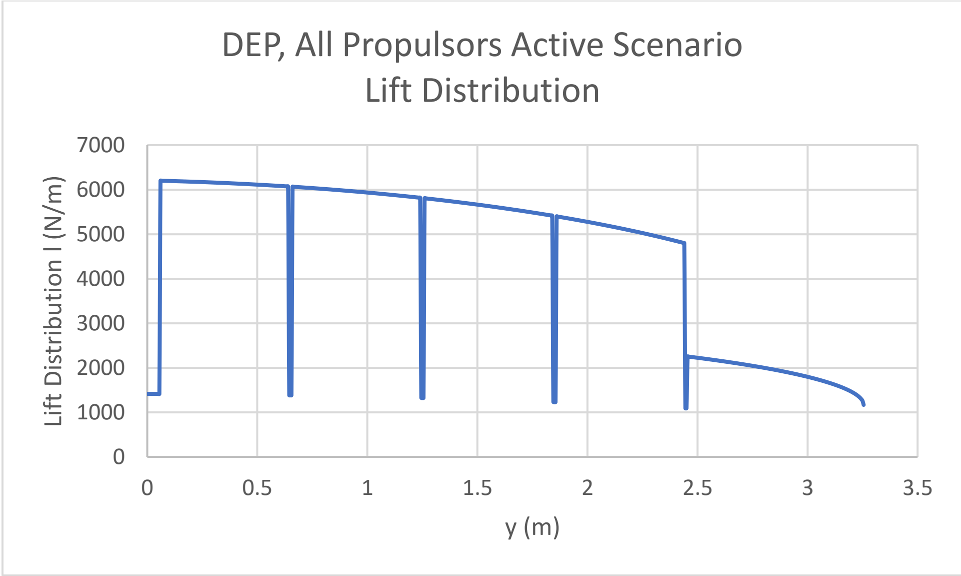

Εικόνα 88: Analysis 2 Lift Distribution l

The structural weight of the wing is distributed equally across the span $l = 3.255\ m$. The structural weight and the respective distributed load regarding one of the two wings are:

$$W_{wing} = 50\ kg = 50g\ N = 50 \cdot 9.81 = 490.5\ N$$

$$w_{wing} = \frac{W_{wing}}{l}\frac{N}{m} = \frac{490.5}{3.255}\frac{N}{m} = 150\frac{N}{m}$$

Fuel is removed from the aircraft in this AEA DEP conversion. However, electric motors and propellers are now mounted on the wing.

The High-Lift and Cruise motor weight distributions are equal to:

$$W_{HL,motor} = 3.75\ kg = 3.75g\ N = 3.75 \cdot 9.81 = 36.7875\ N$$

$$w_{HL,motor} = \frac{W_{HL,motor}}{d_{HL,motor}}\frac{N}{m} = \frac{36.7875}{0.114}\frac{N}{m} = 323\ \frac{N}{m}$$

$$W_{C,motor} = 13\ kg = 13g\ N = 13 \cdot 9.81 = 127.53\ N$$

$$w_{C,motor} = \frac{W_{C,motor}}{d_{C,motor}}\frac{N}{m} = \frac{127.53}{0.224}\frac{N}{m} = 569\ \frac{N}{m}$$

The High-Lift and Cruise propeller weight distributions are equal to:

$$W_{HL,prop} = 3.25\ kg = 3.25g\ N = 3.25 \cdot 9.81 = 31.8825\ N$$

$$w_{HL,prop} = \frac{W_{HL,prop}}{d_{HL,prop}} \frac{N}{m} = \frac{31.8825}{0.58} \frac{N}{m} = 55\ \frac{N}{m}$$

$$W_{C,prop} = 12\ kg = 12g\ N = 12 \cdot 9.81 = 117.72\ N$$

$$w_{C,prop} = \frac{W_{C,prop}}{d_{C,prop}} \frac{N}{m} = \frac{117.72}{1.6} \frac{N}{m} = 73.5\ \frac{N}{m}$$

Due to the analysis describing the most severe load case, the inertial distributed loads are multiplied [15] by the load factor $n = 3.8$ in order to calculate the wing load distribution.

The load distribution is obtained from Eq.(4.27), by superposition of the Lift, Fuel and Wing Distributions regarding the span $l = 3.255\ m$ with a y-step of $h = 0.005\ m$:

$$p(y) = L(y) - n(\ w_{HL,motor}(y) + w_{C,motor}(y) + w_{HL,prop}(y) + w_{C,prop}(y) + w_{wing}(y)\ )\ [\frac{N}{m}]$$

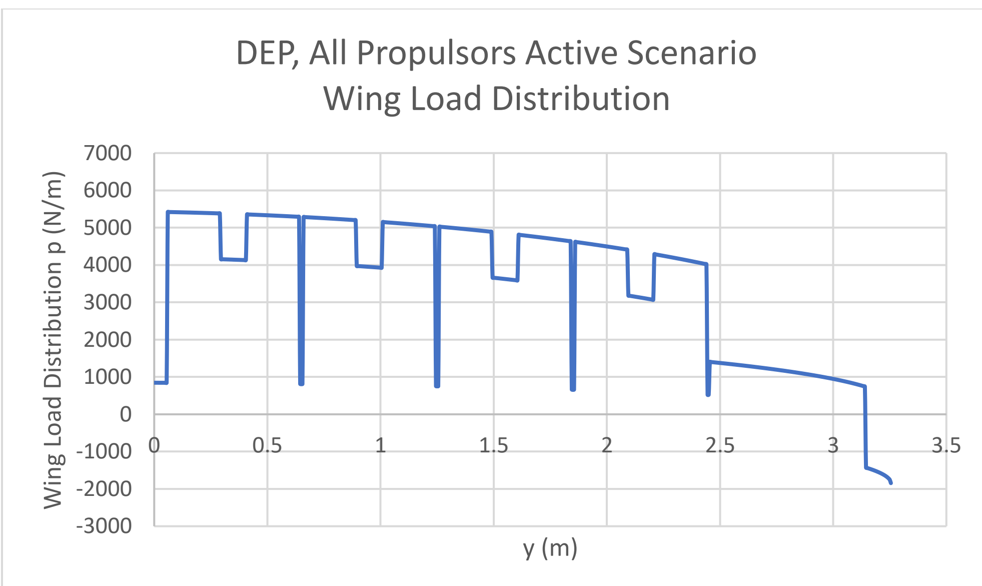

Εικόνα 89: Analysis 2 Load Distribution p

Using the Trapezoid Rule:

$$Q_z(y) = -\int_0^{y_{tip}} p(y)dy = -\sum E(p) \text{ where } E(p) = \frac{p_i(y)+p_{i+1}(y)}{2} h\ \ [N]$$

$$M_x(y) = -\int_0^{y_{tip}} Q_z(y)dy = -\sum E(Q) \text{ where } E(Q) = \frac{Q_i(y)+Q_{i+1}(y)}{2} h\ \ [Nm]$$

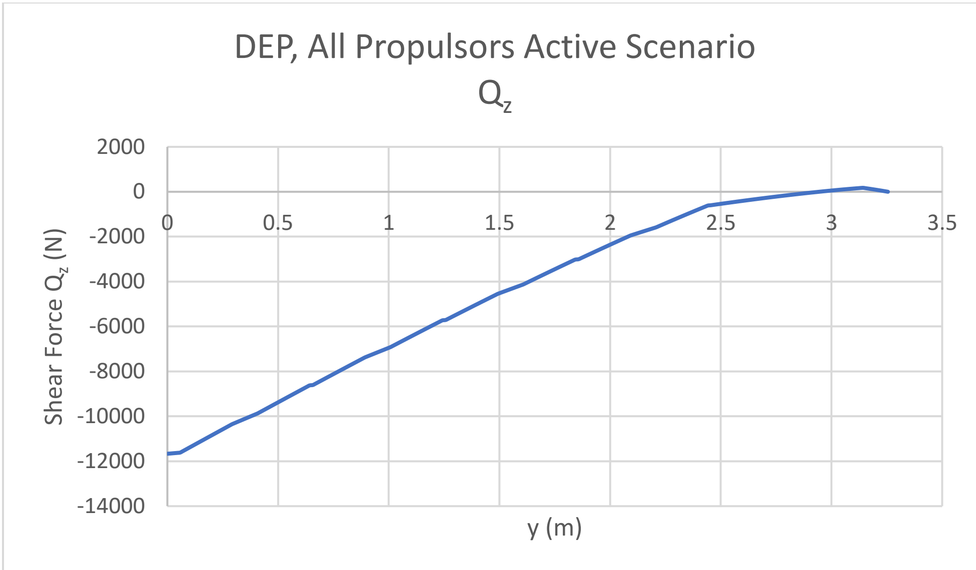

Εικόνα 90: Analysis 2 Shear Force Qz

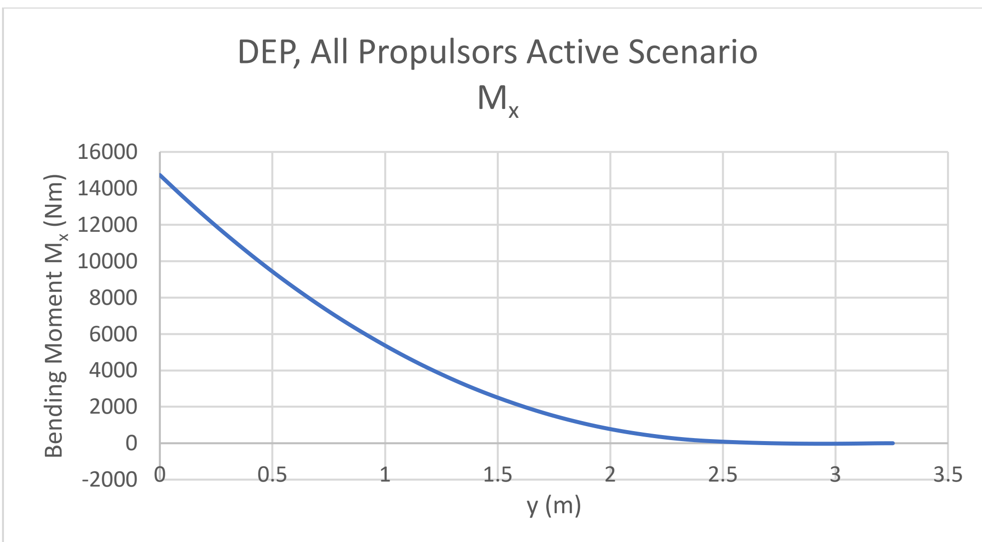

Εικόνα 91: Analysis 2 Bending Moment Mx

The Lift Force at the wing root must be equal to the aircraft's half weight, as a validation. The Lift Force is equal to $L = 15041\ N$. Dividing it by the load factor and the gravity acceleration gives $\frac{L}{ng} = \frac{15041\ N}{3.8 \cdot 9.81 \frac{m}{s^2}} = 403\ kg$, with the aircraft's half MTOW being equal to 400kg.

The airfoil max drag coefficient is obtained from [16], while the wing drag coefficient is equal to:

$$C_{D,airfoil_{max}} = 0.02306$$

$$C_{D,wing_{max}} = \frac{C_{D,airfoil_{max}}}{0.95} = 0.02427$$

The drag distribution for each section of the span $l = 3.255\ m$, regarding one of the two wings is obtained from Eq. (4.30):

The drag distribution of the **Unblown** region [0, 0.06m], [0.64m, 0.66m], [1.24m, 1.26m], [1.84m, 1.86m], [2.44m, 2.455m] is equal to:

$$D_y = \frac{1}{2} \cdot \rho \cdot V_y^2 \cdot c_y \cdot C_D = \frac{1}{2} \cdot 0.9627 \cdot 22^2 \cdot c_y^{schrenk} \cdot 0.02427 = 5.65 \cdot c_y^{schrenk} \qquad [\frac{N}{m}]$$

The drag distribution of the **High-Lift** region [0.06m, 0.64m], [0.66m, 1.24m], [1.26m, 1.84m], [1.86m, 2.44m] is equal to:

$$D_y = \frac{1}{2} \cdot \rho \cdot V_y^2 \cdot c_y \cdot C_D = \frac{1}{2} \cdot 0.9627 \cdot 62^2 \cdot c_y^{schrenk} \cdot 0.02427 = 44.9 \cdot c_y^{schrenk} \qquad [\frac{N}{m}]$$

The drag distribution of the **Cruise** region [2.455m, 3.255m] is equal to:

$$D_y = \frac{1}{2} \cdot \rho \cdot V_y^2 \cdot c_y \cdot C_D = \frac{1}{2} \cdot 0.9627 \cdot 40^2 \cdot c_y^{schrenk} \cdot 0.02427 = 18.7 \cdot c_y^{schrenk} \qquad [\frac{N}{m}]$$

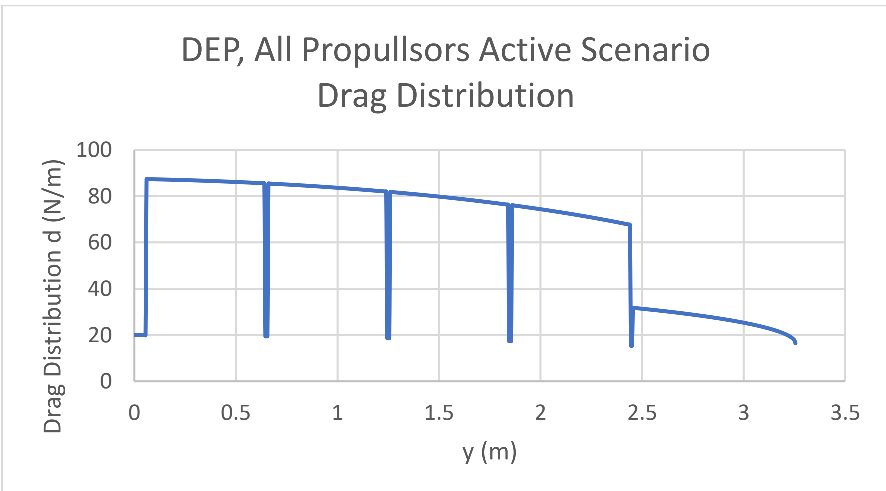

Εικόνα 92: Analysis 2 Drag Distribution d

Using the Trapezoid Rule:

$$Q_x(y) = -\int_0^{y_{tip}} D_y dy = -\sum E(D_y) \text{ where } E(D_y) = \frac{D_y^i + D_y^{i+1}}{2} h \ [N]$$

and:

$$M_z(y) = -\int_0^{y_{tip}} Q_x(y) dy = -\sum E(Q) \text{ where } E(Q) = \frac{Q_i(y) + Q_{i+1}(y)}{2} h \ [Nm]$$

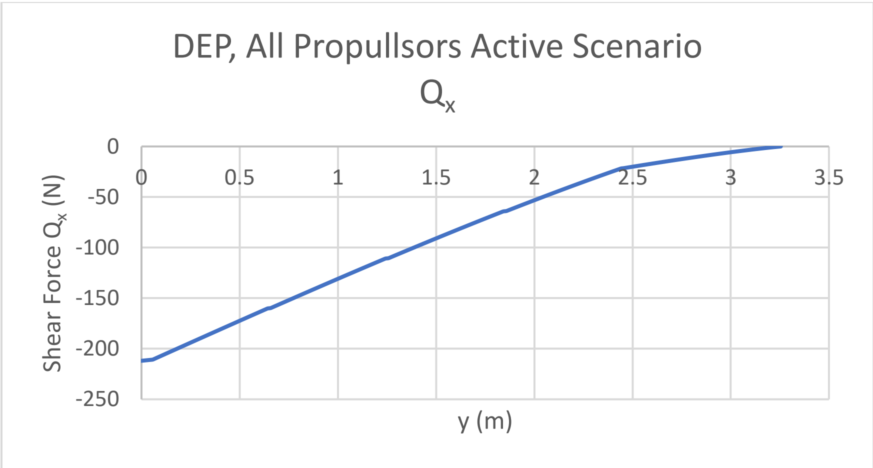

Εικόνα 93: Analysis 2 Shear Force Qx (caused by Drag)

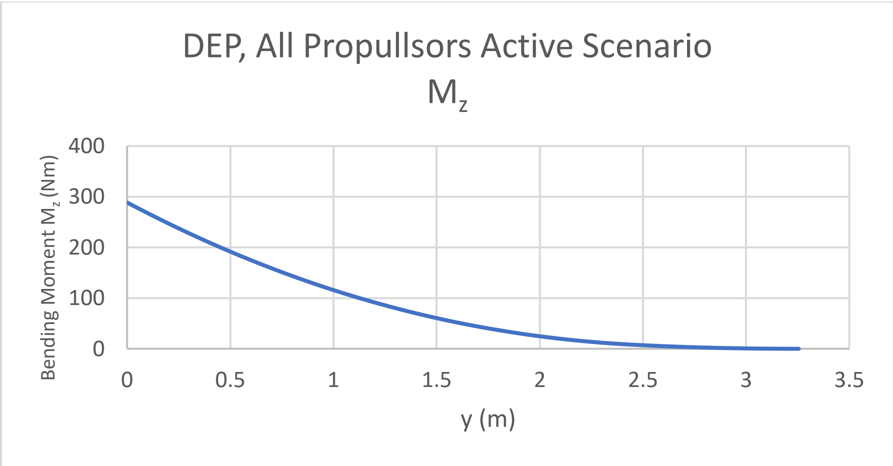

Εικόνα 94: Analysis 2 Bending Moment Mz (caused by Drag)

Comparing the Q,M figures created by Lift and Drag respectively, it is evident that the load caused by drag is significantly lower than the load caused by lift. Combined with the magnitude difference in second moments of inertia ($I_x \ll I_z$), Q_x and M_z are ignored in normal stress calculation.

4.2.2.1 Normal Stresses

Critical Cross-Section I

The maximum Shear Force and Bending Moment can be located at the wing root, where the wing is connected to the fuselage, meaning that is critical cross-section I. Hence, obtaining the data from the Excel sheet for $y = 0$:

$$\boldsymbol{Q_{z,root} = -11666\ N}$$

$$\boldsymbol{M_{x,root} = 14730\ Nm}$$

The critical cross-section I consists of the following components and depicted below:

Wing Root Spar Components			
No.	***Component***	***Thickness***	***mm***
1	Wing Root Doubler	t	3.175
2	Front Upper Spar Doubler	t	5
3	Rear Upper Spar Cap	t	5
4	Upper Extrusion Angle	t	2.5
5	Wing Spar Web	t	1
6	Bottom Spar Cap Angle	t	1.6
7	Rear Lower Spar Cap	t	5
8	Front Lower Spar Doubler	t	5

Πίνακας 19: Wing Root Spar Components (Critical Cross-Section I)

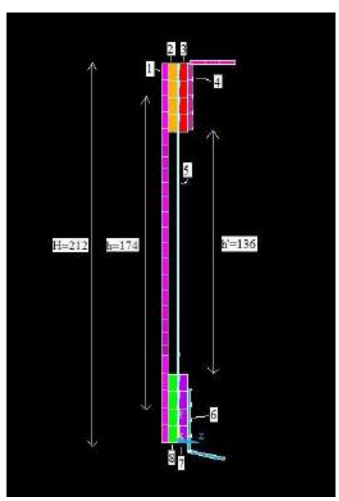

Εικόνα 95: Analysis 2 Wing Root Spar Cross-Section (Critical I)

<table>
<tr><th colspan="3">Wing Spar Component Blueprints</th></tr>
<tr><th>No.</th><th>Component</th><th>Blueprint</th></tr>
<tr><td>1</td><td>Wing Root Doubler</td><td>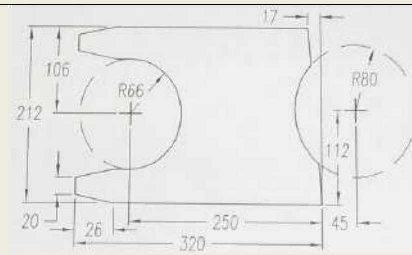
</td></tr>
<tr><td>2</td><td>Front Upper Spar Doubler</td><td>
38mm x 5mm</td></tr>
<tr><td>3</td><td>Rear Upper Spar Cap</td><td>
38mm x 5mm</td></tr>
<tr><td>4</td><td>Upper Extrusion Angle</td><td>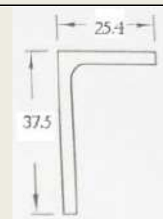
</td></tr>
<tr><td>5</td><td>Wing Spar Web</td><td>212mm x 1mm</td></tr>
<tr><td>6</td><td>Bottom Spar Cap Angle</td><td>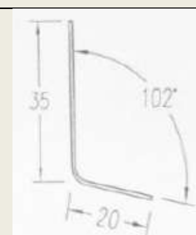
</td></tr>
<tr><td>7</td><td>Rear Lower Spar Cap</td><td>
38mm x 5mm</td></tr>
<tr><td>8</td><td>Front Lower Spar Doubler</td><td>
38mm x 5mm</td></tr>
</table>

Πίνακας 20: Analysis 2 Wing Spar Component Blueprints

The cross-section area under tensile load (upper spar cap) and under compression load (lower spar cap) are equal to:

$$F_{uf,I} = 38 \cdot (3.175 + 5 + 1 + 5) + 37.5 \cdot 2.5 + (25.4 - 2.5) \cdot 2.5 = 689.25\ mm^2$$

$$F_{lf,I} = 38 \cdot (3.175 + 5 + 1 + 5) + 35 \cdot 1.6 + (19.6 - 1.6) \cdot 1.6 = 623.45\ mm^2$$

The tensile and compression normal stresses at the critical cross-section can be obtained from Eq. (4.3):

$$\sigma_{upper,I} = \sigma_{uf} = \frac{M_{x,root}}{h \cdot F_{uf,I}} = \frac{14730\ Nm}{0.174\ m \cdot 689.25\ mm^2} = 122.8\ \frac{N}{mm^2} = 122.8\ MPa$$

$$\sigma_{lower,I} = \sigma_{lf} = \frac{M_{x,root}}{h \cdot F_{lf,I}} = \frac{14730\ Nm}{0.174\ m \cdot 623.45\ mm^2} = 135.8\ \frac{N}{mm^2} = 135.8\ MPa$$

The wing spar Web shear flow and shear stress can be obtained from Eq. (4.2) and (4.11) and are equal to:

$$q_I = \frac{Q_{z,root}}{h} = \frac{11666\ N}{174\ mm} = 67\frac{N}{mm}$$

$$\tau_I = \frac{q}{t} = \frac{Q_{z,root}}{h \cdot t} = \frac{11666\ N}{174\ mm \cdot 1\ mm} = 67\ \frac{N}{mm^2} = 67\ MPa$$

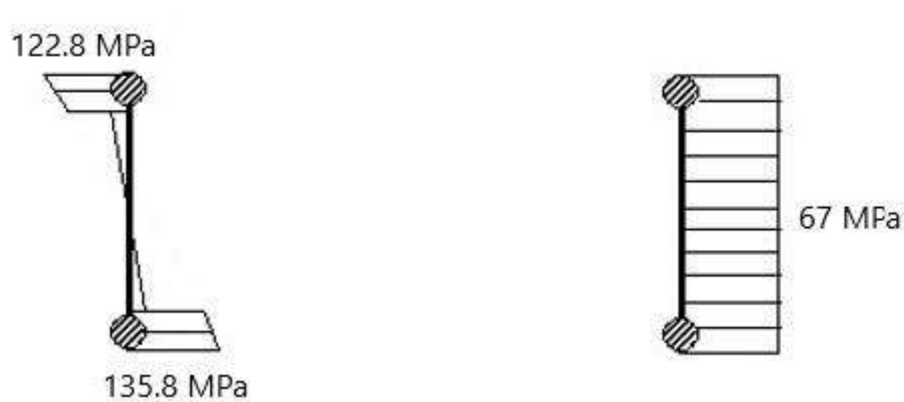

Εικόνα 96: Analysis 2 Stresses (Critical Cross-Section I)

Critical Cross-Section II

Another critical cross-section examined is where the root doubler ends. The critical cross-section II is the same compared to critical cross-section I minus the Root Doubler. It consists of the following components:

Component	***Thickness***	***mm***
Front Upper Spar Doubler	t	5
Rear Upper Spar Cap	t	5
Upper Extrusion Angle	t	2.5
Wing Spar Web	t	1
Bottom Spar Cap Angle	t	1.6
Rear Lower Spar Cap	t	5
Front Lower Spar Doubler	t	5

Πίνακας 21: Analysis 2 Wing Spar Components (Critical Cross-Section II)

The cross-section area under tensile load (upper spar cap) and under compression load (lower spar cap) are equal to:

$$F_{uf,II} = 38 \cdot (1 + 5 + 5) + 37.5 \cdot 2.5 + (25.4 - 2.5) \cdot 2.5 = 569\, mm^2$$

$$F_{lf,II} = 38 \cdot (1 + 5 + 5) + 35 \cdot 1.6 + (19.6 - 1.6) \cdot 1.6 = 502.8\, mm^2$$

The Shear Force and Bending Moment at critical cross-section II can be obtained from the Excel sheet for $y = 0.32\, m$:

$$\boldsymbol{Q_{z,II} = -10234\, N}$$

$$\boldsymbol{M_{x,II} = 11197\, Nm}$$

The tensile and compression normal stresses at the critical cross-section can be obtained from Eq. (4.3):

$$\sigma_{upper,II} = \sigma_{uf} = \frac{M_{x,II}}{h \cdot F_{uf,II}} = \frac{11197\, Nm}{0.174\, m \cdot 569\, mm^2} = 114\, \frac{N}{mm^2} = 114\, MPa$$

$$\sigma_{lower,II} = \sigma_{lf} = \frac{M_{x,II}}{h \cdot F_{lf,II}} = \frac{11197\, Nm}{0.174\, m \cdot 502.8\, mm^2} = 128\, \frac{N}{mm^2} = 128\, MPa$$

The wing spar Web shear flow and shear stress can be obtained from Eq. (4.2) and (4.11) and are equal to:

$$q_{II} = \frac{Q_{z,II}}{h} = \frac{10234\ N}{174\ mm} = 58.8 \frac{N}{mm}$$

$$\tau_{II} = \frac{q}{t} = \frac{Q_{z,II}}{h \cdot t} = \frac{10234\ N}{174\ mm \cdot 1\ mm} = 58.8\ \frac{N}{mm^2} = 58.8\ MPa$$

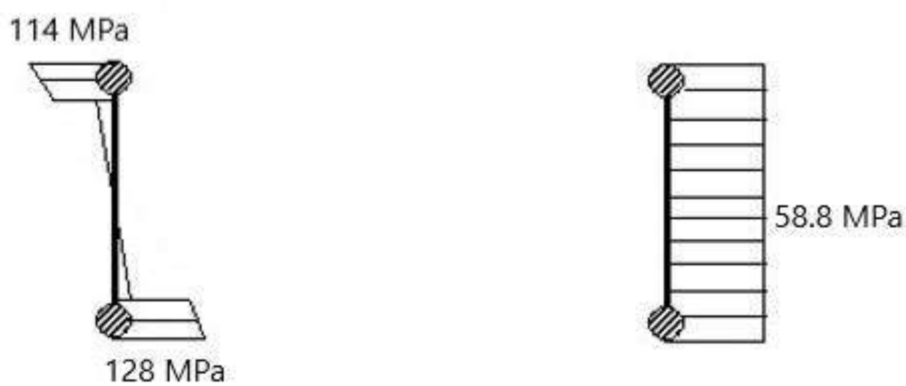

Εικόνα 97: Analysis 2 Stresses (Critical Cross-Section II)

Critical Cross-Section III

Another critical cross-section examined is where the spar doublers end. The critical cross-section III is the same compared to critical cross-section I minus the Root Doubler and the Front Upper and Front Lower Spar Caps. It consists of the following components:

Component	***Thickness***	***mm***
Rear Upper Spar Cap	t	5
Upper Extrusion Angle	t	2.5
Wing Spar Web	t	1
Bottom Spar Cap Angle	t	1.6
Rear Lower Spar Cap	t	5

Πίνακας 22: Analysis 2 Wing Spar Components (Critical Cross-Section III)

The wing root spar cross-section (critical III) is depicted below:

Εικόνα 98: Analysis 2 Wing Spar Cross-Section (Critical III)

The cross-section area under tensile load (upper spar cap) and under compression load (lower spar cap) are equal to:

$$F_{uf,III} = 38 \cdot (1+5) + 37.5 \cdot 2.5 + (25.4 - 2.5) \cdot 2.5 = 379\ mm^2$$

$$F_{lf,III} = 38 \cdot (1+5) + 35 \cdot 1.6 + (19.6 - 1.6) \cdot 1.6 = 312.8\ mm^2$$

The Shear Force and Bending Moment at critical cross-section III can be obtained from the Excel sheet for $y = 1.48\ m$:

$$\boldsymbol{Q_{z,III} = -4606\ N}$$

$$\boldsymbol{M_{x,III} = 2599\ Nm}$$

The tensile and compression normal stresses at the critical cross-section can be obtained from Eq. (4.3):

$$\sigma_{upper,III} = \sigma_{uf} = \frac{M_{x,III}}{h \cdot F_{uf,III}} = \frac{2599\ Nm}{0.174\ m \cdot 379\ mm^2} = 39.4\ \frac{N}{mm^2} = 39.4\ MPa$$

$$\sigma_{lower,III} = \sigma_{lf} = \frac{M_{x,III}}{h \cdot F_{lf,III}} = \frac{2599\ Nm}{0.174\ m \cdot 312.8\ mm^2} = 47.7\ \frac{N}{mm^2} = 47.7\ MPa$$

The wing spar Web shear flow and shear stress can be obtained from Eq. (4.2) and (4.11) and are equal to:

$$q_{III} = \frac{Q_{z,III}}{h} = \frac{4606\ N}{174\ mm} = 26.5\frac{N}{mm}$$

$$\tau_{III} = \frac{q}{t} = \frac{Q_{z,III}}{h \cdot t} = \frac{4066\ N}{174\ mm \cdot 1\ mm} = 26.5\ \frac{N}{mm^2} = 26.5\ MPa$$

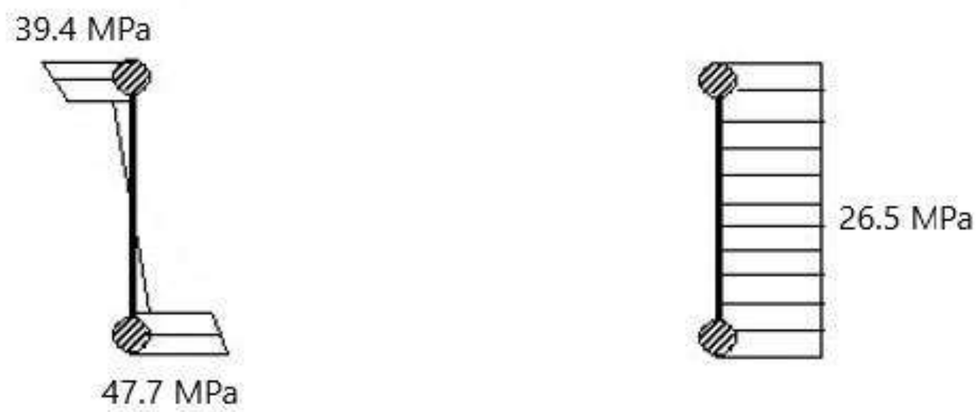

Εικόνα 99: Analysis 2 Stresses (Critical Cross-Section III)

Finally, the equivalent force of the Lift Distribution of each wing has a magnitude of $\boldsymbol{L = 15041}$ **N** at a lever arm to the fuselage axis of $\boldsymbol{y_{Lift,CoG} = 1.26 + \frac{1.12}{2} = 1.82\ m}$

4.2.2.2 Shear Stresses

The airfoil coordinates were inserted into CATIA where the program can easily calculate the desired area and distances (measuring from the airfoil leading edge).

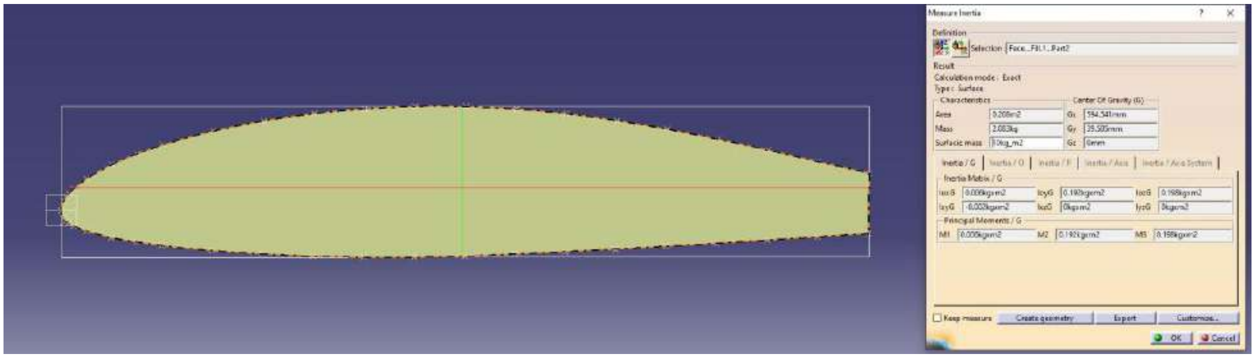

Εικόνα 100: Analysis 2 Airfoil Section CoG and Surface Area

Therefore, the wing's airfoil centroid, aerodynamic center lever arms and profile surface area are equal to:

$$x_c = 594.541\ mm = 0.594541\ m$$

$$z_c = 39.585\ mm = 0.039585\ m$$

$$d_x = x_c - \frac{c}{4} = 594.541 - 375 = 219.5\ mm = 0.2195\ m$$

$$d_z = z_c - z_{chord} = 39.585 - 0 = 39.585\ mm = 0.039585\ m$$

$$\Omega = \Omega_1 + \Omega_2 = 208\ m \cdot mm$$

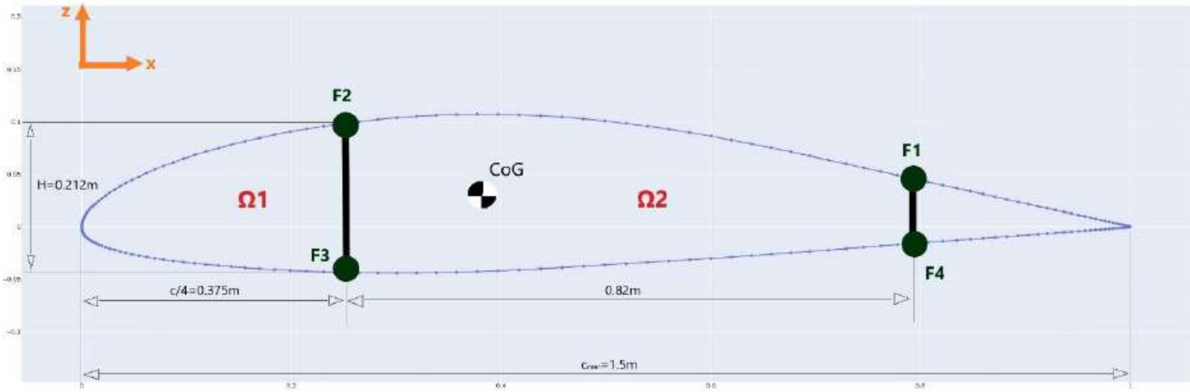

Εικόνα 101: Analysis 2 Airfoil Section for Shear Flow Calculation

Examination Point I (Wing Root, $y = 0$)

The Pitching Moment is obtained from Eq. (4.31) and is equal to:

$$M_P = \frac{1}{2}\rho V^2 S\bar{c}C_{M,wing} = \frac{1}{2}\cdot 0.9627\,\frac{kg}{m^3}\cdot 32^2\left(\frac{m}{s}\right)^2\cdot 4.8825\,m^2\cdot 1.5\,m\cdot\left(-\frac{0.088}{0.95}\right) = -334\,Nm$$

A negative value of Pitching Moment corresponds to a "nose-down" moment or a counter-clockwise direction. Additional Moments are created by loads when they are not applied to the airfoil CoG which is also the Shear Center due to the airfoil being a closed section.

The total Torsion Moment is obtained by addition of the Pitching Moment and the Moments produced by the Shear Force Q_z, the propeller Weight and electric motor Weight and the Thrust about the Shear Center (which is the same with the airfoil CoG since it is a closed section).

The total Torsion Moment is therefore equal to:

$$M_T = M_P + M' = M_P + Q_z\cdot d_x = -334\,Nm - 11666\,N\cdot 0.2195\,m = -2895\,Nm$$

$$\boldsymbol{M_T = -2895\,Nm}$$

The shear flow due to torsion can be obtained from Eq. (4.33) and is equal to:

$$q_T = \frac{M_T}{2\cdot\Omega} = \frac{-2895\,Nm}{2\cdot 208\,m\cdot mm} = -6.96\,\frac{N}{mm}$$

The assumed-open section shear flows can be obtained from Eq. (4.34). The surfaces of the wing root cross section are equal to $F_{1,I} = 113\,mm^2$, $F_{2,I} = 689.25\,mm^2$, $F_{3,I} = 623.45\,mm^2$, $F_{4,I} = 113\,mm^2$. The shear flow between surfaces F_1 and F_4 is assumed equal to zero [5], $\tilde{q}_{4-1} = 0$ and it is also calculated in the end for validation.

The shear force at examination point I is equal to $\boldsymbol{Q_z = -11666\,N}$ and the wing root airfoil cross-section's second moment of inertia can be obtained from the Shear Flow Theory [5] and is equal to:

$$I_x = F_1(z_1 - z_c)^2 + F_2(z_2 - z_c)^2 + F_3(z_3 - z_c)^2 + F_4(z_4 - z_c)^2 = 40.5\cdot 10^6\,mm^4$$

$$\tilde{q}_{4-1} = 0$$

$$\tilde{q}_{4-3} = \tilde{q}_{4-1} + \frac{Q_z}{I_x}F_3(z_3 - z_c) = 2\,\frac{N}{mm}$$

$$\tilde{q}_{3-2} = \tilde{q}_{4-3} + \frac{Q_z}{I_x}F_2(z_2 - z_c) = 20.76\,\frac{N}{mm}$$

$$\tilde{q}_{2-1} = \tilde{q}_{3-2} + \frac{Q_z}{I_x} F_1(z_1 - z_c) = -22.8 \frac{N}{mm}$$

$$\tilde{q}_{1-4} = \tilde{q}_{2-1} + \frac{Q_z}{I_x} F_4(z_4 - z_c) = -2.36 \frac{N}{mm} \simeq 0$$

The surface areas A_{i-j} are consisted of the area formed by the examined element and the reference point which in this case is the aerodynamic center. The areas A_{i-j} are calculated in CATIA and are equal to $A_{1-2} = 0.082\, m^2$, $A_{2-3} = 0.057\, m^2$, $A_{3-4} = 0.032\, m^2$, $A_{4-1} = 0.037\, m^2$.

$$q_0 = -\frac{A_{1-2}\tilde{q}_{1-2} + A_{2-3}\tilde{q}_{2-3} + A_{3-4}\tilde{q}_{3-4} + A_{4-1}\tilde{q}_{4-1}}{A_{1-2} + A_{2-3} + A_{3-4} + A_{4-1}} = 3 \frac{N}{mm}$$

The total shear flows due to shear can be obtained by superposition from Eq. (4.36):

$$q_{4-1} = q_0 = 3 \frac{N}{mm}$$

$$q_{4-3} = q_0 + \tilde{q}_{4-3} = 5 \frac{N}{mm}$$

$$q_{3-2} = q_0 + \tilde{q}_{3-2} = 23.7 \frac{N}{mm}$$

$$q_{2-1} = q_0 + \tilde{q}_{2-1} = -19.8 \frac{N}{mm}$$

The positive value of the Shear Flows refers to a clockwise direction and the negative value refers to a counter-clockwise direction (“nose down”).

The skin Shear Stress for each section can be obtained from Eq. (4.37). The skin width is equal to $t_{skin} = 0.635\, m$, hence:

$$\tau_{4-1} = \frac{q_{4-1} + q_T}{t_{skin}} = \frac{3 - 6.96 \frac{N}{mm}}{0.635\, mm} = -6.3 \text{ MPa}$$

$$\tau_{4-3} = \frac{q_{4-3} + q_T}{t_{skin}} = \frac{5 - 6.96 \frac{N}{mm}}{0.635\, mm} = -3 \text{ MPa}$$

$$\tau_{3-2} = \frac{q_{3-2} + q_T}{t_{skin}} = \frac{23.7 - 6.96 \frac{N}{mm}}{0.635\, mm} = 26.4 \text{ MPa}$$

$$\tau_{2-1} = \frac{q_{2-1} + q_T}{t_{skin}} = \frac{-19.8 - 6.9 \frac{N}{mm}}{0.635\, mm} = -42.2 \text{ MPa}$$

Examination Point A (High-Lift Unit 1 Axis, $y = 0.35\ m$)

The Pitching Moment is obtained from Eq. (4.31) and is equal to:

$$M_P = \frac{1}{2}\rho V^2 S\bar{c}C_{M,wing} = \frac{1}{2} \cdot 0.9627\frac{kg}{m^3} \cdot 67^2\left(\frac{m}{s}\right)^2 \cdot 4.8825\ m^2 \cdot 1.5\ m \cdot \left(-\frac{0.088}{0.95}\right) = -1465\ Nm$$

The total Torsion Moment is therefore equal to:

$$M_T = M_P + M' = M_P + Q_z \cdot d_x + W_p \cdot d_{x,p} + W_{em} \cdot d_{x,em} - T \cdot d_z \Rightarrow$$

$$M_T = -1465\ Nm - 10109\ N \cdot 0.2195\ m - 3.25\ kg \cdot 9.81\frac{m}{s^2} \cdot 0.8\ m - 3.75\ kg \cdot 9.81\frac{m}{s^2} \cdot 0.594541\ m + 618\ N \cdot 0.154585\ m \Rightarrow$$

$$\boldsymbol{M_T = -3635\ Nm}$$

The shear flow due to torsion can be obtained from Eq. (4.33) and is equal to:

$$q_T = \frac{M_T}{2 \cdot \Omega} = \frac{-3635\ Nm}{2 \cdot 208\ m \cdot mm} = -8.73\frac{N}{mm}$$

The assumed-open section shear flows can be obtained from Eq. (4.34). The surfaces of the wing root cross section are equal to $F_{1,A} = F_{1,II} = 81\ mm^2$, $F_{2,A} = F_{2,II} = 569\ mm^2$, $F_{3,A} = F_{3,II} = 502.8\ mm^2$, $F_{4,A} = F_{4,II} = 81\ mm^2$. The shear flow between surfaces F_1 and F_4 is assumed equal to zero [5], $\tilde{q}_{4-1} = 0$ and it is also calculated in the end for validation.

The shear force at examination point A is equal to $\boldsymbol{Q_z = -10109\ N}$ and the airfoil cross-section's second moment of inertia can be obtained from the Shear Flow Theory [5] and is equal to:

$$I_{x,A} = I_{x,II} = F_1(z_1 - z_c)^2 + F_2(z_2 - z_c)^2 + F_3(z_3 - z_c)^2 + F_4(z_4 - z_c)^2 = 33.3 \cdot 10^6\ mm^4$$

$$\tilde{q}_{4-1} = 0$$

$$\tilde{q}_{4-3} = \tilde{q}_{4-1} + \frac{Q_z}{I_x}F_3(z_3 - z_c) = 1.54\frac{N}{mm}$$

$$\tilde{q}_{3-2} = \tilde{q}_{4-3} + \frac{Q_z}{I_x}F_2(z_2 - z_c) = 17.5\frac{N}{mm}$$

$$\tilde{q}_{2-1} = \tilde{q}_{3-2} + \frac{Q_z}{I_x}F_1(z_1 - z_c) = -20.5\frac{N}{mm}$$

The surface areas A_{i-j} are consisted of the area formed by the examined element and the reference point which in this case is the aerodynamic center. The areas A_{i-j} are calculated in CATIA and are equal to $A_{1-2} = 0.082\,m^2$, $A_{2-3} = 0.057\,m^2$, $A_{3-4} = 0.032\,m^2$, $A_{4-1} = 0.037\,m^2$.

$$q_0 = -\frac{A_{1-2}\tilde{q}_{1-2} + A_{2-3}\tilde{q}_{2-3} + A_{3-4}\tilde{q}_{3-4} + A_{4-1}\tilde{q}_{4-1}}{A_{1-2} + A_{2-3} + A_{3-4} + A_{4-1}} = 3\,\frac{N}{mm}$$

The total shear flows due to shear can be obtained by superposition from Eq. (4.36):

$$q_{4-1} = q_0 = 3\,\frac{N}{mm}$$

$$q_{4-3} = q_0 + \tilde{q}_{4-3} = 4.6\,\frac{N}{mm}$$

$$q_{3-2} = q_0 + \tilde{q}_{3-2} = 20.5\,\frac{N}{mm}$$

$$q_{2-1} = q_0 + \tilde{q}_{2-1} = -17.4\,\frac{N}{mm}$$

The positive value of the Shear Flows refers to a clockwise direction and the negative value refers to a counter-clockwise direction ("nose down").

The skin Shear Stress for each section can be obtained from Eq. (4.37). The skin width is equal to $t_{skin} = 0.635\,m$, hence:

$$\tau_{4-1} = \frac{q_{4-1} + q_T}{t_{skin}} = \frac{2.42 - 8.73\,\frac{N}{mm}}{0.635\,mm} = -9 \text{ MPa}$$

$$\tau_{4-3} = \frac{q_{4-3} + q_T}{t_{skin}} = \frac{3.65 - 8.73\,\frac{N}{mm}}{0.635\,mm} = -6.5 \text{ MPa}$$

$$\tau_{3-2} = \frac{q_{3-2} + q_T}{t_{skin}} = \frac{16.32 - 8.73\,\frac{N}{mm}}{0.635\,mm} = 18.6 \text{ MPa}$$

$$\tau_{2-1} = \frac{q_{2-1} + q_T}{t_{skin}} = \frac{-13.86 - 8.73\,\frac{N}{mm}}{0.635\,mm} = -41.2 \text{ MPa}$$

Examination Point B (Cruise Unit Axis, $y = 3.255\ m$)

The Pitching Moment is obtained from Eq. (4.31) and is equal to:

$$M_P = \frac{1}{2}\rho V^2 S\bar{c}C_{M,wing} = \frac{1}{2}\cdot 0.9627\frac{kg}{m^3}\cdot 46^2\left(\frac{m}{s}\right)^2\cdot 4.8825\ m^2\cdot 1.5\ m\cdot\left(-\frac{0.088}{0.95}\right) = -690\ Nm$$

The total Torsion Moment is therefore equal to:

$$M_T = M_P + M' = M_P + Q_z\cdot d_x + W_p\cdot d_{x,p} + W_{em}\cdot d_{x,em} + T\cdot d_z \Rightarrow$$

$$M_T = -690\ Nm - 0\ N\cdot 0.2195\ m - 12\ kg\cdot 9.81\frac{m}{s^2}\cdot 0.8\ m - 13\ kg\cdot 9.81\frac{m}{s^2}\cdot 0.444541\ m$$
$$- 1961\ N\cdot 0.008415\ m \Rightarrow$$

$$\boldsymbol{M_T = -857\ Nm}$$

The shear flow due to torsion can be obtained from Eq. (4.33) and is equal to:

$$q_T = \frac{M_T}{2\cdot\Omega} = \frac{-857\ Nm}{2\cdot 208\ m\cdot mm} = -2\frac{N}{mm}$$

The assumed-open section shear flows can be obtained from Eq. (4.34). The surfaces of the wing root cross section are equal to $F_{1,B} = F_{1,III} = 56\ mm^2$, $F_{2,B} = F_{2,III} = 379\ mm^2$, $F_{3,B} = F_{3,III} = 312.8\ mm^2$, $F_{4,B} = F_{4,III} = 56\ mm^2$. The shear flow between surfaces F_1 and F_4 is assumed equal to zero [5], $\tilde{q}_{4-1} = 0$ and it is also calculated in the end for validation.

The shear force at examination point A is equal to $\boldsymbol{Q_z = 0\ N}$ and the airfoil cross-section's second moment of inertia can be obtained from the Shear Flow Theory [5] and is equal to:

$$I_{x,B} = I_{x,III} = F_1(z_1 - z_c)^2 + F_2(z_2 - z_c)^2 + F_3(z_3 - z_c)^2 + F_4(z_4 - z_c)^2 = 21.9\cdot 10^6\ mm^4$$

$$\tilde{q}_{4-1} = 0$$

$$\tilde{q}_{4-3} = \tilde{q}_{4-1} + \frac{Q_z}{I_x}F_3(z_3 - z_c) = 0\frac{N}{mm}$$

$$\tilde{q}_{3-2} = \tilde{q}_{4-3} + \frac{Q_z}{I_x}F_2(z_2 - z_c) = 0\frac{N}{mm}$$

$$\tilde{q}_{2-1} = \tilde{q}_{3-2} + \frac{Q_z}{I_x}F_1(z_1 - z_c) = 0\frac{N}{mm}$$

The surface areas A_{i-j} are consisted of the area formed by the examined element and the reference point which in this case is the aerodynamic center. The areas A_{i-j} are calculated in CATIA and are equal to $A_{1-2} = 0.082\, m^2$, $A_{2-3} = 0.057\, m^2$, $A_{3-4} = 0.032\, m^2$, $A_{4-1} = 0.037\, m^2$.

$$q_0 = -\frac{A_{1-2}\tilde{q}_{1-2} + A_{2-3}\tilde{q}_{2-3} + A_{3-4}\tilde{q}_{3-4} + A_{4-1}\tilde{q}_{4-1}}{A_{1-2} + A_{2-3} + A_{3-4} + A_{4-1}} = 0\,\frac{N}{mm}$$

The total shear flows due to shear can be obtained by superposition from Eq. (4.36):

$$q_{4-1} = q_0 = 0\,\frac{N}{mm}$$

$$q_{4-3} = q_0 + \tilde{q}_{4-3} = 0\,\frac{N}{mm}$$

$$q_{3-2} = q_0 + \tilde{q}_{3-2} = 0\,\frac{N}{mm}$$

$$q_{2-1} = q_0 + \tilde{q}_{2-1} = 0\,\frac{N}{mm}$$

The positive value of the Shear Flows refers to a clockwise direction and the negative value refers to a counter-clockwise direction ("nose down").

The skin Shear Stress for each section can be obtained from Eq. (4.37). The skin width is equal to $t_{skin} = 0.635\, m$, hence:

$$\tau_{4-1} = \frac{q_{4-1} + q_T}{t_{skin}} = \frac{0 - 2\,\frac{N}{mm}}{0.635\, mm} = -3.1 \text{ MPa}$$

$$\tau_{4-3} = \frac{q_{4-3} + q_T}{t_{skin}} = \frac{0 - 2\,\frac{N}{mm}}{0.635\, mm} = -3.1 \text{ MPa}$$

$$\tau_{3-2} = \frac{q_{3-2} + q_T}{t_{skin}} = \frac{0 - 2\,\frac{N}{mm}}{0.635\, mm} = -3.1 \text{ MPa}$$

$$\tau_{2-1} = \frac{q_{2-1} + q_T}{t_{skin}} = \frac{0 - 2\,\frac{N}{mm}}{0.635\, mm} = -3.1 \text{ MPa}$$

4.2.2.3 Equivalent Stresses

The equivalent normal stress in the most critical cross-section, therefore the upper flange of cross-section I, using the Von Mises criterion, is equal to:

$$\sigma_{eq} = \sqrt{\sigma_{max}^2 + 3\tau_{max}^2} \quad [MPa]$$

For $\sigma_{uf,I} = 122.8\ MPa$ and $t_{us,I} = -42.1\ MPa$ the equivalent Von Mises stress is equal to:

$$\sigma_{eq,I} = \sqrt{122.8^2 + 3 \cdot 42.2^2} = 143\ \ MPa$$

The Al6061-T6 Tensile Yield Strength and Shear Strength are equal to $S_{yield} = 276\ MPa$, $S_{shear} = 207\ MPa$.

$$n_I = \frac{S_y}{\sigma_{eq,I}} = \frac{276}{143} = 1.9$$

4.2.2.4 Riveting

The riveting strength study requires knowledge of the rivet type, rivet diameter and the riveting pitch. The rivet types and riveting pitch used are presented below and their diameter can be obtained from the Table below:

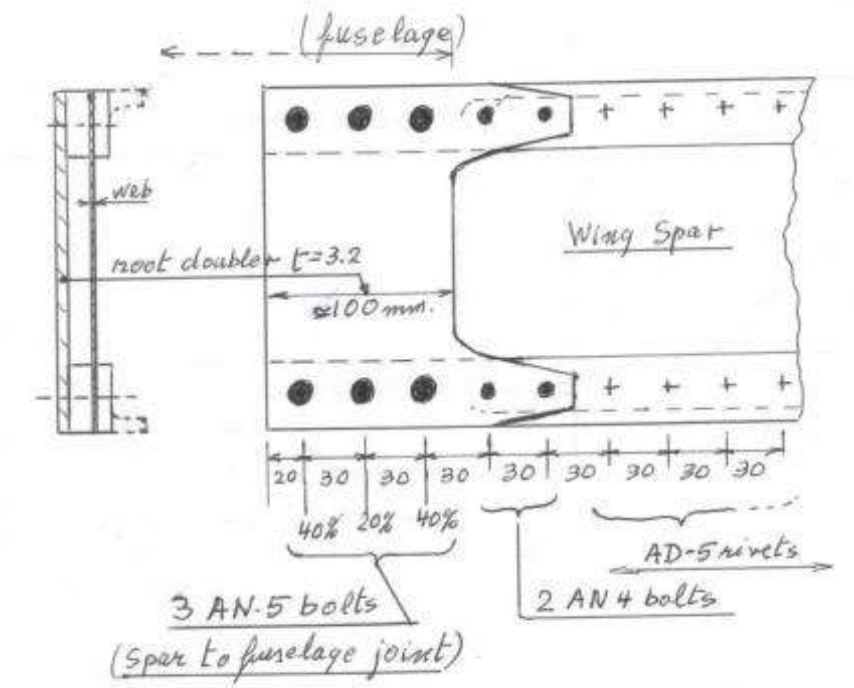

Εικόνα 102: Analysis 2 Spar Rivets at the Wing Root

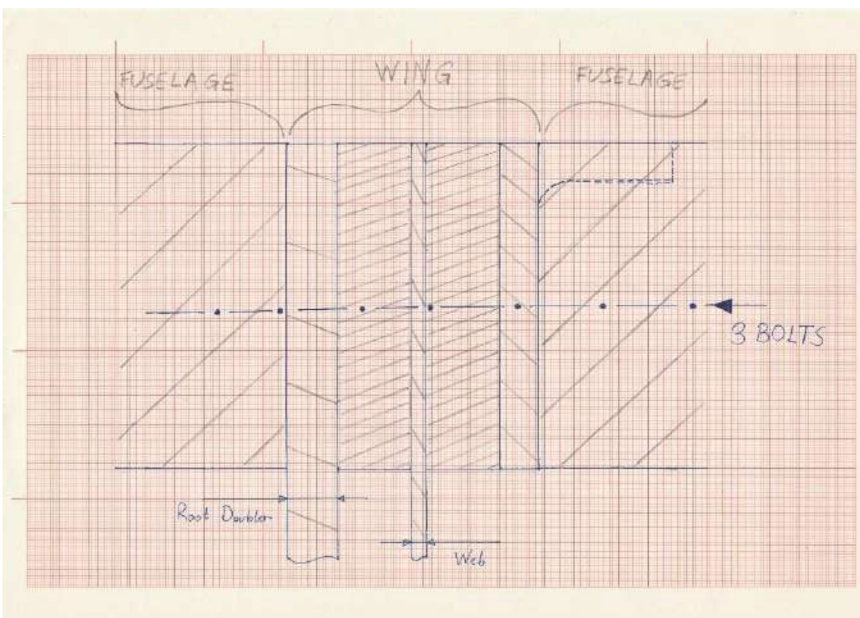

Εικόνα 103: Analysis 2 Wing-Fuselage Joint with AN-5 Bolts

Wing Root-Fuselage Joint

A Root Doubler is added to the Spar structure in the Wing-Fuselage joint. AN-5 Bolts with a diameter of $D = 8\ mm$ are used. The area S, without the Bolt holes is equal to:

$$S = (38 - 8) \cdot (3.175 + 5 + 1 + 5) = 425.25\ mm^2$$

The normal stress is obtained from Eq. (4.11) of Shear Flow Theory. The bending moment at the wing root is $M_o = 14730\ Nm$ and the normal stress is equal to:

$$\sigma = \frac{M_o}{h \cdot S} = \frac{14730\ Nm}{0.174\ m \cdot 425.25\ mm^2} = 199\ MPa$$

The applied Bolt pressure (with a safety factor of $N = 1.2$ for three bolts) is equal to:

$$p_B = \frac{q_{Bolt}}{d_{Bolt} \cdot t} = \frac{\frac{14730}{0.174}\frac{Nm}{m} \cdot 0.4}{8\ mm \cdot (3.175 + 5 + 1 + 5)\ mm} = 298.6\ MPa$$

Root Doubler-Spar Joint

The load applied to the Root Doubler is equal to:

$$q_{RootDoubler} = \frac{14730\ Nm}{0.174\ m} \cdot \frac{3.175\ mm}{(3.175 + 5 + 1 + 5 + 2.5)\ mm} = 16118.7\ N$$

This load is transferred from the front Spar Doubler to the Root Doubler through two (2) AN-4 Bolts with a diameter of $D = 6.35\ mm$. The load is applied to each Bolt is equal to:

$$q_{Bolt} = \frac{q_{RootDoubler}}{N_{AN-4}} = \frac{16118.7\ N}{2} = 8059.35\ N$$

The pressure applied in each Bolt is equal to:

$$p_B = \frac{q_{Bolt}}{d_{Bolt} \cdot t} = \frac{8059.35\ N}{6.35\ mm \cdot (3.175 + 5 + 1 + 5 + 2.5)\ mm} = 76.1\ MPa$$

Bolt diameter	3/16	1/4	5/16	3/8	7/8	1/2	inches
Designation	AN-3	-4	-5	-6	-7	-8	in inch/16
Diameter	4.8	6.3	8	9.5	11.1	12.7	mm
Ult. shear	940	1670	2600	3700	5100	6600	kg
Ult. tension	1000	1850	2900	4500	6100	8400	kg

Πίνακας 23: Analysis 2 Common Types of AN Bolts

4.2.2.5 Deflection

The wing tip deflection can be obtained from Eq. (4.40). Since the integration point 1 is $y = 0$, therefore it refers to the wing root, which is clamped to the aircraft fuselage, it is $v_1 = 0$ and $\theta_1 = 0$. The Young's elastic modulus is constant and equal to $E = 68.9\ GPa = 68.9 \cdot 10^9\ \frac{N}{m^2}$, since the material (Al6061-T6) is isotropic. The cross-section's second moment of inertia is not constant along the wingspan as the flange surfaces vary. From Eq. (4.12), the second moment of inertia is equal to $I = 2\left(\frac{h}{2}\right)^2 F_f = \left(\frac{h}{2}\right)^2 (F_{uf} + F_{lf})$. The upper flange surface is slightly larger than the respective lower flange one, thus the mean value will be used. The second moment of inertia has three different values, concerning the sections $[0,\ 0.32\ m], [0.32\ m,\ 1.48\ m]$ and $[1.48\ m,\ 3.255\ m]$. Hence:

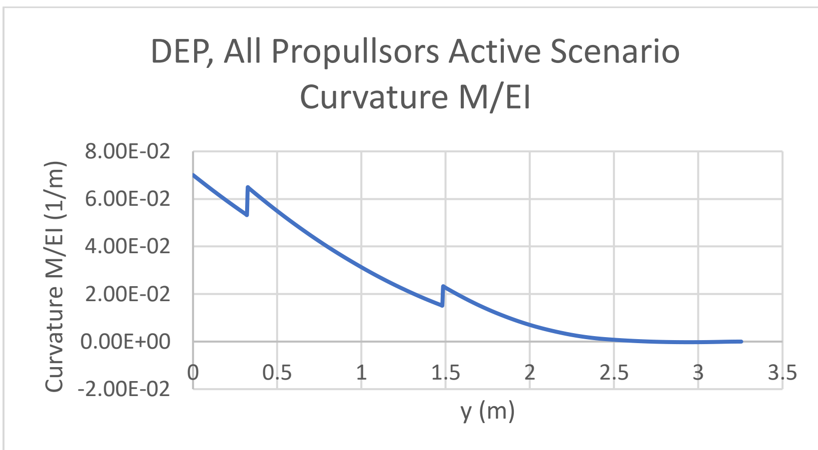

Εικόνα 104: Analysis 2 Curvature M/EI

$$v_2 = v_1 + \theta_1(y_2 - y_1) + \int_{y_1}^{y_2} \frac{M_x(y)}{E \cdot I_x(y)}(y_2 - y_1)dy$$

$$v_2 = 0 + 0 \cdot (3.255 - 0) + \int_0^{3.255} \frac{M_x(y)\ Nm}{68.9 \cdot 10^9\ \frac{N}{m^2} \cdot I_x(y)\ m^4}(3.255 - 0)m\ dy = 0.07155\ m$$

with the integration completed numerically in the Excel sheet. The wing tip deflection is therefore equal to:

$$v_{wing\ tip} = v_2 = 0.07155\ m = 71.55\ mm$$

4.2.2.6 Runway Length

In the X-57 Maxwell the unblown flapped wing max lift coefficient is equal to 2.78 whereas the blown flapped wing max lift coefficient rises to 4.95, hence a blown-to-unblown ratio of 1.78. Since the studied Zodiac CH 650 B uses a configuration with similar power, same propeller diameter etc., a more conservative blown-to-unblown ratio of 1.6 will be used. Therefore the blown flapped-wing maximum lift coefficient is equal to $C_{L,max} = 1.6 \cdot 2.61 = 4.2$

The air density at sea level is equal to $\rho = 1.225\,\frac{kg}{m^3}$ and the wing surface is equal to $S = 9.765\ m^2$. The aircraft MTOW is 800kg or 1764lbs, and the blown flapped-wing maximum lift coefficient of the DEP configuration was assumed $C_{L,max} = 4.2$

Therefore, the flaps-down stall speed is equal to:

$$L = \frac{1}{2}\rho V_{stall}^2 C_{L,max} \xRightarrow{L=W=7848N} V_{stall} = 17.6\,\frac{m}{s}\ or\ 63\,\frac{km}{h}$$

The wing loading is equal to:

$$\left(\frac{W}{S}\right)_{TO} = \frac{800kg}{9.765m^2} = 16.77\,\frac{lb}{ft^2}$$

The power-to-weight ratio is equal to:

$$\frac{HP}{W} = \frac{272HP}{800kg} = \frac{272HP}{1764lb} = 0.15\,\frac{HP}{lb}$$

The Take Off Parameter (TOP) is equal to:

$$(TOP) = \frac{(W/S)}{\sigma C_{L,max}(HP/W)} = \frac{800kg/9.765m^2}{1 \cdot 4.2 \cdot 272HP/800kg} = \frac{16.77\ lb/ft^2}{1 \cdot 4.2 \cdot 272HP/1764\ lb} = 26$$

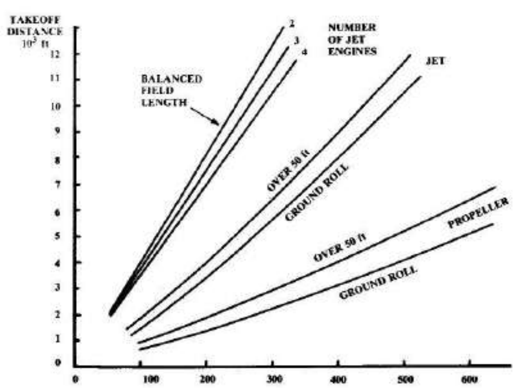

Using the graph curves we can approximate a DEP Configuration takeoff distance of $TOD_{DEP} = 350ft\ or\ 107m.$

4.2.3 Results

PERFORMANCE	**REFERENCE Configuration**	**DEP Configuration**
MTOW [kg]	600	800
Max Power [HP]	120	272
Cruise Power [HP]	120	160
Analysis Load Factor	+3.8	+3.8
Correctly Banked Turn Angle (deg)	74.74	74.74
Total Lift (with Load Factor) [N]	11217	15041
Lift Lever Arm (to Fuselage axis) [m]	2.1	1.82
Stall Speed (no flaps, with Load Factor) [km/h | knots]	195 | 105.3	115 | 62
Minimum Maneuver Radius (with Load Factor) [m | ft]	81 | 265.75	28.5 | 93.5
Stall Speed* [km/h | knots]	70 | 37.8	63 | 34
Takeoff Distance* [m | ft]	152 | 500	107 | 350

Πίνακας 24: Analysis Performance Results

**Taking into consideration the blown flapped-wing maximum lift coefficient assumption*

STRUCTURAL	**REFERENCE Configuration**	**DEP Configuration**
Max Pitching Moment (with Load Factor) [Nm]	952	1465
Max Torsion Moment (with Load Factor) [Nm]	2740	3635
Max Aerodynamic Lift (with Load Factor) [N]	11217	15041
Max Aerodynamic Drag (with Load Factor) [N]	166	223
Max Shear Force Qz [N]	8145	11666
Max Bending Moment Mx [Nm]	12449	14730
Max Shear Force Qx [N]	166	223
Max Bending Moment Mz [Nm]	247	304
Max Flange Normal Stress [MPa]	114.8	135.8
Max Web Shear Stress [MPa]	46.3	67
Max Skin Shear Stress [MPa]	32.1	42.2
Max Equivalent Stress [MPa]	118	143
Minimum Safety Factor	2.3	1.9
Wing Tip Deflection [mm]	78.4	71.55

Πίνακας 25: Analysis Structural Results

4.3 ANALYSIS ASSUMPTIONS

As far as this Thesis is concerned, several assumptions were made regarding the all-electric conversion, the configuration topology and the structural analysis. The assumptions are presented below:

- The aircraft has a trapezoidal wing planform with a straight leading edge and a tapered trailing edge. For the calculation of chord and lift distributions, the Schrenk method was used.
- The motor and propeller weights were distributed along their respective regions. Electricity power lines made from Aluminum are considered, but their weight and positioning is not taken into account.
- The reduction in weight due to liquid hydrogen use is minimal (11kg). Therefore, the aircraft weight is assumed constant (and equal to the MTOW) during the whole flight. As a result, the structural safety in reality is increased.
- The analysis was performed numerically in Excel, discretizing the wingspan in sections.
- When calculating the velocity from the lift equation for a given load factor, half of the MTOW is used since only the semispan is studied.
- In DEP configurations, where propellers create the slipstream effect, the velocity calculated from the lift equation for a given load factor is not equal to the True Aircraft Speed, due to the increase in dynamic pressure of air.
- In this particular DEP configuration the High-Lift units cover 72% of the semispan, therefore a correction in the calculated velocity from the lift equation for a given load factor must be made, to achieve the precise amount of lift produced for a given load factor.
- The slipstream rotation and thus the propeller radially-induced velocity, are not taken into account while calculating the lift distribution.
- The correctly banked turn with a given load factor takes place in a cruise altitude of 8000 feet, therefore the air density is lower than the sea level respective magnitude.

- The wingtip vortex is eliminated due to the wingtip-mounted cruise propeller. Thus, induced drag is also eliminated, and the Schrenk method can also be used to calculate the drag distribution.
- The induced drag in the original configuration is ignored due to its calculation escaping the purposes of this Thesis. Hence, the drag distribution is calculated using the Schrenk method.
- The shear force and bending moment created by the drag distribution are not taken into account during normal stress calculations, first due to drag being significantly lower compared to lift according to the airfoil lift-to-drag ratio and second due to difference in second moments of inertia of the airfoil cross-section, corresponding to the direction lift and drag are acting. Essentially, drag is a low-magnitude load acting on a direction with a high second moment of inertia, while lift is a high-magnitude load acting on a direction with a low second moment of inertia.
- The lift force is applied on the wing spar, which is located at the aerodynamic center, at 25% of the chord distance, measuring from the leading edge.
- Normal stresses (compression and tension) are not handled by the skin (upper and lower respectively), only by the wing spar.
- The wing spar flanges handle the normal stresses, while the wing spar web handles the shear stresses, both due by bending.
- The wing spar web, located between the two flanges, is flat and remains flat during bending.
- The wing spar cross-section is thin walled ($t/H < 0.1$), where t is the width and H is a characteristic dimension of the cross-section.
- The beam (wing) length is large ($t/L < 0.1$), where L is the beam length (semispan).
- During skin shear flow and stress calculations due to shear, a constant wing cross-section with a mean chord calculated from the root and tip chord values is assumed, thus not taking into account the wing taper ratio.
- The material used (Al6061-T6) is isotropic.

- The potential stream created by the vortex of the outboard-down rotating propeller adjacent flows overlapping, is ignored and has no impact on the quality of airflow interacting with the wing.
- The potential lift losses caused by the nacelles of the High-Lift units are ignored and have no impact on the quality of airflow interacting with the wing.
- The potential thermal expansion of the propeller blades is not taken into account and therefore the propeller spacing is assumed constant at all conditions.
- The horizontal correctly banked turn in the analysis corresponds to a pure roll maneuver of the aircraft, assuming that the roll and yaw maneuvers are decoupled.
- A conservative approach was made regarding the MTOW increase due to the Distributed Electric Propulsion conversion and more specifically regarding the weight of the Fuel-Cell and liquid Hydrogen storage systems.
- The nacelles housing the High-Lift and Cruise electric motors, are not considered a structural member of the wing and thus are assumed not stressed.
- The blown flapped-wing maximum lift coefficient of the DEP configuration during takeoff was assumed equal to 4.2 after using an X-57 Maxwell analogy and its blown-to-unblown max lift coefficient ratio.

5.0 WING STRUCTURAL ANALYSIS WITH COMPUTATIONAL METHOD

5.1 FINITE ELEMENT THEORY

Finite Element Methods were developed in the 1950s, due to the need for more accurate studies compared to analytical methods, and are used in a wide range of applications. In this Thesis, Finite Elements are used in the Static Analysis of the Wing.

The simplest FEA is that of a 2D truss. From the relation between forces and displacements, we can obtain the vector equation for a bar element:

$$\{P\} = [K]\{u\} \tag{5.1}$$

where P are the nodal forces and u the respective displacements. The stiffness matrix K connects forces and displacements. In a typical analysis, the forces and the stiffness matrix are known. By solving the system, the displacements are obtained and thus the strains. Forces are essentially the system's boundary conditions. The stiffness matrix K depends on the local geometry of each element, the material and the type of analysis performed.

For the 2D bar example, the steps are the following: 1) System discretization/meshing, 2) Calculation of the stiffness matrix, 3) Calculation of the bar forces, 4) Equation solving

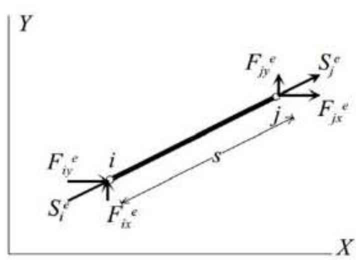

Εικόνα 105: 2D Bar Element Free Body Diagram

FEA procedure includes matrix calculations, geometrical transform implementation and requires deep understanding of each element's theoretical background. The analysis is completed by computer.

In this Thesis, the use of a commercial program is necessary, as the wing geometry is very complicated. Thus, ANSYS Workbench Structural is used for a 3D analysis utilizing three-dimensional elements.

5.2 MODELING

The software chosen to model the wing geometry was CATIA V5. The high-fidelity model of the wing was designed according to the official Zenith Zodiac CH 650 B blueprints.

Simple components were designed in CATIA's Part Design environment, while most components were designed in CATIA's Aerospace Sheet Metal Design environment, utilizing the very useful Flange feature. The Nose, Upper and Lower Skin were designed in CATIA's Generative Shape Design environment, utilizing surfaces. The Nose and Rear Ribs' curves were created by inserting blueprint coordinate points to CATIA using macro-commands in Excel.

The design sequence of the wing assembly was divided to:

- **Component Design**, i.e. Spar Web, Extrusion Angle, Hat Stiffener, Rear Ribs 1-9, Nose/Upper/Lower Skin etc.
- **Sub-Assemblies**, i.e. Wing Spar, Nose Ribs Assembly, Rear Ribs Assembly, Rear Channel Assembly, Bolt Assemblies.
- **Wing Assembly**, i.e. correct placement of Components and constraints between Sub-Assemblies.

Upon completion of the Wing Assembly, the CAT Product was saved as an STP file, which is compatible and can be inserted in ANSYS Workbench in "Geometry".

The modeled geometry corresponds to the left wing of Zenith Zodiac CH 650 B and is depicted below:

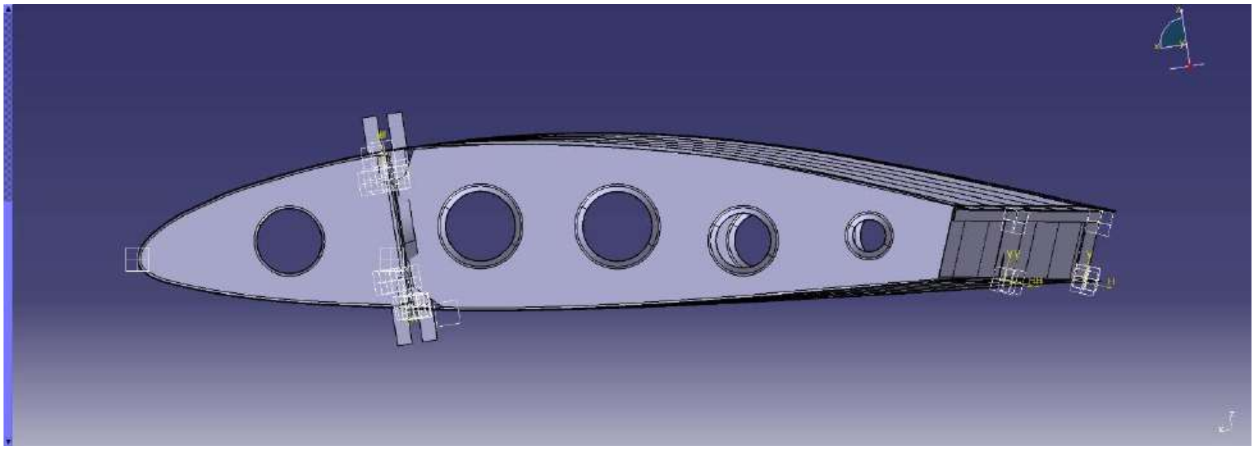

Εικόνα 106: Wing Isometric View in CATIA (Hidden Skin, Hidden Edges)

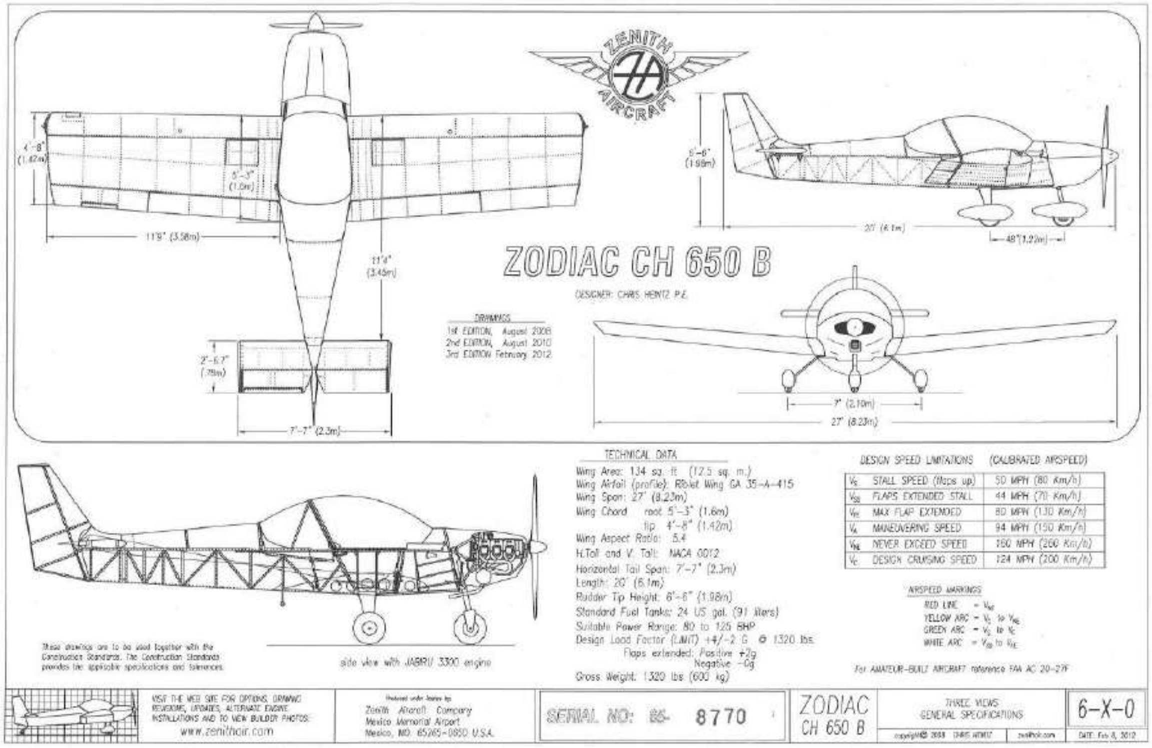

Εικόνα 107: Zenith Zodiac CH 650 B Three Views Blueprint

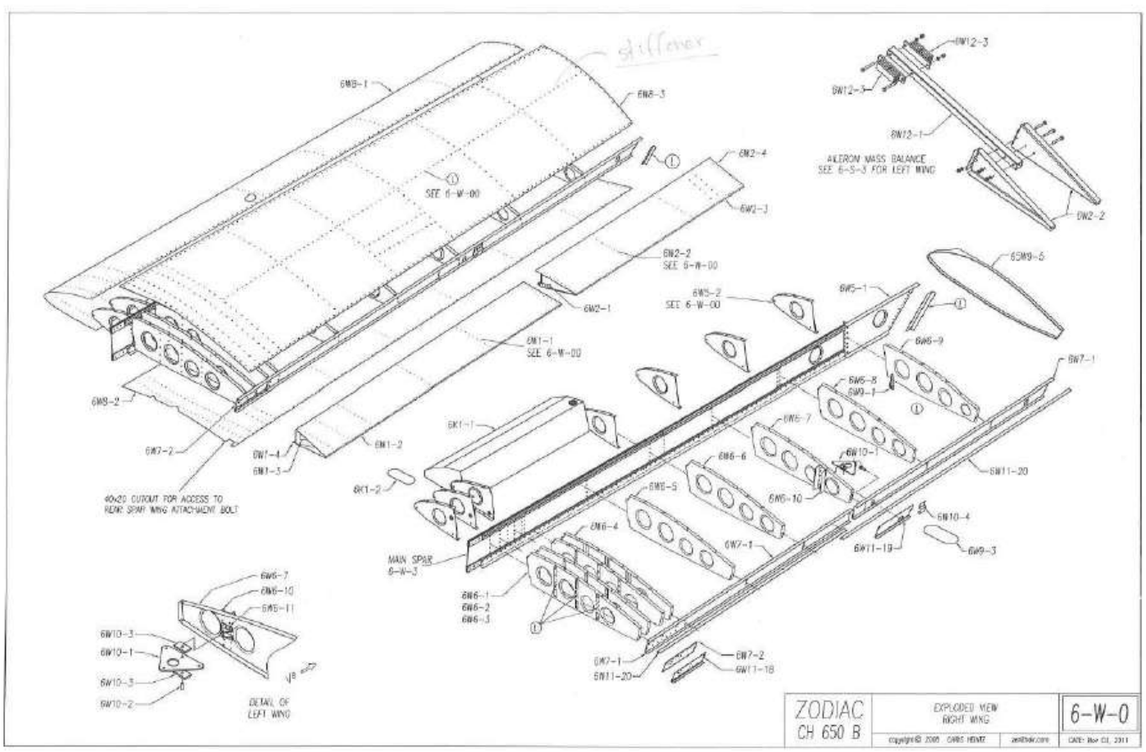

Εικόνα 108: Zenith Zodiac CH 650 B Wing Structure Blueprint

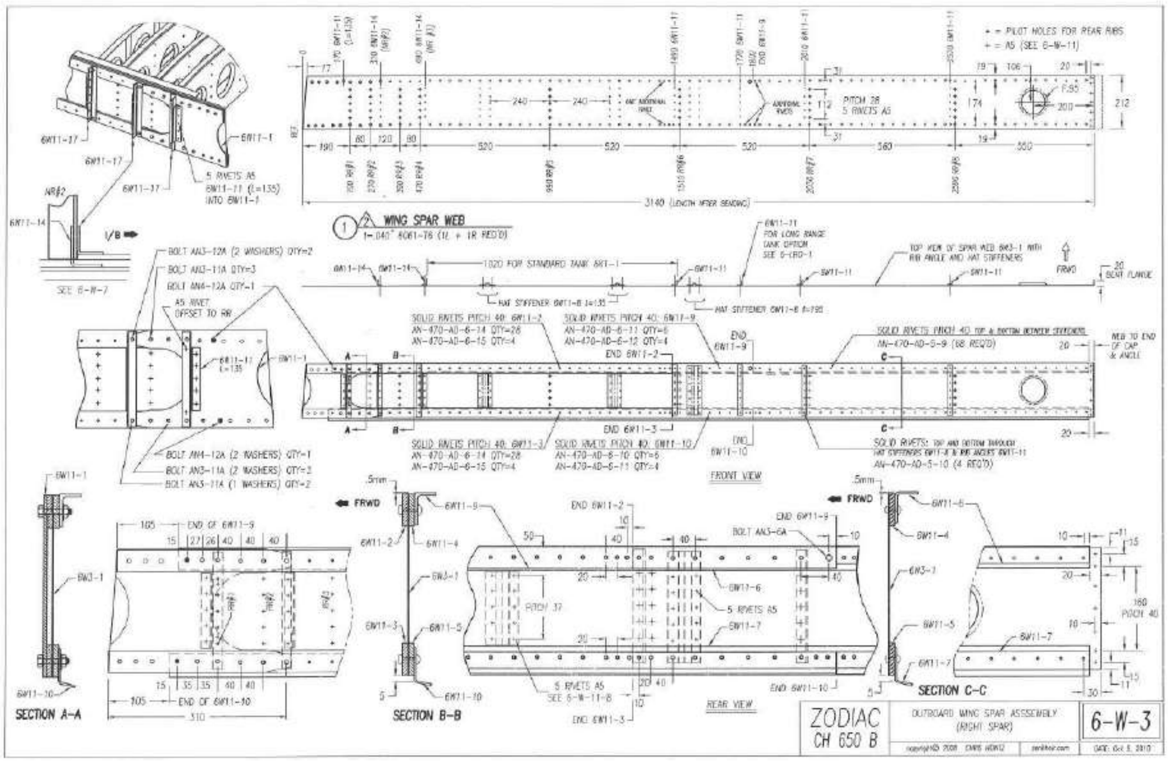

Εικόνα 109: Zenith Zodiac CH 650 B Wing Spar Blueprint

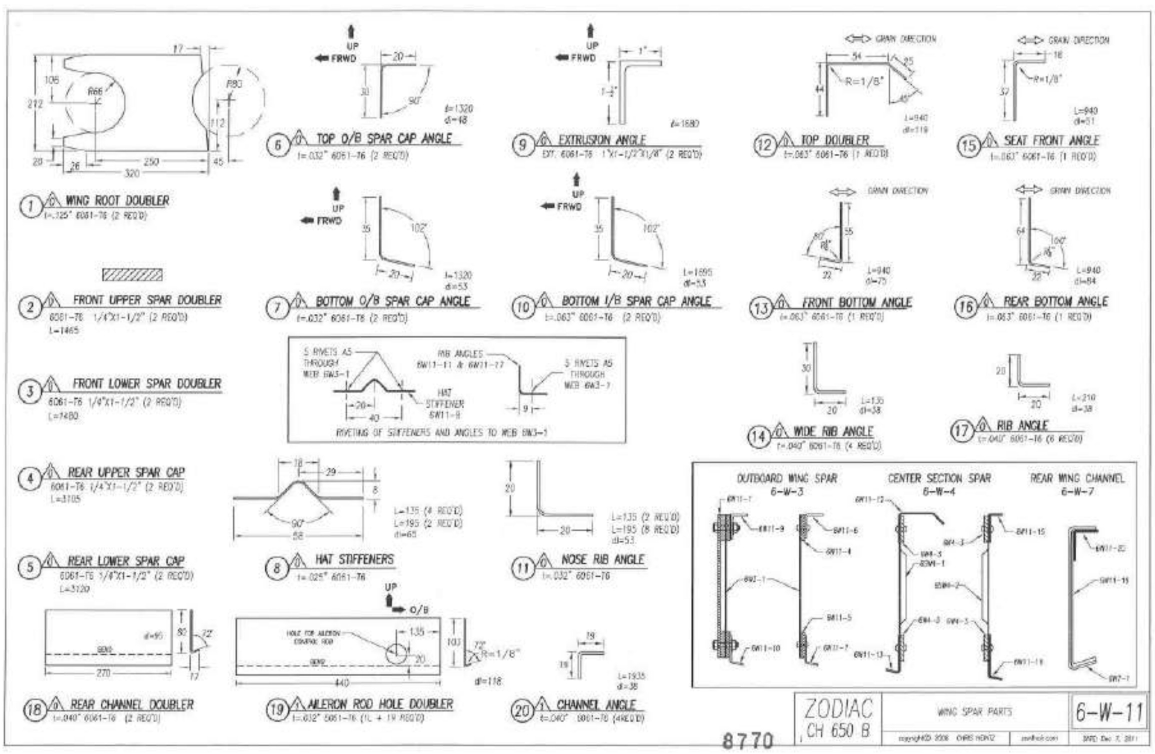

Εικόνα 110: Zenith Zodiac CH 650 B Wing Spar Parts Blueprint

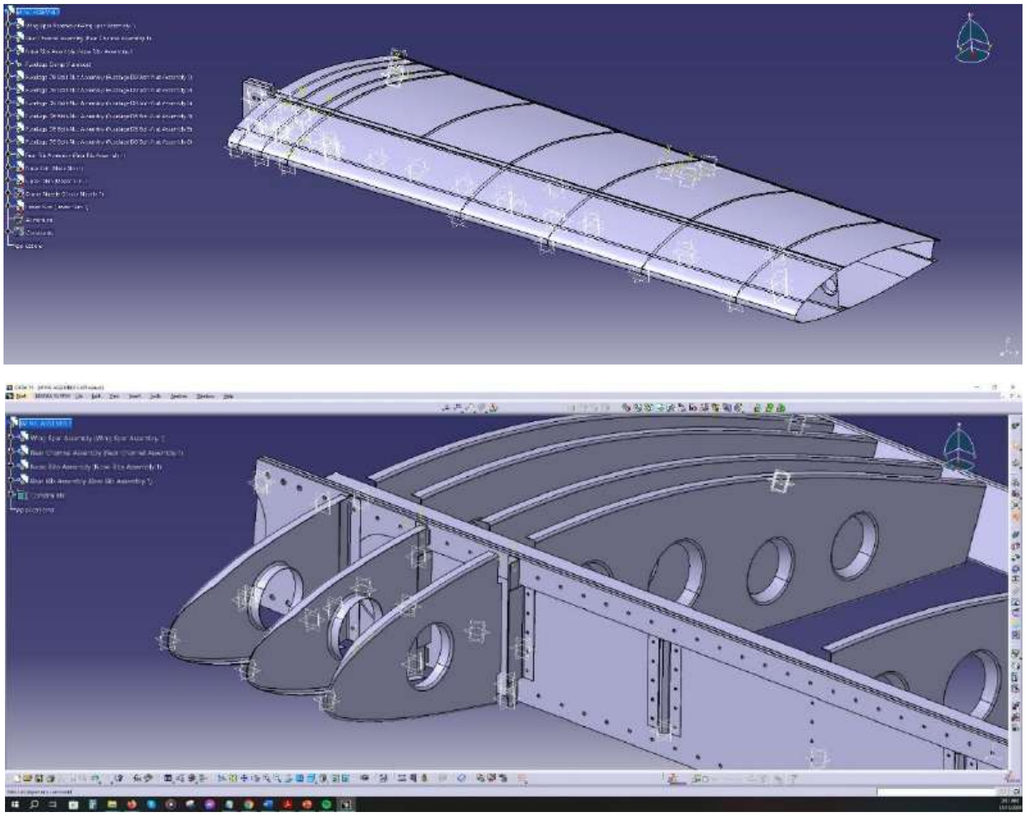

Εικόνα 111: Wing Views in CATIA (Visible Edges)

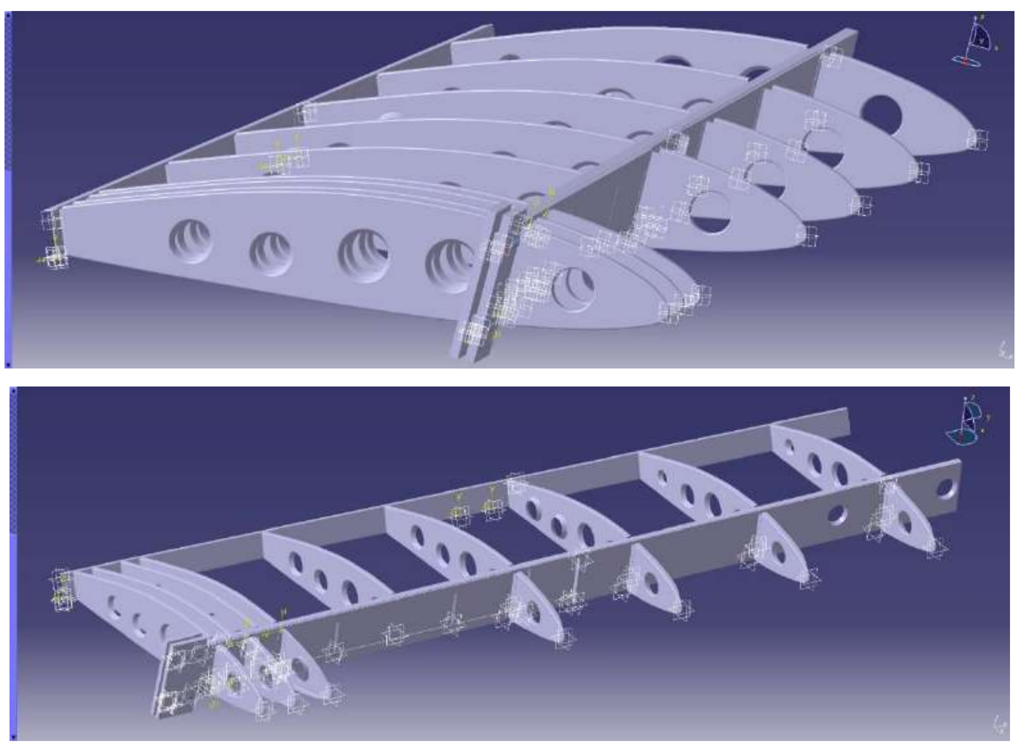

Εικόνα 112: Wing Inner Structure in CATIA (Hidden Skin, Hidden Edges)

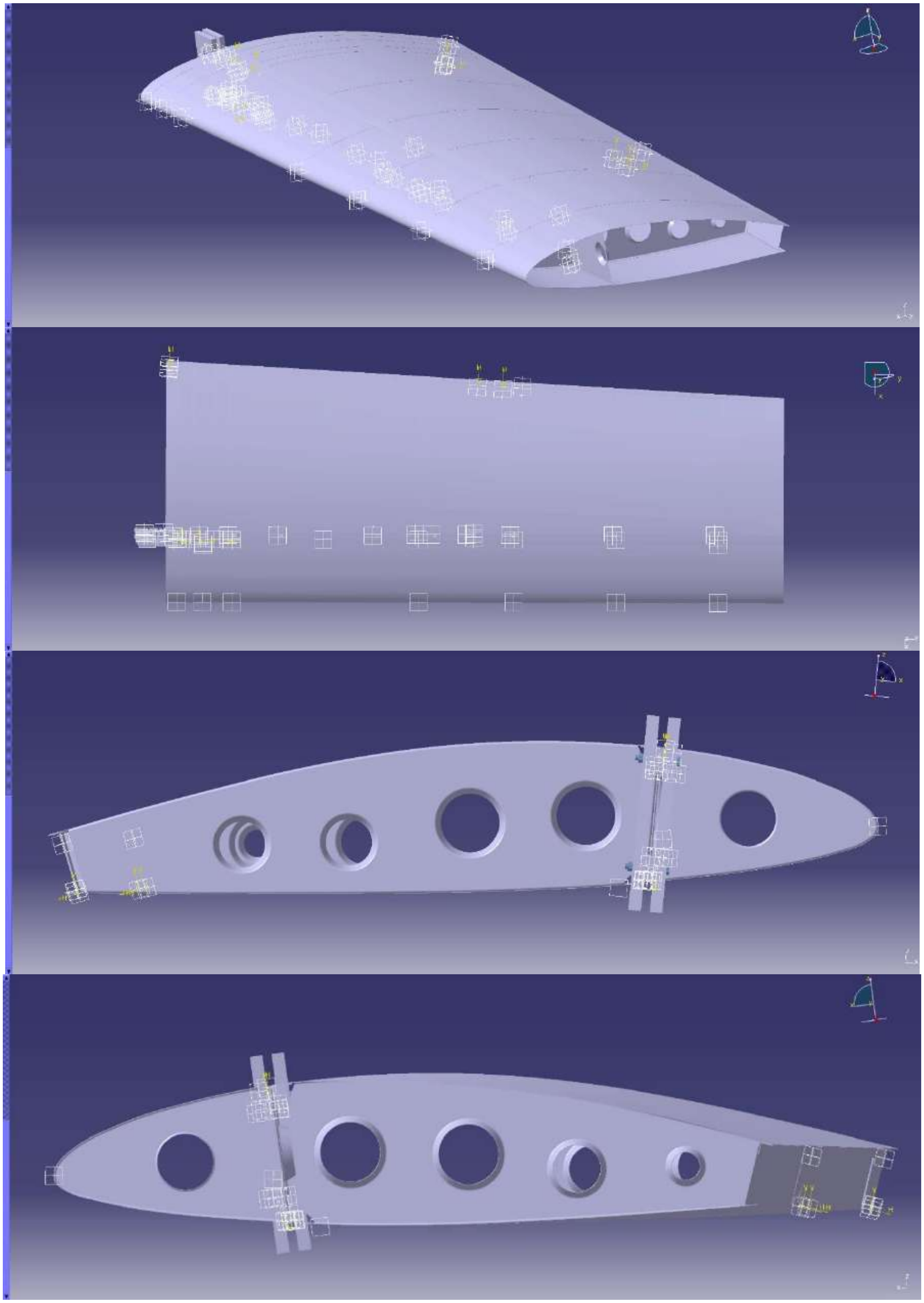

Εικόνα 113: Wing Top, Side and Isometric Views in CATIA (Hidden Edges)

5.3 ANSYS

ANSYS Workbench is used to perform FEA. The Workbench environment is split into 7 entities:

1. Analysis Type
2. Engineering Data
3. Geometry
4. Model
5. Setup
6. Solution
7. Results

Analysis Type

A Static Structural analysis is selected.

Engineering Data

In the Engineering Data Sources Tab, the materials needed for the FEA are assigned. Structural Steel and Aluminum Alloy are selected from General. Material Properties values can be altered if needed.

Geometry

The CATIA-modeled wing geometry is saved as an STP file and inserted to ANSYS Workbench through “Import Geometry”.

Model

ANSYS Mechanical is opened. The User Interface is activated and the imported wing geometry can be seen. Many adjustments can be made from the tree.

The first task is the “Material” assignment to each body. Structural Steel is assigned to the AN-5 and AN-4 Bolts and Nuts, while Aluminum Alloy is assigned to all other bodies.

The next task is to define the faces of adjacent bodies with contact between them, as well as the type of contact. There were 399 auto-generated “Contacts” that needed to be corrected or in some cases deleted. The correction mentioned corresponds to the auto-selected faces i.e. some faces that are not connected must be unselected, as well as the type of contact. The types of contact used in this Thesis FEA are ***"rough"***, which corresponds to a simple contact and ***"bonded"***, which corresponds to a joint contact i.e. a bolt thread with a nut thread.

Then, a convenient "Coordinate System" is set, with its origin located at the center of the lower edge of the Spar Web. Y is the wingspan axis; X is the axis parallel to the fuselage axis and Z is the vertical axis. Convenient "Remote Points" will be set based on this custom Coordinate System, instead of the Global one.

Most inserted Remote Points are located at the Aerodynamic Center (X, Y, Z)=(0, Y, 60), with Y regarding the 21 points (further explained below), as well as each of the 20 wing sections' center. Remote Points are also used in different locations such as the fuel tank centroid (in the Reference analysis), as well as the high-lift and cruise units (in the DEP analysis).

The next and very important task is the "Mesh" generation. The method is set to automatic and the element order is set to program controlled. Multiple "body sizing" are inserted, each one regarding different bodies. After some trial-and-error, the element size of the Bolts is set to 10mm, the element size of Skin is set to 50mm and the element size of the remaining geometry is set to 30mm. An "edge sizing" is also inserted, and the number of divisions is set to two. This is a necessary measure in order to solve an error regarding some bodies aspect ratio, where only one element was used in more than one direction. The mesh is generated.

Finally, "Named Selections" (body and nodal) are inserted. Body Named Selections are used to select and group certain bodies i.e. the Bolts or the Spar components. Nodal Named Selections are created through individual node selection and are used to form the wing sections where the Nodal Forces (representing lift and drag) are applied.

Setup

The analysis boundary conditions must be defined. A "Fixed Support" is inserted and a total of 31 faces are selected. The selected faces regard the fuselage clamps, the spar cross-section and rear channel cross-section at the wing root.

Since the structural analysis is performed for a safety factor of $n = 3.8$, the gravitational acceleration is equal to 3.8g. Therefore an "Acceleration" with a Z component of $a = 3.8 \cdot 9.81 \frac{m}{s^2} 1000 \frac{mm}{m} = 37278 \frac{mm}{s^2}$ is inserted to improve result accuracy.

Next, the loads applied to the wing structure are defined. A “Nodal Force” with Z and X components (representing lift & drag) is applied at each wing section. In the DEP analysis, Nodal Forces with Z and X components (representing weight & thrust) are also applied at corresponding sections. A “Moment” is applied at each wing section center., utilizing the aerodynamic center Remote Points along the wingspan. In the Reference analysis, a “Remote Force” representing the fuel weight is also applied at the fuel tank centroid Remote Point.

Solution

The solver is assigned with the following calculations (regarding either the whole structure, named selections, or individual bodies: “Equivalent Stress (Von Mises)”, “Maximum Shear Stress”, “Normal Stress” (Y Axis), “Shear Stress” (XY, XZ, YZ Planes), “Total Deformation”, “Directional Deformation” (Z Axis), “Equivalent Elastic Strain”, “Structural Error”.

In order to define the magnitude of Nodal Forces and Moments applied in the ANSYS FEA, a new computational analysis was performed in Excel, where the wing was divided into a reasonable number of 20 sections. The procedure followed is exactly the same as in Chapter 4, thus discretizing wingspan y into 21 points, calculating the chord distribution and then the lift and drag and distribution in each one of them. The nodal force of each section is calculated by multiplying the section’s mean distribution (lift or drag) with Δy [15]. The moment of each section is calculated by multiplying the section’s mean pitching moment distribution with Δy.

A manual convergence study was implemented in Excel, investigating the magnitude of total Lift as a function of discrete points and comparing it to the magnitude calculated from the wing equation $L = \frac{1}{2}\rho V^2 S C_L$ and to the magnitude calculated from the 651-point division computational analysis in Excel. Since the points are inserted manually and the nodes handling the Nodal Force are selected manually, the difference of 7 N (corresponding to a 31-point division) was deemed negligible.

The studied wingspan y was therefore divided by 21 points, thus creating 20 wing sections. A Nodal Force is applied to each wing section, with its components consisting of local Lift and Drag. Moreover, a Moment is also applied to each wing section, corresponding to the local Pitching Moment.

5.3.1 Reference Configuration

The sectional Lift (yellow region), Drag (green region) and Pitching Moment (blue region) values used in Nodal Forces and Moments in the Reference analysis are depicted below in red.

The Lift component of the sectional Nodal Force is positive in Z direction and the Drag component is negative in X direction. The sectional Pitching Moments tend to rotate the wing "nose-down" and thus their direction must be carefully defined in ANSYS.

The Remote Force $W_{fuel} = -m_{fuel} \cdot g \cdot n = 32.5\, kg \cdot 9.81 \frac{m}{s^2} \cdot 3.8 = -1212\, N$ is representing the fuel weight and applied at the Remote Point named "FUEL CoG".

	y (m)	$c_{elliptical}$ (m)	$c_{trapezoid}$ (m)	$c_{schrenk}$ (m)	v (m/s)	LIFT distr. (N/m)	Sectional LIFT Force (N)	Qz (N)	E2	Mx (Nm)	DRAG distr. (N/m)	Sectional DRAG Force (N)	Qx (N)	E2	Mz (Nm)	PM distr. (Nm/m)	Sectional PM (Nm)	PM (Nm)
	0	1.90985	1.6	1.7549	54	4031.94		-10354		15081	59.79		-154		224	-342.26		879
N	0.16275	1.86149	1.59	1.7257	54	3964.90	651	-9703	-1632.1	13448	58.80	10	-144	-24.2	199	-336.57	-55.24	824
O	0.3255	1.81184	1.58	1.6959	54	3896.38	640	-9063	-1527.1	11921	57.78	9	-134	-22.6	177	-330.75	-54.30	769
	0.48825	1.76079	1.57	1.6654	54	3826.25	628	-8435	-1423.9	10497	56.74	9	-125	-21.1	156	-324.80	-53.35	716
D	0.651	1.70822	1.56	1.6341	54	3754.37	617	-7818	-1322.6	9175	55.68	9	-116	-19.6	136	-318.70	-52.36	664
E	0.81375	1.65398	1.55	1.6020	54	3680.57	605	-7213	-1223.1	7952	54.58	9	-107	-18.1	118	-312.43	-51.36	612
P	0.9765	1.59790	1.54	1.5689	54	3604.66	593	-6620	-1125.7	6826	53.46	9	-98	-16.7	101	-305.99	-50.32	562
	1.13925	1.53977	1.53	1.5349	54	3526.40	580	-6040	-1030.2	5796	52.29	9	-90	-15.3	86	-299.35	-49.26	513
-	1.302	1.47936	1.52	1.4997	54	3445.52	567	-5473	-936.8	4859	51.10	8	-81	-13.9	72	-292.48	-48.16	465
	1.46475	1.41638	1.51	1.4632	54	3361.68	554	-4919	-845.6	4013	49.85	8	-73	-12.5	60	-285.36	-47.02	418
R	1.6275	1.35047	1.5	1.4252	54	3274.47	540	-4379	-756.6	3257	48.56	8	-65	-11.2	48	-277.96	-45.84	372
E	1.79025	1.28117	1.49	1.3856	54	3183.38	526	-3853	-669.8	2587	47.21	8	-57	-9.9	38	-270.23	-44.61	327
F	1.953	1.20790	1.48	1.3439	54	3087.72	510	-3343	-585.6	2001	45.79	8	-50	-8.7	30	-262.11	-43.32	284
E	2.11575	1.12988	1.47	1.2999	54	2986.61	494	-2848	-503.8	1498	44.29	7	-42	-7.5	22	-253.53	-41.96	242
R	2.2785	1.04607	1.46	1.2530	54	2878.84	477	-2371	-424.7	1073	42.69	7	-35	-6.3	16	-244.38	-40.52	201
E	2.44125	0.95493	1.45	1.2025	54	2762.66	459	-1912	-348.5	724	40.97	7	-28	-5.2	11	-234.51	-38.97	162
N	2.604	0.85411	1.44	1.1471	54	2635.36	439	-1473	-275.4	449	39.08	7	-22	-4.1	7	-223.71	-37.29	125
C	2.76675	0.73968	1.43	1.0848	54	2492.42	417	-1056	-205.7	243	36.96	6	-16	-3.1	4	-211.58	-35.42	90
E	2.9295	0.60395	1.42	1.0120	54	2325.01	392	-664	-139.9	103	34.48	6	-10	-2.1	2	-197.36	-33.28	56
	3.09225	0.42706	1.41	0.9185	54	2110.32	361	-303	-78.6	25	31.30	5	-4	-1.2	0	-179.14	-30.64	26
	3.255	0.00000	1.4	0.7000	54	1608.25	303	0	-24.6	0	23.85	4	0	-0.4	0	-136.52	-25.69	0

Πίνακας 26: Reference FEA Sectional Lift, Drag Forces and Pitching Moments in Excel

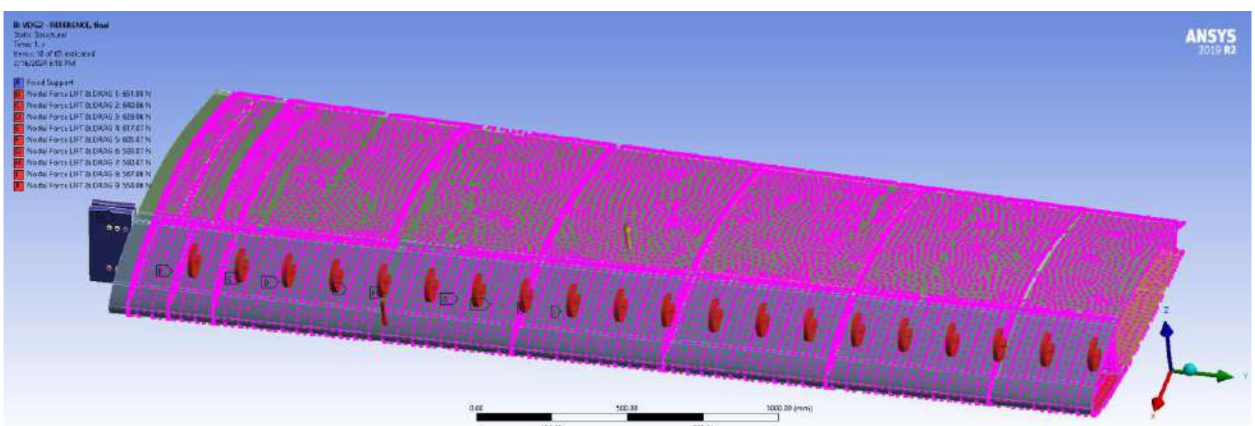

Εικόνα 114: Reference FEA ANSYS Workbench Setup (Nodal Forces, Remote Force, Moments, Fixed Support, Acceleration)

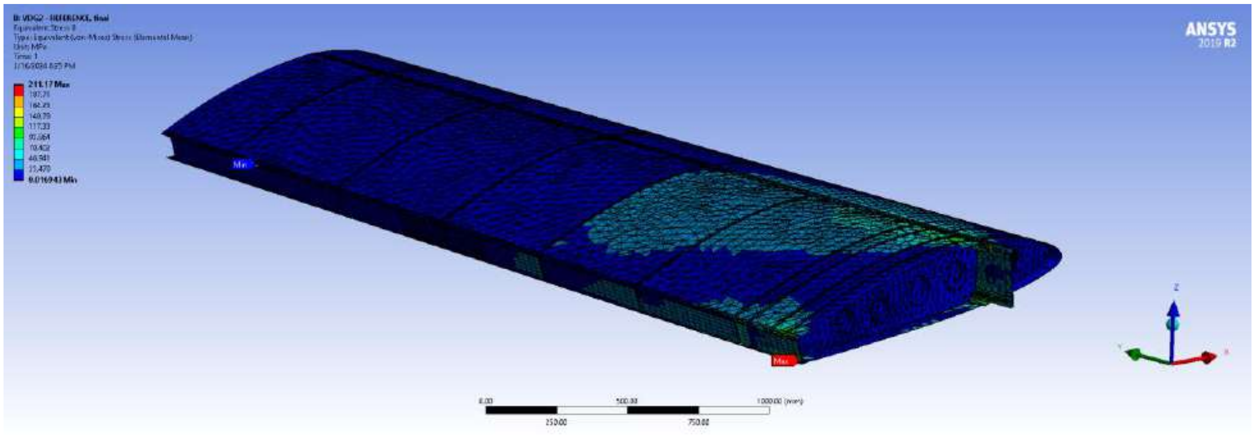

Εικόνα 115: Reference FEA Wing Equivalent Stress

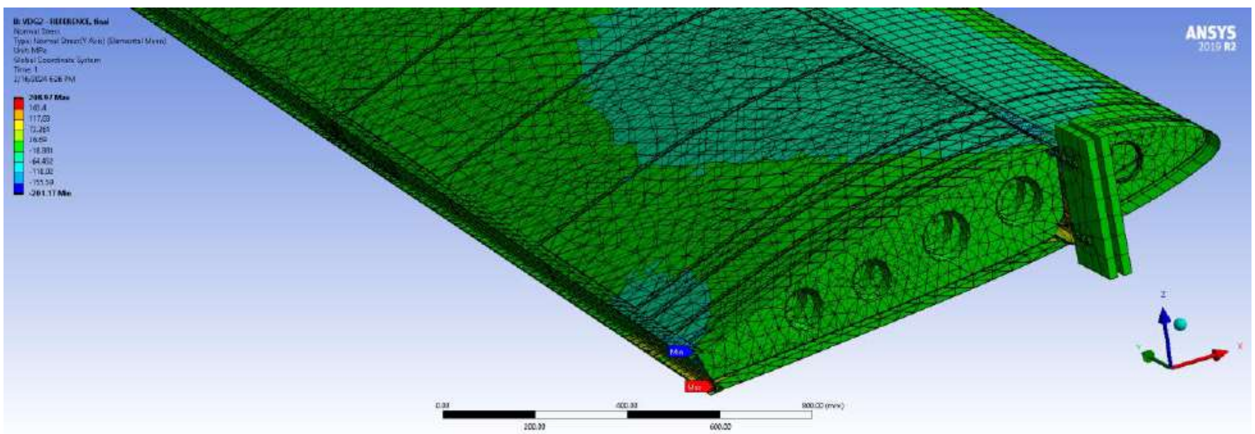

Εικόνα 116: Reference FEA Wing Normal Stress (Y Axis)

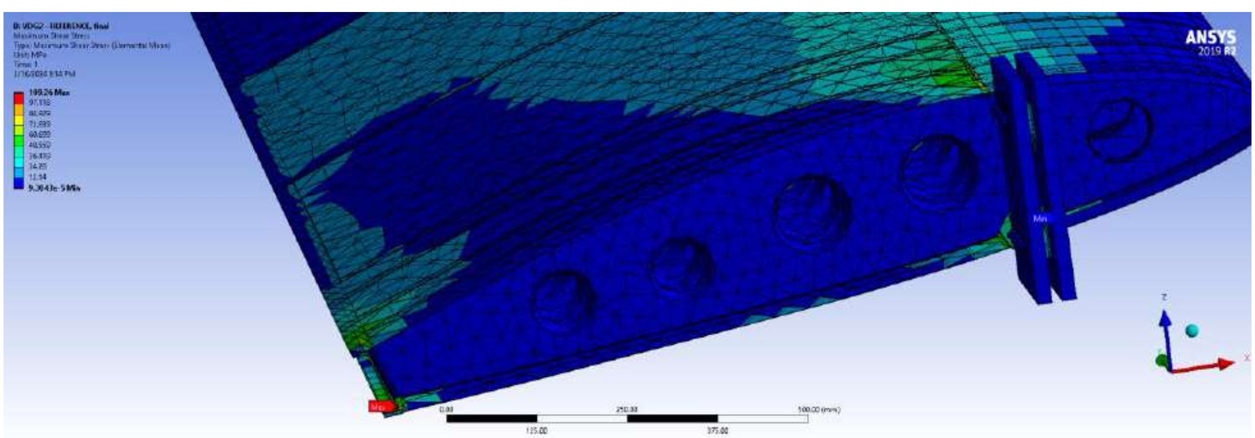

Εικόνα 117: Reference FEA Wing Maximum Shear Stress

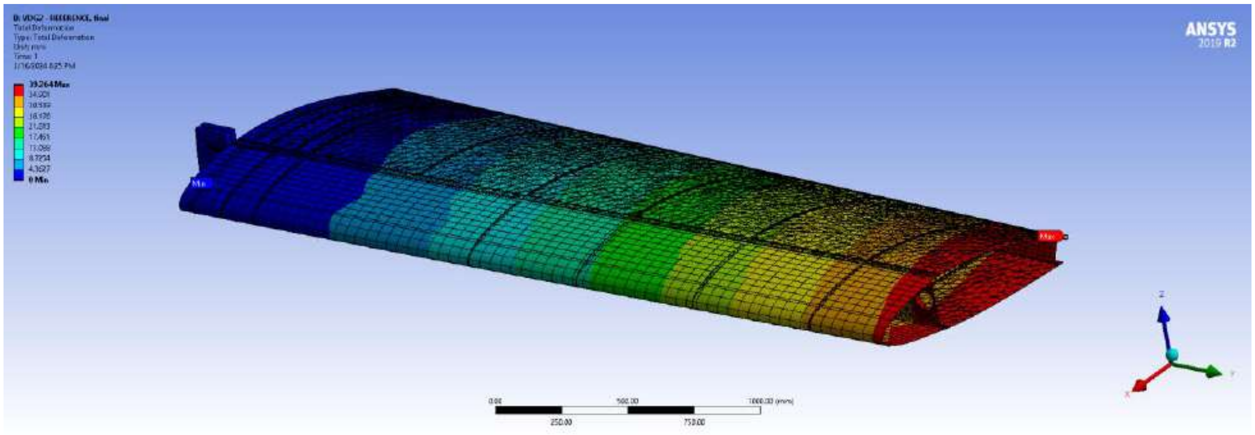

Εικόνα 118: Reference FEA Wing Total Deformation

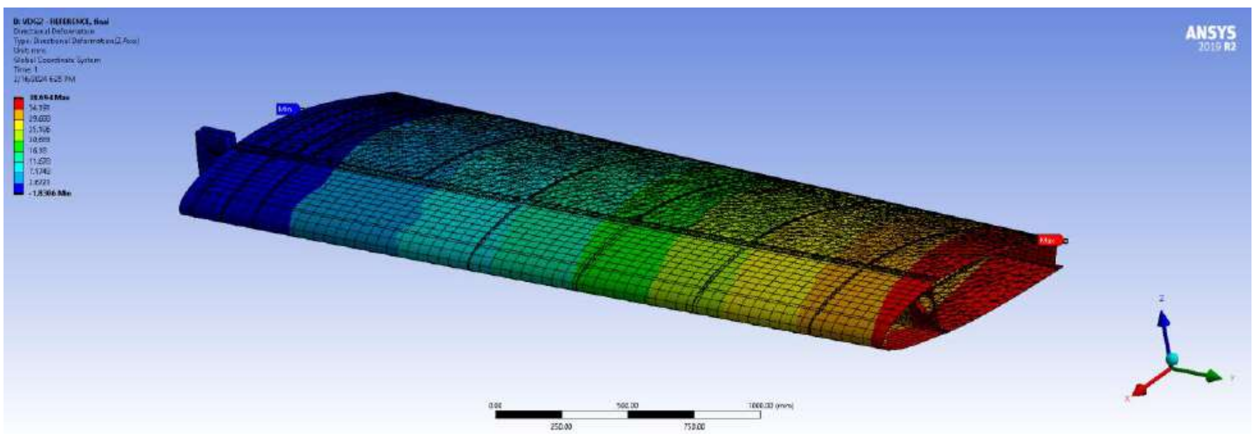

Εικόνα 119: Reference FEA Wing Directional Deformation (Z Axis)

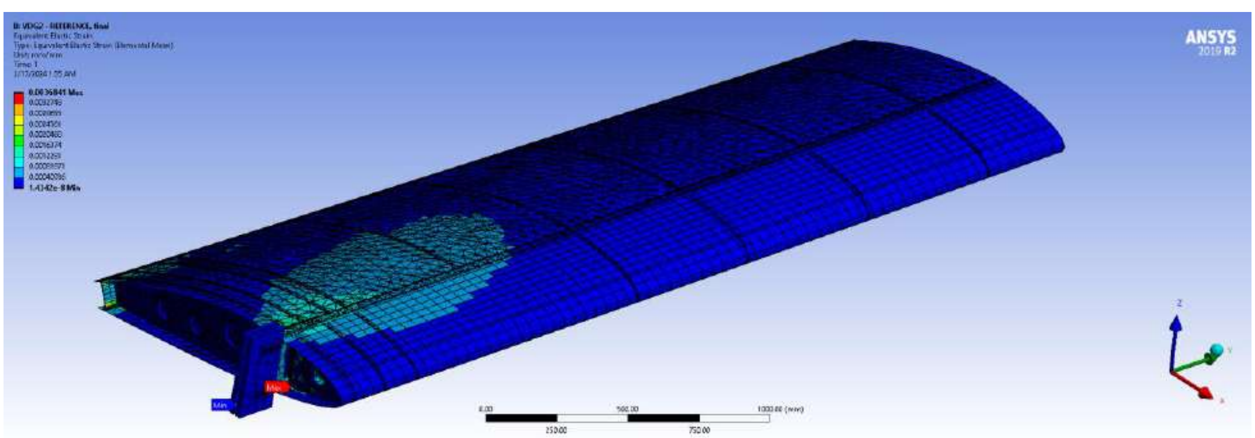

Εικόνα 120: Reference FEA Wing Equivalent Elastic Strain

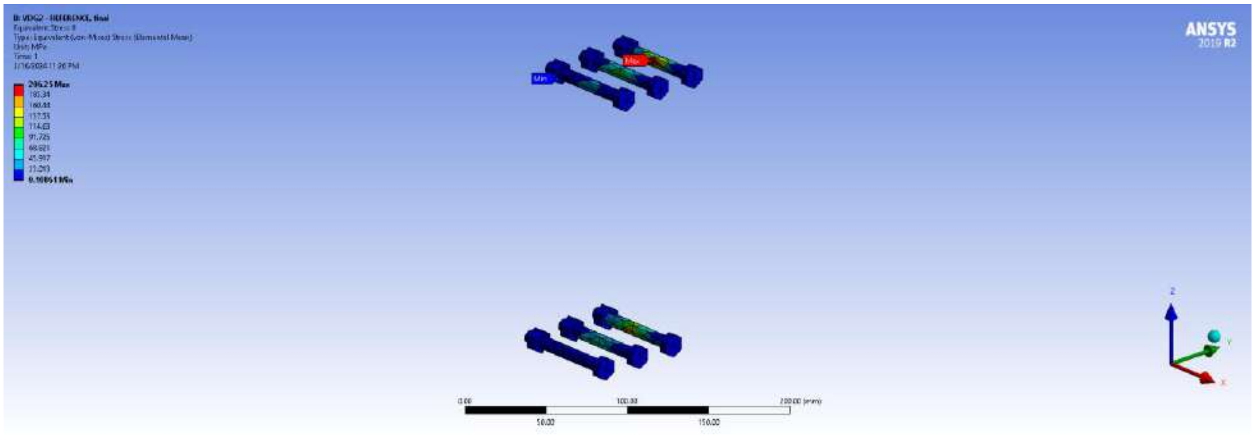

Εικόνα 121: Reference FEA AN-5 Bolts Equivalent Stress

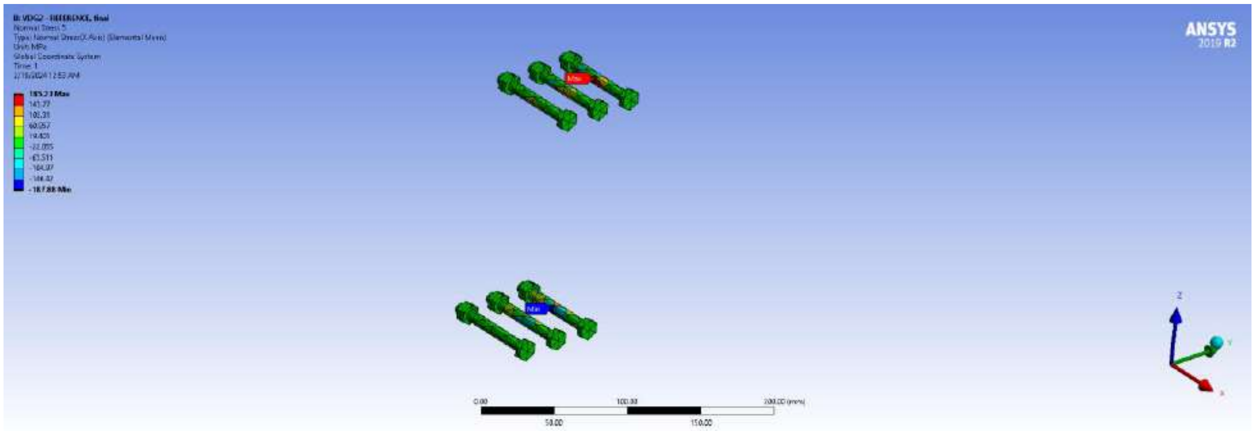

Εικόνα 122: Reference FEA AN-5 Bolts Normal Stress (X Axis)

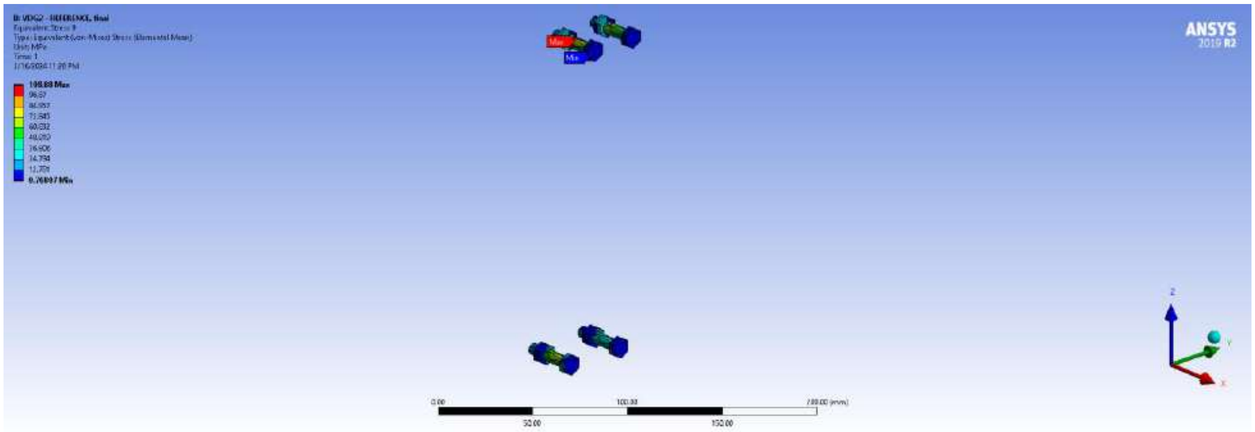

Εικόνα 123: Reference FEA AN-4 Bolts Equivalent Stress

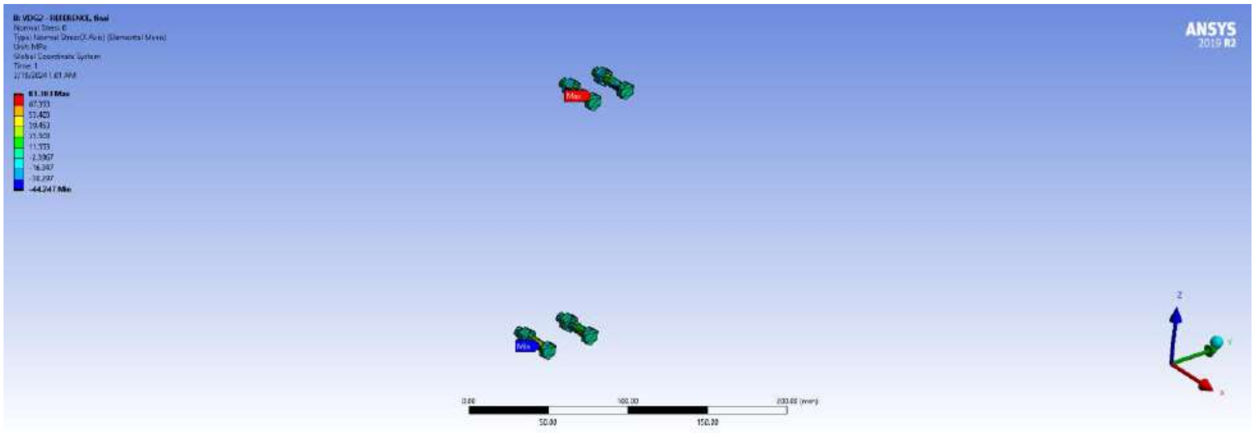

Εικόνα 124: Reference FEA AN-4 Bolts Normal Stress (X Axis)

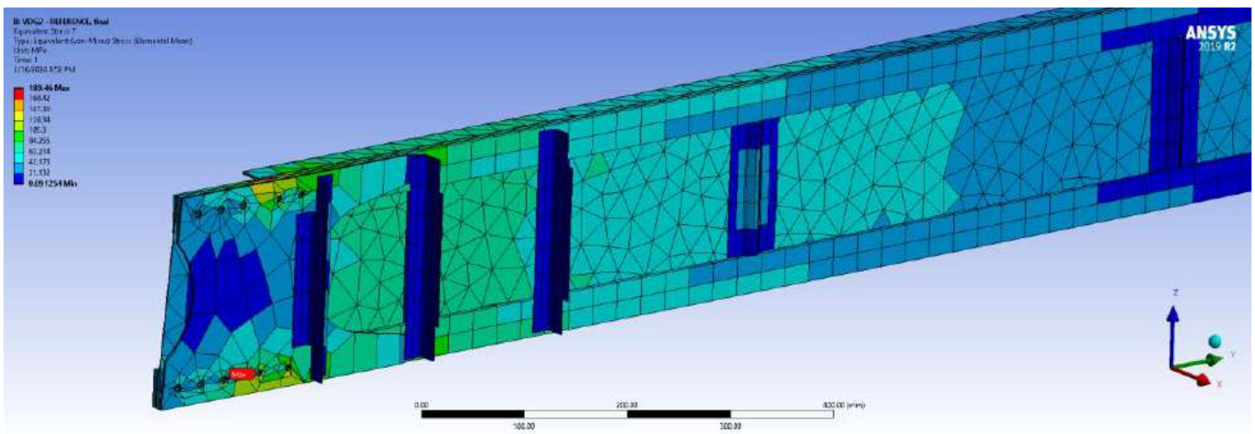

Εικόνα 125: Reference FEA Spar Equivalent Stress

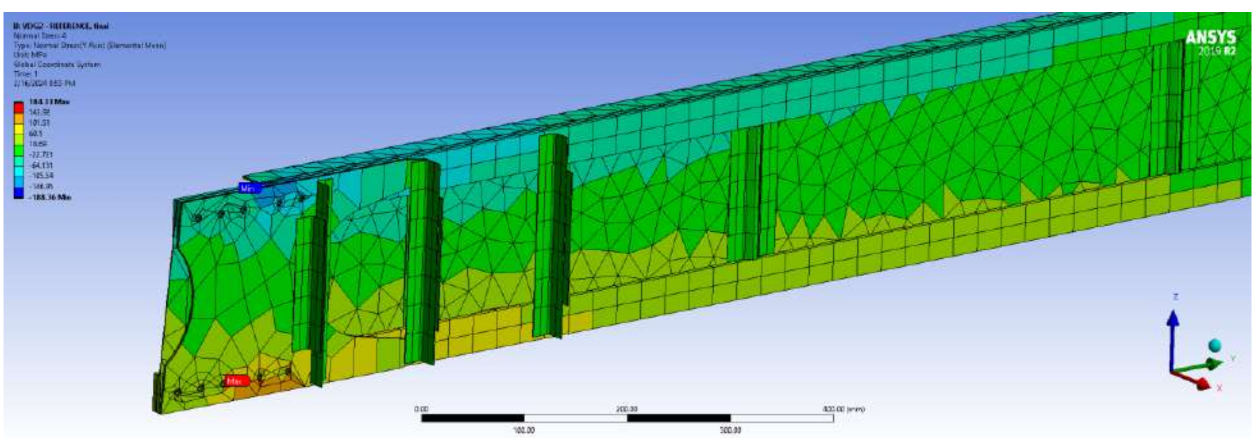

Εικόνα 126: Reference FEA Spar Normal Stress (Y Axis)

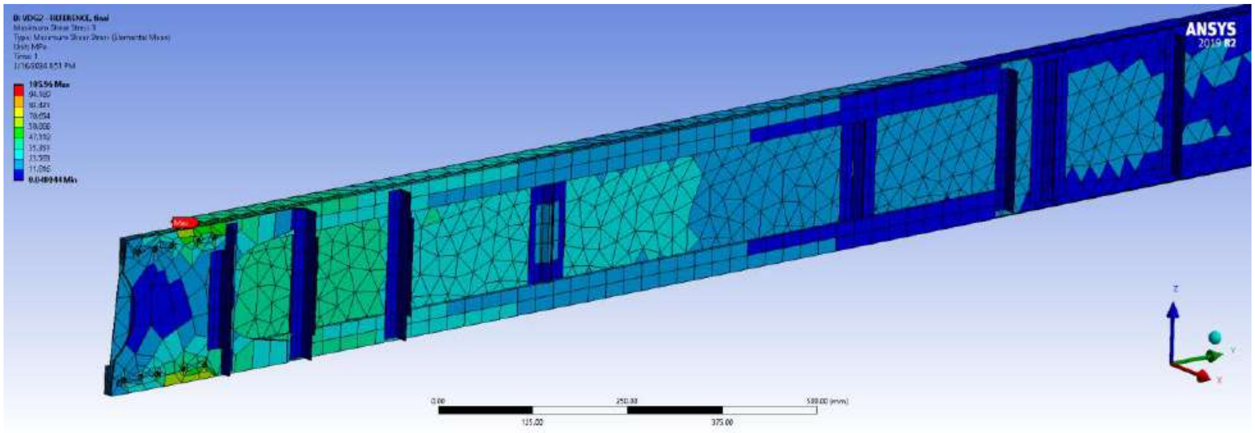

Εικόνα 127: Reference FEA Spar Maximum Shear Stress

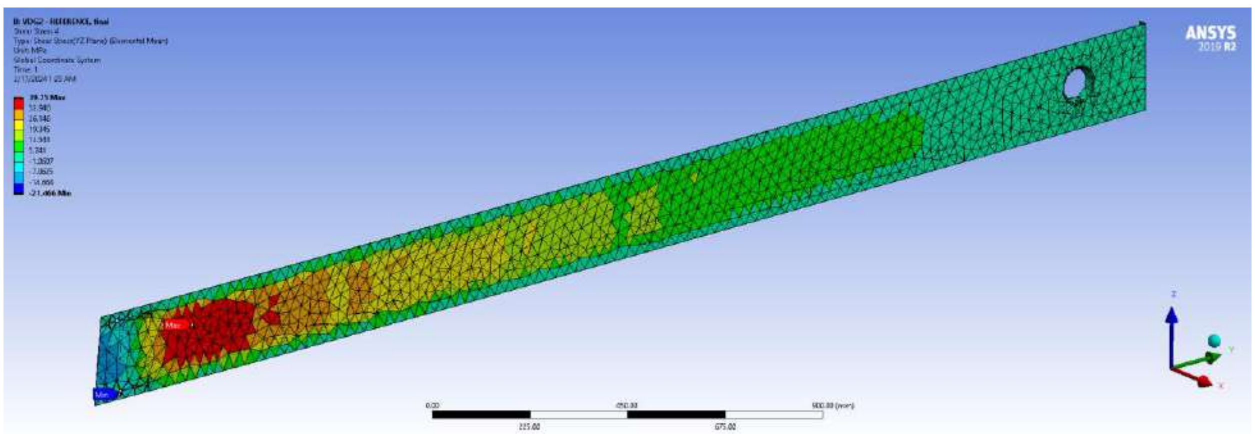

Εικόνα 128: Reference FEA Spar Web Shear Stress (YZ Plane)

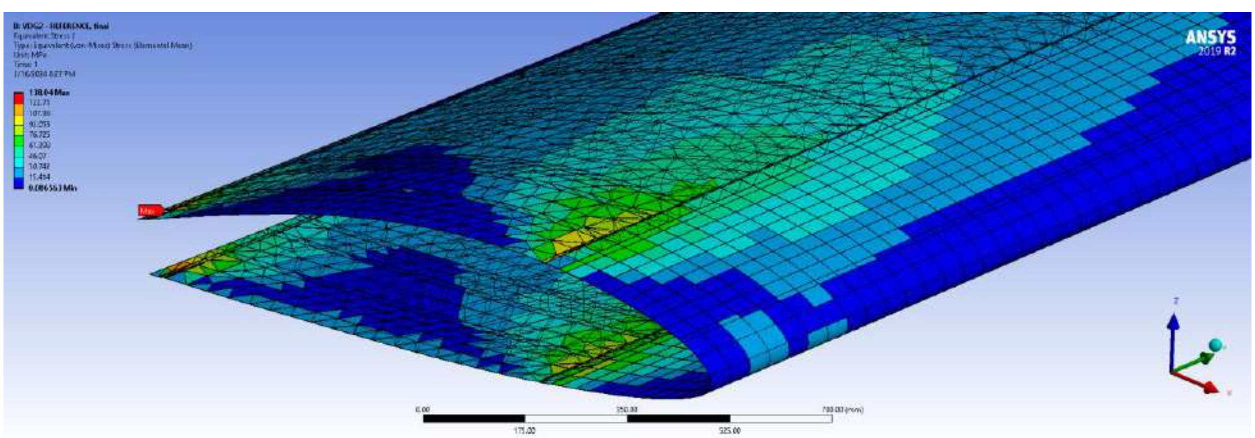

Εικόνα 129: Reference FEA Skin Equivalent Stress

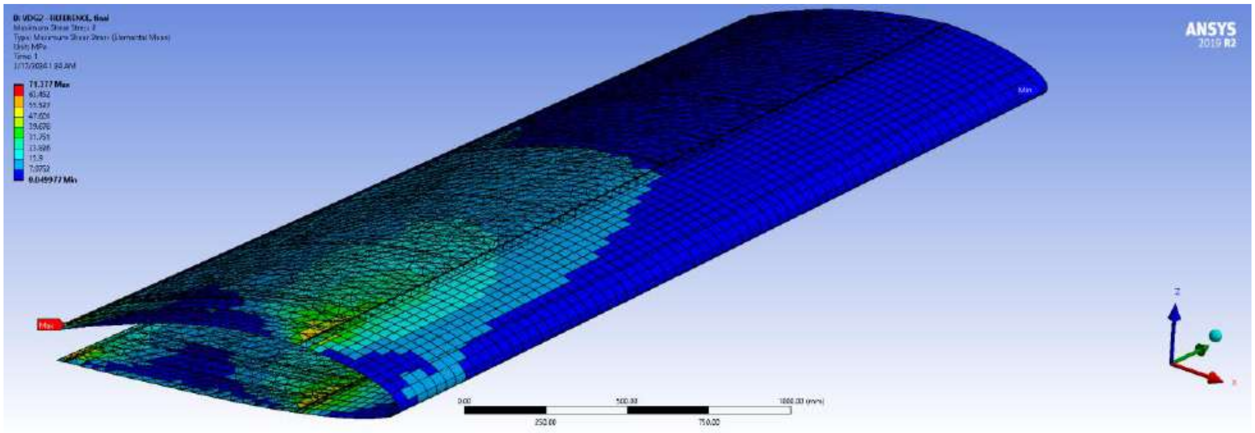

Εικόνα 130: Reference FEA Skin Maximum Shear Stress

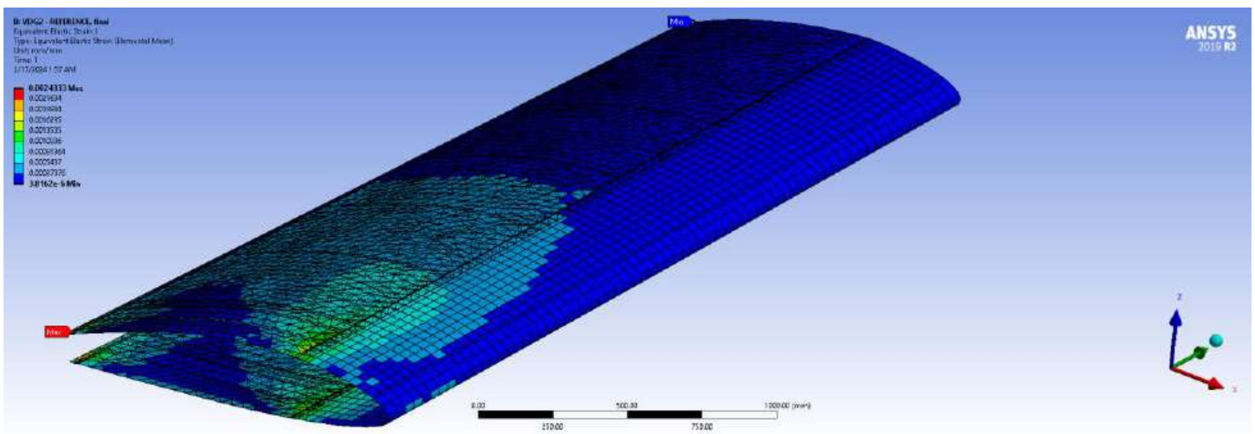

Εικόνα 131: Reference FEA Skin Equivalent Elastic Strain

<u>WING (AL6061-T6) STRENGTH</u>

Yield Tensile Strength: 276 MPa

Shear Strength: 207 MPa

<u>AN BOLT (STEEL) STRENGTH</u>

Tensile Strength: 862 MPa

Shear Strength: 524 MPa

5.3.2 Distributed Electric Propulsion Configuration

The sectional Lift (yellow region), Drag (green region) and Pitching Moment (blue region) values used in Nodal Forces and Moments in the DEP analysis are depicted below in red.

The Lift component of the sectional Nodal Force is positive in Z direction and the Drag component is negative in X direction. The sectional Pitching Moments tend to rotate the wing "nose-down" and thus their direction must be carefully defined in ANSYS.

The Nodal Force representing the High-Lift unit load constitutes of the thrust component $T_{HL} = 618\ N$ and the weight component $W_{HL} = -261\ N$ and is applied at Remote Points named "HL1", "HL2", "HL3", "HL4". The Nodal Force representing the Cruise unit load constitutes of the thrust component $T_C = 1961\ N$ and the weight component $W_C = -932\ N$ and is applied at the Remote Point named "CRUISE".

DEP - PROJECT

y (m)	$c_{elliptical}$ (m)	$c_{trapezoid}$ (m)	$c_{schrenk}$ (m)	v (m/s)	LIFT distr. (N/m)	Sectional LIFT Force	Qz (N)	E2	Mx (Nm)	DRAG distr. (N/m)	Sectional DRAG Force (N)	Qx (N)	E2	Mz (Nm)	PM distr. (Nm/m)	Sectional PM (Nm)	PM (Nm)
0	1.90985	1.6	1.7549	32	1415.88		-15432		22684	21.00		-229		336	-120.19		1310
0.16275	1.90966	1.59	1.7498	67	6188.90	619	-14813	-2461.1	20223	91.78	9	-220	-36.5	300	-525.36	-52.53	1257
0.3255	1.90947	1.58	1.7447	67	6170.88	1006	-13807	-2328.9	17894	91.51	15	-205	-34.5	265	-523.83	-85.38	1172
0.48825	1.90928	1.57	1.7396	67	6152.86	1003	-12804	-2165.5	15728	91.24	15	-190	-32.1	233	-522.30	-85.13	1087
0.651	1.90910	1.56	1.7345	32	1399.44	615	-12190	-2033.9	13694	20.75	9	-181	-30.2	203	-118.79	-52.17	1035
0.81375	1.90891	1.55	1.7295	67	6116.83	612	-11578	-1934.1	11760	90.71	9	-172	-28.7	174	-519.24	-51.92	983
0.9765	1.90872	1.54	1.7244	67	6098.81	994	-10584	-1803.4	9957	90.44	15	-157	-26.7	148	-517.71	-84.38	898
1.13925	1.90853	1.53	1.7193	67	6080.79	991	-9593	-1641.9	8315	90.18	15	-142	-24.3	123	-516.18	-84.13	814
1.302	1.90834	1.52	1.7142	67	6062.77	988	-8605	-1480.8	6834	89.91	15	-128	-22.0	101	-514.65	-83.88	730
1.46475	1.90815	1.51	1.7091	67	6044.75	985	-7619	-1320.2	5514	89.64	15	-113	-19.6	82	-513.12	-83.64	647
1.6275	1.90796	1.5	1.7040	67	6026.74	982	-6637	-1160.1	4354	89.37	15	-98	-17.2	65	-511.59	-83.39	563
1.79025	1.90777	1.49	1.6989	67	6008.72	979	-5658	-1000.5	3353	89.11	15	-84	-14.8	50	-510.06	-83.14	480
1.953	1.90758	1.48	1.6938	67	5990.70	976	-4681	-841.3	2512	88.84	14	-69	-12.5	37	-508.54	-82.89	397
2.11575	1.90740	1.47	1.6887	67	5972.68	974	-3708	-682.7	1829	88.57	14	-55	-10.1	27	-507.01	-82.64	315
2.2785	1.90721	1.46	1.6836	67	5954.66	971	-2737	-524.5	1305	88.31	14	-41	-7.8	19	-505.48	-82.39	232
2.44125	1.90702	1.45	1.6785	32	1354.23	595	-2142	-397.1	908	20.08	9	-32	-5.9	13	-114.96	-50.49	182
2.604	1.90683	1.44	1.6734	46	2789.89	337	-1805	-321.2	586	41.37	5	-27	-4.8	9	-236.83	-28.63	153
2.76675	1.90664	1.43	1.6683	46	2781.40	453	-1352	-256.9	330	41.25	7	-20	-3.8	5	-236.11	-38.48	115
2.9295	1.90645	1.42	1.6632	46	2772.90	452	-900	-183.2	146	41.12	7	-13	-2.7	2	-235.38	-38.37	76
3.09225	1.90626	1.41	1.6581	46	2764.41	451	-449	-109.8	37	41.00	7	-7	-1.6	1	-234.66	-38.25	38
3.255	1.90607	1.4	1.6530	46	2755.91	449	0	-36.6	0	40.87	7	0	-0.5	0	-233.94	-38.13	0

Πίνακας 27: DEP FEA Sectional Lift, Drag Forces and Pitching Moments in Excel

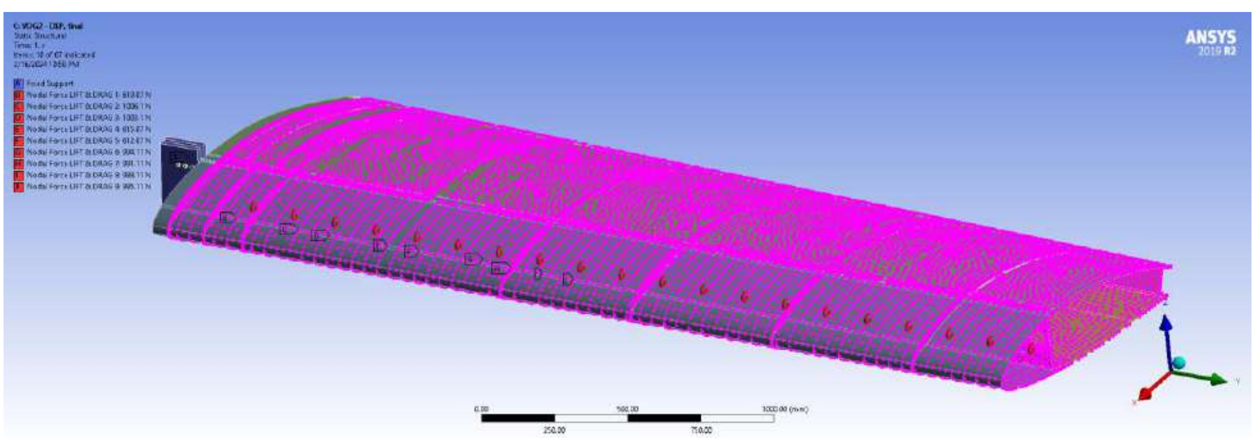

Εικόνα 132: DEP FEA ANSYS Workbench Setup (Nodal Forces, Moments, Fixed Support, Acceleration)

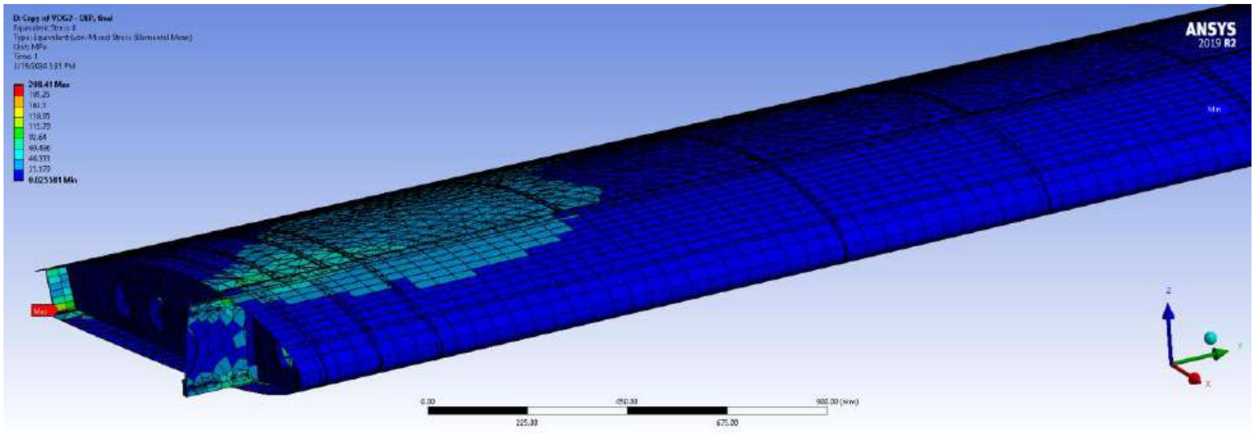

Εικόνα 133: DEP FEA Wing Equivalent Stress

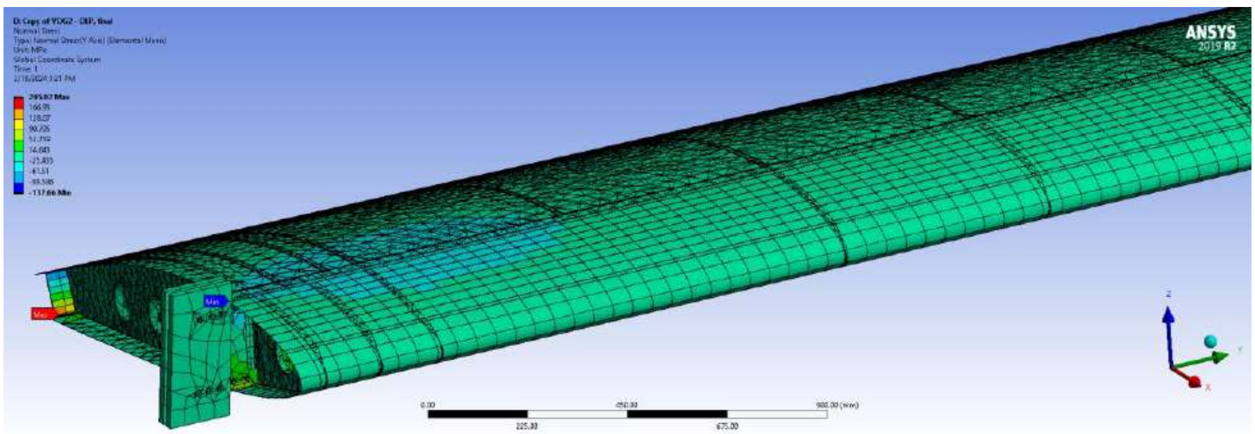

Εικόνα 134: DEP FEA Wing Normal Stress (Y Axis)

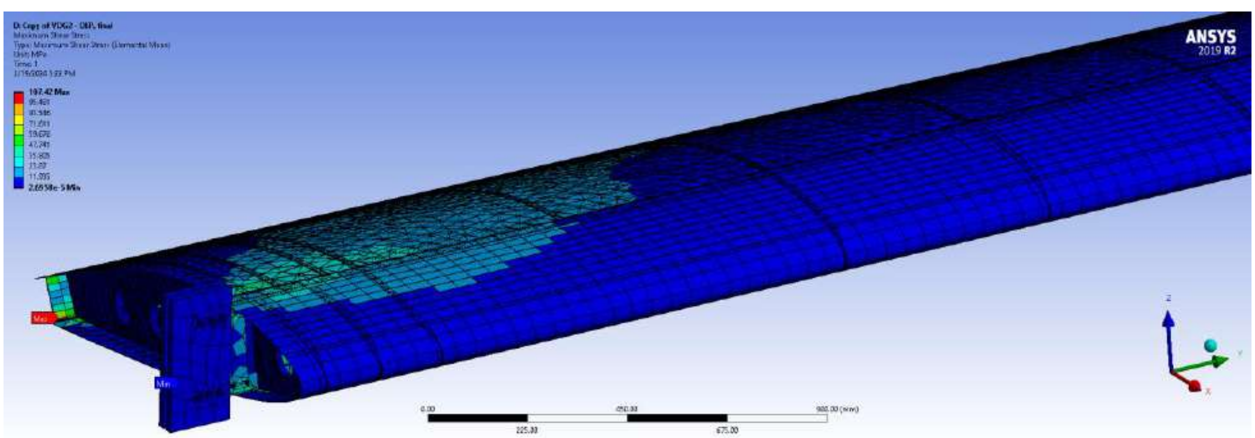

Εικόνα 135: DEP FEA Wing Maximum Shear Stress

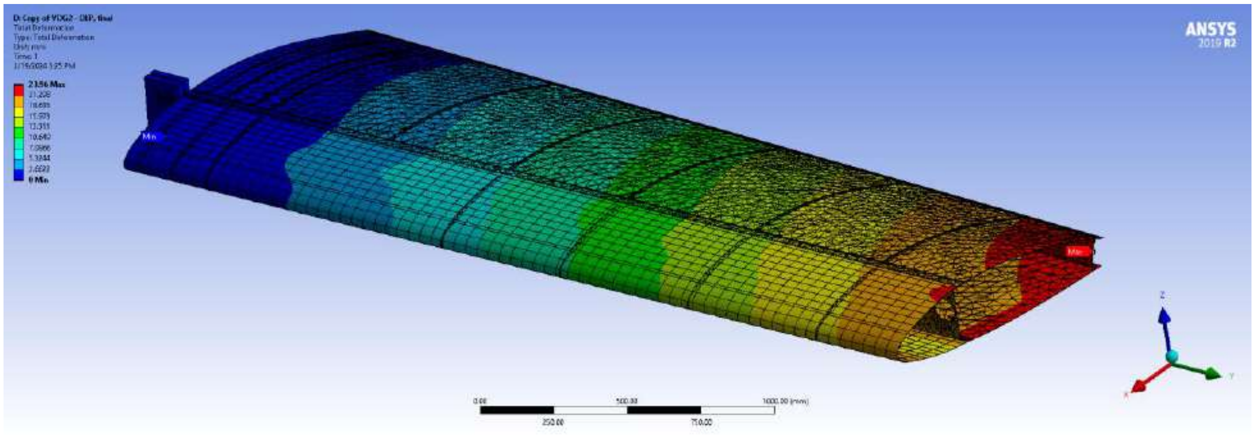

Εικόνα 136: DEP FEA Wing Total Deformation

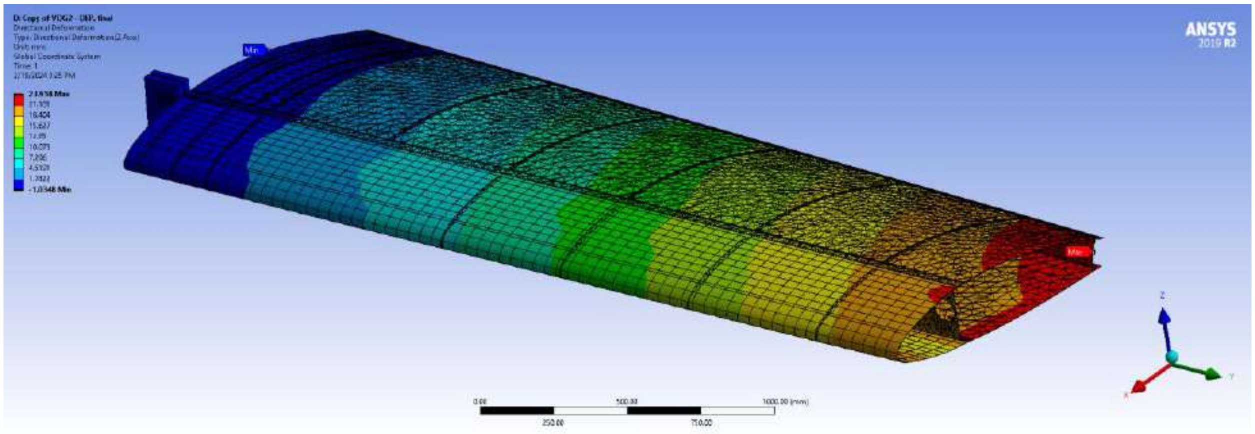

Εικόνα 137: DEP FEA Wing Directional Deformation (Z Axis)

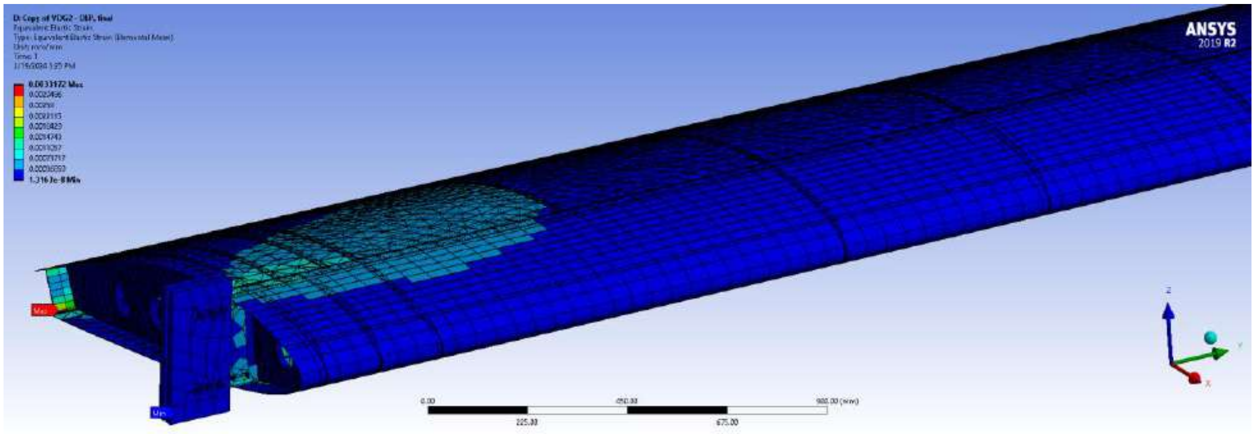

Εικόνα 138: DEP FEA Wing Equivalent Elastic Strain

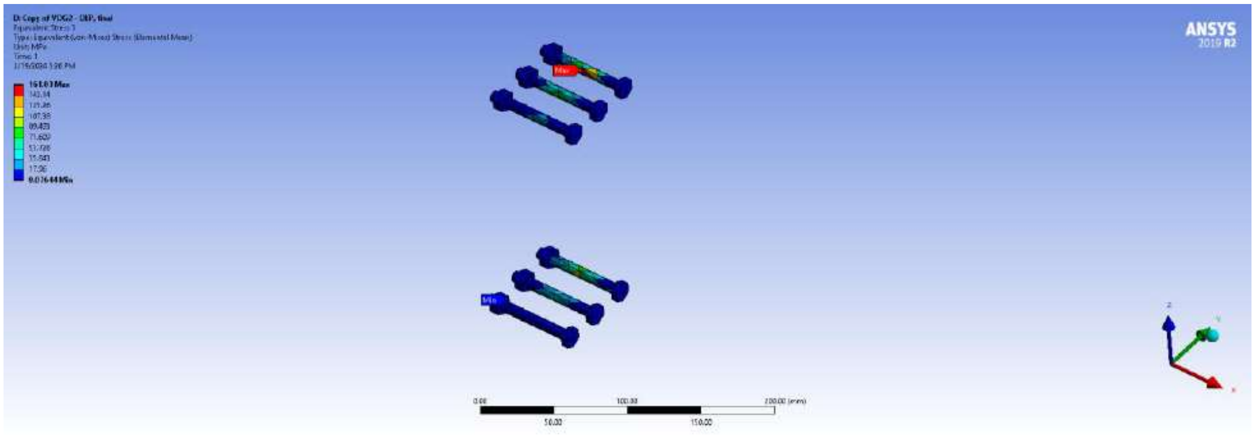

Εικόνα 139: DEP FEA AN-5 Bolts Equivalent Stress

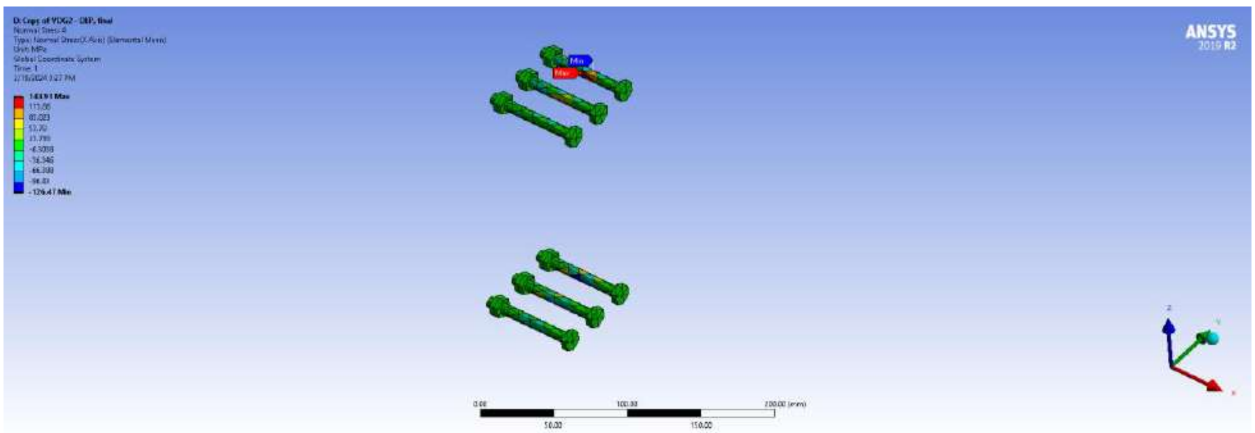

Εικόνα 140: DEP FEA AN-5 Bolts Normal Stress (X Axis)

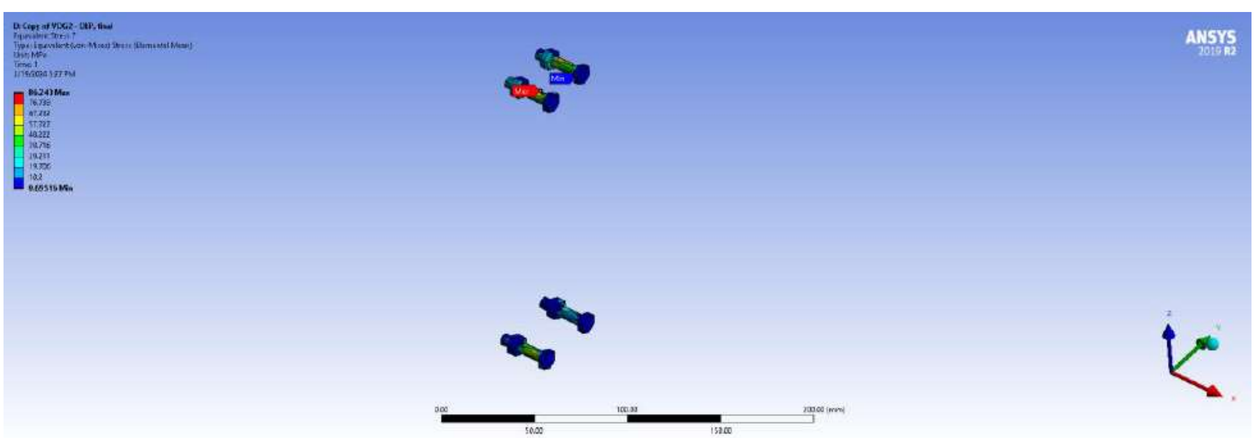

Εικόνα 141: DEP FEA AN-4 Bolts Equivalent Stress

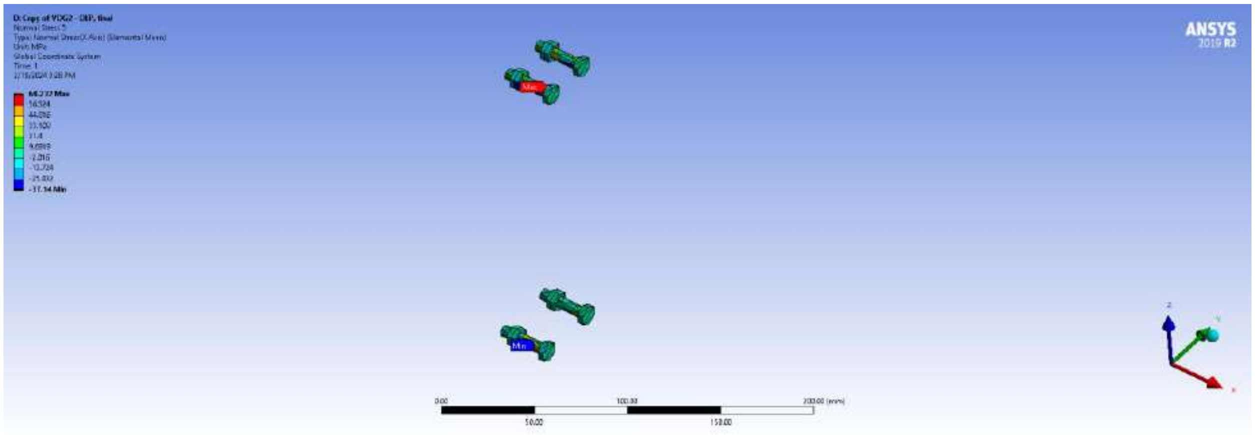

Εικόνα 142: DEP FEA AN-5 Normal Stress (X Axis)

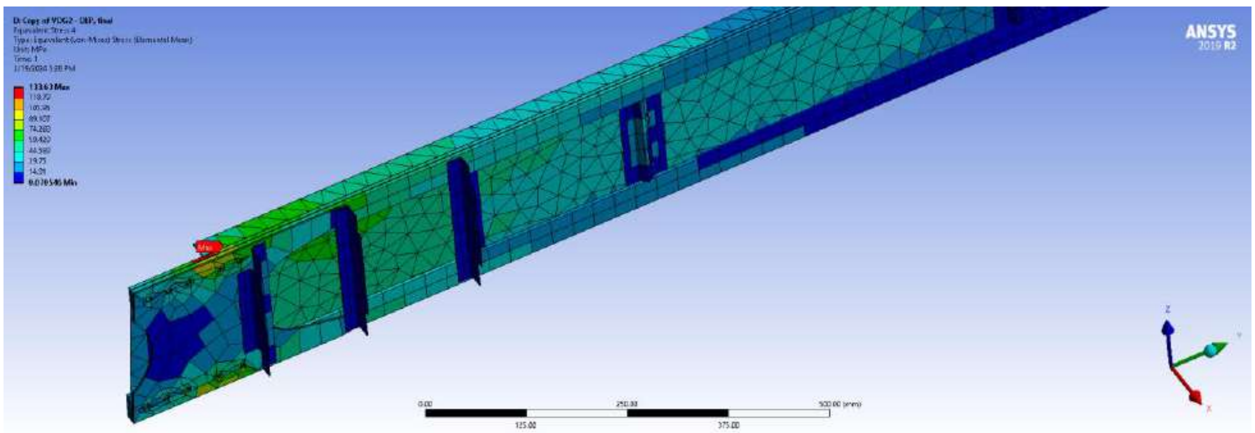

Εικόνα 143: DEP FEA Spar Equivalent Stress

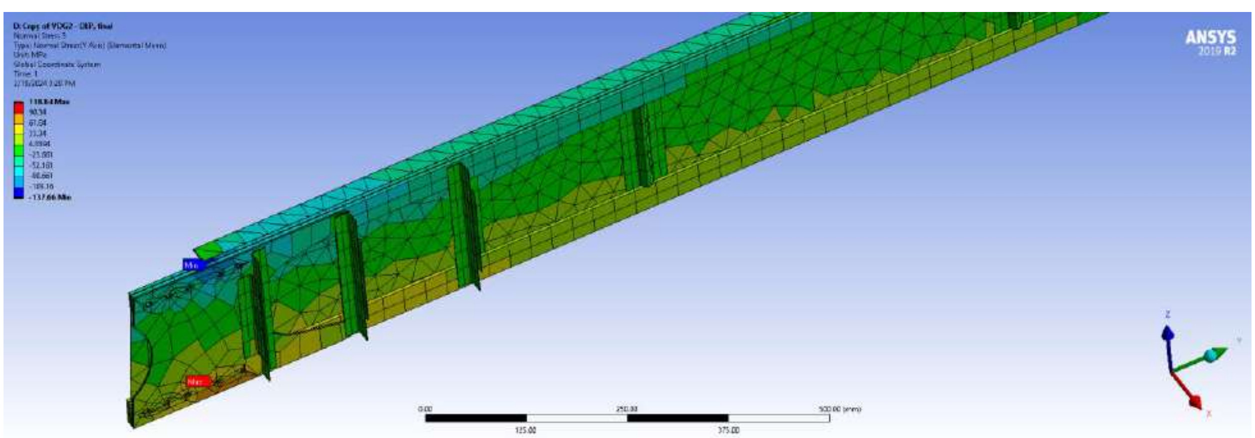

Εικόνα 144: DEP FEA Spar Normal Stress (Y Axis)

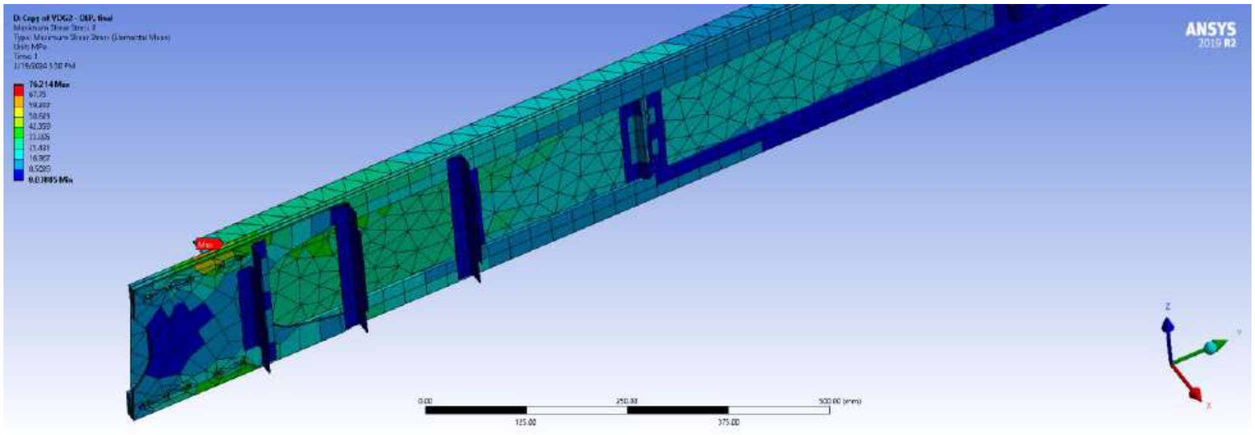

Εικόνα 145: DEP FEA Spar Equivalent Elastic Strain

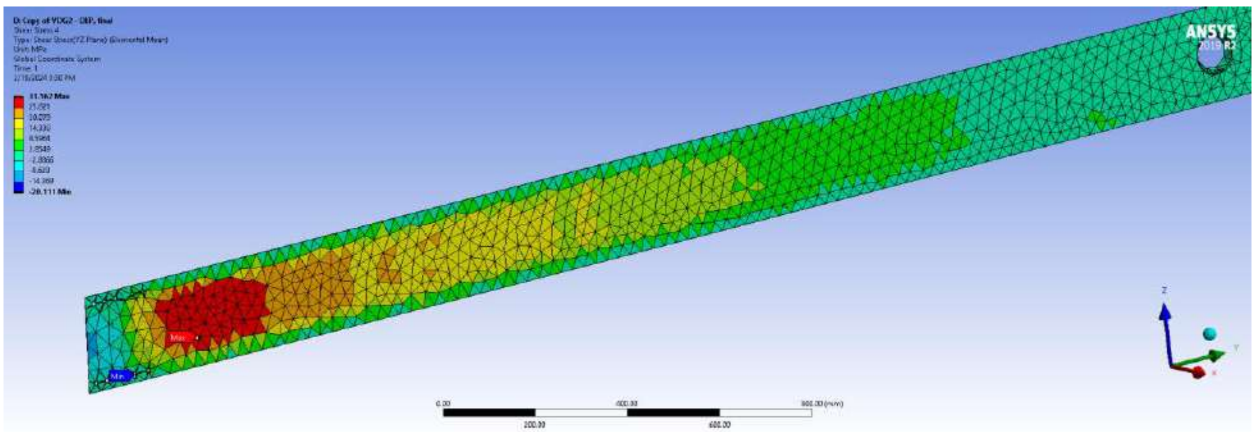

Εικόνα 146: DEP FEA Spar Web Shear Stress (YZ Plane)

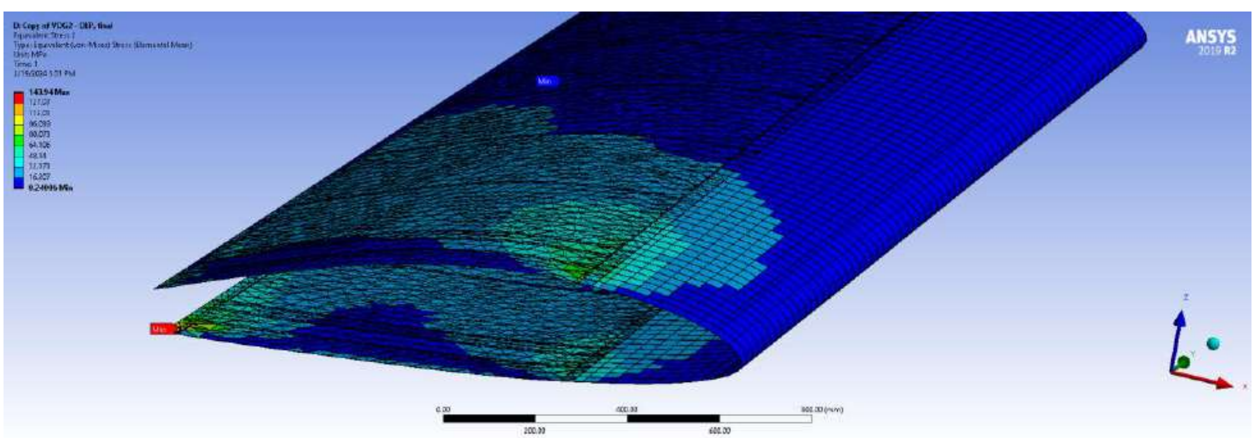

Εικόνα 147: DEP FEA Skin Equivalent Stress

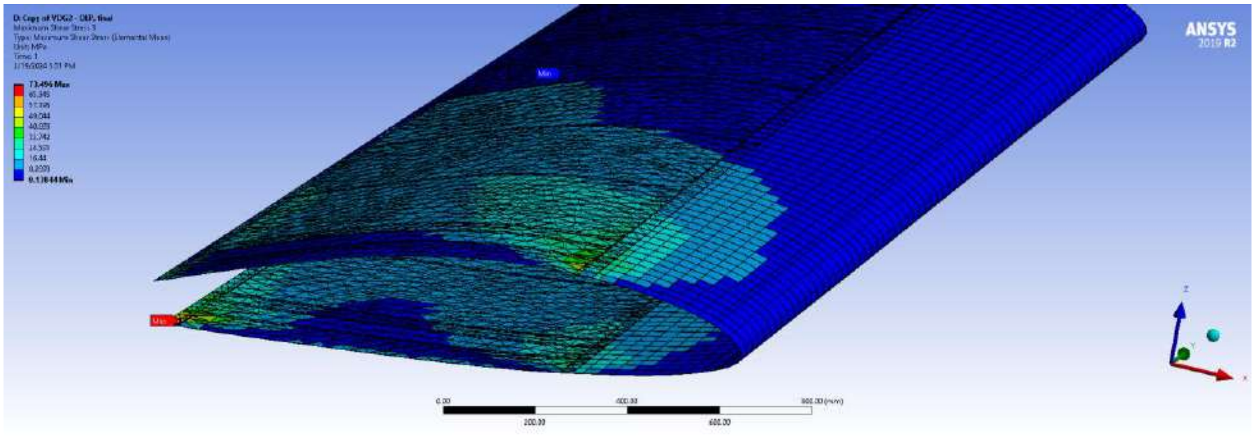

Εικόνα 148: DEP FEA Skin Maximum Shear Stress

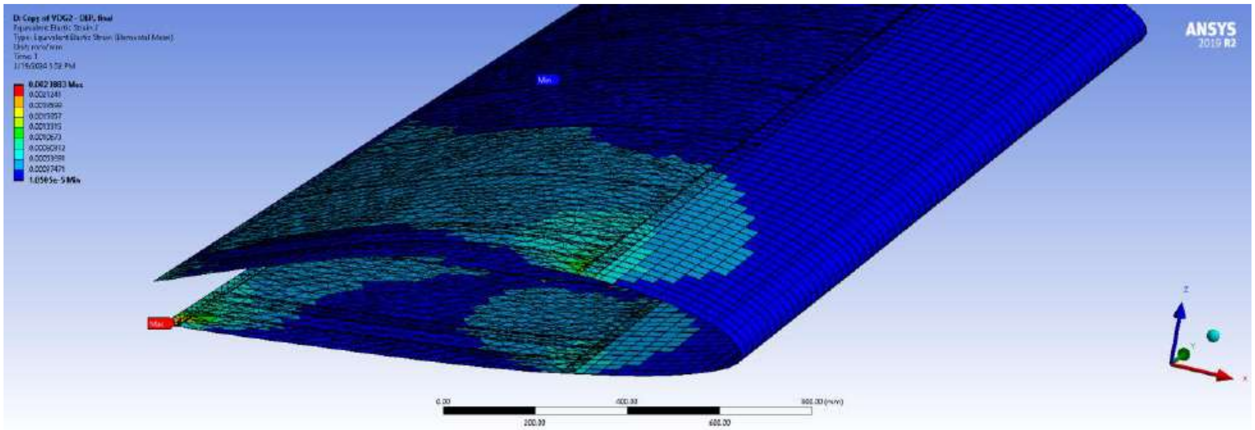

Εικόνα 149: DEP FEA Skin Equivalent Elastic Strain

WING (AL6061-T6) STRENGTH

Yield Tensile Strength: 276 MPa

Shear Strength: 207 MPa

AN BOLT (STEEL) STRENGTH

Tensile Strength: 862 MPa

Shear Strength: 524 MPa

5.3.3 Results

STRUCTURAL *(Wing)*	**REFERENCE Configuration**	**DEP Configuration**
Max Equivalent (Von Mises) Stress [MPa]	211.17	208.41
Max Normal Stress (Y Axis) [MPa]	208.97	205.02
Maximum Shear Stress [MPa]	109.26	107.42
Max Shear Stress (XY Plane) [MPa]	72.32	69.73
Max Shear Stress (XZ Plane) [MPa]	31.97	75.44
Max Shear Stress (YZ Plane) [MPa]	44.09	40.32
Max Total Deformation [mm]	39.26	23.96
Max Directional Deformation (Z Axis) [mm]	38.69	23.95
Max Equivalent (Von Mises) Elastic Strain [-]	0.0036841	0.0033172
Max Normal Elastic Strain (X Axis) [-]	0.0011009	0.0013957
Max Normal Elastic Strain (Y Axis) [-]	0.0029410	0.0027715
Max Normal Elastic Strain (Z Axis) [-]	0.0009089	0.0010821

Πίνακας 28: FEA Structural Results (Wing)

STRUCTURAL *(Bolts)*	**REFERENCE Configuration**	**DEP Configuration**
Max Equivalent (Von Mises) Stress (AN-5 BOLTS) [MPa]	206.25	161.03
Max Normal Stress (X Axis) (AN-5 BOLTS) [MPa]	187.88	143.91
Max Equivalent (Von Mises) Stress (AN-4 BOLTS) [MPa]	108.88	86.24
Max Normal Stress (X Axis) (AN-4 BOLTS) [MPa]	81.3	68.23

Πίνακας 29: FEA Structural Results (Bolts)

STRUCTURAL *(Spar)*	**REFERENCE Configuration**	**DEP Configuration**
Max Equivalent (Von Mises) Stress [MPa]	189.46	133.63
Max Normal Stress (Y Axis) [MPa]	184.33	137.66
Maximum Shear Stress [MPa]	105.96	76.21
Max Shear Stress (YZ Plane) (Spar Web) [MPa]	39.75	31.56

Πίνακας 30: FEA Structural Results (Spar)

STRUCTURAL *(Skin)*	**REFERENCE Configuration**	**DEP Configuration**
Max Equivalent (Von Mises) Stress [MPa]	138.04	143.94
Maximum Shear Stress [MPa]	71.37	73.49
Max Equivalent Elastic Strain [-]	0.0024333	0.0023883

Πίνακας 31: FEA Structural Results (Skin)

5.4 MODELING ASSUMPTIONS

- The wing geometry is modeled in CATIA V5 as an assembly of solid bodies.
- The aircraft control surfaces i.e. flaps and ailerons are not modeled in CAD since they are assumed a non-structural member of the wing.
- The nacelles housing the High-Lift and Cruise electric motors, are also assumed a non-structural member of the wing and are not included in the structural analysis. Therefore, the nacelles and their respective wing mounts are not modeled in the CAD file used in the ANSYS Workbench FEA.
- Riveting Holes across the geometry were designed in CATIA as they were necessary for the constraints and correct placement of parts and sub-assemblies. However, when the wing model was completed, the riveting holes were deactivated before saving the product as an STP, to be imported in ANSYS Workbench. The riveting holes are excluded due to mesh and computational cost implications, and also the immense amount of rivets that would require face selection with the adjacent wing components during "Contacts" refinement.
- Consequently, riveting is approximated using "bonded" type of contact between joint components.
- The wing root boundary condition of "Fixed Support" is an approximation. In reality, a wing is not exactly clamped at the fuselage, as some relative displacement is allowed.
- A software glitch in ANSYS was spotted, where the "Acceleration" Z component was applied in the opposite direction the +/- sign dictated. Inserting an "Acceleration" with a Z component of $-9806\,\frac{mm}{s^2}$ netted different results compared to inserting a "Standard Earth Gravity" with a Z component of $-9806\,\frac{mm}{s^2}$, whereas an "Acceleration" with a Z component of $9806\,\frac{mm}{s^2}$ netted the same results compared to inserting a "Standard Earth Gravity" with a Z component of $-9806\,\frac{mm}{s^2}$. Therefore, since the analysis corresponds to a load factor of $n = 3.8$,

an "Acceleration" with a Z component of $37278\frac{mm}{s^2}$ and not $-37278\frac{mm}{s^2}$ was inserted.

- "Geometry Selection" is selected as the "Scoping Method" of the spanwise aerodynamic center Remote Points, and the Spar Web faces were applied. A "Free Standing" scoping method would result in the Pitching Moments not applied to the wing structure and thus must be avoided.
- The 20 wing sections are created with "Nodal Named Selection". The nodes are manually selected and the Remote Points displaying the starting and ending points of each section lead to a smooth and complete wing discretization.
- The Element Method is set by default to "Automatic". The generated mesh consists of both triangular and rectangular finite elements, depending on the geometry, the existence of holes etc.
- The "Element Order" is set by default to "Program Controlled". "Quadratic" offers higher accuracy than "Linear" at the expense of computational cost. "Program Controlled" offers the best compromise between accuracy and computational cost and hence is selected.
- The smaller the mesh sizing, the greater accuracy results present. However a significant consequence of small mesh sizing is large computational cost. Due to the wing geometry being a very large model, a large computational cost can lead to errors and/or inability to solve the mathematical model, therefore the mesh sizing is not set lower than 10mm.
- An "Edge Sizing" is inserted and its entity "Number of divisions" is set to 2 in order to eliminate aspect ratio errors in thin-walled bodies where a single element was used in more than one directions.
- "Elemental Mean" option is selected in "Display Option" of "Integration Point Results" in order to eliminate mesh edge errors and local mesh issues. This option is applied to Stress and Strain calculations and essentially displays an elemental mean stress/strain value instead of nodal stress/strain values.
- Environment temperature is set by default to 22 °C.

6.0 THESIS REVIEW

6.1 ANALYTICAL & COMPUTATIONAL METHOD COMPARISON

Presented below are Spar stress and deformation results produced by the analytical method and the FEA method regarding both the Reference Configuration and the DEP Configuration.

The deviation e can be calculated from the equation below:

$$e = \frac{r - a}{r} \cdot (100\%)$$

where a is the analytical method value and r is the FEA method value.

REFERENCE Configuration	**Analytical Method**	**FEA Method**	***Deviation (%)***
Max Normal Stress (Spar) [MPa]	114.8	184.3	*37*
Max Equivalent Stress (Spar) [MPa]	118	189	*37*
Max Shear Stress (Skin) [MPa]	32.1	71.3	*55*
Max YZ Shear Stress (Web) [MPa]	46.8	39.7	*18*
Deflection (Z Axis) [mm]	78.4	38.7	*102*
Max Normal Stress (X Axis) (AN-5 Bolts) [MPa]	252.3	187.9	*34*
Max Normal Stress (X Axis) (AN-4 Bolts) [MPa]	64.3	81.3	*21*

Πίνακας 32: Analytical-FEA Results Comparison (Reference Configuration)

DEP Configuration	**Analytical Method**	**FEA Method**	***Deviation (%)***
Max Normal Stress (Spar) [MPa]	135.8	137.6	*2*
Max Equivalent Stress (Spar) [MPa]	143	133.6	*7*
Max Shear Stress (Skin) [MPa]	42.2	73.5	*42*
Max YZ Shear Stress (Web) [MPa]	67	31.5	*113*
Deflection (Z Axis) [mm]	71.5	23.9	*199*
Max Normal Stress (X Axis) (AN-5 Bolts) [MPa]	298.6	143.9	*107*
Max Normal Stress (X Axis) (AN-4 Bolts) [MPa]	76.1	68.2	*12*

Πίνακας 33: Analytical-FEA Results Comparison (DEP Configuration)

In the analytical method the Shear Flow Theory is used, assuming that only the wing spar flanges handle the normal loads, while in the FEA method, the wing loads are applied across the whole wing structure and the results are far more accurate.

Another reason for some cases of large deviation between analytical and FEA methods is that the analytical method is performed by superposition of 2-dimensional analyses in the YZ and XY planes, whereas the FEA method is a more precise, 3-dimensional analysis.

The comparison of results between analytical and FEA methods presents the respective maximum values. The large deviation can be attributed to some of those maximum values not sharing the same location, i.e. the wing root is assumed to be located 3.255m from the wing tip in the analytical method, whereas in the FEA method calculations were performed everywhere.

Especially in the case of Z Axis Directional Deformation, the analytical method calculates the spar deflection, while the FEA method calculates the total wing deflection. The whole wing structure obviously has a higher second moment of inertia than the spar, hence the significantly lower wing deflection calculated in FEA in both configurations.

6.2 STRUCTURAL ANALYSIS DISCUSSION

According to the FEA results in Chapter 5.3.3, the DEP configuration results in generally lower equivalent normal and shear stresses compared to the Reference configuration, despite producing more lift. Therefore, the DEP configuration is deemed a better configuration from a structural perspective.

The wing root bending moment is a function of load distribution. The center of load distribution in the DEP configuration is closer to the Fuselage centerline compared to the respective center of load distribution in the Reference configuration. Therefore, the closer the load distribution CoG to the wing root, the lower the bending moment is at the wing root. Moreover, loads such as motor and propeller weights that act in the opposite direction of lift are applied to the wing. Therefore, alleviation of Stress Concentration at Wing Root is achieved [20], as evidenced by the Results in Chapter 5.3.3.

The placement of motor-propeller cruise units at the wing tips increases the wing mass moment of inertia about the X axis and theoretically deteriorates lateral control due to slower roll [20]. However, the lower stresses in the DEP configuration could potentially enable making the wing structure more lightweight, thus eliminating the X axis mass moment of inertia increase. Moreover, in reality yaw and roll movements are coupled and as evidenced in Chapter 4.2 the yaw capability is massively improved, also influencing roll and thus minimizing the effect of extra wing tip weight.

The load case studied in this Thesis is an extreme scenario, where the aircraft is performing a correctly banked turn at 8000 ft. with maximum acceleration of 3.8g, with all propulsion units active, deploying full thrust. In general, the structural load would be significantly lower, i.e. in cruising condition where only the wingtip-mounted cruise units are responsible for propulsion, and high-lift propellers are folded, to increase efficiency. The high-lift propellers are mostly intended for STOL use or when very agile maneuvers are needed to be performed.

6.3 CONCLUSION

Distributed Electric Propulsion offers higher lift production. This feature can be utilized by implementing the system:

- to the existing wing, offering greater Lift production, STOL capabilities and massively increased maneuverability.
- to a new, smaller surface wing in order to improve efficiency while producing the same amount of Lift.

A Distributed Electric Propulsion system implementation does not come without drawbacks, with the most significant being a gross weight penalty affiliated with the Fuel-Cell system and the liquid Hydrogen tank. However, the benefits of such a configuration (structural stress concentration alleviation, dramatic performance improvement and greatly reduced environmental impact due to zero-emission LH2 Fuel-Cell system) far outweigh the drawbacks and make this an attractive configuration for current and future commercial aircraft.

Since the aircraft studied in this Thesis is a Light Sports Aircraft, the Distributed Electric Propulsion implementation was performance-oriented, installing the system to the existing wing in order to improve its maneuverability, increase lift production and enable STOL capabilities.

In larger commercial airliners, the Distributed Electric Propulsion implementation could be efficiency-oriented, installing the system to a new, smaller area wing in order to reduce drag and improve efficiency while maintaining the existing lift production.

A Distributed Electric Propulsion system implementation is deemed easier in larger aircraft with higher gravimetric index. That is due to the decreased weight penalty of the Fuel-Cell system and liquid Hydrogen tank compared to the total aircraft mass, thus maximizing the pros and minimizing the cons of such a configuration.

6.4 FUTURE RESEARCH

Further research can be initiated, either by building upon the findings of this Thesis, by addressing potential study limitations or by expanding the framework or model addressed in this Diploma Thesis.

Regarding structure optimization, minding the DEP configuration’s alleviated stress concentration, a more lightweight wing structure could be investigated using the same material. Taking a step further, composite material use in wing structure or individual components could be studied, investigating the application of anisotropic materials.

Regarding aerodynamics, a parametric CFD analysis could be performed to achieve aerodynamic topology optimization, investigating motor/propeller location relative to the wing, number and spacing of high-lift units, as well as motor specifications (power, torque, RPM) and propeller specifications (radius, blade geometry, thrust), as it is evident that the performance of the DEP blown wing is highly dependent on the flow acceleration. Then, a CFD analysis can calculate a very accurate Pressure Distribution to be inserted into the Structural analysis, replacing the need of discretized lift, drag and pitching moment calculation, and provide excellent result accuracy.

Regarding finite elements, a parametric mesh convergence study could be investigated. The purpose of Mesh optimization is to run a structural analysis with maximum accuracy, either by much smaller mesh sizing and quadratic element order, or by optimizing the mesh in areas where it is more critical (i.e. the structural error is higher). Moreover, a structural analysis with a CAD model that includes the very large number of rivets could be performed, in order to compare it with the “bonded” contact approximation and also calculate rivet stresses. A computer able to handle the much higher computational cost is required.

Finally, regarding structural analysis completeness, a total wing, skin and individual stiffener buckling analysis could be performed, especially if combined with the procedure of making the wing structure more lightweight. Moreover, a structural analysis with a CAD model that includes the very large number of rivets could be performed, in order to compare it with the “bonded” contact approximation and also calculate rivet stresses. A computer able to handle the much higher computational cost is again required.

REFERENCES

1. Gohardani, A. S., Doulgeris, G., & Singh, R. (2011). Challenges of future aircraft propulsion: A review of distributed propulsion technology and its potential application for the all-electric commercial aircraft. In *Progress in Aerospace Sciences* (Vol. 47, Issue 5, pp. 369–391). https://doi.org/10.1016/j.paerosci.2010.09.001
2. Kim, Hyun Dae (2010). Distributed Propulsion Vehicles, 27th International Congress of the Aeronautical Sciences, 2010
   https://ntrs.nasa.gov/citations/20100036222
3. Ko, A., Schetz, J. A., & Mason, W. H. (2003). Assessment of the Potential Advantages of Distributed Propulsion for Aircraft
   https://www.academia.edu/80005621/Assessment_of_the_potential_advantages_of_distributed_propulsion_for_aircraft?f_ri=24557
4. Katsiropoulos, C. (2018), Introduction to Aeronautical Materials, Lecture 10: New Trends in Aviation, University of Patras, Greece
5. Kermanidis T., Labeas G., (2021), Lightweight Structures and Aircraft Structure Analysis, University of Patras, Greece
6. Anderson Jr, J., (2017), Fundamentals of Aerodynamics - Sixth Edition, McGraw-Hill Education, USA
   https://aviationdose.com/wp-content/uploads/2020/01/Fundamentals-of-aerodynamics-6Edition.pdf
7. Unifier-19, retrieved from:
   https://www.unifier19.eu/www.unifier19.eu/index.html
8. HY4, retrieved from:
   https://www.h2fly.de/
9. X-57 Maxwell, retrieved from:
   https://www.nasa.gov/aeronautics/x-57-maxwell/
10. Al6061-T6, retrieved from:
    https://www.makeitfrom.com/material-properties/6061-T6-Aluminum
11. Zenith Zodiac CH 650 B Engines, retrieved from:
    http://www.zenithair.com/zodiac/xl/3300.html
    http://www.zenithair.com/zodiac/xl/o200.html
12. Zenith Zodiac CH 650 B, retrieved from:
    https://zenithair.net/
13. Cusati, V., Corcione, S., Nicolosi, F., & Zhang, Q. (2023). Improvement of Take-Off Performance for an Electric Commuter Aircraft Due to Distributed Electric Propulsion. Aerospace, 10(3). https://doi.org/10.3390/aerospace10030276
14. Hospodář, P., Klesa, J., Demovič, D., & Žižkovský, N. (2022). Aerodynamic and Structural Aspects of a Distributed Propulsion System for Commuter Airplane. *Aerospace*, *9*(11). https://doi.org/10.3390/aerospace9110712

15. 10 Prepared, C., & Al-Hussaini, A. A. (2013). UOT Mechanical Department / Aeronautical Branch Aircraft Design Chapter Ten / Air-Inertia Load Distribution.
https://uotechnology.edu.iq/dep-MechanicsandEquipment/Lectures%20and%20Syllabus/Lectures/Aircraft/Foruth%20Grade/Aircraft%20Design3.pdf
16. GA 35-A-415 Airfoil Data, retrieved from:
https://www.bigfoil.com/f775da41-bbff-4788-9a16-5afd1009622f_info.php
17. E-Props Thrust Data, retrieved from:
https://vtol.e-props.fr/DOCS/curves_hep_apm2.pdf
https://vtol.e-props.fr/DOCS/curves_hep_fpm.pdf
18. Ganesh, R. V. (2018). Design Optimization of a Regional Transport Aircraft with Hybrid Electric Distributed Propulsion Systems.
https://vtechworks.lib.vt.edu/bitstream/handle/10919/84494/Rajkumar_V_T_2018.pdf?isAllowed=y&sequence=1
19. Load Factors, Maneuvers, Banked Turns Flight Design Envelope, retrieved from:
https://www.flight-study.com/2021/01/load-factors-aerodynamics-of-flight.html?m=1&expand_article=1
20. Sadraey, M. (n.d.). *CHAPTER 5 WING DESIGN*.
http://wpage.unina.it/fabrnico/DIDATTICA/PGV_2012/MAT_DID_CORSO/09_Progetto_Ala/Wing_Design_Sadraey.pdf
21. Boundy, B; Diegel, S; Wright, L.; Davis, S. (2011). Biomass Energy Databook, Oak Ridge National Laboratory 4th Edition
https://info.ornl.gov/sites/publications/Files/Pub33120.pdf
22. U.S. Department of Energy. Fuel-Cell Fact Sheet
https://www.energy.gov/eere/fuelcells/articles/fuel-cells-fact-sheet
23. Dinc, A.; Gharbia, Y. Exergy Analysis of a Turboprop Engine at Different Flight Altitude and Speeds using Novel Consideration. (2022).
https://www.degruyter.com/document/doi/10.1515/tjeng-2020-0017/html
24. RAYMER(*Aircraft Design - A Conceptual Approach 2nd Ed. - D. Raymer (1992) WW*, n.d.)
https://www.airloads.net/Downloads/Textbooks/Aircraft%20Design-A%20Conceptual%20Approach.pdf
25. AN Bolts Material and Strength Data, retrieved from:
https://www.aircraftspruce.com/catalog/hapages/an5.php